H_2O LASER ABSORPTION AND OH* CHEMILUMINESCENCE MEASUREMENTS OF H_2-NO_2 OXIDATION IN A SHOCK TUBE

A Dissertation

by

CLAYTON REED MULVIHILL

Submitted to the Office of Graduate and Professional Studies of
Texas A&M University
in partial fulfillment of the requirements for the degree of

DOCTOR OF PHILOSOPHY

Chair of Committee,	Eric L. Petersen
Committee Members,	Rodney D.W. Bowersox
	Waruna D. Kulatilaka
	David Staack
Head of Department,	Andreas Polycarpou

August 2019

Major Subject: Mechanical Engineering

ABSTRACT

The mitigation of NOx pollutants continues to be a matter of environmental and economic interest in the gas-turbine industry, and an improved understanding of fundamental NOx chemical kinetics has led to reductions in NOx emissions. However, the exhaust gas recirculation (EGR) method necessitates an accurate understanding of NOx/fuel interactions, and few experimental data with NOx as the sole oxidizer exist. New measurements of this kind would provide unique target data for the continuing design and optimization of NOx chemical kinetics mechanisms.

To this end, new combustion data in the H_2-NO_2 system were acquired. Experiments were performed behind reflected shock waves near 1 atm and at temperatures between 917 and 2003 K. Fuel-lean, near-stoichiometric, and fuel-rich mixtures of H_2-NO_2 diluted in ~99% Ar were studied. A laser absorption diagnostic near 1.39 μm measured H_2O time histories, while an emission diagnostic near 307 nm measured exited-state OH (OH*) time histories. Kinetic modeling of the H_2O data revealed the species HONO and NO_3 are important in the H_2O reaction pathways. Newer mechanisms predicted the experimental H_2O profiles quite well at fuel-lean and high-temperature conditions, but discrepancies persisted at fuel-rich and low-temperature conditions despite variation of the most-sensitive reactions. The kinetic models were unable to predict the experimental OH* profile shapes with any sort of accuracy, suggesting the need for a new OH*-forming reaction. By fitting the OH* profile shapes and considering exothermicity, the reaction NH + NO_2 ⇄ N_2O + OH* was identified, and a tentative rate constant of $k_{13} = 5.0\times10^{16}\cdot\exp(-40{,}000/RT)$ was proposed (units of [cal], [mol], [cm^3], [s]).

ACKNOWLEDGMENTS

I would like to thank my committee members Drs. Rodney Bowersox, Waruna Kulatilaka, and David Staack for their time and oversight throughout the course of my graduate studies, and also Dr. Adonios Karpetis for serving as a substitute at my defense.

Eight years in the Petersen research group have encompassed so many memorable experiences it would be difficult to recount them all here. Traveling the world, surviving classes, troubleshooting experiments, betraying one another in board games, running experiments late at night, enjoying good food, hiking through nature; these are but a few. So, to the colleagues past and present who have made my time in this research group such a pleasure: thank you for the years of camaraderie. I treasure the memories we've made.

To Dr. Petersen: it would be difficult to express the level of respect I have for you. Your hardworking yet kind nature makes this research group the best there is. Thank you for the support, guidance, prodding, encouragement, and opportunity you have so graciously provided for the last eight years. It has been an honor to be your student.

To my family: times with you are some of my favorite moments, and each one of you has shaped me in different ways. I am beyond thankful for you all, both those who are of blood and those I gained four years ago.

And finally, to Meredith: your help in these last few months and years has been far beyond what I could have expected. Thank you for your sacrifices to make this dissertation a reality. I would not have survived the process without your encouragement, smiles, service, laughter, and love (not to mention a huge amount of proofreading). It is a blessing to have you by my side as my wife and best friend.

CONTRIBUTORS AND FUNDING SOURCES

Contributors

This work was supported by a dissertation committee consisting of Professors Eric L. Petersen, Waruna D. Kulatilaka, and David Staack of the Department of Mechanical Engineering and Professor Rodney D.W. Bowersox of the Department of Aerospace Engineering.

The H_2O time-history data in Section 5 were obtained with the help of Professor Olivier Mathieu and were published in 2019 in an article by Mulvihill et al., as listed in the References of Section 5. The analysis pertaining to the detector offsets in Appendix B was developed with the help of Joshua Hargis.

All other work conducted for the dissertation was completed by the student independently.

Funding sources

Graduate study was supported by a Graduate Research Fellowship from the National Science Foundation under Grant Number DGE-1252521 and by a Graduate Summer Research Grant from the Department of Mechanical Engineering.

Additional support for this work came from the National Science Foundation under Grant Number CBET-1706825. The contents of this work are solely the responsibility of the author and do not necessarily represent the official views of the National Science Foundation.

TABLE OF CONTENTS

Page

ABSTRACT ii

ACKNOWLEDGMENTS iii

CONTRIBUTORS AND FUNDING SOURCES iv

TABLE OF CONTENTS v

LIST OF FIGURES x

LIST OF TABLES xvi

1. INTRODUCTION 1

1.1 Spectroscopy 2
1.2 Optical diagnostics 3
1.3 Shock tubes 5
1.4 The H_2-NO_2 system 7
1.5 Organization of the dissertation 9
1.6 References 11

2. TERMINOLOGY OF MOLECULAR SPECTROSCOPY 15

2.1 Preliminary considerations 15
2.1.1 Potential energy wells 17
2.1.2 Dipole moments 20
2.2 Spectroscopy of diatomic molecules 20
2.2.1 Rotational spectroscopy of diatomic molecules 21
2.2.2 Vibrational spectroscopy of diatomic molecules 24
2.2.3 Rovibrational spectroscopy of diatomic molecules 27
2.2.4 Rovibronic spectroscopy of diatomic molecules 30
2.3 Spectroscopy of polyatomic molecules 36
2.3.1 Rotational spectroscopy of polyatomic molecules 36
2.3.2 Vibrational spectroscopy of polyatomic molecules 39
2.3.3 Rovibrational spectroscopy of polyatomic molecules 40
2.3.4 Rovibronic spectroscopy of polyatomic molecules 41
2.4 Summary 41
2.5 References 42

Page

3. THEORY OF QUANTITATIVE OPTICAL DIAGNOSTICS 44

3.1 The Beer-Lambert law 45
3.1.1 Derivation of the Beer-Lambert law 46
3.1.2 Assumptions of the Beer-Lambert law 55
3.1.3 Spectroscopic saturation effects 57
3.2 Calculation of the line strength 62
3.2.1 Transition probabilities and Boltzmann populations 63
3.2.2 Temperature dependence 65
3.3 Calculation of the line shape 68
3.3.1 The Gaussian (Doppler) profile 68
3.3.2 The Lorentzian (collisional) profile 70
3.3.3 The Voigt profile 71
3.3.4 Collisional line shift 74
3.4 Emission spectroscopy 76
3.4.1 Basic principles of emission spectroscopy 76
3.4.2 Population of the upper state 78
3.4.3 Reaction rates for collisional processes 80
3.4.4 Challenges of emission diagnostics 81
3.5 Summary 82
3.6 References 84

4. METHODOLOGY OF SHOCK-TUBE OPTICAL DIAGNOSTICS 87

4.1 Shock tube 87
4.1.1 Analysis of a normal shock wave 88
4.1.2 Vibrational relaxation 90
4.1.3 Configuration of the shock tube 95
4.1.4 Diagnostic access 99
4.2 H_2O laser absorption diagnostic 101
4.2.1 Tunable diode laser 102
4.2.2 Configuration of the laser diagnostic 102
4.2.3 Selection and modeling of the H_2O transition 106
4.2.4 Analysis of laser data 109
4.2.5 Interference from broadband emission 111
4.2.6 Interference from other absorbing species 114
4.3 OH* chemiluminescence diagnostic 116
4.3.1 Configuration of the emission diagnostic 116
4.3.2 Analysis of emission data 117
4.3.3 Interference from other emitting species 119
4.4 NO_2 LED absorption diagnostic 124
4.4.1 Configuration of the LED diagnostic 125
4.4.2 Modeling and validation of the NO_2 absorption coefficient 126
4.5 Summary 129

Page

4.6 References 131

5. MEASUREMENTS AND MODELING OF H_2-NO_2 OXIDATION 135

5.1 Verification of shock-tube test mixtures 135
5.1.1 NO_2 dimerization issues 135
5.1.2 Measurements of mixture NO_2 concentrations 139
5.2 Chemical kinetics modeling 141
5.2.1 Introductory comments on chemical kinetics 141
5.2.2 Numerical solution techniques 143
5.2.3 Updates to OH*-quenching reactions 145
5.3 H_2O time histories and modeling 146
5.3.1 H_2O time histories 147
5.3.2 Reaction pathway analysis at fuel-lean conditions 149
5.3.3 Reaction pathway analysis at fuel-rich conditions 152
5.3.4 Sensitivity analysis 153
5.3.5 Initial H_2O formation 155
5.3.6 Interfering absorption from NO_2 157
5.4 OH* time histories and modeling 161
5.4.1 OH* time histories 162
5.4.2 Identifying a new chemiluminescent reaction 164
5.4.3 Modifications to k_{14} 169
5.4.4 Mechanism-dependent nature of fitting 170
5.4.5 Energetic considerations for chemiluminescent reactions 171
5.5 Summary 173
5.6 References 174

6. CONCLUSIONS 178

6.1 Molecular spectroscopy 178
6.2 Quantitative optical diagnostics 179
6.3 Experimental methodology 182
6.4 H_2-NO_2 experiments and modeling 184
6.5 Future outlook 187
6.6 References 189

APPENDIX A. NOISE REDUCTION TECHNIQUES FOR LASER ABSORPTION EXPERIMENTS 190

A.1 Vibrational noise: Physical suppression of vibrations 190
A.1.1 Clamping of TEC fans 191
A.1.2 Isolation of shock tube and optics 192
A.1.3 Placements of shock-tube supports 192
A.1.4 Actively damped optical table 192

Page

A.1.5 Straps 193
A.2 Vibrational noise: Reduction of sensitivity to vibrations 193
A.2.1 Tightening of optics 193
A.2.2 Lens orientation 194
A.2.3 Centering through lenses 195
A.2.4 Cleaning of windows 195
A.2.5 Iris opening size 196
A.2.6 Detector face orientation 197
A.2.7 Alignment through shock-tube windows 198
A.2.8 Relocation of polarizers 200
A.2.9 Overhanging optical tables 200
A.2.10 Shortening optical path length 200
A.3 Electrical noise 201
A.3.1 Bit noise 202
A.3.2 Differential preamplifier 203
A.3.3 Cable impedance 205
A.3.4 Signal filtering 205
A.3.5 Wall-socket noise 206
A.3.6 Grounding of electronics 206
A.4 Optical noise 207
A.5 Summary 208
A.6 References 209

APPENDIX B. DATA ANALYSIS PROCEDURES FOR LASER ABSORPTION EXPERIMENTS 210

B.1 Detector offsets and imbalances 210
B.2 Correcting for the non-ideal pressure rise 214
B.3 Correcting for temperature change due to reactivity 216
B.4 Scanned-wavelength measurements 218
B.5 Summary 220
B.6 References 221

APPENDIX C. THEORY AND TECHNIQUES FOR STABLE OPERATION OF THE TUNABLE DIODE LASER 223

C.1 Basic laser theory 223
C.1.1 Components of a laser 223
C.1.2 Population inversion 224
C.1.3 Lasing threshold 225
C.2 External-cavity diode lasers 227
C.2.1 Diodes 227
C.2.2 The Littrow configuration 228
C.2.3 Suppression of longitudinal modes 231

Page

C.3 Techniques for stable operation 233
C.3.1 Tuning the laser 234
C.3.2 Single-mode operation 235
C.3.3 Mode-hopping issues 236
C.3.4 Adjusting the feedback 237
C.4 Summary 238
C.5 References 238

APPENDIX D. UTILIZATION OF THE HITRAN DATABASE 239

D.1 Overview of the database 240
D.2 The line-by-line format 241
D.3 Using HITRAN at high temperatures 247
D.4 Sorting through HITRAN 249
D.5 Summary 250
D.6 References 250

LIST OF FIGURES

Page

Figure 1.1 Depiction of a triatomic molecule, denoting some of the molecular features that can be determined with high accuracy using spectroscopic techniques. 3

Figure 1.2 Attenuation of a light source traversing an absorbing gas as described by the Beer-Lambert law. 4

Figure 1.3 Illustration of a conventional shock tube, showing (a) an x-t diagram, (b) the corresponding axial pressure distributions at times t_1 and t_2, and (c) the corresponding axial temperature distributions at times t_1 and t_2 7

Figure 2.1 Emission and absorption processes between the discrete energy levels of a generic diatomic molecule. 16

Figure 2.2 Molecular potential energy diagram for a general diatomic bond, showing discrete vibrational and rotational energy levels. 17

Figure 2.3 (a) Electronic, vibrational, and rotational transitions and (b) their approximate locations on the electromagnetic spectrum. 19

Figure 2.4 The P and R branches of the 1←0 band of $^{12}C^{16}O$ at 296 K according to HITRAN 2004 29

Figure 2.5 Angular momentum diagram for the electron orbital angular momentum in a diatomic molecule. 31

Figure 2.6 Angular momentum diagram for the coupling scheme of Hund's case (a). 33

Figure 2.7 Calculated spectrum of the CH *A*←*X* band according to Mulvihill et al., showing (a) the P, Q, and R branches and (b) Λ-type doubling. 36

Figure 2.8 Angular momentum vector diagram for the symmetric top 38

Figure 2.9 The vibrational modes of H_2O: (a) symmetric stretching, (b) bending, and (c) asymmetric stretching. 40

Figure 3.1 The two-level spectroscopic model of a system with $\Delta E_{12} = h\nu_{12}$,

Page

showing radiative and non-radiative processes..... 48

Figure 3.2 Comparison of the Beer-Lambert law and the optically thin approximation. 54

Figure 3.3 Illustration of the cases of (a) spectrally broad and (b) spectrally narrow sources ρ_v as compared to the absorption line shape ϕ. 59

Figure 3.4 Graphical depiction of Eq. (3.27) using arbitrary values, demonstrating the line strength is the integrated area under the absorption coefficient..... 63

Figure 3.5 Temperature dependence of various terms in Eq. (3.36) for varying values of $\bar{E}''$ and $\bar{\nu}_{12}$. 67

Figure 3.6 Gaussian, Lorentzian, and Voigt line shape models with $\Delta\bar{\nu}_D$ set equal to $\Delta\bar{\nu}_C$. 73

Figure 3.7 Example of a collisional line shift. 75

Figure 3.8 Ratio of the upper- to lower-state populations as a function of T according to the Boltzmann distribution, Eq. (3.29), for various values of $\bar{\nu}_{12}$. 79

Figure 4.1 Control volume around a normal shock wave with velocity v_s using (a) lab-fixed coordinates and (b) shock-fixed coordinates..... 89

Figure 4.2 Illustration of the 1/e vibration relaxation time τ_{vib}..... 92

Figure 4.3 τ_{vib} versus temperature at 1 atm and 5 atm for a mixture of 0.2% H_2, balance Ar. 95

Figure 4.4 Schematic of the shock tube, mixing tank, and mixing manifold (not drawn to scale)..... 96

Figure 4.5 Sample (a) raw pressure transducer signals and (b) measured values of v_s at the different measurement locations (i.e., in between each pair of transducers). 100

Figure 4.6 Schematic of the H_2O laser absorption diagnostic..... 103

Figure 4.7 H_2O line strengths at 1600 K according to HITRAN 2004, showing (a) vibrational structure across the near/mid-IR and (b) rotational structure near the selected transition..... 107

Page

Figure 4.8 Temperature and pressure dependence of (a) k_v and (b) Δ_s for the $5_{5,1}\leftarrow5_{5,0}$, 101←000 transition of H_2O. 109

Figure 4.9 Sample experimental traces for (a) I_t/I_0 and (b) sidewall pressure. ... 110

Figure 4.10 Experimental (a) sidewall pressure and (b) detector signals during a shock experiment with the laser turned off to check for broadband emission. 113

Figure 4.11 Neighboring absorption spectra of the $5_{5,1}\leftarrow5_{5,0}$ transition of H_2O..... 115

Figure 4.12 Schematic of the OH* chemiluminescence diagnostic. 117

Figure 4.13 Sample OH* measurement and sidewall pressure trace, showing the definition of $\tau_{50\%}$. 118

Figure 4.14 Log-log plot of the gain versus the supply voltage for the PMT 119

Figure 4.15 OH line strengths in the $A\,^2\Sigma^+\rightarrow X\,^2\Pi$ band at 1800 K and measured transmission curves of two bandpass filters. 120

Figure 4.16 Comparison of normalized emission signals obtained using different bandpass filters. 121

Figure 4.17 Comparison of PMT signals obtained at similar conditions in mixtures with H_2 (0.222% H_2, 0.392% NO_2, balance Ar) and without H_2 (0.392% NO_2, balance Ar)..... 123

Figure 4.18 Comparison of (a) PMT signals obtained using different bandpass filters at similar conditions and (b) measured transmission curves for the two filters. 124

Figure 4.19 Schematic of the LED-based NO_2 diagnostic. 125

Figure 4.20 Raw and averaged detector signals from a LED absorption measurement in a mixture of 1.03% NO_2, balance Ar before and after filling the absorption cell. 126

Figure 4.21 Literature values for absorption coefficients of NO_2 and N_2O_4 at 298 K in air. 127

Figure 4.22 Experimental and predicted absorbance values in a mixture of 1.03% NO_2, balance Ar. 129

Page

Figure 5.1 Experimental plateau H_2O values for (a) fuel-lean and (b) fuel-rich mixtures of H_2-NO_2-Ar. 136

Figure 5.2 Equilibrium mole fractions of N_2O_4 in initially pure NO_2 assuming constant pressure and constant temperature. 138

Figure 5.3 Experimental absorbance data and their best-fit line for a set of tests using the LED absorption diagnostic. 139

Figure 5.4 Comparison of the LED and H_2O measurement methods of determining the NO_2 concentration in the mixtures. 141

Figure 5.5 Rate constants for quenching of the OH $A\,^2\Sigma^+$ state by (a) Ar, (b) NO, (c) NH_3, and (d) N_2O. 146

Figure 5.6 Representative H_2O time histories measured in (a-d) Mix 1, (e-h) Mix 2, and (i-l) Mix 3 compared to the results of several chemical kinetics mechanisms. 148

Figure 5.7 Arrhenius plot of the time to half the maximum possible H_2O for (a) Mix 1, (b) Mix 2, and (c) Mix 3. 149

Figure 5.8 Normalized H_2O sensitivity coefficients at conditions corresponding to (a) Fig. 5.6(b) and (b) Fig. 5.6(j). 154

Figure 5.9 H_2O time history at the conditions of Fig. 5.6(f) alongside model predictions from Zhang et al. with variations in k_7 and k_5. 156

Figure 5.10 Offline and online laser tests in Mix 1 at similar conditions. 158

Figure 5.11 Absorption time history in a mixture of 0.444% NO_2/Ar with the laser tuned offline to 1388.108 nm. 159

Figure 5.12 NO_2 absorption coefficients versus temperature at 1388.140 nm, derived from the initial level of absorption immediately after the reflected shock wave in the Mix 1 experiments using the known value of 0.375% NO_2. 160

Figure 5.13 Normalized OH* profiles in Mix 4 at various temperatures..... 163

Figure 5.14 Arrhenius plots of (a) normalized peak OH* and (b) $\tau_{50\%}$ in Mix 4... 164

Figure 5.15 Effects of varying k_{13} and removing R14. 167

Figure 5.16 Quantitative OH* levels from Hidaka et al. in (a) 1.0% N_2O, 0.5% H_2, (b) 1.0% N_2O, 1.0% H_2, and (c) 2.0% N_2O, 1.0% H_2, all in balance Ar.. 169

Figure 5.17 Illustrations of $\Delta\bar{H}_R^0$ for the ground-state forms of R13 and R14 alongside an illustration of ΔE for the OH $A\,^2\Sigma^+ \rightarrow X\,^2\Pi$ transition (potential energy curves for OH not drawn to scale). 172

Figure A.1 Representative ray-tracing diagram for a plano-convex lens with the planar side (a) away from and (b) toward the focal point. 194

Figure A.2 Shock-tube laser experiments in Ar near 1 atm (a) before and (b) after cleaning the windows. 196

Figure A.3 Exaggerated demonstration of the behavior of a laser beam passing through a shock-tube window for an incident angle θ of (a) 0° and (b) greater than 0°. 198

Figure A.4 Exaggerated demonstration of the behavior of stray internal reflections for a case of (a) nearly dead-center alignment through both windows and (b) intentional misalignment. 199

Figure A.5 Demonstration of the effect of oscilloscope voltage input setting on the level of bit noise. 203

Figure A.6 Effect of filtering raw $I_0 - I_t$ data with a first-order, low-pass Butterworth filter with a 150-kHz cutoff. 206

Figure A.7 Demonstration of (a) high-frequency optical noise and (b) its removal through an extremely small change in angle of the optic creating the noise. 207

Figure B.1 Synthesized examples of (a) detector offsets Δ_{I_0} and $\Delta_{I_0-I_t}$ measured prior to an experiment by shielding the detectors and (b) a speciation experiment, showing the initial imbalance $\delta_{initial}$ in $I_0 - I_t$. 211

Figure B.2 $(I_t/I_0)_{true}$ time history for the example in Fig. B.1(b) according to Eq. (B.2). 213

Figure B.3 Effects of the non-ideal pressure rise dP/dt on the evaluation of X_{abs} using the Beer-Lambert law. 215

Figure B.4 Representative (a) temperature rise due to exothermicity

Page

with the corresponding change in k_v and (b) effect on the calculated X_{abs} profile. 217

Figure B.5 Example data analysis procedure for a scanned-wavelength experiment showing (a) signals obtained during the shock experiment, (b) the third-order polynomial fit to the etalon fringe peaks, and (c) the processed absorption versus frequency. 219

Figure C.1 Schematic of the Littrow-configured TDL used in the H_2O experiments. 230

Figure C.2 Behavior of the various gain or loss modes within the TDL. 233

Figure C.3 Schematic of the physical layout of the TDL, with features pertinent to laser tuning highlighted in red. 235

LIST OF TABLES

		Page
Table 3.1	Advantages and disadvantages of emission and absorption diagnostics	46
Table 4.1	Spectroscopic parameters of the $5_{5,1}\leftarrow5_{5,0}$, 101←000 transition of H_2O.	107
Table 5.1	H_2-NO_2 mixture compositions.	140
Table 5.2	$\Delta\bar{H}_R^0$ for N-containing reactions that produce OH with $\Delta\bar{H}_R^0$ < -50 kcal/mol.	166
Table 5.3	The OH* sub-mechanism of this work.	168
Table A.1	Typical frequencies of various noise sources and their possible solutions.	208
Table B.1	Values of terms in Eq. (B.2) according to the example in Fig. B.1.	213
Table D.1	Example spectral databases and fitting/prediction programs.	239
Table D.2	Description of the line-by-line, 160-character output format of HITRAN.	242
Table D.3	Sample global and local quantum numbers using the HITRAN format.	246

1. INTRODUCTION

NOx pollutants are highly toxic to human health and are therefore regulated by the EPA [1]. In the gas turbine industry, an oft-employed technique to reduce NOx formation is exhaust gas recirculation (EGR), wherein a fraction of the exhaust gases are reintroduced to the turbine combustor [2]. These recycled gases inevitably contain some level of NOx that can influence the operation of the combustor. As such, NOx-sensitized combustion of CH_4 in air or O_2 has been studied numerous times (see [3] and references therein). However, studies with a NOx species as the sole oxidizer are largely absent from the literature (Sect. 1.4). Such data would be of fundamental interest and would serve as target data for design and validation of chemical kinetics mechanisms. Accordingly, this dissertation provides some of the first H_2-NO_2 oxidation data at high temperatures.

The study of high-temperature combustion chemistry encompasses a host of real-world applications and fundamental challenges. Reduction of pollutant emissions, materials synthesis, and process safety are but a few applications, while extreme experimental conditions, turbulent environments, and molecular-level phenomena are some of the challenges. Shock tubes are experimental tools well-suited to provide useful data for such applications and address many of the associated challenges. The shock tube has been in use since 1899 and has seen worldwide use since then [4], with applications to combustion chemistry studies since at least the mid-20th century [5]. The application of optical diagnostics to fundamental combustion studies behind reflected shock waves exists at the intersection of molecular spectroscopy, laser technology, gas dynamics, and chemical kinetics. Each field possesses unique capabilities, challenges, and terminology,

and each is presented in this Section.

Spectroscopy and optical diagnostics are briefly introduced using a handful of references, each of which represents either a landmark work or a topical review containing many references to the pertinent literature. The field of shock tubes is then presented, including a discussion of the basic principles and applications of shock-tube experiments as well as a walkthrough of the famous x-t diagram. Lastly, an overview of the relatively small body of literature on experimental chemical kinetics studies in the H_2-NO_2 system is provided, followed by the organization of the dissertation.

1.1 Spectroscopy

Spectroscopy refers to the study of the interaction of light and matter. The origins of modern spectroscopy are generally attributed to Isaac Newton's observations of the colors within sunlight in the 17th century [6]. Of interest to the present work is the field of molecular spectroscopy, which was greatly aided in the early 20th century due to the advent of quantum mechanics. Quantum mechanics provided a theory to explain the discretized nature of observed molecular spectra. Since that time, numerous studies of molecular structure have been afforded by way of studying the nature of light interaction with those molecules. Such studies can provide values of bond lengths and bond angles (Fig. 1.1) with five significant figures of precision or more. Numerous other molecular properties can also be derived from such studies, and thorough texts exist concerning such techniques [7-9].

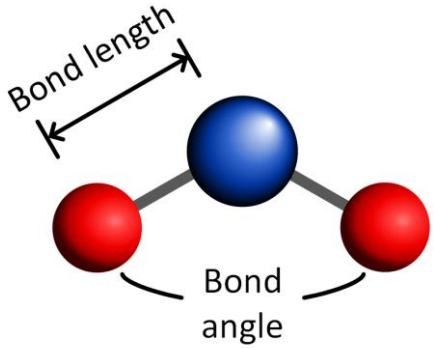

Figure 1.1 Depiction of a triatomic molecule, denoting some of the molecular features that can be determined with high accuracy using spectroscopic techniques.

In the present context, however, the most useful facet of molecular spectroscopy is not the determination of molecular structure. Rather, the result of discretized molecular energy levels of molecules, as described by quantum mechanics, is that molecules exhibit absorption/emission "fingerprints" throughout the electromagnetic spectrum. These unique features can be used to identify an unknown species or, as performed in this dissertation, to employ a specific wavelength of light with the goal of quantifying an unknown amount of some target species.

1.2 Optical diagnostics

Optical diagnostics are the methods through which the benefits of spectroscopy can be realized. Such diagnostics can generally be categorized into two groups: emission diagnostics, wherein light from the test region is passively collected, and absorption diagnostics, wherein a light source is used to illuminate the test region and the resulting light/matter interaction is somehow observed. Some techniques, such as laser-induced fluorescence, combine aspects of both emission and absorption spectroscopy.

The key equation in absorption spectroscopy is the Beer-Lambert law, which is illustrated in a simple fashion in Fig. 1.2. Through knowledge of the propensity with which an absorbing gas species will absorb a certain frequency of light, the measured attenuation of light can be used to determine the concentration of the absorbing gas. Laser-based diagnostics employing this phenomenon have been widely used in gas-sensing applications [10, 11].

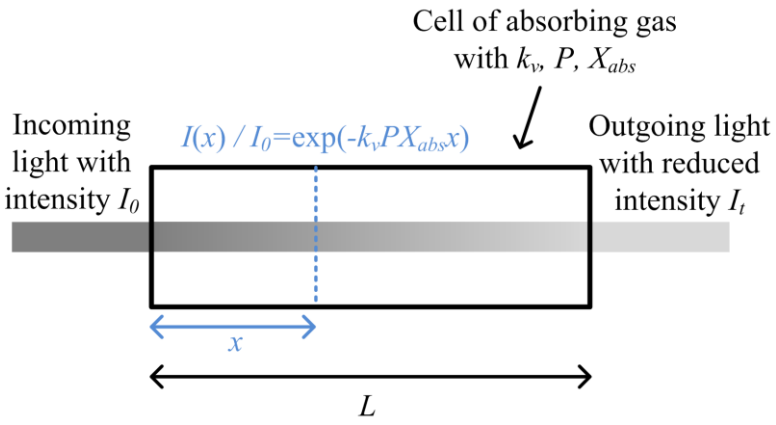

Figure 1.2 Attenuation of a light source traversing an absorbing gas as described by the Beer-Lambert law.

Optical diagnostics have played a role in shock-tube chemical kinetics studies for many decades. With the advent of the laser in 1960 and the subsequent rush of developments in this new technology [12], the pairing of laser diagnostics and shock tubes was not far behind. The first demonstration of a shock-tube laser diagnostic occurred in 1977 [13], and the number of shock-tube studies employing laser diagnostics has grown immensely since that time with the increasing affordability and spectral coverage of commercial laser sources [14, 15].

1.3 Shock tubes

Shock tubes are devices that create shock waves within a long enclosure. Generally, they consist of a driver side, from whence the shock wave is generated, and a driven side, into which the shock wave propagates. Despite this underlying fundamental principle, the methods of shock-wave generation in the driver side vary widely, as do the applications studied in the driven side. Different methods for shock-wave generation include bursting a single-use diaphragm via combustion of gaseous mixtures [16], bursting a single-use diaphragm via high-pressure inert gases [17], and exposing the driven side to the high-pressure, inert driver side via fast-acting pneumatic valves [18]. Different applications of shock tubes span an even broader range, and include the influence of shock waves on structures [19], fluid mechanics in shock-driven flows [20], aerodynamics of objects placed in shock-driven flows (in this case, the term "shock tunnel" is often used) [21], chemical kinetics [22], and spectroscopy [23].

In the context of gas-phase media, a shock wave is a discontinuity in gas properties that propagates through the gaseous medium at a speed, by definition, greater than the local sound speed. An observer standing at a fixed location will experience a sudden increase in both static temperature and static pressure following the passage of a shock wave. Shock tubes utilize this sudden change in conditions to produce extreme environments for short durations of time.

The workings of a shock tube can be understood through an x-t diagram, an example of which is shown in Fig. 1.3. Following the bursting of the diaphragm, the large pressure differential between the driver and driven sections causes the incident shock wave to form, which propagates through the driven section. Convention is to name the state

behind the incident shock wave region 2 with properties T_2, P_2, etc.; other conventional state numberings are given in Fig. 1.3. Some experiments utilize the conditions behind the incident shock wave [24, 25], but the present work utilized the conditions behind the reflected shock wave. When the incident shock wave strikes the endwall of the driven section, it is reflected, thereby shock-heating region 2 to create region 5. The values of T_5 and P_5 can be extremely high (>5000 K and ~1000 atm). These extreme conditions and their nearly instantaneous achievement make shock tubes ideally suited for chemical kinetics studies. Furthermore, the reflection of the incident shock wave effectively halts the flow induced behind the reflected shock wave, thereby creating a stagnant, constant-pressure, constant-temperature region (region 5). The test is ended when the reflected expansion fan reaches the endwall of the driven section.[1]

In reality, several phenomena serve to complicate the situation in Fig. 1.3. Non-ideal effects such as attenuation of the incident shock wave [26], boundary-layer growth [27], reflected-shock bifurcation [28], contact-surface mixing [29], and pressure rise in P_5 (commonly referred to as dP/dt) [30] all occur to varying degrees. Various methods of solving or avoiding these problems have been developed; for example, the use of driver inserts can mitigate or eliminate dP/dt effects [31]. Non-idealities are not the focus of this work, and the interested reader is directed to the provided references for more reading on these topics.

[1] There is another possibility by which the test time may be ended. Depending on the test gas compositions and conditions, the contact surface may encounter the reflected shock wave before the expansion fan. In such a case, the interaction of the contact surface and the reflected shock wave may reflect either a compression or an expansion back to the endwall region, thereby ending the test time. A specialized case is that of a "tailored" driver gas, wherein neither a compression nor an expansion is reflected back to the endwall and the test time persists until the arrival of the expansion fan.

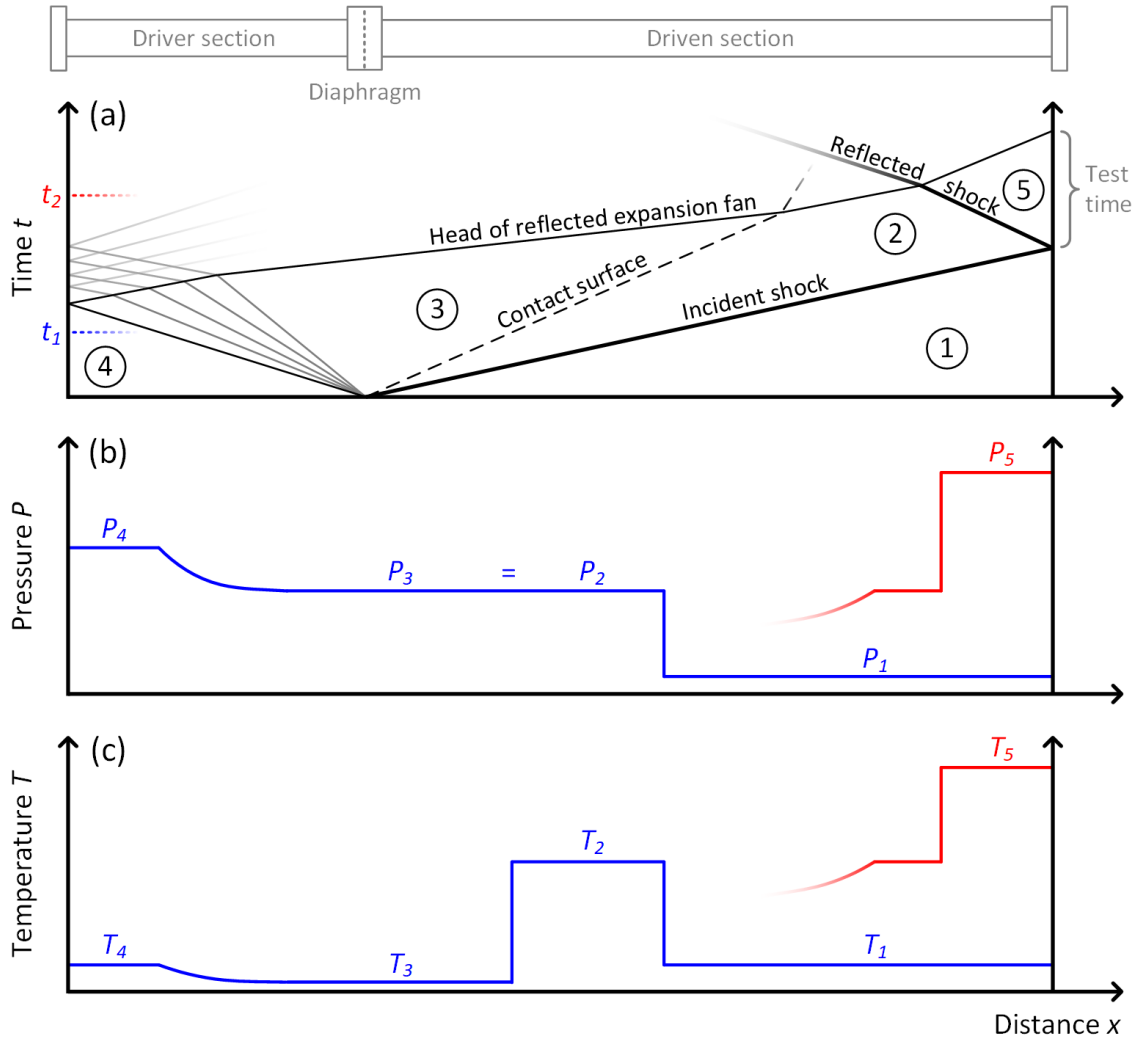

Figure 1.3 Illustration of a conventional shock tube, showing (a) an x-t diagram, (b) the corresponding axial pressure distributions at times t_1 and t_2, and (c) the corresponding axial temperature distributions at times t_1 and t_2. The distributions for t_2 have been cut off past the expansion fan for clarity.

1.4 The H_2-NO_2 system

Of interest to the present work is the effect of NOx (specifically NO_2) on H_2 combustion chemistry. The H_2-O_2 mechanism is at the core of every hydrocarbon combustion mechanism since it contains some of the most important elementary reactions in combustion chemistry involving highly reactive radicals (O, H, and OH). Furthermore,

H_2 is formed to some degree during the combustion of any larger hydrocarbons. For these reasons, the H_2-O_2 system is the most fundamental combustion system and has accordingly been the topic of a vast number of experimental, theoretical, and modeling studies (see [32] and references therein).

The H_2-NO_2 system is of interest because many of the elementary reactions related to NOx formation/mitigation are key reactions in these simple fuel systems, making them insightful from a fundamental standpoint. From a practical perspective, H_2-NO_2 kinetics are applicable to rocket-propellant applications [33]. NO_2-sensitized H_2-O_2 oxidation has been studied in shock tubes [34], flow reactors [35], and jet-stirred reactors [36], among others. However, in each of these cases, the primary combustion system was H_2-O_2, with only trace amounts of NO_2 added to the mixtures.

On the other hand, studies of the H_2-NO_2 system are relatively few in number, and most were performed at low temperatures (< 1000 K). In the 1950s, Ashmore and Levitt [37-39] measured NO_2 time histories between 684 and 843 K using a broadband absorption diagnostic between 445 and 500 nm. They performed measurements in mixtures with differing amounts of H_2 and also NO [38, 39]. Around the same time, Rosser and Wise [40] employed NO_2 broadband absorption near 440 nm to measure time histories in H_2-NO_2 mixtures. A quartz static reactor was used to investigate temperatures between 600 and 700 K. Sawyer and Glassman [41] used a flow reactor to investigate H_2-NO_2 combustion between 850 and 1110 K. They measured temperature profiles with a thermocouple inserted into the flow and ultimately obtained several reaction rate coefficients from their data. Park et al. [42] used a quartz static reactor to measure the oxidation of H_2-NO_2 between 602 and 954 K. They utilized Fourier transform infrared spectroscopy to measure

concentrations of NO, NO_2, CO, and CO_2 versus temperature. From their data, Park et al. extracted rate constants for the reactions $H_2 + NO_2 \leftrightarrows HONO + H$ and $2NO_2 \leftrightarrows 2NO + O_2$. Mueller et al. [43] performed flow reactor studies of H_2-NO_2 mixtures, measuring concentrations of NO, NO_2, and H_2O. From their data, they provided a reaction rate for $H_2 + NO_2 \leftrightarrows HONO + H$ at the single temperature of 833 K.

In summary, there appears to be only a small amount of experimental data obtained in the H_2-NO_2 system, with a particular gap at high temperatures (> 1000 K). The H_2-NO_2 measurements provided herein will help rectify this lack of data and provide combustion modelers data with which to refine NOx-related chemical kinetics mechanisms.

1.5 Organization of the dissertation

Section 2 presents an overview of the notation used to describe molecular spectroscopy. Following an introduction of the basic concepts, the notation and analytical formulae for describing diatomic spectroscopy are developed. Separate discussions of rotational, vibrational, rovibrational, and rovibronic spectroscopy of diatomic molecules are given. Finally, a treatment of polyatomic molecules is provided.

Section 3 presents the theory and equations used in making quantitative measurements with both laser absorption and emission diagnostics. A detailed derivation of the Beer-Lambert law is provided along with a discussion of several accompanying assumptions. The theory and equations used to calculate the line strength and the line shape are then provided. Finally, the basic elements of emission diagnostics theory are addressed, with a focus on chemiluminescent emission.

Section 4 provides a detailed description of the four experimental apparatus

employed in this dissertation: the shock tube, the H_2O laser absorption diagnostic, the OH* chemiluminescence diagnostic, and the LED-based NO_2 diagnostic. Details pertaining to the physical configuration, data acquisition/analysis, and experimental challenges are addressed, and sample experimental results are shown for each apparatus.

Section 5 includes the results and analysis of the H_2-NO_2 oxidation experiments: the static measurements of NO_2 concentrations for mixture validation, the H_2O time-histories obtained in the shock tube, and the OH* time-histories obtained in the shock tube. Details on the chemical kinetic modeling are provided, including updates to OH*-quenching reactions. Reaction pathway and sensitivity analyses are provided in relation to the H_2O measurements, while fitting of the rate constant of a new OH*-forming reaction is provided in relation to the OH* measurements.

Section 6 provides concluding remarks on the theoretical and experimental methodology developed throughout the dissertation, in addition to summarizing statements on the experimental results obtained in the H_2-NO_2 oxidation experiments. Finally, an overview of potential directions for future research is given.

Several appendices related mostly to miscellaneous experimental details have also been supplied. Appendix A details techniques for identifying and eliminating sources of noise in shock-tube laser absorption experiments. The types of noise addressed include vibrational, electrical, and optical noise.

Appendix B provides a discussion of the minutia associated with the analysis of the raw data from laser absorption experiments. Topics addressed include detector offsets, non-ideal pressure increases, and temperature changes due to chemical reactions. An introduction to the analysis of scanned-wavelength direct absorption measurements is also

given, even though such a diagnostic was not employed herein.

Appendix C describes tips and techniques for achieving stable laser operation. The operating principle of the tunable diode laser utilized in this dissertation is covered, and possible sources of laser instability and their remedies are outlined.

Finally, Appendix D addresses the use of the spectral database HITRAN. The general uses and benefits of HTIRAN are discussed and the output format is given in tabular form. Special attention is granted to potentially confusing unit conversions, and references are provided for several tools that can aid in accessing the desired data.

1.6 References

[1] Environmental Protection Agency, "Nitrogen oxides (NOx), why and how they are controlled", Report no. EPA 456/F-99-006R (1999).

[2] J.A. Caton, "Thermodynamic considerations regarding the use of exhaust gas recirculation for conventional and high efficiency engines" *Journal of Engineering for Gas Turbines and Power* **139** (2017) 09280301-09280308.

[3] Y.L. Chan, F.J. Barnes, J.H. Bromly, A.A. Konnov, D.K. Zhang, "The differentiated effect of NO and NO_2 in promoting methane oxidation" *Proceedings of the Combustion Institute* **33** (2011) 441-447.

[4] N.A. Fomin, "110 years of experiments on shock tubes" *Journal of Engineering Physics and Thermophysics* **83** (2010) 1118-1135.

[5] A.G.H. Gaydon, I.R., "The Shock Tube in High-Temperature Chemical Physics" Reinhold Pub. Corp., New York (1963).

[6] N.C. Thomas, "The early history of spectroscopy" *Journal of Chemical Education* **68** (1991) 631-634.

[7] G. Herzberg, "Molecular Spectra and Molecular Structure: I. Spectra of Diatomic Molecules" 2nd ed., Van Nostrand, Princeton, NJ (1950).

[8] G. Herzberg, "Molecular Spectra and Molecular Structure: II. Infrared and Raman Spectra of Polyatomic Molecules" Van Nostrand, Princeton, NJ (1945).

[9] G. Herzberg, "Molecular Spectra and Molecular Structure: III. Electronic Spectra and Electronic Structure of Polyatomic Molecules" 2nd ed., Van Nostrand, Princeton,

NJ (1966).

[10] J. Hodgkinson, R.P. Tatam, "Optical gas sensing: A review" *Measurement Science and Technology* **24** (2013) 012004.

[11] C.S. Goldenstein, R.M. Spearrin, J.B. Jeffries, R.K. Hanson, "Infrared laser-absorption sensing for combustion gases" *Progress in Energy and Combustion Science* **60** (2017) 132-176.

[12] J. Hecht, "A short history of laser development" *Applied Optics* **49** (2010) F99-F122.

[13] R.K. Hanson, "Shock tube spectroscopy: Advanced instrumentation with a tunable diode laser" *Applied Optics* **16** (1977) 1479-1481.

[14] R.K. Hanson, "Applications of quantitative laser sensors to kinetics, propulsion and practical energy systems" *Proceedings of the Combustion Institute* **33** (2011) 1-40.

[15] R.K. Hanson, D.F. Davidson, "Recent advances in laser absorption and shock tube methods for studies of combustion chemistry" *Progress in Energy and Combustion Science* **44** (2014) 103-114.

[16] X. Yu, F. Li, L. Chen, X.Y. Chang, "A compact sensor based on near infrared absorption spectroscopy for flow diagnostics in a low density hydrogen and oxygen combustion driven shock tube" *Lasers in Engineering* **23** (2012) 1-17.

[17] E.L. Petersen, M.J. Rickard, M.W. Crofton, E.D. Abbey, M.J. Traum, D.M. Kalitan, "A facility for gas- and condensed-phase measurements behind shock waves" *Measurement Science and Technology* **16** (2005) 1716-1729.

[18] R.S. Tranter, P.T. Lynch, "A miniature high repetition rate shock tube" *Review of Scientific Instruments* **84** (2013) 094102.

[19] W. Bleakney, D.R. White, W.C. Griffith, "Measurement of diffraction of shock waves and resultant loading of structures" *Journal of Applied Mechanics* **17** (1950) 439-445.

[20] M. Mohaghar, J. Carter, B. Musci, D. Reilly, J. McFarland, D. Ranjan, "Evaluation of turbulent mixing transition in a shock-driven variable-density flow" *Journal of Fluid Mechanics* **831** (2017) 779-825.

[21] V. Menezes, S. Saravanan, K.P.J. Reddy, "Shock tunnel study of spiked aerodynamic bodies flying at hypersonic Mach numbers" *Shock Waves* **12** (2002) 197-204.

[22] D.F. Davidson, R.K. Hanson, "Recent advances in shock tube/laser diagnostic methods for improved chemical kinetics measurements" *Shock Waves* **19** (2009) 271-283.

[23] C.R. Mulvihill, S.A. Alturaifi, E.L. Petersen, "High-temperature He- and O_2-

broadening of the R(12) line in the 1←0 band of carbon monoxide" *Journal of Quantitative Spectroscopy and Radiative Transfer* **217** (2018) 432-439.

[24] D.A. Masten, R.K. Hanson, C.T. Bowman, "Shock tube study of the reaction H + O_2 → OH + O using OH laser absorption" *Journal of Physical Chemistry* **94** (1990) 7119-7128.

[25] R.S. Tranter, P.T. Lynch, J.B. Randazzo, J.P.A. Lockhart, X. Chen, C.F. Goldsmith, "High temperature pyrolysis of 2-methyl furan" *Physical Chemistry Chemical Physics* **20** (2018) 10826-10837.

[26] E.L. Petersen, R.K. Hanson, "Nonideal effects behind reflected shock waves in a high-pressure shock tube" *Shock Waves* **10** (2001) 405-420.

[27] E.L. Petersen, R.K. Hanson, "Improved turbulent boundary-layer model for shock tubes" *AIAA Journal* **41** (2003) 1314-1322.

[28] E.L. Petersen, R.K. Hanson, "Measurement of reflected-shock bifurcation over a wide range of gas composition and pressure" *Shock Waves* **15** (2006) 333-340.

[29] W.J. Hooker, "Testing time and contact-zone phenomena in shock-tube flows" *The Physics of Fluids* **4** (1961) 1451-1463.

[30] J.W. Hargis, E.L. Petersen, "Shock-tube boundary-layer effects on reflected-shock conditions with and without CO_2" *AIAA Journal* **55** (2017) 902-912.

[31] Z.K. Hong, G.A. Pang, S.S. Vasu, D.F. Davidson, R.K. Hanson, "The use of driver inserts to reduce non-ideal pressure variations behind reflected shock waves" *Shock Waves* **19** (2009) 113-123.

[32] C. Olm, I.G. Zsély, R. Pálvölgyi, T. Varga, T. Nagy, H.J. Curran, T. Turányi, "Comparison of the performance of several recent hydrogen combustion mechanisms" *Combustion and Flame* **161** (2014) 2219-2234.

[33] W. Tsang, J.T. Herron, "Chemical kinetic data base for propellant combustion I. Reactions involving NO, NO_2, HNO, HNO_2, HCN and N_2O" *Journal of Physical and Chemical Reference Data* **20** (1991) 609-663.

[34] O. Mathieu, A. Levacque, E.L. Petersen, "Effects of NO_2 addition on hydrogen ignition behind reflected shock waves" *Proceedings of the Combustion Institute* **34** (2013) 633-640.

[35] M.A. Mueller, R.A. Yetter, F.L. Dryer, "Flow reactor studies and kinetic modeling of the $H_2/O_2/NO_x$ and $CO/H_2O/O_2/NO_x$ reactions" *International Journal of Chemical Kinetics* **31** (1999) 705-724.

[36] G. Dayma, P. Dagaut, "Effects of air contamination on the combustion of hydrogen—Effect of NO and NO_2 addition on hydrogen ignition and oxidation kinetics"

Combustion Science and Technology **178** (2006) 1999-2024.

[37] P.G. Ashmore, B.P. Levitt, "The thermal reaction between hydrogen and nitrogen dioxide. Part 2. Experimental work on the kinetics of the reaction" *Transactions of the Faraday Society* **52** (1956) 835-848.

[38] P.G. Ashmore, B.P. Levitt, "The thermal reaction between hydrogen and nitrogen dioxide. Part 3. Further experimental work on the kinetics: Reaction mechanism" *Transactions of the Faraday Society* **53** (1957) 945-954.

[39] P.G. Ashmore, B.P. Levitt, "The thermal reaction between hydrogen and nitrogen dioxide. Part 4. Thermal ignitions of hydrogen and nitrogen dioxide" *Transactions of the Faraday Society* **54** (1958) 390-393.

[40] W.A. Rosser, H. Wise, "Kinetics of reaction between hydrogen and nitrogen dioxide" *The Journal of Chemical Physics* **26** (1957) 571-576.

[41] R.F. Sawyer, I. Glassman, "The reactions of hydrogen with nitrogen dioxide, oxygen, and mixtures of oxygen and nitric oxide" *Symposium (International) on Combustion* **12** (1969) 469-479.

[42] J. Park, N.D. Giles, J. Moore, M.C. Lin, "A comprehensive kinetic study of thermal reduction of NO_2 by H_2" *The Journal of Physical Chemistry A* **102** (1998) 10099-10105.

[43] M.A. Mueller, J.L. Gatto, R.A. Yetter, F.L. Dryer, "Hydrogen/nitrogen dioxide kinetics: Derived rate data for the reaction $H_2 + NO_2 = HONO + H$ at 833 K" *Combustion and Flame* **120** (2000) 589-594.

2. TERMINOLOGY OF MOLECULAR SPECTROSCOPY

Molecular spectroscopy has yielded and continues to yield a wealth of knowledge to the scientific community and has particularly revolutionized the understanding of atomic and molecular structure. While many spectroscopic techniques exist including fluorescence, laser-induced fluorescence, ionization, and laser-induced incandescence, the present work utilizes direct laser absorption and chemiluminescent emission. These techniques are predicated upon the interaction of electromagnetic radiation with a molecule via quantifiable absorption or emission of that radiation, which takes place at discrete frequencies specific to that molecule. This natural phenomenon provides two key benefits to the spectroscopist: such diagnostics can be both species-specific and quantitative.

Discussed in this chapter is the species-specific aspect of spectroscopy. A brief overview of basic concepts is first given. Next, a broad coverage of diatomic spectroscopy is given, including rotational, vibrational, rovibrational, and rovibronic spectroscopy. Finally, rotational, vibrational, and rovibrational spectroscopy of polyatomic molecules are discussed. The primary references for this Section are the works of Herzberg [1, 2], Hollas [3], and Hanson et al. [4].

2.1 Preliminary considerations

The species-specific nature of absorption spectroscopy is a facet shared by all fields of spectroscopy. This nature stems from the fact that molecular energy levels (translation, rotational, vibrational, and electronic) are quantized rather than continuous, and that molecules transition between these different levels, either absorbing or emitting

electromagnetic radiation during such transitions. A simple depiction of such transitions is shown in Fig. 2.1 for the cases of emission and absorption, where the horizontal lines depict discrete energy levels of the molecule. The change in energy ΔE_{12} [J] experienced by the molecule as it transitions between two energy levels denoted by 1 and 2 is accompanied by an emitted or absorbed photon, whose frequency v_{12} [Hz] is given by

$$v_{12} = \Delta E_{12}/h. \tag{2.1}$$

Here, h is Planck's constant [J·s]. Thus, the spacing between the various discrete energy levels of a molecule can be deduced by measuring the frequencies[1] at which light is emitted/absorbed by that molecule. The locations of these energy levels are dictated by the structure of the molecule; for this reason, the field of spectroscopy lends itself well to the study of molecular structure.

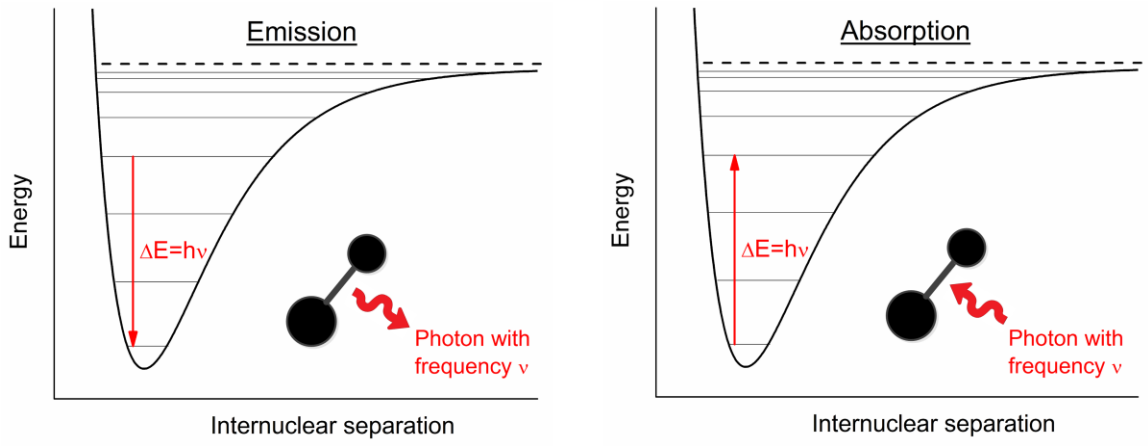

Figure 2.1 Emission and absorption processes between the discrete energy levels of a generic diatomic molecule.

[1] The wavelength λ of the light, typically in [nm], [μm], or Angstroms [Å] (1 Å = 10^{-8} cm), can also be used and is related to the frequency v [Hz] by $\lambda = c/v$, where c is the speed of light in the appropriate units.

2.1.1 Potential energy wells

The curves shown in Fig. 2.1 are plots of the intermolecular potential energy $V(r)$ [cm^{-1}] versus internuclear separation r and are often referred to as potential energy wells. A detailed version is shown in Fig. 2.2, wherein several key features can be noted. First, the shape of the curve is given by the Morse potential, which gives $V(r)$ as

$$V(r) = D_e\left[1 - \exp\left(-\beta(r - r_e)\right)\right]^2. \tag{2.2}$$

Here, D_e [cm^{-1}] is the dissociation energy; β [cm^{-1}] is a constant related to the vibrational frequency and D_e; and r_e [cm] is the equilibrium separation of the atoms (pgs. 24-25 of Hanson et al. [4]). The rise in $V(r)$ below r_e is due to repulsive forces between the atoms, while the rise above r_e is due to attractive forces between the atoms. Other potentials besides the Morse potential are also commonly used; see Ch. 7 of Steinfeld et al. [5].

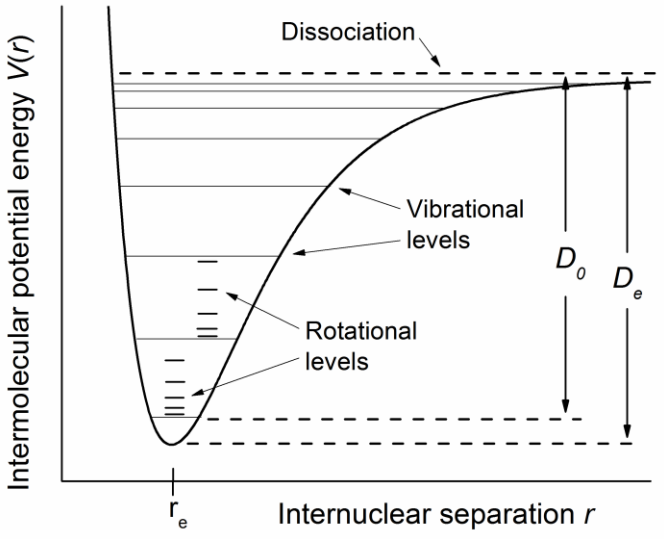

Figure 2.2 Molecular potential energy diagram for a general diatomic bond, showing discrete vibrational and rotational energy levels.

Another feature of Fig. 2.2 is the depiction of discrete vibrational and rotational energy levels. While Fig. 2.2 is only qualitative in nature and is not drawn to scale, several trends shown are accurate: (1) the spacing between vibrational levels is much larger than between rotational levels, (2) vibrational levels become increasingly closely spaced, and (3) rotational levels become increasingly separated. It should be stressed that a fundamental principle of quantum mechanics is the molecule can only exist at and transition between the discrete energy levels[2] depicted in Fig. 2.2.

A third feature of Fig. 2.2 is the dissociation energy. As more energy is added to the molecule, the molecules vibrate and rotate with increasing frequencies and force the atoms closer and farther from r_e, causing the increasing width of the potential energy well with increasing $V(r)$. However, at a certain separation distance, the bond between the molecules will become so weak as to be non-existent, and the molecule is now said to be dissociated (this places a limit on the vibrational levels, which become more tightly spaced with increasing $V(r)$ but are finite in number due to dissociation). The amount of energy required to dissociate the molecule is called the zero-point dissociation energy, D_0 [cm^{-1}]. D_0 is slightly smaller than D_e because even at the lowest-lying vibrational and rotational state, the molecule still vibrates/rotates between the limits of the potential energy well, existing at an energy level called the zero-point energy that is higher than the energy level at the bottommost point of the well. D_0 is the experimentally measured value of the dissociation energy (see pgs. 142-146 of Hollas [3]).

The Morse potential shown in Fig. 2.2 is specific to a certain electronic configuration of the molecule. With increasing energy, the valence electrons of a molecule

[2] Exceptions to this do occur in cases such as coherent anti-Raman Stokes (CARS) spectroscopy, but this is not of interest in the present work.

can reconfigure themselves such that a new potential energy curve is obtained, and transitions between these different electronic energy levels can occur. Figure 2.3(a) shows a depiction of two such electronic states, with representative rotational, vibrational, and electronic transitions illustrated. Although Fig. 2.3(a) is not drawn to scale, one can see the general trend that electronic transitions are more energetic than vibrational transitions, which are in turn more energetic than rotational transitions. In accordance with these trends, general ranges of rotational, vibrational, and electronic transitions are depicted on an electromagnetic spectrum in Fig. 2.3(b), indicating the ranges of the spectrum where one would expect to observe pure transitions of each type. Here, "pure" indicates a change in only type of energy level; the transitions portrayed in Fig. 2.3(a) are pure transitions. Of course, mixed transitions can also occur, wherein there is a simultaneous change in more than one type of energy level. Simultaneous rotational and vibrational transitions are termed rovibrational transitions, while simultaneous rotational, vibrational, and electronic transitions are called rovibronic transitions.

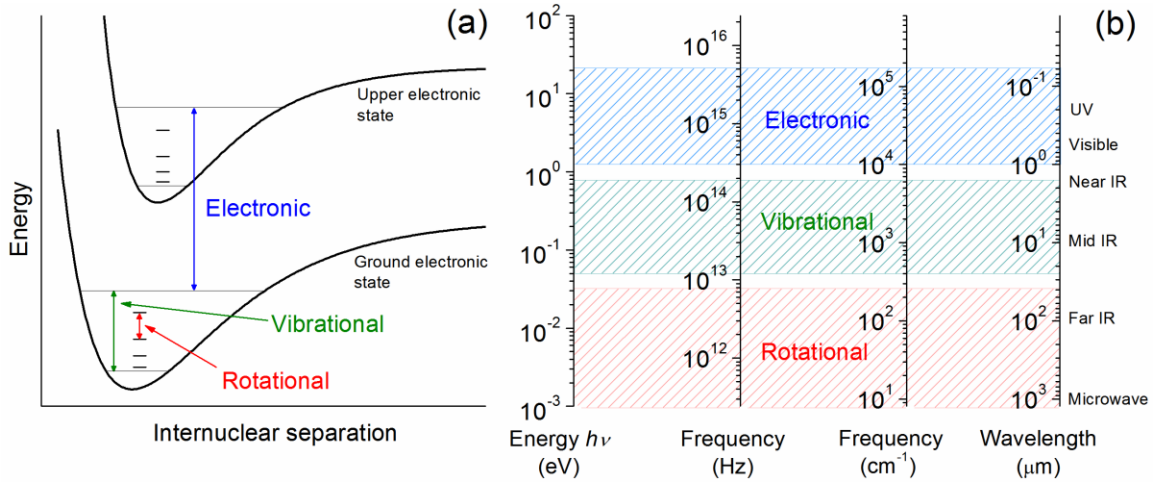

Figure 2.3 (a) Electronic, vibrational, and rotational transitions and (b) their approximate locations on the electromagnetic spectrum.

2.1.2 Dipole moments

A primary avenue of light interaction with matter is through the electric dipole moment.[3] The motion of the dipole moment via changes in rotational, vibrational, or electronic energy (or some combination thereof) leads to the emission or absorption of electromagnetic radiation.[4] The electric dipole moment $\vec{\mu}$ [C·cm] is (pg. 10 of [4])

$$\vec{\mu} = \sum_i q_i \, \vec{r}_i, \tag{2.3}$$

where q_i [C] is the charge of the i-th particle and $\vec{r}_i$ [cm] is the location vector of that particle. Heteronuclear diatomic molecules (e.g., CO) possess a permanent dipole moment due to the different charges of the atoms, while homonuclear diatomic molecules (e.g., N_2) do not possess a permanent dipole moment.

The existence of a pure rotational (i.e., no changes in vibrational or electronic energy) spectrum is predicated on the existence of a permanent electric dipole moment. Therefore, CO will possess a pure rotational spectrum, while N_2 will not. (Another class of molecules that does not possess a permanent dipole moment is linear, symmetric polyatomic molecules such as CO_2.) Similarly, the existence of a vibrational spectrum is dependent on whether a dipole moment moves in association with that vibrational mode. For example, a homonuclear molecule such as Cl_2 will not possess vibrational spectra.

2.2 Spectroscopy of diatomic molecules

Diatomic molecules represent the simplest case of molecular spectroscopy: there is

[3] Other avenues include Raman scattering and Rayleigh scattering.
[4] Other opportunities for radiation interaction include quadrupoles, octopoles, and magnetic dipoles.

only one axis of molecular rotation and only one vibrational mode. Given this simplicity, the basics of molecular spectroscopy can best be understood by starting with the diatomic case, from which the more-complex polyatomic case can be readily extrapolated. The treatment of rotational spectroscopy largely follows that of Hanson et al. (Ch. 2 of [4]).

2.2.1 Rotational spectroscopy of diatomic molecules

Motion of the dipole moment of a molecule can take place due to rotation of the molecule. A profound result of quantum mechanics (not derived here but rather taken as an axiom) is that molecular motion, both rotational and otherwise, is quantized and can be described by an appropriate set of quantum numbers. The quantization of angular momentum[5] is described by the rotational quantum number J. Quantum mechanics states (see pgs. 160-170 of Griffiths [6]) the magnitude of the angular momentum $\vec{\boldsymbol{J}}$ as

$$\left|\vec{\boldsymbol{J}}\right| = \hbar\sqrt{J(J+1)}, \quad J = 0, 1, 2, \cdots . \tag{2.4}$$

The symbol $\hbar$ is ubiquitous in quantum mechanics and is defined as $\hbar = h/2\pi$. $\left|\vec{\boldsymbol{J}}\right|$ can be related to the classical notion of angular momentum by

$$\left|\vec{\boldsymbol{J}}\right| = |I\omega|, \tag{2.5}$$

where I is the angular moment of inertia and ω is the angular velocity. I is related to the

[5] Although not discussed at any length here, conservation of angular momentum is perhaps one of the most important considerations in both quantum mechanics and spectroscopy.

distance from the axis r of the i nuclei with mass m by

$$I = \sum m_i r_i^2. \tag{2.6}$$

From classical mechanics, it is known that the kinetic energy of a rotating body E_{rot} is

$$E_{rot} = \frac{1}{2} I \omega^2. \tag{2.7}$$

Using Eqs. (2.4), (2.5), and (2.7), the following set of equalities can be written to express E_{rot} as a function of J:

$$E_{rot} = \frac{1}{2I}(I\omega)^2 = \frac{1}{2I}\hbar^2 J(J+1) = \frac{h^2}{8\pi^2 I} J(J+1). \tag{2.8}$$

In SI units, E_{rot} would be given in [J]. However, spectroscopists prefer to work in wavenumbers, which have units of [cm^{-1}]. The conversion from [J] to [cm^{-1}] is a factor of $\frac{1}{hc}$, where c is the speed of light [cm/s]. Applying this conversion, the rotational term values (i.e., energy levels) $F_{rr}(J)$ [cm^{-1}] can be written as

$$F_{rr}(J) = \frac{h}{8\pi^2 Ic} J(J+1) = B_e J(J+1). \tag{2.9}$$

The symbol B_e [cm^{-1}] is called the rotational constant. The subscript on $F_{rr}(J)$ indicates a rigid rotor was assumed; more on this later.

To describe the rotational spectra of diatomic molecules, a further piece of information is needed in addition to Eq. (2.9). This is another result of quantum mechanics called the selection rules. Essentially, the probability overlaps of quantum states give the result that only certain transitions between states are allowed. For pure rotational spectra, the selection rules are defined equivalently by either one of

$$\Delta J = +1 \tag{2.10}$$

$$J' - J'' = +1, \tag{2.11}$$

where the upper and lower rotational states are denoted by J' and J'', respectively. The present discussion is limited to absorption spectra; $\Delta J = -1$ is also allowed but corresponds to emission. Applying the selection rules to the $F_{rr}(J)$ values, the difference[6] $\bar{\nu}_{J' \leftarrow J''}$ [cm^{-1}] between two rotational states can be written (see pgs. 15-16 of Hanson et al. [4]) as

$$\bar{\nu}_{J' \leftarrow J''} = 2B_e(J'' + 1). \tag{2.12}$$

Equation (2.12) is a simple but important result. It predicts the locations of transitions (i.e., the frequencies at which rotational spectra will be observed) between rotational quantum states as a function of J'' and B_e. More specifically, it predicts the spacing between the

[6] The term $J' \leftarrow J''$ in the subscript of $\bar{\nu}_{J' \leftarrow J''}$ is standard notation. The upper (higher-energy) state is written first and is followed by the lower (lower-energy) state, with a left- or right-pointing arrow separating the two to indicate the type of process. A left-pointing arrow indicates absorption, while a right-pointing arrowing indicates emission.

rotational transitions will increase linearly as $2B_eJ''$. Given the relation of B_e to the structure of the molecule via I, it becomes evident how rotational spectroscopy can be used to determine aspects of molecular structure.

Equation (2.12) can be employed to approximately describe the pure rotational spectrum of a diatomic molecule. However, discrepancies between experimental data and Eq. (2.12) will rapidly become evident, particularly at large J''. This discrepancy is due to the implicit assumption of a rigid rotor in the preceding derivation, i.e., that I was independent of J. In actuality, centrifugal distortion increases the bond length slightly as the molecule rotates at increasing speeds, resulting in increasing I with increasing J. This effect is typically incorporated into the calculation of $F(J)$ (where the rr subscript has been dropped) through the addition of a second term (pg. 103 of [1]):[7]

$$F(J) = B_eJ(J+1) - D_eJ^2(J+1)^2. \tag{2.13}$$

D_e [cm^{-1}] is the centrifugal distortion constant and unfortunately shares the same symbol used for the dissociation energy. Equation (2.13) will better predict the rotational energy levels of diatomic molecules than will Eq. (2.9). Typically, $D_e << B_e$; this is generally true for all constants associated with higher-order corrections.

2.2.2 Vibrational spectroscopy of diatomic molecules

Movements of the dipole moment can also occur due to vibrations of the molecule.

[7] A higher-order term is sometimes added such that $F(J) = B_eJ(J+1) - D_eJ^2(J+1)^2 + H_eJ^3(J+1)^3$; see pg. 104 of [1].

These vibrations take place according to various possible modes, the number of which is dictated by the number of atoms in the molecule. For diatomic molecules, there is only one mode of vibration, namely the movement of the atoms relative to one another along the internuclear axis. The term "band" is used to describe the grouping of spectra that arise from a particular type of transition (typically vibrational or electronic) and is sometimes used interchangeably with "mode". Vibrational motion is described by the vibrational quantum number v (which can be easily confused with the symbol for frequency, ν). For $\mathrm{v}'' = 0$, a transition with $\Delta\mathrm{v} = +1$ (which could be written more succinctly as 1←0) is called the fundamental, $\Delta\mathrm{v} = +2$ (2←0) is called the first overtone, $\Delta\mathrm{v} = +3$ (3←0) is called the second overtone, etc. (As with rotation, the cases of $\Delta\mathrm{v} = -1, -2, \ldots$ are also allowed but correspond to emission.) Although the terms "fundamental" and "first overtone", etc. are understood to have the definitions given above, to fully specify the transition in question it is generally helpful to specify the value of Δv and either v' or v'' to avoid confusion. In the polyatomic case, a subscript on v is used to denote which mode is being addressed (see Sect. 2.3.2).

Modeling the motion of the two atoms as simple spring motion with a fixed spring constant (i.e., a simple harmonic oscillator) and solving the Schrödinger wave equation (see pgs. 52-53 of Griffiths [6]), the vibrational term values $G_{SHO}(\mathrm{v})$ [cm^{-1}] are simply

$$G_{SHO}(\mathrm{v}) = \omega_e \left(\mathrm{v} + \frac{1}{2}\right), \tag{2.14}$$

where ω_e [cm^{-1}] is the vibrational frequency of the vibrational mode. The simple model proposed by Eq. (2.14) implies the vibrational energy levels are equally spaced by ω_e and

also the vibrational energy is non-zero in the vibrational ground state (this is the zero-point energy mentioned earlier).

Equation (2.14) is appealing due to its simplicity. However, the anharmonicity of molecular vibrations leads to the general failure of Eq. (2.14) at larger v. This phenomenon serves to decrease the spacing between the vibrational levels with increasing v and also leads to a finite number of vibrational levels (see Fig. 2.2). Anharmonicity is modeled by writing $G(\mathrm{v})$, where the SHO subscript has been dropped, as (pg. 24 of [4])

$$G(\mathrm{v}) = \omega_e\left(\mathrm{v}+\frac{1}{2}\right) - \omega_e\chi_e\left(\mathrm{v}+\frac{1}{2}\right)^2. \tag{2.15}$$

The term $\omega_e\chi_e$ [cm^{-1}] is the first anharmonicity constant. Higher-order terms are possible,[8] but Eq. (2.15) is often truncated after the $\omega_e\chi_e$ term. The selection rule for the SHO in absorption is

$$\Delta\mathrm{v} = +1. \tag{2.16}$$

However, as indicated above, overtone transitions with $\Delta\mathrm{v} > 1$ are possible. This is because the SHO is merely an approximation. Molecules which closely approximate the SHO will follow the selection rule of Eq. (2.16) very closely and will consequently have very weak overtone bands. For example, CO closely follows the SHO approximation: its first overtone band is ~2 orders of magnitude weaker than the fundamental band. For

[8] For example, the term $\omega_e y_e\left(\mathrm{v}+\frac{1}{2}\right)^3$ can be added, where $\omega_e y_e$ is the second anharmonicity constant (see pgs. 90-92 of [1]).

molecules which do not follow the SHO approximation, the overtone bands can be quite comparable in strength to the fundamental band.

2.2.3 Rovibrational spectroscopy of diatomic molecules

Rovibrational spectra introduce an additional complexity in that the rotation of the molecule can be influenced by the vibration of the molecule. This results in a dependence of the rotational constants B_e and D_e on v. Consequently, the new variables B_v and D_v [cm^{-1}] must be introduced. These are given by[9]

$$B_\mathrm{v} = B_e - \alpha_e\left(\mathrm{v} + \frac{1}{2}\right) \tag{2.17}$$

$$D_\mathrm{v} = D_e + \beta_e\left(\mathrm{v} + \frac{1}{2}\right). \tag{2.18}$$

α_e and β_e [cm^{-1}] are the vibration-rotation interaction constants for rigid-rotor motion and centrifugal distortion, respectively. B_v and D_v replace B_e and D_e in Eq. (2.13) so that the rotational term values can be written as[10]

$$F_\mathrm{v}(\mathrm{v}, J) = B_\mathrm{v}J(J+1) - D_\mathrm{v}J^2(J+1)^2, \tag{2.19}$$

where the subscript on $F_\mathrm{v}(\mathrm{v}, J)$ [cm^{-1}] denotes the vibrational dependence. Incorporating the effect of vibration on rotation, the rovibrational term values $T(\mathrm{v}, J)$ [cm^{-1}] can be

[9] A higher-order term can be included in the definition of B_v so $B_\mathrm{v} = B_e - \alpha_e\left(\mathrm{v} + \frac{1}{2}\right) + \gamma_e\left(\mathrm{v} + \frac{1}{2}\right)^2$; see pg. 108 of [1].

[10] A higher-order can be added such that $F_\mathrm{v}(\mathrm{v}, J) = B_\mathrm{v}J(J+1) - D_\mathrm{v}J^2(J+1)^2 + H_\mathrm{v}J^3(J+1)^3$. H_v can be modeled using a formula similar to Eq. (2.18) or can be assumed to be equal to H_e; see pg. 109 of [1].

obtained as the sum of $G(\mathrm{v})$ and $F_{\mathrm{v}}(\mathrm{v}, J)$:

$$T(\mathrm{v}, J) = \omega_e \left(\mathrm{v} + \tfrac{1}{2}\right) - \omega_e \chi_e \left(\mathrm{v} + \tfrac{1}{2}\right)^2 + B_{\mathrm{v}} J(J+1) - D_{\mathrm{v}} J^2 (J+1)^2. \qquad (2.20)$$

Here, the higher-order terms have been neglected.

Rovibrational transitions follow specific sets of selection rules. In the SHO approximation for a diatomic molecule, the selection rules are:

$$\Delta \mathrm{v} = +1, \quad \Delta J = \pm 1. \qquad (2.21)$$

Although the selection rules in Eq. (2.21) are written for absorption only (i.e., there is no $\Delta \mathrm{v} = -1$ rule corresponding to emission), $\Delta J = \pm 1$ is now allowed since transitions with $\Delta \mathrm{v} = +1$, $\Delta J = -1$ will still have a larger upper-state energy. A consequence of the rotational selection rule is that two branches will manifest themselves in a rovibrational spectrum: the P branch, corresponding to $\Delta J = -1$, and the R branch, corresponding to $\Delta J = +1$. Transitions within the two branches are typically written as P(J'') or R(J''). A classic example of the P and R branches is the rovibrational spectrum of the fundamental band of CO. This band is shown in Fig. 2.4, as taken from the HITRAN 2004 database [7] for the $^{12}C^{16}O$ isotopologue. Several interesting features can be observed in Fig. 2.4. First, there is no line present at the location where the $\Delta J = 0$ transition would exist (the "null gap") as it is forbidden according to the selection rules. Second, the line spacings in the P and R branches are not constant with increasing J'' due to vibration-rotation interaction via B_{v} and D_{v}. In the P branch, the line spacing increases with increasing J'', while the opposite

is true in the R branch. The line positions in the R branch will eventually wrap back on themselves, forming what is known as a bandhead (in CO, this only becomes evident at $J'' \approx 100$, which is not shown in Fig. 2.4).

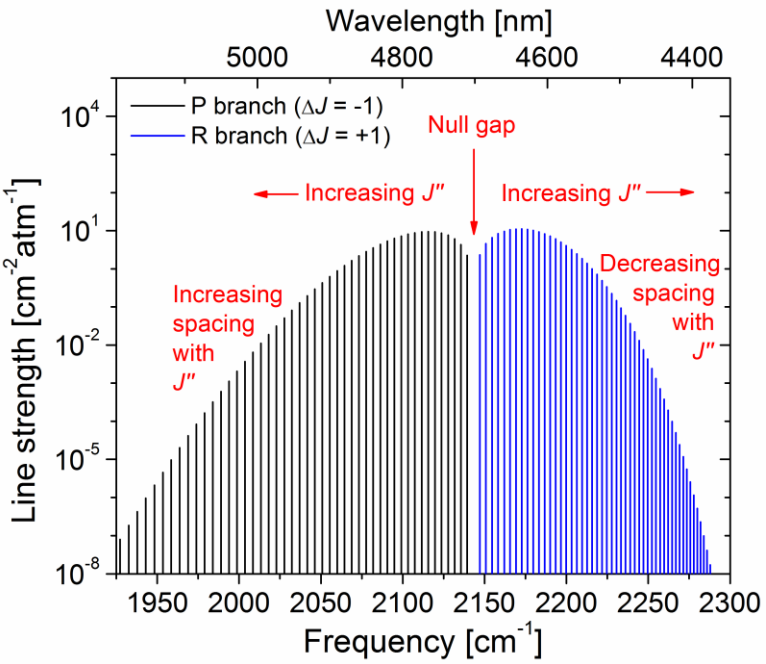

Figure 2.4 The P and R branches of the 1←0 band of $^{12}C^{16}O$ at 296 K according to HITRAN 2004 [7].

Another branch, the Q branch, is also possible in rovibrational (and rovibronic) spectra corresponding to the selection rules

$$\Delta v = +1, \quad \Delta J = 0. \tag{2.22}$$

The Q branch only appears in diatomic molecules when the electronic angular momentum about the internuclear axis is nonzero (i.e., $\Lambda \neq 0$; see Sect. 2.2.4) for the ground electronic

state. Most diatomic molecules do not possess a rovibrational Q branch.

2.2.4 Rovibronic spectroscopy of diatomic molecules

The previous coverages of rotational, vibrational, and rovibrational spectroscopy all assumed the molecule was in a fixed electronic state. However, transitions between electronic states can also occur (Fig. 2.3). In general, the rovibronic term values T can be written as the sum of the electronic, vibrational, and rotational term values:

$$T = T_e + G(\mathrm{v}) + F_{\mathrm{v}}(\mathrm{v}, J). \tag{2.23}$$

Here, T_e is the electronic term value. The gap between the two electronic states in Fig. 2.3 is a constant value for a given electronic transition and is written in [cm^{-1}] as $T_e' - T_e''$. T_e'' is defined to be zero for the ground electronic state. The terms $G(\mathrm{v})$ and $F_{\mathrm{v}}(\mathrm{v}, J)$ have their definitions as given in Eqs. (2.15) and (2.19). However, the parameters involved in the evaluation of $G(\mathrm{v})$ and $F_{\mathrm{v}}(\mathrm{v}, J)$ (e.g., B_e, ω_e) are now specific to an electronic state. In general, rovibronic spectra can display P, Q, and R branches.

A further complication introduced with the consideration of electronic motion is the addition of two new components of angular momentum: the electron orbital angular momentum and the electron spin angular momentum. The orbital angular momentum may be likened to the angular momentum of the Earth due to its orbital motion relative to the Sun, while the spin angular momentum may be likened to the angular momentum of the Earth due to rotation about its own axis (this second analogy only applies loosely).

The electron orbital angular momentum is described by the vector $\vec{\boldsymbol{L}}$ and is

generated by the motion of the electron(s) about the nucleus. Although the mass of the electron is over 10^3 times smaller than the mass of a single proton, the speed at which the electrons orbit is much faster than the molecule's rotation, meaning $\vec{\boldsymbol{L}}$ can be of the same magnitude as the total angular momentum $\vec{\boldsymbol{J}}$. Temporarily neglecting the effect of electron spin, $\vec{\boldsymbol{L}}$ can be thought of as precessing[11] around the cone created by rotating $\vec{\boldsymbol{L}}$ around the circle drawn in Fig. 2.5. The component along the internuclear axis, however, is constant and is called $\vec{\boldsymbol{\Lambda}}$. Its magnitude is

$$\left|\vec{\boldsymbol{\Lambda}}\right| = \hbar\Lambda. \tag{2.24}$$

Λ is a new quantum number corresponding to the projection of the electron orbital angular momentum onto the internuclear axis and can take the values $\Lambda = 0, 1, 2, \cdots$. When naming electronic states for molecules, the value of Λ determines the capital Greek letter used to name the state (more on this later).

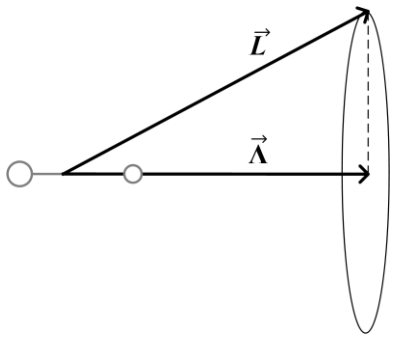

Figure 2.5 Angular momentum diagram for the electron orbital angular momentum in a diatomic molecule.

[11] A synonymous term to "precessing" is "nutating". Both terms refer to the movement of an angular momentum vector. In most cases (the asymmetric top is an exception), such a vector moves around a path so as to carve out a cone in 3-D space.

The other component of the electron angular momentum is the spin angular momentum. As described by Griffiths (pgs. 171-172 of [6]), the explanation for this momentum is not the electron spin about its axis but rather that elementary particles possess an intrinsic spin value termed s. For electrons (among other particles), $s = \frac{1}{2}$, and the vectors corresponding to this spin can be up (positive) or down (negative). The resultant vector $\vec{\boldsymbol{S}}$ corresponding to the electron spin angular momentum is the sum of the spin vectors of each unpaired electron. The magnitude of $\vec{\boldsymbol{S}}$ is

$$\left|\vec{\boldsymbol{S}}\right| = \hbar S, \tag{2.25}$$

where S is the total spin quantum number. For one unpaired electron, S will have the value of ½. For two unpaired electrons, S can either be 0 or 1.

The coupling between the orbital and spin angular momenta of electrons can take one of several different forms. The coupling schemes are described by Hund's rules, of which there are five cases: (a), (b), (c), (d), and (e). The most common occurrence is Hund's case (a), which is illustrated in Fig. 2.6. The ellipses represent the precession of the vectors to which they are attached. The vector $\vec{\boldsymbol{N}}$ is the angular momentum due to the nuclear rotation: in the case that $\Lambda = S = 0$, $\vec{\boldsymbol{N}} = \vec{\boldsymbol{J}}$ and the diatomic molecule is now the vibrating rotor described in Sect. 2.2.3. The vector $\vec{\boldsymbol{\Sigma}}$ is the projection of the spin angular momentum along the internuclear axis and its magnitude is related to the quantum number Σ by

$$\left|\vec{\boldsymbol{\Sigma}}\right| = \hbar\Sigma. \tag{2.26}$$

Σ can take values from $-S$ to S in integer steps so that there are $2S + 1$ possible values of Σ.[12] The value $2S + 1$ is called the multiplicity of the electronic state. For more on the various Hund's cases, see pgs. 218-226 of Herzberg [1].

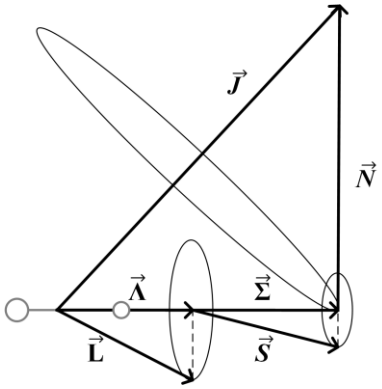

Figure 2.6 Angular momentum diagram for the coupling scheme of Hund's case (a). The ellipse around $\vec{\boldsymbol{J}}$ represents the precession of $\vec{\boldsymbol{N}}$ and $\vec{\boldsymbol{\Omega}}$, which is not labelled.

The final quantum number used to identify electronic states is Ω:

$$\Omega = |\Lambda + \Sigma|. \tag{2.27}$$

The corresponding vector $\vec{\boldsymbol{\Omega}}$ was omitted from Fig. 2.6 but would lie immediately on top of the vectors $\vec{\boldsymbol{\Lambda}}$ and $\vec{\boldsymbol{\Sigma}}$.

Finally, the term symbols used to describe electronic states should be explained. These symbols appear daunting but can be mostly explained in the context of the quantum numbers just introduced. The general form of the electronic term symbol for a diatomic

[12] The quantum number Σ should not be confused with the term symbol Σ used to represent electronic states with $\Lambda = 0$.

molecule is

$$^{2S+1}\Lambda^{+/-}_{\Omega,g/u}. \tag{2.28}$$

Here, Λ is not the numerical value of Λ but rather the capital Greek letter corresponding to the numerical value of Λ,. For example, values of $\Lambda = 0, 1, 2$ correspond to Σ, Π, and Δ, respectively. The $+/-$ refers to the change in the sign of the wave function upon reflection around the nuclear axis; this term is only important for states with $\Lambda = 0$ (i.e., Σ states) and is excluded elsewhere.[13] The g/u refers to the change in the sign of the wave function upon reflection around the axis of symmetry through the center of the molecule; this portion of the term symbol is only included for homonuclear molecules. Often, italicized English letters are added to the front of the term symbol as a shorthand notation: the capital letter *X* is typically used to denote the ground state, and the letters *A*, *B*, … are used to denote upper states of the same multiplicity as the ground state (*a*, *b*, … are used for upper states with different multiplicity than the ground state). Occasionally, one will see the detailed term symbol format of Eq. (2.28) dropped in favor of the shorthand notation. For example, the $^2\Delta \leftarrow {}^2\Pi$ transition of CH is labelled as $A\,^2\Delta \leftarrow X\,^2\Pi$ but will often be shortened to simply $A \leftarrow X$. It is also common for the Ω subscript to be omitted from the term symbol when specifying an electronic band. For example, the $A \leftarrow X$ band of OH is commonly written as $A\,^2\Sigma^+ \leftarrow X\,^2\Pi$, where the inclusion of both the $X\,^2\Pi_{1/2}$ and $X\,^2\Pi_{3/2}$ states is implied.

Many other considerations can be made in the analysis of diatomic electronic spectra. Λ-type doubling occurs due to interaction between $\vec{\boldsymbol{\Lambda}}$ and $\vec{\boldsymbol{N}}$; the two different

[13] See pg. 230 of Hollas [3] for an illustration of wave functions which do/do not change sign upon inversion.

levels associated with Λ-type doubling for each J value are typically denoted by F_c and F_d (see pgs. 226-231 of Herzberg [1]). Spin splitting, or spin-orbit coupling, results from interaction of $\vec{\boldsymbol{S}}$ with the magnetic field that is present when $\vec{\boldsymbol{\Lambda}} \neq 0$; this results in differences in energy between electronic states with different $\vec{\boldsymbol{\Omega}}$ (e.g., $^3\Delta_3$ versus $^3\Delta_2$ versus $^3\Delta_1$) and is typically denoted with numerical subscripts such as F_1, F_2, F_3 (see pgs. 231-237 of Herzberg [1]). In certain cases, spin splitting leads to the existence of specific P, Q, and R satellite branches between states of different $\vec{\boldsymbol{\Omega}}$. For example, the P branch between upper and lower states both with $\vec{\boldsymbol{\Omega}} = 1$ would be the P_{11} (or simply P_1) branch, while the R branch from an upper state with $\vec{\boldsymbol{\Omega}} = 1$ to a lower state with $\vec{\boldsymbol{\Omega}} = 2$ would be the R_{12} branch (see pgs. 258-261 of Herzberg [1]). As an example of an electronic spectrum, Fig. 2.7(a) shows the CH $A\,^2\Delta(v = 0) \leftarrow X\,^2\Pi(v = 0)$ band at 2000 K, displaying the P, Q, and R branches. Note that in the case of electronic spectra, the vibrational quantum numbers of the upper and lower states must be specified. Figure 2.7(b) shows a particular rotational transition in the R branch, demonstrating Λ-type doubling. Spin-orbit coupling is also evident in the splitting between the R_1 and R_2 branches. For more details on CH spectroscopy, the interested reader is referred to other works [8-11].

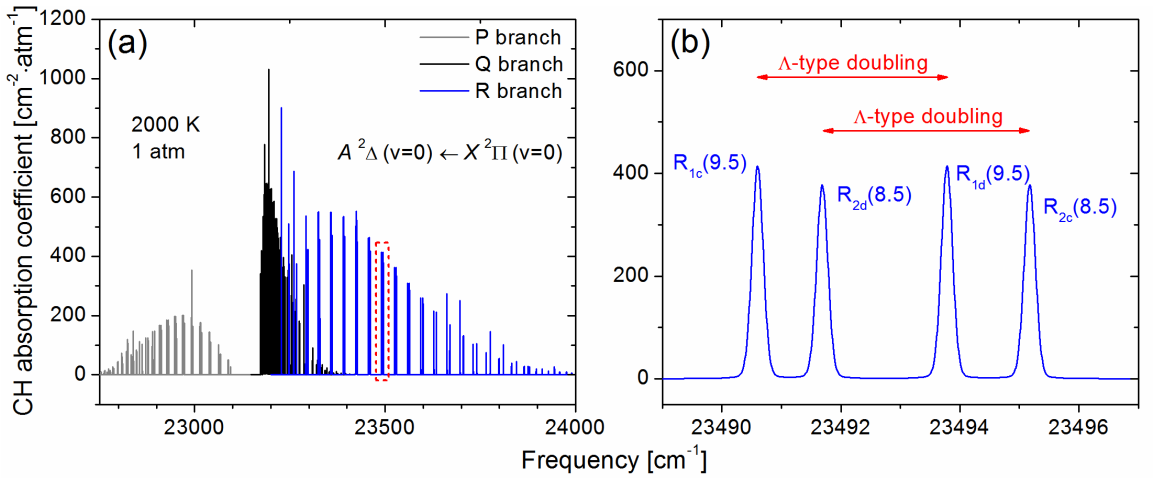

Figure 2.7 Calculated spectrum of the CH $A \leftarrow X$ band according to Mulvihill et al. [12], showing (a) the P, Q, and R branches and (b) Λ-type doubling.

2.3 Spectroscopy of polyatomic molecules

Polyatomic molecules are defined as those with $N \geq 3$, where N is the number of atoms in the molecule. The spectroscopic analysis of non-linear polyatomic molecules is significantly more complicated than that of diatomic molecules.

2.3.1 Rotational spectroscopy of polyatomic molecules

A helpful first step is to introduce the concepts of symmetric and asymmetric tops,[14] both of which can be explained in the context of moments of inertia. A molecule may have up to three non-equal moments of inertia corresponding to the three orthogonal axes in a Cartesian coordinate system. These moments of inertia are each defined quantitatively using Eq. (2.6) but need to be differentiated. The standard notation for the three moments of inertia are, in order of increasing magnitude, I_A, I_B, and I_C. For a symmetric top, there are two cases: a prolate top in which $I_B = I_C$ and an oblate top in which $I_B = I_A$. An

[14] Spherical tops also exist, for which $I_A = I_B = I_C$. An example is CH_4.

asymmetric top[15] has $I_A \neq I_B \neq I_C$. To characterize how relatively prolate or oblate an asymmetric top is, Ray's asymmetry parameter κ is often used (pg. 47 of [2]):

$$\kappa = \frac{2\left[B - \frac{1}{2}(A+C)\right]}{A-C}, \tag{2.29}$$

where the rotational constants A, B, and C are related to I_A, I_B, and I_C by

$$A = \frac{h}{8\pi^2 c I_A}, \quad B = \frac{h}{8\pi^2 c I_B}, \quad C = \frac{h}{8\pi^2 c I_C}. \tag{2.30}$$

Note the analogy between Eq. (2.30) for the polyatomic molecule and the definition of B_e for the diatomic molecule (Eq. (2.9)). The values of κ range from -1 for a prolate top to 1 for an oblate top. For the most-asymmetric top, when B is halfway between A and C, κ is 0. Since convention dictates $I_A < I_B < I_C$, $A > B > C$.

For diatomic molecules, the angular momentum vector is perpendicular to the internuclear axis (excluding angular momenta related to electronic motion). For polyatomic molecules, even in the absence of any electronic angular momenta, there is now also a component of the angular momentum corresponding called $\overrightarrow{\boldsymbol{J_z}}$ that resides along the primary axis of symmetry of the molecule, as shown in Fig. 2.8. This situation is analogous to that of electronic angular momentum in the diatomic molecule (i.e., Fig. 2.5). The magnitude of $\overrightarrow{\boldsymbol{J_z}}$ is given by

[15] The term "asymmetric top" can be rather confusing at first since many asymmetric tops (e.g., H_2O) do possess an axis of symmetry. The important consideration here is that $I_A \neq I_B \neq I_C$.

$$\left|\overrightarrow{\boldsymbol{J_z}}\right| = \hbar K, \tag{2.31}$$

where K is a new quantum number that describes the rotation of the molecule about the two axes of the molecule with identical moments of inertia. Since the magnitudes of $\vec{\boldsymbol{J}}$ and $\overrightarrow{\boldsymbol{J_z}}$ are both integral (when divided by $\hbar$), the magnitude of the other component of angular momentum $\overrightarrow{\boldsymbol{N}}$ cannot be integral except by accident The precession of $\vec{\boldsymbol{J}}$ has been omitted from Fig. 2.8 because it is more complicated in the polyatomic case; see pg. 23 of [2].

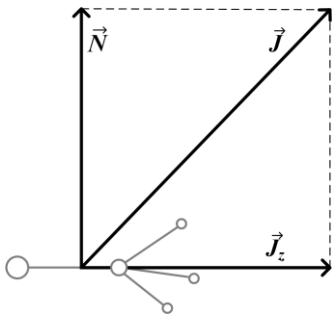

Figure 2.8 Angular momentum vector diagram for the symmetric top. The precession of $\vec{\boldsymbol{J}}$ is not shown as it is not a simple cone in this case.

The case of the asymmetric rotor is the most complicated. In this case, an additional quantum number is needed to describe the rotation of the molecule about the third axis. The quantum number K is replaced by K_a and K_c. However, the behavior of asymmetric tops is quite unlike diatomic molecules or symmetric tops (or spherical tops): the description of the rotational motion of the molecule cannot be simply described by K_a and K_c in addition to J because K_a and K_c are not good quantum numbers (see pgs. 103 and 205 of Bernath [13] for a brief discussion of good quantum numbers). K_a and K_c are instead referred to as quantum labels, where K_a is associated with the behavior of the

asymmetric top in the prolate limit and K_c is associated with the oblate limit. Since K_a and K_c are quantum labels rather than quantum numbers, rotational transitions for asymmetric tops are typically written as ${J'}_{K_a',K_c'} \leftarrow {J''}_{K_a'',K_c''}$. In summary, the analysis of asymmetric top spectra is complicated and there are "no simple series of rotational levels as there are for the symmetric top" (pg. 48, Herzberg [2]), meaning that simple formulae such as Eq. (2.13) cannot be used for asymmetric tops. The preferred method of modeling such molecules is through calculation and subsequent numerical diagonalization of the effective Hamiltonian to find the eigenvalues of the discrete energy levels. Computer programs such as SPFIT/SPCAT [14] exist for such tasks.

2.3.2 Vibrational spectroscopy of polyatomic molecules

For diatomic molecules, there is only one mode of vibrational motion. Polyatomic molecules, however, possess additional modes of vibration. For non-linear molecules, the number of possible vibrational modes is $3N - 6$. For linear molecules, the number of possible modes is $3N - 5$. For example, H_2O is a non-linear molecule and has three modes of vibration: symmetric stretching, bending, and asymmetric stretching, as illustrated in Fig. 2.9. On the other hand, CO_2 is a linear molecule and so has four modes of vibration (the additional mode is another bending mode that occurs in a plane orthogonal to the other bending mode; the two bending modes exist at the same frequency and are therefore said to be degenerate). As mentioned in Sect. 2.1.2, only vibrational modes which produce a motion in the dipole moment will possess corresponding IR spectra. For example, the ν_1 (symmetric stretching) mode of CO_2 does not produce any movement of the dipole moment, so it does not possess an IR spectrum (i.e., it is not IR active).

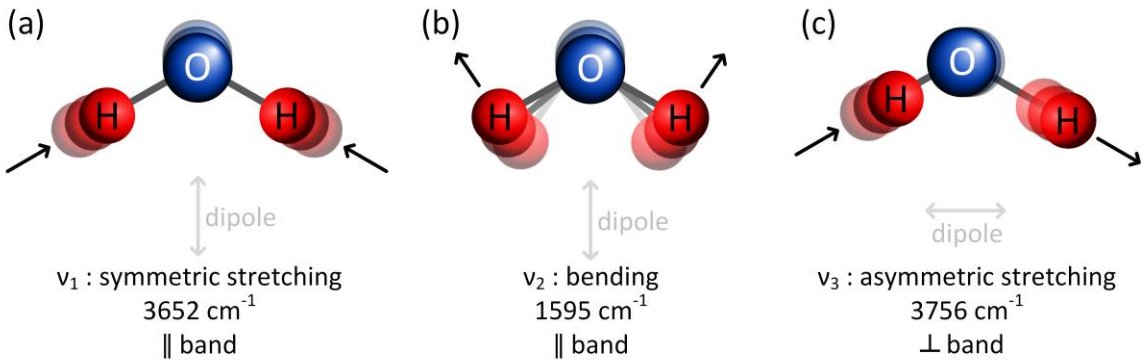

Figure 2.9 The vibrational modes of H_2O: (a) symmetric stretching, (b) bending, and (c) asymmetric stretching.

The || and ⊥ symbols in Fig. 2.9 are associated with the symmetry of the molecule. The axis of symmetry of H_2O passes vertically through the O atom. Vibrational modes for which the change in dipole moment is parallel to this axis are parallel (||) bands, while modes for which the change in dipole moment moves perpendicular to this axis are called perpendicular (⊥) bands.

The general convention for numbering the vibrational modes of a molecule is to first number the parallel bands in order of decreasing frequency and then to number the perpendicular bands in order of decreasing frequency. Combination bands can also exist, wherein more than one vibrational quantum number changes. For example, the fundamental $v_1 + v_3$ band in absorption would represent a change of $+1$ in both the v_1 and v_3 quantum numbers, which can be written succinctly as $101 \leftarrow 000$.

2.3.3 Rovibrational spectroscopy of polyatomic molecules

The rovibrational spectra of polyatomic molecules depend on many factors. For example, linear molecules may or may not manifest a Q branch (depending partially on the

degeneracy of the vibrational state) while symmetric tops and asymmetric tops will generally manifest a Q branch (except in the case of $K = 0$ for symmetric tops). Furthermore, even within the subcategory of asymmetric tops, there are three categories of bands: A-type, B-type, or C-type bands. Each band possesses unique features and vibrational (or rovibrational) selection rules; see pgs. 468-482 of Herzberg [2] for more on the different types of bands. In general, the rovibrational spectra of asymmetric tops is beyond the scope of this work, and the interested reader is referred to Ch. 4 of Herzberg [2].

2.3.4 Rovibronic spectroscopy of polyatomic molecules

This spectroscopy is complicated enough for Herzberg to have dedicated an entire volume to the topic [15], and the interested reader is referred therein for more information.

2.4 Summary

This Section provided a high-level overview of the basic principles and notation of molecular spectroscopy. Basic concepts such as absorption/emission, dipole moments, discretized energy levels, and potential energy wells were introduced. The spectroscopy of diatomic molecules was then addressed, including the relatively simple formulae that exist to model diatomic spectroscopy. The quantum numbers used to describe molecular energy levels were defined, and a sample rovibrational spectrum of CO was calculated as a demonstration of some pertinent features. Several angular momentum vector diagrams were drawn, and coupling schemes were discussed.

The term symbols of electronic energy levels were introduced in their general form.

These symbols are perhaps the most intimidating of the many complicated notations in spectroscopy. However, a basic understanding of these symbols can help the reader interpret the general nature of the specific electronic energy level to which these symbols refer, even if the fine details of the observed electronic spectra are quite intricate. A sample rovibronic spectrum of CH was calculated as a demonstration of some pertinent features.

Finally, a brief treatment of polyatomic spectroscopy was provided with introductions to the different categories of tops. In general, the spectra of polyatomic molecules are quite complicated, with the asymmetric top being the most complicated case. In fact, no analytical formulae exist to model the energy levels of asymmetric tops, and numerical methods are the preferred form of analysis. The naming conventions of vibrational modes were also provided.

2.5 References

[1] G. Herzberg, "Molecular Spectra and Molecular Structure: I. Spectra of Diatomic Molecules" 2nd ed., Van Nostrand, Princeton, NJ (1950).

[2] G. Herzberg, "Molecular Spectra and Molecular Structure: II. Infrared and Raman Spectra of Polyatomic Molecules" Van Nostrand, Princeton, NJ (1945).

[3] J.M. Hollas, "Modern Spectroscopy" 4th ed., John Wiley & Sons, Chichester, UK (2004).

[4] R.K. Hanson, R.M. Spearrin, C.S. Goldenstein, "Spectroscopy and Optical Diagnostics for Gases" Springer, Cham, Switzerland (2016).

[5] J.I. Steinfeld, J.S. Francisco, W.L. Hase, "Chemical Kinetics and Dynamics" 2nd ed., Prentice-Hall, Upper Saddle River, NJ (1999).

[6] D.J. Griffiths, "Introduction to Quantum Mechanics" 2nd ed., Pearson Prentice Hall, Upper Saddle River, NJ (2005).

[7] L.S. Rothman, D. Jacquemart, A. Barbe, D.C. Benner, M. Birk, L.R. Brown, M.R. Carleer, et al., "The HITRAN 2004 molecular spectroscopic database" *Journal of Quantitative Spectroscopy and Radiative Transfer* **96** (2005) 139-204.

[8] I. Botterud, A. Lofthus, L. Veseth, "Term values and molecular parameters for CH and CH^+" *Physica Scripta* **8** (1973) 218-224.

[9] C.R. Brazier, J.M. Brown, "A measurement of the lambda-type doubling spectrum of the CH radical by microwave-optical double resonance: Further characterization of the $A\,^2\Delta$ state" *Canadian Journal of Physics* **62** (1984) 1563-1578.

[10] M. Zachwieja, "New investigations of the $A\,^2\Delta$-$X\,^2\Pi$ band system in the CH radical and a new reduction of the vibration-rotation spectrum of CH from the ATMOS spectra" *Journal of Molecular Spectroscopy* **170** (1995) 285-309.

[11] J. Luque, D.R. Crosley, "Electronic transition moment and rotational transition probabilities in CH. I. $A\,^2\Delta$–$X\,^2\Pi$ system" *Journal of Chemical Physics* **104** (1996) 2146-2155.

[12] C.R. Mulvihill, M.W. Crofton, D.G. Arnold, E.L. Petersen, K.Y. Lam, "A laser diagnostic at 427 nm for quantitative measurements of CH in a shock tube" *Applied Physics B* **125** (2019) 78.

[13] P.F. Bernath, "Spectra of Atoms and Molecules" 3rd ed., Oxford University Press, Oxford, UK (2016).

[14] H.M. Pickett, "The fitting and prediction of vibration-rotation spectra with spin interactions" *Journal of Molecular Spectroscopy* **148** (1991) 371-377.

[15] G. Herzberg, "Molecular Spectra and Molecular Structure: III. Electronic Spectra and Electronic Structure of Polyatomic Molecules" 2nd ed., Van Nostrand, Princeton, NJ (1966).

3. THEORY OF QUANTITATIVE OPTICAL DIAGNOSTICS

Perhaps no single tool has so impacted the field of spectroscopy as the laser, a light source with high spatial and temporal coherence. Spatial coherence refers to the highly collimated nature of most laser beams, which often have divergence angles of ~5 mrad or less depending on the wavelength of the laser. This aspect of lasers allows for long-range applications or for short-range measurements with high spatial resolution. However, more pertinent in the present context, and likely to the scientific realm in general, is the high temporal coherence of lasers. Temporal coherence refers to the nearly monochromatic nature of many laser sources. For example, typical line widths in the near-IR region are 1 MHz or less, which is orders of magnitude narrower than light from light-emitting diodes or monochromators. The high temporal coherence of laser light allows for individual transitions of specific molecules to be probed independently of instrument-broadening phenomena since laser line widths can easily be orders of magnitude narrower than molecular line widths.

Combustion flow fields are ideal environments for the application of various laser diagnostics. Potential perturbation of the flow field by a probe is avoided with the use of a non-intrusive laser beam, which has no effect on the flow field except in the cases of photodissociation or photoionization (not of concern for the wavelengths utilized in this work). The spatial coherence of lasers lends itself to high-spatial-resolution measurements and/or to measurements in confined spaces. The temporal coherence of lasers allows for measurements of temperature and species concentrations.

The many potential benefits of laser absorption diagnostics make their application

to quantitative measurements in combustion applications desirable; however, a number of intricacies must be addressed. Therefore, while Chapter 2 focused on the species-specific nature of spectroscopy, this chapter focuses on the equations needed to perform quantitative measurements of individual gas species using laser diagnostics and, secondarily, emission diagnostics. First, the derivation of the Beer-Lambert law is given and discussed. Next, the calculations of the line strength and the line shape are addressed. Finally, emission diagnostics are briefly addressed.

3.1 The Beer-Lambert law

While both emission and absorption spectroscopy are inherently species-specific, absorption spectroscopy is the superior method for quantitative measurements of a specific species as the quantitative nature of an absorption diagnostic is independent of the optical setup. Emission diagnostics can indeed be quantitative, but this requires calibration with each new optical setup, making accidental misalignments quite costly in terms of time. Additionally, while line shapes can be measured using emission diagnostics in conjunction with spectrometers, such measurements will be affected by instrument (slit) broadening; narrow-line-width laser absorption diagnostics do not experience this confounding phenomenon. Table 3.1 draws several additional comparisons between emission and absorption diagnostics.

Table 3.1 Advantages and disadvantages of emission and absorption diagnostics.

	Emission spectroscopy	Absorption spectroscopy
Advantages	– species-specific – no light source needed – simple alignment; relatively vibration-insensitive	– species-specific – quantitative nature is independent of optical setup – no instrument broadening
Disadvantages	– quantitative nature is dependent on optical setup – subject to instrument broadening	– light source required – complicated alignment; can be vibration-sensitive

The cornerstone equation of absorption spectroscopy is the Beer-Lambert law, which relates the attenuation of a light source by an absorbing species to the concentration of that absorbing species and is perhaps the most important equation in absorption spectroscopy. In this subsection, a very general form of the Beer-Lambert law is derived from the equation of radiative transfer and then simplified to a familiar form. The assumptions involved in the simplified form are then addressed, with particular attention given to saturation effects.

3.1.1 Derivation of the Beer-Lambert law

The following derivation generally resembles the treatment in pgs. 50-64 of Linne [1]. Considering an infinitesimal three-dimensional block that experiences energy transfer via radiation and performing a radiative energy balance, the equation of radiative transfer can be written as

$$\frac{\partial}{\partial t}(\rho_\nu d\nu) + \vec{\nabla} \cdot (\rho_\nu \, \vec{\boldsymbol{c}} d\nu) = creation - loss, \tag{3.1}$$

where ρ_v is the spectral energy density [J/(cm^3·Hz)] of the radiation field, dv is the differential frequency [Hz], and $\vec{\boldsymbol{c}}$ is the velocity vector for light [cm/s]. The first term represents the time rate of change of energy density within dv stored within the volume, while the second term represents the net convection of energy density within dv flowing out of the volume. The creation term [W/cm^3] describes the generation of radiant energy at frequency v within the bandwidth dv (e.g., due to spontaneous emission), while the loss term [W/cm^3] describes the destruction of radiant energy at frequency v within the bandwidth dv (e.g., due to absorption). The details of the derivation of Eq. (3.1) can be found in [1], although the general form of Eq. (3.1) is identical to that of the familiar balance laws that can be written for quantities such as heat transfer and momentum transfer. The tasks at hand are to specify the creation and loss terms and to simplify Eq. (3.1) to a more useful form.

To specify the creation and loss terms in Eq. (3.1), consider the simple case of the two-level system depicted in Fig. 3.1, which consists of a ground state and an excited state separated by ΔE_{12}. The number density populations of the ground and excited states are N_1 and N_2 [cm^{-3}], respectively. In this simplified system, there are two categories of transfer processes between the upper and lower states: radiative processes, which are associated with the emission or absorption of a photon, and non-radiative processes, which do not involve emission or absorption of a photon.

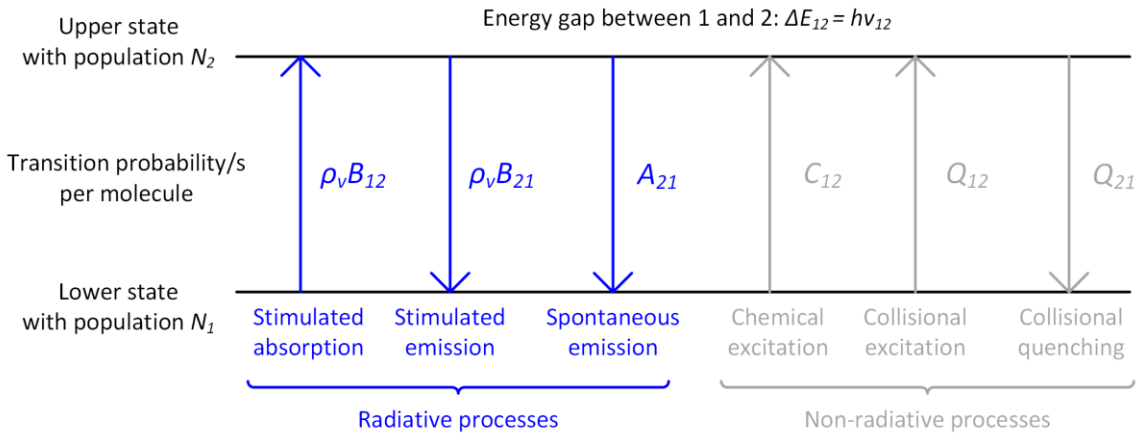

Figure 3.1 The two-level spectroscopic model of a system with $\Delta E_{12} = h\nu_{12}$, showing radiative and non-radiative processes.

The radiative processes consist of stimulated absorption, stimulated emission, and spontaneous emission.[1] When a molecule (or atom) in the ground state interacts with radiation of spectral energy density ρ_ν, the probability/s that this molecule will absorb a photon and transition to the excited state is given by $\rho_\nu B_{12}$, where B_{12} [cm^3·Hz/(J·s)] is the Einstein coefficient of stimulated absorption. Likewise, the probability/s that a molecule in the excited state that interacts with radiation of spectral density ρ_ν will emit a photon and transition to the ground state is given by $\rho_\nu B_{21}$, where B_{21} [cm^3·Hz/(J·s)] is the Einstein coefficient for stimulated emission. The probability/s that a molecule in in the excited state will spontaneously (i.e., regardless of the incoming radiation ρ_ν) emit a photon and transition to the ground state is given by A_{21}, where A_{21} [Hz] is the Einstein coefficient for spontaneous emission.

The non-radiative processes include chemical reactions, collisional excitation, and

[1] This neglects the effects of predissociation and photoionization, both of which are not concerns due to the low (rovibrational) frequencies of laser light utilized herein.

collisional quenching. The probability/s that a molecule in the ground state will be excited via a chemical reaction is given by C_{12} [Hz]; these types of reactions can take several different forms and are discussed in more detail in Sect. 3.4.2. The probability/s that a molecule in the ground state will be excited via a collision with another molecule is given by Q_{12} [Hz]. Finally, the probability/s that a molecule in the upper state will be returned to the ground state via a collision with another molecule is given by Q_{21} [Hz]. Collisional excitation and quenching are the means of establishing thermal equilibrium and are discussed in more detail in Sect. 3.4.2 and 3.4.3.

Returning to the issue of the creation and loss terms in Eq. (3.1), it is important to remember that Eq. (3.1) is a radiative energy balance such that non-radiative processes do not play a role. Keeping this is mind, the creation and loss terms can now be assessed using the Einstein coefficients so that Eq. (3.1) can be written as

$$\frac{\partial}{\partial t}\left(\rho_v dv\right) + \nabla \cdot \left(\rho_v \vec{c} dv\right) = h v_{12} N_2 A_{21} \frac{\phi}{c} dv + h v_{12} (N_2 B_{21} - N_1 B_{12}) \rho_v \frac{\phi}{c} dv. \quad (3.2)$$

Here, the term hv_{12} [J] represents the photon energy corresponding to the transition between levels 1 and 2, while ϕ [cm] is the spectral line shape that distributes emission and absorption probabilities in a spread around the central frequency v_{12}. Since ϕ is associated with a probability distribution, the following relation can be written:

$$\int_{-\infty}^{\infty} \frac{\phi}{c}\, dv = 1. \quad (3.3)$$

The behavior and modeling of ϕ is discussed in more detail in Sect. 3.3.

To reduce Eq. (3.2) to a more tenable form, several simplifying assumptions can be made (see Sect. 3.1.2 for a discussion of these assumptions). First, steady state can be assumed. Second, arranging the coordinate system so that the light passes along the x axis, it is assumed the solid angle Ω [sr] subtended by the imaging optics is small so the partial derivatives $\partial/\partial y$ and $\partial/\partial z$ are negligible. Incorporating these two assumptions and dividing out dv, one obtains[2]

$$\frac{d}{dx}\,(c\rho_v) = hv_{12}N_2A_{21}\frac{\phi}{c}\frac{\Omega}{4\pi} + hv_{12}(N_2B_{21} - N_1B_{12})\frac{\phi}{c}\rho_v. \tag{3.4}$$

The dimensionless[3] factor $\frac{\Omega}{4\pi}$ has been added to the spontaneous emission term to indicate only the emission contained in Ω is being considered. The spectral irradiance I_v [W/(cm^2·Hz)] is defined[4] as the power per unit area and unit bandwidth and is described by

$$I_v = c\rho_v. \tag{3.5}$$

The term "intensity" is often used to refer to either the spectral irradiance I_v or to the irradiance I [W/cm^2], which is defined by

$$I = \int_{-\infty}^{\infty} I_v\, dv. \tag{3.6}$$

[2] Note that the vector notation on $\vec{\boldsymbol{c}}$ was dropped upon making the one-dimensional assumption.

[3] Ω and 4π are both in steradians [sr], making $\frac{\Omega}{4\pi}$ dimensionless.

[4] The units of I_v could be simplified to [J/cm^2], but this would obscure their physical significance.

Using I_ν, Eq. (3.4) can be written as

$$\frac{dI_\nu}{dx} = \frac{h\nu_{12}}{4\pi c} N_2 A_{21} \phi \Omega + \frac{h\nu_{12}}{c^2} (N_2 B_{21} - N_1 B_{12}) \phi I_\nu. \tag{3.7}$$

Volume emission and absorption coefficients ϵ_ν [W/(cm^3·sr·Hz)] and κ_ν [cm^{-1}] can be respectively defined as

$$\epsilon_\nu(x) = \frac{h\nu_{12}}{4\pi c} N_2 A_{21} \phi \tag{3.8}$$

$$\kappa_\nu(x) = \frac{h\nu_{12}}{c^2} (N_1 B_{12} - N_2 B_{21}) \phi, \tag{3.9}$$

where both coefficients can generally be functions of the distance x along the beam path due to fluctuations in the number density, temperature, etc. Equation (3.7) can now be written as

$$\frac{dI_\nu}{dx} = \epsilon_\nu(x) \Omega - \kappa_\nu(x) I_\nu. \tag{3.10}$$

For absorption experiments, the emission contribution to the signal is much less than that from the radiation source so that the $\epsilon_\nu(x)\Omega$ term can be neglected and Eq. (3.10) simplifies to

$$\frac{dI_\nu}{dx} = -\kappa_\nu(x) I_\nu. \tag{3.11}$$

Equation (3.11) is the differential form of the Beer-Lambert law.

Assuming the absorption coefficient is constant along the beam path and integrating Eq. (3.11) from $x = 0$ to $x = L$, one obtains

$$\ln\big(I_\nu(L)/I_\nu(0)\big) = -\kappa_\nu L, \tag{3.12}$$

where $I_\nu(L)$ is the intensity at $x = L$ and $I_\nu(0)$ is the intensity at $x = 0$; these two terms are more commonly written as I_t and I_0, respectively.[5] Finally, it is common to normalize the volume absorption coefficient κ_ν to the partial pressure of the absorbing species P_{abs} by defining the spectral absorption coefficient k_ν [$\mathrm{cm^{-1}\cdot atm^{-1}}$] (often referred to as simply the absorption coefficient). The two variables are related by

$$k_\nu = \frac{\kappa_\nu}{P_{abs}}, \tag{3.13}$$

where P_{abs} is related to the total pressure P and the mole fraction of the absorbing species X_{abs} by

$$P_{abs} = X_{abs}P. \tag{3.14}$$

Incorporating k_ν and the definitions of I_t and I_0 into Eq. (3.12), an alternate form of the Beer-Lambert law can be written as

[5] This notation drops the ν subscript, but it is still implied. Of course, even a photodetector with a narrow bandpass filter will still effectively measure the spectrally integrated I instead of I_ν, although for a narrow-line-width laser the distribution in ν will be very narrow. Ultimately, it is the ratio I_t/I_0 that matters.

$$\ln(I_t/I_0) = -k_v P X_{abs} L. \tag{3.15}$$

A common tool for analyzing absorbing systems is the optically thin approximation. To employ this approximation, it is useful to introduce the absorbance[6] A, which is defined as

$$A = \kappa_v L = k_v P X_{abs} L \tag{3.16}$$

so that Eq. (3.15) can be written as

$$\ln(I_t/I_0) = -A. \tag{3.17}$$

In the case where A is very small, the optically thin approximation can be invoked by expressing Eq. (3.17) as a series and then truncating it to yield

$$I_t/I_0 = 1 - A. \tag{3.18}$$

The behaviors of the actual Beer-Lambert law, Eq. (3.17), and the optically thin approximation, Eq. (3.18), are compared graphically in Fig. 3.2. The optically thin approximation breaks down at $A \approx 0.1$, at which point the Beer-Lambert law predicts a percent absorption of 9.52% while the optically thin approximation predicts a percent

[6] This is also commonly referred to as the optical depth. However, some authors utilize the term "absorbance" to describe a similar quantity that is defined using the base 10 logarithm instead of the natural logarithm. Care should be taken to ensure that the proper quantity is being described/employed.

absorption of 10.0%.

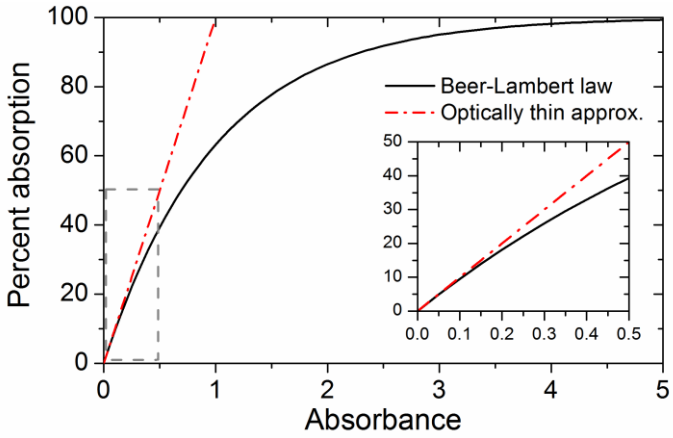

Figure 3.2 Comparison of the Beer-Lambert law and the optically thin approximation. The inset shows the deviation of the two relations near $A \approx 0.1$.

The two-level system (Fig. 3.1) used to derive the forms of the creation and loss terms in Eq. (3.1) was rather quickly abstracted away by the introduction of $\epsilon_\nu(x)$ and $\kappa_\nu(x)$. This may seem concerning given that some systems must be described by three- or four-level models (see the review by Daily [2]). However, even if a three- or four-level system were incorporated into this derivation, all that would change would be the definitions of $\epsilon_\nu(x)$ and $\kappa_\nu(x)$; the abstraction of the Einstein coefficients would still take place, and the same form of the Beer-Lambert law would still be obtained. Ultimately, the key assumption involved in the Beer-Lambert law is that absorption is the dominant mechanism of change in signal intensity and that other forms of radiation interaction (emission, reflection, and scattering) are negligible. The validity of this assumption and others is discussed in the following pages.

3.1.2 Assumptions of the Beer-Lambert law

In the preceding derivation, it was first assumed the spectroscopic system was at steady state. This assumption is appropriate when the characteristic optical time is much longer than the characteristic times of the energy transfers within the molecules due to excitation and collisions. For extremely fast, pulsed lasers, this assumption may not be valid and rate equations may need to be employed (see Settersten and Linne [3]). For continuous wave lasers such as the laser employed in this dissertation, steady state is typically a valid assumption.

A second assumption was a small solid angle Ω such that the partial derivatives in the transverse directions were negligible. This assumption depends largely on the optical configuration of the experimental setup and primarily affects the emission term $\epsilon_v(x)\Omega$ since emission is spatially isotropic. High-pressure, high-temperature combustion applications typically involve relatively small areas of optical access with correspondingly small values of Ω. In the case of laser absorption experiments, typical divergence angles and beam waists of commercial lasers are <5 mrad and <5 mm, respectively, so that optical access can be further restricted using apertures (see Sect. 4.2.5) and the assumption of small Ω can thereby be further improved.

It was also assumed κ_v and k_v were constant along the beam path. This assumption of the Beer-Lambert law can be invalid in turbulent combustion environments. Shock tubes, however, can closely produce the homogenous conditions needed to validate this assumption. In shock-tube experiments, a potential source of non-uniformity along the beam path is the presence of the boundary layer that forms behind the incident shock wave. For the large shock tube (inner diameter of 16.2 cm) and high levels of Ar dilution (~99%)

used in this work, boundary-layer effects within the shock tube are expected to be minimal according to the following reasoning. At the typical temperatures behind the reflected shock wave used herein (~900 K and above), it was estimated that 30-50 μs will elapse between the arrivals of the incident shock wave and reflected shock wave at the optical sidewall port (located 1.6 cm from the shock-tube endwall). During this time, calculations according to Hargis and Petersen [4] suggest that a boundary layer of ≤2 mm will develop (corresponding to a total boundary layer of ≤4 mm), thus composing only 2.5% of the total beam path length through the shock tube. This small value suggests non-uniformities in temperature/pressure/density along the beam path length due to the cold boundary layer should have a relatively small effect.

It was assumed that the absorbing species was in local thermodynamic equilibrium (LTE) such that the Boltzmann distribution was valid. Until LTE is achieved, the calculations of the population levels will not be accurate as their temperature dependence assumes the Boltzmann distribution (see Sect. 3.2) and the calculation of the line strength will therefore be incorrect. Of particular concern in shock-tube experiments, wherein the test gas is rapidly shock-heated over the course of a few μs, is the vibrational relaxation time, which is the time required for the vibrational energy levels to achieve LTE and is much longer than the relatively rapid establishment of translational and rotational equilibrium. Vibrational relaxation is discussed in further detail in Sect. 4.1.2, with the conclusion that such effects were not of concern for the present experiments.

Another assumption was that emission, reflection, and scattering were all negligible. Emission is spatially isotropic and is typically much weaker than spatially coherent, strong laser radiation. In the context of shock-tube experiments, simple checks

for emission effects can be performed by shutting off or blocking the radiation source (see Sect. 4.2.5). Reflection and scattering from particulate matter can create an artificial absorption effect; however, for the strictly gas-phase mixtures used in this dissertation, no particles were present to cause scattering.

It was assumed the gas was not in the optically thick regime, where high concentrations of absorbing molecules cause the Beer-Lambert law to become invalid [5]. While there is no exact limitation, ~85% absorption levels have been achieved in shock tubes with no adverse effects [6]. In the present work, all absorption levels were kept much lower than this limit, typically at ~2% or less.

Finally, although not explicitly stated in Sect. 3.1.1, it is generally assumed that the radiation source is nearly monochromatic so that k_ν can be calculated at a particular frequency ν. While no perfectly monochromatic light source exists, lasers approximate this behavior extremely well for typical combustion conditions: mid-IR transitions of molecules at 1000-2000 K and ≥1 atm are at least 100 times broader than commercially available lasers. Corrections can be made in the case of spectrally broad light sources; see Sect. 4.4 for more on such corrections.

3.1.3 Spectroscopic saturation effects

Another assumption made in the Beer-Lambert law was that the two-level system was not saturated; this assumption merits slightly more attention. Saturation occurs when sufficiently large incident light intensities cause the population in the upper state, N_2, to approach the population in the lower state, N_1. When this condition is approached, the effective absorption coefficient goes to 0 so that the medium appears to be non-absorbing

and the Beer-Lambert law becomes invalid.

The effects of saturation can be estimated for the two-level system by first considering the various processes in Fig. 3.1 that transfer molecules[7] between the two levels. Neglecting the collisional excitation and chemical reaction terms, a rate equation for N_2 can be written as (pg. 58 of Linne [1]):

$$\frac{dN_2}{dt} = N_1 B_{12} \int \rho_v \frac{\phi}{c} dv - N_2 \left[B_{21} \int \rho_v \frac{\phi}{c} dv + A_{21} \int \frac{\phi}{c} dv + Q_{21} \right]. \qquad (3.19)$$

From the conservation of mass (Eq. (3.23)), $\frac{dN_1}{dt}$ is equal to $-\frac{dN_2}{dt}$ in the two-level model of Fig. 3.1.

A matter of difficulty is the evaluation of the two occurrences of $\int \rho_v \frac{\phi}{c} dv$ in Eq. (3.19). In some texts (e.g., pgs. 60-61 of Linne [1] and pgs. 385-390 of Eckbreth [7]), it is assumed the spectral source is very broad so that ρ_v is approximately constant over the line shape ϕ and can consequently be removed from the integral; this is illustrated as Case 1 in Fig. 3.3(a). Invoking this assumption and employing Eq. (3.3), the two $\int \rho_v \frac{\phi}{c} dv$ terms simplify to ρ_v. However, while the assumption of Case 1 may be appropriate to short-duration pulsed lasers, it is not valid in the case of narrow-line-width laser sources as utilized in the present work. A more appropriate assumption is that the spectral source is

[7] This is an important distinction. The equation of radiative transfer, Eq. (3.1), is simply an expression of the conservation of energy and describes the transfer of *energy* into or out of a bandwidth dv due to radiative processes only. On the other hand, Eq. (3.19) describes the transfer rate of *molecules* between states 1 and 2 due to the radiative and non-radiative processes shown in Fig. 3.1. Therefore, while radiative processes can both directly affect the populations N_1 and N_2 *and* cause absorption and/or emission, non-radiative processes can *only* directly affect N_1 and N_2 (indirectly, non-radiative processes can influence radiative processes by changing the weighting of probabilities through changing N_1 and N_2).

very narrow compared to the line shape; this is illustrated as Case 2 in Fig. 3.3(b).

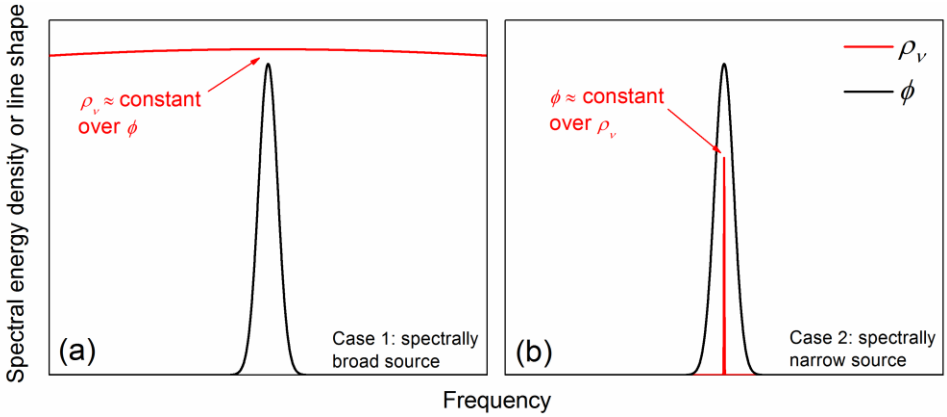

Figure 3.3 Illustration of the cases of (a) spectrally broad and (b) spectrally narrow sources ρ_v as compared to the absorption line shape ϕ.

To evaluate the integral $\int \rho_v \frac{\phi}{c} dv$ for Case 2, the following reasoning was employed. If the line shape ϕ is much wider than the spectral energy density ρ_v, it may be assumed that ϕ is constant over ρ_v at the peak value of ϕ, ϕ_{peak}. Then, the integral terms may be written as

$$\int \rho_v \frac{\phi}{c} dv \approx \frac{\phi_{peak}}{c} \int \rho_v dv = \frac{\phi_{peak}}{c} \frac{I}{c}, \tag{3.20}$$

where $\frac{I}{c}$ was introduced by way of Eqs. (3.5) and (3.6). Inserting the result of Eq. (3.20) into Eq. (3.19), Eq. (3.19) becomes

$$\frac{dN_2}{dt} = N_1 B_{12} \frac{\phi_{peak}}{c} \frac{I}{c} - N_2 \left[B_{21} \frac{\phi_{peak}}{c} \frac{I}{c} + A_{21} + Q_{21} \right]. \tag{3.21}$$

At saturation, the rates of excitation and de-excitation are equalized so that the system is at steady state. Thus, $\frac{dN_2}{dt}$ can be set to 0 and Eq. (3.21) can be rearranged to obtain

$$N_1 B_{12} \frac{\phi_{peak}}{c} \frac{I}{c} = N_2 \left[B_{21} \frac{\phi_{peak}}{c} \frac{I}{c} + A_{21} + Q_{21} \right]. \tag{3.22}$$

Writing the mass conservation for the system as

$$N_1 + N_2 = N_{tot}, \tag{3.23}$$

one can eliminate N_1 from Eq. (3.22) using Eq. (3.23) and rearrange to obtain

$$\frac{N_2}{N_{tot}} = \frac{B_{12} \frac{\phi_{peak}}{c} \frac{I}{c}}{(B_{12}+B_{21}) \frac{\phi_{peak}}{c} \frac{I}{c} + A_{21} + Q_{21}}. \tag{3.24}$$

Equation (3.24) can be further rearranged to read

$$\frac{N_2}{N_{tot}} = \left(\frac{B_{12}}{B_{12}+B_{21}} \right) \left(\frac{1}{1+\frac{I_{sat}}{I}} \right), \tag{3.25}$$

where I_{sat} [W/(cm^2)] is defined as

$$I_{sat} = \frac{(A_{21}+Q_{21})c^2}{(B_{12}+B_{21})\phi_{peak}}. \tag{3.26}$$

When $I = I_{sat}$ and assuming that $B_{12} = B_{21}$, N_2 is 25% of N_{tot}. As I becomes much larger than I_{sat}, N_2 approaches 50% of N_{tot}. Equation (3.26) indicates the irradiance at which saturation will start to come into play. Most textbooks use the broad-spectral-source assumption (Fig. 3.3(a)) to provide an expression for the saturated spectral irradiance, $I_{v,sat}$, at which saturation will come into effect. Equation (3.26) does not make the spectrally broad assumption and is therefore a new development. For narrow-line-width applications, Eq. (3.26) may be a more appropriate relation than the expression for $I_{v,sat}$ that is often provided.

The following serves as an example estimation of I_{sat}. The H_2O transition utilized in the present work, the $5_{5,1} \leftarrow 5_{5,0}$ transition within the fundamental $v_1 + v_3$ band at 7203.890 cm^{-1}, has an A_{21} value of 22.77 Hz [8]. Utilizing the relations between A_{21}, B_{21}, and B_{12} (see Sect. 3.2.1) and the fact that the upper- and lower-state degeneracies g_2 and g_1 (see Sect. 3.2.1) are both equal to 33 for this transition [8], B_{21} and B_{12} can be calculated to both be 3.66×10^{21} $cm^3 \cdot Hz/(J \cdot s)$. Quenching rates Q_{21} in the IR are typically 3-5 orders of magnitude greater than A_{21} (pg. 187 of Hanson et al. [9]). To obtain a worst-case (i.e., lowest value of I_{sat}) estimate, Q_{21} was assumed to be 10^3 times A_{21}. Finally, it is necessary to evaluate ϕ to obtain an estimate of ϕ_{peak}. Evaluating the Ar-broadening parameters for this line (Sect. 4.2.3) to calculate the Voigt line shape (Sect. 3.3) at 1 atm and 1500 K, ϕ_{peak} was determined[8] to be ~30 cm. Evaluating Eq. (3.26) with the above

[8] The temperature and pressure dependence of ϕ_{peak} cannot be ignored. For example, as the pressure increases, the line shape will become broader and will thus possess a lower value of ϕ_{peak} (in accord with the general notion that the saturation limit increases with pressure). It is perhaps for this reason that most authors simply provide an estimate for $I_{v,sat}$, as this is independent of the line shape. However, the estimate of 30 cm provided herein is expected to be quite accurate for the H_2O transition in consideration and is certainly appropriate for an order-of-magnitude estimate of I_{sat}.

values, I_{sat} was estimated to be 93.3 W/cm^2, or 933 mW/mm^2. Inspecting previous experimental work on saturation limits, it was found that SF_6 displayed saturation limits near 100 mW/mm^2 for pressures of ~8 Torr for absorption of CO_2 laser radiation near 10 μm according to Burak et al. [10]. Given the saturation limit increases with pressure, the I_{sat} estimate of 933 mW/mm^2 obtained at 1 atm seems reasonable in comparison with the results of Burak et al. at 8 Torr. The laser power traversing the test section in this work was ~3 mW. Estimating the laser beam diameter at 4 mm, the estimated laser intensity passing through the shock tube was 0.24 mW/mm^2. Thus, saturation effects can be neglected. If the laser intensity were significantly attenuated to avoid saturation complications, this should be done before traversing the test section.

3.2 Calculation of the line strength

The absorption coefficient k_v in the Beer-Lambert law, Eq. (3.15), can be written

$$k_v = S_{12}\phi, \tag{3.27}$$

where S_{12} [cm^{-2}·atm^{-1}] is the line strength and ϕ is the line shape introduced earlier. The line strength S_{12} of a transition describes the probability of that transition occurring, while the line shape ϕ describes the spread of that probability around the central frequency v_{12}. Graphically, S_{12} can be pictured as the area under the spectral line shape on a k_v vs. $\bar{v}$ plot (Fig. 3.4), where $\bar{v}$ [cm^{-1}] is the frequency in wavenumbers.[9] Figure 3.4 illustrates the

[9] The frequency in wavenumbers (i.e., [cm^{-1}]) is related to the frequency in [Hz] by the relation $\bar{v} = v/c$ and is the number of oscillations per cm. The overbar is used throughout to denote units of wavenumbers.

significance of the integrated areas under the k_v and ϕ curves and serves as a useful demonstration of a proper way to handle one possible set of units for S_{12}, ϕ, and k_v. A broader line shape will shift the transition probability away from $\bar{\nu}_{12}$, while a narrower line shape will focus the transition probability tightly around $\bar{\nu}_{12}$. The calculation of the line strength is addressed here, while the calculation of the line shape using various models is discussed in Sect. 3.3.

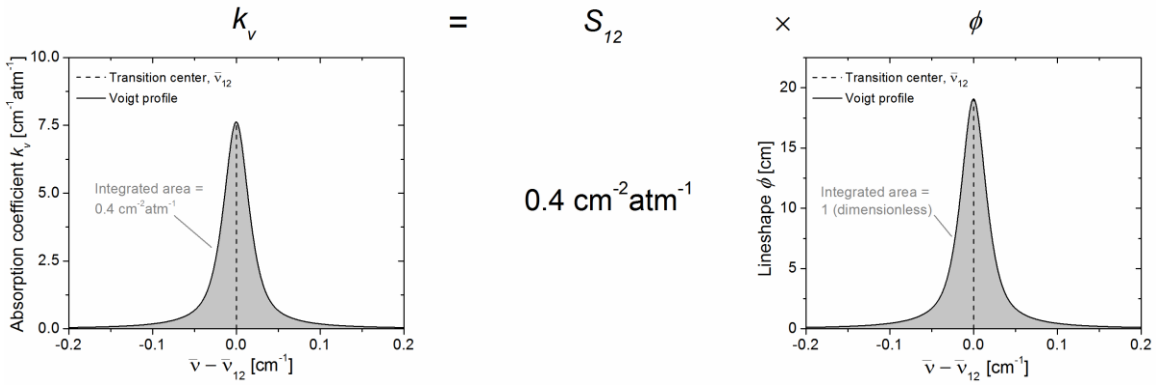

Figure 3.4 Graphical depiction of Eq. (3.27) using arbitrary values, demonstrating the line strength is the integrated area under the absorption coefficient.

3.2.1 Transition probabilities and Boltzmann populations

The absorption line strength is directly proportional to two parameters: (1) the probability of a molecule either absorbing or emitting when impinged upon by a photon of frequency ν_{12} and (2) the population of the ground state. The first parameter is directly related to the Einstein coefficients, while the second can be obtained via statistical mechanics. By considering Eqs. (3.9), (3.13), and (3.27), S_{12} can be written as

$$S_{12} = \frac{h\nu_{12}}{c^2}\frac{1}{P_{abs}}(N_1 B_{12} - N_2 B_{21}), \tag{3.28}$$

where, as before, the Einstein coefficients B_{12} and B_{21} are related to the probability of transitioning between states 1 and 2 while N_1 and N_2 are the populations of states 1 and 2.

Invoking the results of statistical mechanics (see pgs. 96-102 of Eckbreth [7]), the distribution of molecules throughout the available discrete energy levels can be described by the Boltzmann distribution

$$\frac{N_i}{N_{tot}} = \frac{g_i \exp\left(-\frac{E_i}{kT}\right)}{Q}, \tag{3.29}$$

where N_i is the number density population in state i [cm^{-3}], N_{tot} is the total number density population [cm^{-3}], g_i is the degeneracy of state i, E_i [J] is the i-th energy level, k is Boltzmann's constant [J/K], and Q is the partition function. Q is an energy-weighted sum over all available energy levels:

$$Q = \sum_i g_i \exp\left(-\frac{E_i}{kT}\right). \tag{3.30}$$

$\frac{N_i}{N_{tot}}$ is often referred to as the Boltzmann fraction. The total number of molecules N_{tot} is given by

$$N_{tot} = \frac{PN_A}{R_u T} \tag{3.31}$$

where N_A is Avogadro's number [mol^{-1}] and R_u is the universal gas constant [cm^3·atm/(K·mol)].

Additionally, considerations of the Planck blackbody distribution reveal that the Einstein coefficients can be related to one another (see pgs. 67-68 of Linne [1]) by

$$g_1 B_{12} = g_2 B_{21} \tag{3.32}$$

$$A_{21} = \frac{8\pi h \nu_{12}^3}{c^3} B_{21}, \tag{3.33}$$

where g_1 and g_2 are the degeneracies of states 1 and 2. Utilizing Eqs. (3.29) and (3.32) and performing some manipulation, Eq. (3.28) can be written as

$$S_{12} = \frac{h\nu_{12}}{c^2} \frac{1}{P_{abs}} N_1 B_{12} \left(1 - \exp\left(-\frac{h\nu_{12}}{kT}\right)\right). \tag{3.34}$$

Using Eqs. (3.32) and (3.33), S_{12} can also be written in terms of the spontaneous emission coefficient:

$$S_{12} = \frac{c}{8\pi\nu_{12}^2} \frac{1}{P_{abs}} N_1 \frac{g_2}{g_1} \mathrm{A}_{21} \left(1 - \exp\left(-\frac{h\nu_{12}}{kT}\right)\right). \tag{3.35}$$

Equations (3.34) and (3.35) are equivalent ways of evaluating S_{12} in [$cm^{-2} \cdot atm^{-1}$]. For other formulations and unit systems that can be used to write S_{12}, see pgs. 124-126 of Hanson et al. [9].

3.2.2 Temperature dependence

In combustion applications, it is typically necessary to model the temperature

dependence of the line strength. Inspecting Eq. (3.34), the temperature dependence of each term can be assessed. The Einstein coefficients are associated with the probabilities of single particles undergoing changes and thus are independent of temperature. The lower-state population N_1 is temperature-dependent according to the Boltzmann distribution, Eq. (3.29), as well as the total number of molecules, Eq. (3.31). Taking the ratio of line strengths at a reference temperature[10] T_0 [K] and at some other temperature T [K], the temperature-independent terms drop out to yield the relation

$$S_{12}(T) = S_{12}(T_0)\frac{T_0}{T}\frac{Q(T_0)}{Q(T)}\frac{\exp(-E''/kT)}{\exp(-E''/kT_0)}\frac{[1-\exp(-hv_{12}/kT)]}{[1-\exp(-hv_{12}/kT_0)]}. \tag{3.36}$$

Here, the symbol E'' [J] for the lower-state energy has been adopted in place of E_1 in deference to standard spectroscopic notation. The first fractional term in Eq. (3.36) is due to the temperature dependence of the number density,[11] the second and third fractional terms result from the Boltzmann population, and the fourth fractional term is due to stimulated emission.

The temperature dependence of $S(T)/S(T_0)$ as well as the last three terms in Eq. (3.36) is illustrated in Fig. 3.5 for three different cases of the lower-state energy and the transition frequency. By comparing Figs. 3.5(a) and 3.5(b), one can see that the temperature-dependent effect of the lower-state energy generally becomes significantly larger for transitions with larger values of E'', such that $S_{12}(T)$ exhibits a peak at a

[10] The HITRAN database employs the widely used T_0 of 296 K. This value is used here.

[11] Note that the first fractional term is only included if the units chosen for S_{12} (in this case, [cm^{-2}·atm^{-1}]) involve a dependence on number density. For example, if the units are [cm^{-1}/(molecule·cm^{-2})], this term will not be present (although a number density dependence will need to be added into the Beer-Lambert law).

temperature above T_0 before decreasing at higher temperatures. By comparing Figs. 3.5(a) and 3.5(c), one can observe that the stimulated emission term becomes practically negligible for higher frequencies:[12] for visible/UV transitions, stimulated emission can often be completely neglected in the evaluation of $S_{12}(T)$ (for example, see Mulvihill et al. [11]). The partition function temperature dependence is molecule-dependent; shown in Fig. 3.5 is the partition function for H_2O, which was evaluated according to Laraia et al. [12] and is the same in each panel. Not shown in Fig. 3.5 is the first fractional term of Eq. (3.36), $\frac{T_0}{T}$, as this follows a straightforward inverse temperature dependence. Finally, note that Fig. 3.5 incorporates $\bar{E}''$ [cm^{-1}] and $\bar{\nu}_{12}$ [cm^{-1}] in place of E'' and ν_{12}.

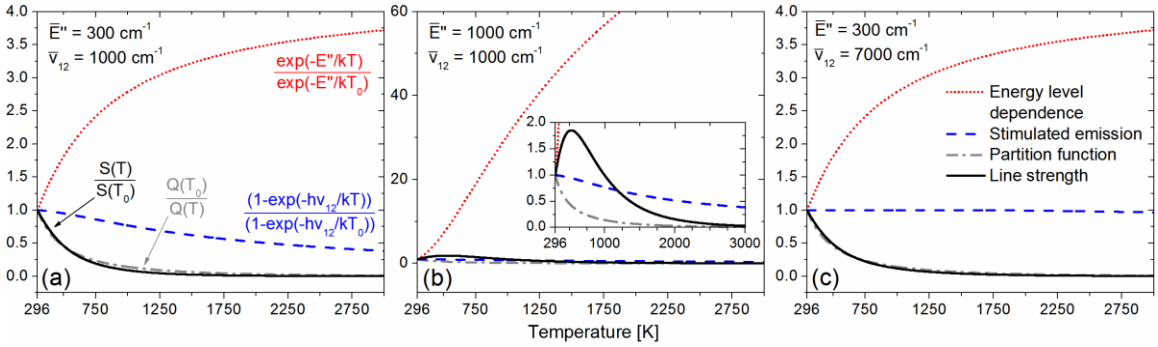

Figure 3.5 Temperature dependence of various terms in Eq. (3.36) for varying values of $\bar{E}''$ and $\bar{\nu}_{12}$. $Q(T)$ was evaluated for H_2O using Laraia et al. [12].

As mentioned in Sect. 3.2.1, the Einstein coefficients can be obtained from quantum mechanics through relation to the dipole matrix elements (see Ch. 9 of Griffiths [13]). Similarly, the partition function $Q(T)$ can be obtained through knowledge of all the possible energy levels of a molecule. Both of these methods are beyond the scope of this

[12] Strictly speaking, stimulated emission becomes negligible when $h\nu_{12} >> kT$.

work, however, and a simpler method is to access tabulated data. For example, the HITRAN database can be used to obtain values of $S_{12}(T_0)$. For more on obtaining line strengths and partition function values from tabulated sources, see Appendix D.

3.3 Calculation of the line shape

Ideally, transitions from one energy level of a molecule to another would take place at a single, discrete frequency as predicted by quantum mechanical considerations. However, various phenomena serve to broaden the transition probability away from the line center. The modeling of these phenomena is accomplished using the line shape ϕ. Therefore, while the total transition probability (i.e., the line strength) is fixed by the temperature,[13] the distribution of that probability about the line center is controlled by the line shape (see Fig. 3.4), which is a function of temperature, pressure, and frequency.

A variety of line shapes can be employed to model spectral line shapes. Perhaps the most commonly used among these is the Voigt line shape, which is preferred for its relative accuracy and its simplicity. The Voigt line shape incorporates both Doppler broadening and collisional broadening of spectral line shapes.

3.3.1 The Gaussian (Doppler) profile

Doppler broadening takes place due to the thermal motion of absorbing molecules. The kinetic theory of gases postulates that all molecules in a gaseous sample are rapidly moving in a series of random directions with varying velocities; the distribution of these speeds amongst all the molecules is related to the temperature of the gas by the Maxwell-

[13] This excludes the case of collisional line mixing.

Boltzmann distribution (see pgs. 21-32 of Stupochenko et al. [14]). A molecule moving away from the photon source will have a higher velocity (i.e., kinetic energy) relative to the incoming photons and will thus require a photon of higher energy to excite the molecular transition in question, while a molecule moving toward the photon source will require a photon of lower energy. This leads to a symmetric spread, or broadening, of the energies which can excite a given molecular transition. The Doppler-broadened profile, ϕ_G [cm^{-1}], is Gaussian and is described as a function of frequency $\bar{\nu}$ by

$$\phi_G = \frac{2}{\Delta\bar{\nu}_D}\left(\frac{\ln(2)}{\pi}\right)^{\frac{1}{2}} \exp\left[-4\ln(2)\left(\frac{\bar{\nu}-\bar{\nu}_{12}}{\Delta\bar{\nu}_D}\right)^2\right], \tag{3.37}$$

where $\Delta\bar{\nu}_D$ is the Doppler full-width at half-maximum (FWHM) [cm^{-1}] and $\bar{\nu}_{12}$ is the transition center [cm^{-1}]. All parameters are given in wavenumbers, which is the preferred notation throughout the discussion of line shapes.

The Gaussian line shape ϕ_G described by Eq. (3.37) is symmetrically centered around $\bar{\nu}_{12}$ and is normalized to have an integrated area of 1. Equation (3.37) is written in a slightly more elongated form than a typical Gaussian function to accommodate the use of the FWHM $\Delta\bar{\nu}_D$ rather than the usual standard deviation, which is often symbolized by σ and sometimes referred to as the 1/e half width. Care should be taken when using different formulations of ϕ_G to avoid errors concerning the definition of profile width.

The Doppler FWHM $\Delta\bar{\nu}_D$ can be expressed in [cm^{-1}] as

$$\Delta\bar{\nu}_D = 7.162 \times 10^{-7}\bar{\nu}_{12}\sqrt{T/M}, \tag{3.38}$$

where M is the molecular weight of the gas and $\bar{\nu}_{12}$ and T should be in [cm^{-1}] and [K], respectively. Equation (3.38) indicates that Doppler broadening becomes stronger at higher frequencies and temperatures and for lighter molecules. Because of the dependence on $\bar{\nu}_{12}$, Doppler broadening is said to be inhomogeneous.

3.3.2 The Lorentzian (collisional) profile

Collisional broadening takes place by phase-shifting of the dipoles due to collisions with other molecules (also called perturbers). The broadening by such collisions is modeled by the Lorentzian profile ϕ_L [cm], which is described by

$$\phi_L = \frac{\Delta\bar{\nu}_C}{2\pi} \frac{1}{(\bar{\nu}-\bar{\nu}_{12})^2+(\Delta\bar{\nu}_C/2)^2}. \tag{3.39}$$

Here, $\Delta\bar{\nu}_C$ is the collisional FWHM in [cm^{-1}]. The Lorentzian line shape described by Eq. (3.39) is symmetrically centered around $\bar{\nu}_{12}$ and is normalized to have an integrated area of 1. The collisional FWHM $\Delta\bar{\nu}_C$ of transition is a function of temperature, pressure, and concentration of the j-th perturbing species X_j and is given by

$$\Delta\bar{\nu}_C = 2P \sum_j X_j \gamma_j(T), \tag{3.40}$$

where $\gamma_j(T)$ [cm^{-1}·atm^{-1}] is the broadening coefficient of the j-th perturber. The summation in Eq. (3.40) extends over all j perturbers, including the absorbing species itself. The broadening coefficient $\gamma_j(T)$ is given as a function of temperature by

$$\gamma_j(T) = \gamma_j(T_0)\left(\frac{T_0}{T}\right)^{n_j}, \tag{3.41}$$

where n_j is the temperature exponent for the j-th perturber. The collisional broadening parameters $\gamma_j(T_0)$ and n_j are perturber-specific and generally transition-specific, although some molecules exhibit broadening that is independent of the rotational quantum number [15]. $\gamma_j(T_0)$ is commonly referred to as the broadening coefficient. $\gamma_j(T_0)$ and n_j may either be determined experimentally [6] or may be derived from theoretical considerations [16]. From Eq. (3.40), $\Delta\bar{v}_C$ increases with pressure. Due to the lack of dependence of $\Delta\bar{v}_C$ on $\bar{v}_{12}$, collisional broadening is often referred to as homogeneous broadening.

The validity of the power law temperature dependence described in Eq. (3.41) has been questioned on several occasions [17, 18] and may only be valid across smaller temperature ranges. Gamache and Vispoel [19] have recently proposed a double power law to describe the temperature dependence of $\gamma_j(T)$, and this formulation may find traction in the future. With the goal of using Eq. (3.41) due to its simplicity and familiarity, one possible solution is to use the reasoning of Ren et al. [20]. Ren et al. postulated that although the value of n_j determined at high temperatures to model $\gamma_j(T)$ caused a disagreement with the experimentally determined value of $\gamma_j(T_0)$, this could be explained by the idea that n_j can itself be a function of temperature. This reasoning allows one to employ Eq. (3.41) at high temperatures to predict $\gamma_j(T)$.

3.3.3 The Voigt profile

The Voigt profile is a simple and widely used line shape model incorporating both Doppler and collisional broadening. The Voigt profile is valid with the assumption that

velocity-changing collisions can be neglected (i.e., collisional narrowing effects are negligible) [21]. With this assumption, the Voigt line shape ϕ_V is defined as the convolution of the Gaussian and Lorentzian profiles:

$$\phi_V = \phi_G * \phi_L, \tag{3.42}$$

which, modifying the expressions of Gharavi and Buckley [22], can be written as

$$\phi_V = \left\{\frac{1}{\Delta\bar{\nu}_D/2}\sqrt{\frac{\ln(2)}{\pi}}\right\}\left\{\frac{y}{\pi}\int_{-\infty}^{+\infty}\frac{\exp(-t^2)}{y^2+(x-t)^2}\,dt\right\} \tag{3.43}$$

$$x = \left\{\frac{\bar{\nu}-\bar{\nu}_{12}}{\Delta\bar{\nu}_D/2}\right\}\sqrt{\ln(2)} \tag{3.44}$$

$$y = \frac{\Delta\bar{\nu}_C}{\Delta\bar{\nu}_D}\sqrt{\ln(2)}, \tag{3.45}$$

where t is a variable of integration.

The expression in Eq. (3.43) is quite complicated and cannot be solved analytically. Solution methods for Eq. (3.43) include numerical convolution of Eq. (3.42) and numerical integration of Eq. (3.43). However, these methods are computationally expensive. The preferred method of evaluating ϕ_V is via pseudo-Voigt profiles, made possible through numerical correlations. For example, approximations of ϕ_V have been provided by Whiting [23] and Liu et al. [24], among many others. Some algorithms may be preferred over others due to accuracy in certain calculation regions or due to improved speed. For example, the approximation by Liu et al. is preferred over that by Whiting as the Liu et al. algorithm is ~10 times faster.

Examples of Gaussian, Lorentzian, and Voigt line shapes are shown in Fig. 3.6. The x axis has been normalized by $\Delta\bar{\nu}_D$, making both the x and y axes dimensionless.[14] By definition (see Eq. (3.3)), each line shape is normalized to have an integrated area of 1. The Doppler and collisional widths $\Delta\bar{\nu}_D$ and $\Delta\bar{\nu}_C$ have been set equal in this plot. The Voigt line shape is broader in the core region than both the Gaussian and Lorentzian line shapes and is consequently less intense in this regime. In the wings outside the core region, where the Gaussian line shape rapidly approaches zero, the Voigt profile adopts the behavior of the Lorentzian profile, being slightly more intense than the Lorentzian profile. The relative shapes of the three profiles depicted in Fig. 3.6 will change with the relative weighting of $\Delta\bar{\nu}_D$ and $\Delta\bar{\nu}_C$ (e.g., the Voigt profile will closely resemble the Lorentzian profile if $\Delta\bar{\nu}_D << \Delta\bar{\nu}_C$), but the general trends observed will hold true.

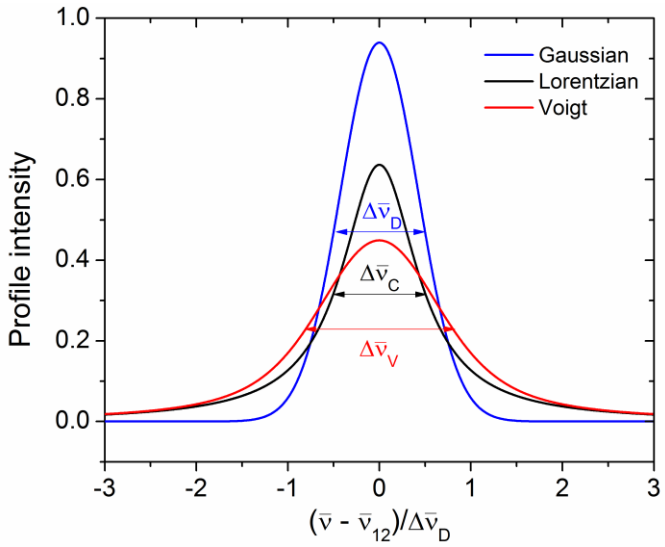

Figure 3.6 Gaussian, Lorentzian, and Voigt line shape models with $\Delta\bar{\nu}_D$ set equal to $\Delta\bar{\nu}_C$. Both axes are dimensionless.

[14] In practice, the x axis has units of frequency, while the y axis has units of inverse frequency. In the unit system chosen for ϕ in the present work, these units are [cm^{-1}] and [cm], respectively.

There are numerous other line shape models beyond the three discussed above. The influences of Dicke narrowing, hard/soft collisions, and correlations between different types of collisions can all be appropriately described using models of increasing complexity. However, such topics are beyond the scope of this work, and the interested reader is referred to Chapter III of the monograph by Hartmann et al. [25]. The Voigt profile was used for all calculations of the line shape in this work.

3.3.4 Collisional line shift

The collisional interactions of molecules can also result in a shift of the frequency $\bar{\nu}_{12}$ of the transition. The physical explanation is collisions that cause phase shifting of the dipoles[15] but affect the lower and upper states 1 and 2 to different degrees, leading to a slight change in the difference $\bar{\nu}_{12}$. As with collisional broadening, the collisional shift is highly dependent on the pair of absorbing and perturbing molecules in question. This shift tends to be negative in frequency space for many absorbing-perturbing pairs, although exceptions do exist.

The modeling of the collisional line shift is typically described in a manner similar to collisional broadening. The collisional shift is symbolized by Δ_s [cm^{-1}] and can be expressed as

$$\Delta_s = P \sum_j X_j \delta_j(T), \tag{3.46}$$

[15] Phase shifting of dipoles is the same phenomenon that causes collisional broadening. However, collisional shift coefficients are typically much smaller (a factor of 10 or more is common) than collisional broadening coefficients.

where $\delta_j(T)$ [cm^{-1}·atm^{-1}] is the shift coefficient of the j-th perturber at T. The summation in Eq. (3.46) extends over all j perturbers, including the absorbing species itself. The temperature dependence of $\delta_j(T)$ is

$$\delta_j(T) = \delta_j(T_0)\left(\frac{T_0}{T}\right)^{m_j}, \tag{3.47}$$

where $\delta_j(T_0)$ [cm^{-1}·atm^{-1}] is the shift coefficient of the j-th perturber at T_0 and m_j is the temperature exponent of the j-th perturber. Figure 3.7 shows a simple illustration of a collisional line shift using arbitrary values.

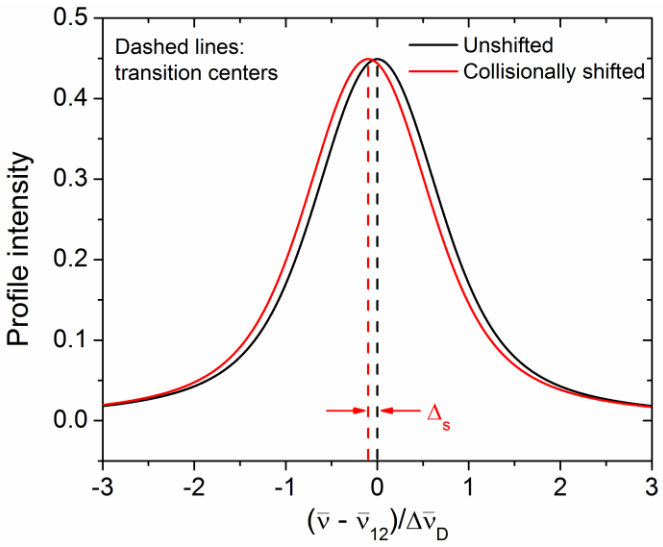

Figure 3.7 Example of a collisional line shift. The line shape is the Voigt profile from Fig. 3.6.

Some absorber-perturber pairs display an interesting behavior wherein Δ_s changes sign with temperature (for an example of such a change in sign for HD, see Ulivi et al.

[26]). Since Eq. (3.47) is unable to predict such changes in sign, there is debate as to the proper form of the temperature dependence of $\delta_j(T)$. However, such discussions are beyond the scope of this work, and Li et al. [27] have demonstrated that the $\delta_j(T)$ model proposed in Eq. (3.47) is appropriate for H_2O. The interested reader is directed to Cybulski et al. [18] for more on the temperature dependence of $\delta_j(T)$.

3.4 Emission spectroscopy

Emission diagnostics do not utilize a radiation source but instead capture the emission emanating from the test gas. Experimentally, emission diagnostics are simpler to implement as compared to absorption diagnostics, but their quantitative nature is problematic, among other issues (Table 3.1). Discussed in this subsection are the principles of emission spectroscopy including basic equations and upper-state populations. Some of the challenges associated with emission diagnostics are also discussed. A slight focus is given to electronic emission (in the visible/UV), but the general principles introduced also apply to IR emission.

3.4.1 Basic principles of emission spectroscopy

In the derivation of the Beer-Lambert law it was assumed the emission contribution was negligible compared to the radiation source I_v. In developing a relation for the emitted light intensity, the opposite assumption will be made. Assuming the I_v term in Eq. (3.7) is negligible, one obtains

$$\frac{dI_v}{dx} = \frac{h\nu_{12}}{4\pi c} N_2 A_{21} \phi \Omega. \tag{3.48}$$

In contrast to the Beer-Lambert law, the emission signal increases with increasing path length. Integrating Eq. (3.48) along the path length L and assuming that all variables are constant in x, Eq. (3.48) can be written as

$$I_v = \frac{hv_{12}}{c} N_2 A_{21} \phi \frac{\Omega}{4\pi} L, \tag{3.49}$$

where a similar result is given by Linne (pg. 65 of [1]). Equation (3.49) is written for an individual transition. However, laser diagnostics are the preferred method of investigating individual transitions since emission diagnostics suffer from instrument broadening. Instead, emission diagnostics are typically employed to capture broadband emission that is being emitted from multiple transitions. Therefore, it is appropriate to effectively integrate Eq. (3.49) over an arbitrary range of frequencies containing a number of transitions to obtain

$$I = \frac{hv}{c} N_2 A \frac{\Omega}{4\pi} L. \tag{3.50}$$

Here the dependence on ϕ is gone; the subscripts on v and A have been dropped to indicate a number of transitions are being considered; and N_2 now represents an average of the upper-state populations across these transitions. The I in Eq. (3.50) represents the signal one collects with an emission diagnostic.

Equation (3.50) has three implications for emission diagnostics. First, I is directly proportional to the number density of molecules in the upper state. Emission diagnostics can therefore only provide information on the excited-state population, whereas absorption

diagnostics provide information on the ground-state population. Second, the dependence of I on the flow conditions (e.g., temperature, pressure, concentration of the emitting species) is entirely contained in the number density term N_2; the other variables in Eq. (3.50) are either spectral or geometric in nature. Finally, I is a function of Ω, meaning I will depend on the optical setup employed, in contrast to an absorption diagnostic.

3.4.2 Population of the upper state

In the two-level model (Fig. 3.1), the mechanisms controlling N_2 are either radiative (stimulated absorption, stimulated emission, and spontaneous emission) or non-radiative (collisional quenching, collisional excitation, and chemical reactions).

In Sect. 3.4.1, it was assumed that there was no radiation source so that neither stimulated absorption nor stimulated emission occur. Thus, the only radiative process considered was spontaneous emission. One possible exception to this would be the case of laser-induced fluorescence (see pgs. 414-424 of Demtröder [28]), but for the chemiluminescence diagnostic employed here, the assumption of $I_\nu = 0$ is appropriate. A resulting feature of the two-level system in electronic emission is that the populations N_1 and N_2 are completely controlled by non-radiative processes. This is because the spontaneous emission rates are typically at least three orders of magnitude slower than the collisional and chemiluminescent processes. Therefore, while the spontaneous emission process associated with A_{21} is entirely responsible for the observed emission, it has a negligible effect on the population N_2 (see Kathrotia et al. [29]).

Collisional excitation and quenching are the energy transfer processes associated with the achievement of thermal equilibrium, as described by the Boltzmann distribution,

Eq. (3.29), and are described by the rates Q_{12} and Q_{21} in Fig. 3.1. The importance of collisional excitation depends on the temperature of the medium and the energy gap ΔE_{12} associated with the emission. Figure 3.8 shows calculations of N_2/N_1 for various values of $\bar{\nu}_{12}$ according to the Boltzmann distribution [16] and reveals thermal excitation is negligible even at 3000 K for UV transitions ($\lambda \approx 300$ nm) but is appreciable for mid-IR transitions ($\lambda \approx 6500$ nm) even at 500 K. The curves in Fig. 3.8 give a general sense of the relative weightings of Q_{12} and Q_{21} for different wavelengths and temperatures; a low value of N_2/N_1 implies that $Q_{21} \gg Q_{12}$, which was the case with the emission diagnostic near 300 nm utilized in this work (see Sect. 4.3). From Fig. 3.8, thermal excitation will generally provide good signal levels for mid-IR emission diagnostics but will not do so for UV or visible emission diagnostics; a different process of excitation is needed to populate the upper state at these higher frequencies.

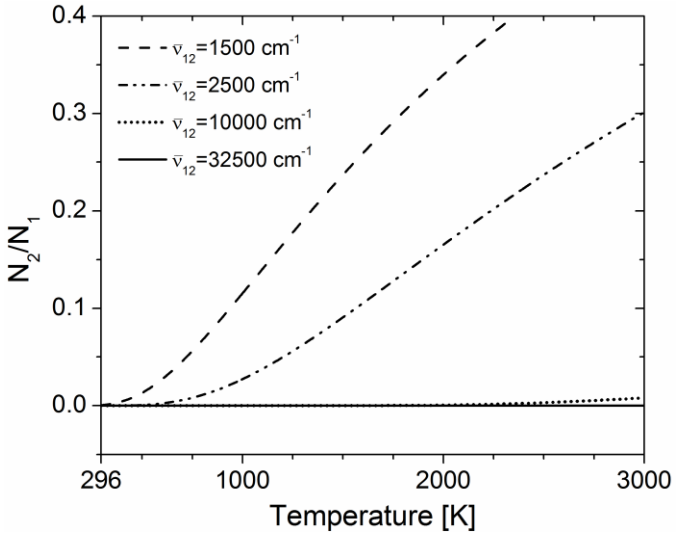

Figure 3.8 Ratio of the upper- to lower-state populations as a function of T according to the Boltzmann distribution, Eq. (3.29), for various values of $\bar{\nu}_{12}$.

[16] The y axis in Fig. 3.8 is N_2/N_1, making the curves in Fig. 3.8 essentially inversions (i.e., increasing from 0 toward 1 rather than decreasing from 1 toward 0) of the stimulated emission curves in Fig. 3.5.

The final avenue of upper-state excitation in Fig. 3.1 is via chemical reactions in a process called chemiluminescence. Chemiluminescence is dependent on the existence of chemiluminescent reactions that proceed at a sufficiently rapid rate to populate the upper state. According to Laidler and Shuler, these reactions can take one of several forms (see pgs. 187-201 of [30]); one possibility is A + B + C ⇄ AB* + C, where AB* is some electronically excited species. In the realm of combustion science, two common chemiluminescence diagnostics are OH* diagnostics targeting emission near 306 nm from the $A\,^2\Sigma^+ \rightarrow X\,^2\Pi$ transition and CH* diagnostics targeting emission near 430 nm from the $A\,^2\Delta \rightarrow X\,^2\Pi$ transition (CH* emission near 390 nm from the $B\,^2\Sigma^- \rightarrow X\,^2\Pi$ transition has also been used but is weaker than the $A \rightarrow X$ band [31]). Chemiluminescent reactions commonly associated with OH* and CH* in hydrocarbon flames include H + O + M ⇄ OH* + M [32], CH + O_2 ⇄ OH* + CO [32], C_2 + OH ⇄ CH* + CO [33], and C_2H + O ⇄ CH* + CO [33].

3.4.3 Reaction rates for collisional processes

The collisional probability rates Q_{12} and Q_{21} are related to reaction rates of collisional processes. For a generic excited-state species AB*, a generic quenching reaction with the quenching partner C could be written as AB* + C ⇄ AB + C, with a forward rate constant of k [cm^3/(mol·s)] and a reverse rate constant of k_- [cm^3/(mol·s)]. The forward process is associated with Q_{21} and the reverse with Q_{12}. If this were the only collisional quenching/excitation reaction taking place in the system, Q_{21} and Q_{12} could be written in terms of the species concentrations and the rate constant. In reality, an excited species AB* can be quenched/excited by multiple collision partners so that Q_{21} and Q_{12} are the combination of several collisional pathways. Consequently, it is necessary to have accurate

rate constants for each of these possible pathways. Quenching rate constants[17] are typically measured for a number of collisional partners across a range of temperatures, and literature data are available on the quenching of electronically excited species such as OH $A\ ^2\Sigma^+$ [34, 35], CH $A\ ^2\Delta$ [35, 36], and NO $A\ ^2\Sigma^+$ [35, 37]. A basic introduction to chemical kinetics is provided in Sect. 5.2.1, while quenching rate constants for OH $A\ ^2\Sigma^+$ are discussed in more detail in Sect. 5.2.3.

3.4.4 Challenges of emission diagnostics

Equation (3.50) highlights one of the primary difficulties associated with quantitative emission measurements: the emission depends on the solid angle Ω, which is dependent on the optical setup. It can also be difficult to accurately understand how the interior of the shock tube is imaged by the emission setup. For these reasons, the only reliable method with which to make quantitative emission measurements is to introduce a known amount of the emitting species and characterize the response of the optical setup/detector, typically as a function of temperature (e.g., Fig. 3.11 of Petersen [5]). This calibration must be repeated following any alterations to the optical setup. The calibration procedure is further complicated when the emitting species is a radical species such as OH*, as one cannot simply prepare a mixture with a known quantity of a radical. In such a case, the best practice is to make measurements at sufficiently high temperatures such that the excited-state formation is independent of the chemiluminescent reactions and only depends on the quenching reactions acting in reverse. In this manner, a concentration

[17] Rates of the collisional quenching reactions (i.e., AB* + C ⇄ AB + C in the forward direction) are typically measured. However, assuming that accurate thermochemical properties are available for the species involved, the collisional excitation rate can be simply related to the collisional quenching rate through the equilibrium constant; see Sect. 5.2.1 for a brief introduction to chemical kinetics.

versus voltage curve can be obtained and later used to make quantitative measurements of the excited-state radical species at various desired conditions. However, the calibration relies on accurate rates for the quenching reactions. Such calibration procedures have been used to make quantitative measurements of OH* by Kathrotia et al. [29], Bozkurt et al. [38], and Hidaka et al. [39].

A second issue with quantitative emission diagnostics is signal trapping. This refers to the fact that when light at frequency v_{12} is emitted by a molecule via spontaneous emission, a neighboring molecule may re-absorb the molecule, leading to an overall lower amount of signal collected at the detector. Modeling the signal trapping would involve utilizing an unsimplified version of Eq. (3.7) such that both emission and absorption are considered. Kathrotia et al. [29] performed such an exercise and determined the signal-trapping correction for their OH* measurements was 10% or less, which was well within their ±20% calibration uncertainty. Conditions similar to those of Kathrotia et al. were employed in this work so that a similar amount of signal trapping was likely present. However, since the measurements performed herein were qualitative rather than quantitative, the relative importance of signal trapping was likely even smaller than 10% and was consequently neglected.

3.5 Summary

The Beer-Lambert law was derived beginning from a radiative energy balance. The assumptions involved in deriving this relation were discussed and found to be valid for the conditions employed in this dissertation. The assumption of a small boundary layer was determined to be appropriate for this study but may merit scrutiny at other conditions.

Spectroscopic saturation effects were considered and a new relation for narrow-line-width light sources was developed. Saturation effects were found to be negligible at the present conditions.

The calculation of the line strength was addressed. The line strength depends on transition probabilities (i.e., the Einstein coefficients) and energy level populations (related to the molecular partition function). Of particular relevance to combustion studies, a widely used relation for the temperature dependence of the line strength was developed. Values of line strengths and partition functions can be obtained from tabulated sources and scaled to the appropriate temperature using this temperature scaling.

The calculation of the Voigt line shape was addressed. The forms and physical mechanisms of the underlying Gaussian and Lorentzian profiles were discussed. Methods of numerically evaluating the complicated Voigt function were mentioned. The equations needed to model the profile parameters (i.e., FWHM values) were provided for both the Gaussian and Lorentzian profiles. Finally, the collisional line shift was covered and relations used in its modeling were provided.

Emission spectroscopy was given an overview. A simple relation for the dependence of the emission intensity was developed, which revealed some of the challenges of making quantitative emission measurements (namely, the dependence on the optical setup). The different mechanisms of populating/depopulating the upper state in emission diagnostics were discussed, including collisions and chemical reactions. Finally, some of the challenges associated with quantitative emission diagnostics were introduced, as well as potential solutions.

3.6 References

[1] M.A. Linne, "Spectroscopic Measurement" Academic Press, London, UK (2002).

[2] J.W. Daily, "Laser induced fluorescence spectroscopy in flames" *Progress in Energy and Combustion Science* **23** (1997) 133-199.

[3] T.B. Settersten, M.A. Linne, "Modeling pulsed excitation for gas-phase laser diagnostics" *Journal of the Optical Society of America B* **19** (2002) 954-964.

[4] J.W. Hargis, E.L. Petersen, "Shock-tube boundary-layer effects on reflected-shock conditions with and without CO_2" *AIAA Journal* **55** (2017) 902-912.

[5] E.L. Petersen, "A shock tube and diagnostics for chemistry measurements at elevated pressures with application to methane ignition" Ph.D. dissertation, Stanford University, (1998).

[6] C.R. Mulvihill, S.A. Alturaifi, E.L. Petersen, "High-temperature He- and O_2-broadening of the R(12) line in the 1←0 band of carbon monoxide" *Journal of Quantitative Spectroscopy and Radiative Transfer* **217** (2018) 432-439.

[7] A.C. Eckbreth, "Laser diagnostics for combustion temperature and species" 2nd ed., Taylor and Francis, London, UK (1996).

[8] L.S. Rothman, D. Jacquemart, A. Barbe, D.C. Benner, M. Birk, L.R. Brown, M.R. Carleer, et al., "The HITRAN 2004 molecular spectroscopic database" *Journal of Quantitative Spectroscopy and Radiative Transfer* **96** (2005) 139-204.

[9] R.K. Hanson, R.M. Spearrin, C.S. Goldenstein, "Spectroscopy and Optical Diagnostics for Gases" Springer, Cham, Switzerland (2016).

[10] I. Burak, J.I. Steinfeld, D.G. Sutton, "Infrared saturation in sulfur hexafluoride" *Journal of Quantitative Spectroscopy and Radiative Transfer* **9** (1969) 959-980.

[11] C.R. Mulvihill, M.W. Crofton, D.G. Arnold, E.L. Petersen, K.Y. Lam, "A laser diagnostic at 427 nm for quantitative measurements of CH in a shock tube" *Applied Physics B* **125** (2019) 78.

[12] A.L. Laraia, R.R. Gamache, J. Lamouroux, I.E. Gordon, L.S. Rothman, "Total internal partition sums to support planetary remote sensing" *Icarus* **215** (2011) 391-400.

[13] D.J. Griffiths, "Introduction to Quantum Mechanics" 2nd ed., Pearson Prentice Hall, Upper Saddle River, NJ (2005).

[14] Y.V. Stupochenko, S.A. Losev, A.I. Osipov, "Relaxation in Shock Waves" Springer-Verlag, New York, NY (1967).

[15] A.Y. Chang, M.D. DiRosa, R.K. Hanson, "Temperature dependence of collision

broadening and shift in the NO $A \leftarrow X$ (0, 0) band in the presence of argon and nitrogen" *Journal of Quantitative Spectroscopy and Radiative Transfer* **47** (1992) 375-390.

[16] A. Predoi-Cross, K. Esteki, H. Rozario, H. Naseri, S. Latif, F. Thibault, V. Malathy Devi, et al., "Theoretical and revisited experimentally retrieved He-broadened line parameters of carbon monoxide in the fundamental band" *Journal of Quantitative Spectroscopy and Radiative Transfer* **184** (2016) 322-340.

[17] R.T. Pack, "Pressure broadening of the dipole and Raman lines of CO_2 by He and Ar. Temperature dependence" *Journal of Chemical Physics* **70** (1979) 3424-3433.

[18] H. Cybulski, A. Bielski, R. Ciuryło, J. Szudy, R.S. Trawiński, "Power-law temperature dependence of collision broadening and shift of atomic and molecular rovibronic lines" *Journal of Quantitative Spectroscopy and Radiative Transfer* **120** (2013) 90-103.

[19] R.R. Gamache, B. Vispoel, "On the temperature dependence of half-widths and line shifts for molecular transitions in the microwave and infrared regions" *Journal of Quantitative Spectroscopy and Radiative Transfer* **217** (2018) 440-452.

[20] W. Ren, A. Farooq, D.F. Davidson, R.K. Hanson, "CO concentration and temperature sensor for combustion gases using quantum-cascade laser absorption near 4.7 μm" *Applied Physics B* **107** (2012) 849-860.

[21] P.L. Varghese, R.K. Hanson, "Collisional narrowing effects on spectral line shapes measured at high resolution" *Applied Optics* **23** (1984) 2376-2385.

[22] M. Gharavi, S.G. Buckley, "Single diode laser sensor for wide-range H_2O temperature measurements" *Applied Spectroscopy* **58** (2004) 468-473.

[23] E.E. Whiting, "An empirical approximation to the Voigt profile" *Journal of Quantitative Spectroscopy and Radiative Transfer* **8** (1968) 1379-1384.

[24] Y. Liu, J. Lin, G. Huang, Y. Guo, C. Duan, "Simple empirical analytical approximation to the Voigt profile" *Journal of the Optical Society of America B* **18** (2001) 666-672.

[25] J.-M. Hartmann, C. Boulet, D. Robert, "Collisional Effects on Molecular Spectra" Elsevier Science, Amsterdam, Netherlands (2008).

[26] L. Ulivi, Z. Lu, G.C. Tabisz, "Temperature dependence of the collisional interference in the pure rotational far-infrared spectrum of HD" *Physical Review A* **40** (1989) 642-651.

[27] H. Li, A. Farooq, J.B. Jeffries, R.K. Hanson, "Diode laser measurements of temperature-dependent collisional-narrowing and broadening parameters of Ar-perturbed H_2O transitions at 1391.7 and 1397.8 nm" *Journal of Quantitative*

Spectroscopy and Radiative Transfer **109** (2008) 132-143.

[28] W. Demtröder, "Laser Spectroscopy: Basic Concepts and Instrumentation" 2nd enlarged ed., Springer, Berlin, Germany (1996).

[29] T. Kathrotia, M. Fikri, M. Bozkurt, M. Hartmann, U. Riedel, C. Schulz, "Study of the H+O+M reaction forming OH*: Kinetics of OH* chemiluminescence in hydrogen combustion systems" *Combustion and Flame* **157** (2010) 1261-1273.

[30] K.J. Laidler, K.E. Shuler, "Elementary reactions in the gas phase involving excited electronic states" *Chemical Reviews* **48** (1951) 153-224.

[31] T. Kathrotia, U. Riedel, A. Seipel, K. Moshammer, A. Brockhinke, "Experimental and numerical study of chemiluminescent species in low-pressure flames" *Applied Physics B* **107** (2012) 571-584.

[32] J.M. Hall, E.L. Petersen, "An optimized kinetics model for OH chemiluminescence at high temperatures and atmospheric pressures" *International Journal of Chemical Kinetics* **38** (2006) 714-724.

[33] V.N. Nori, J.M. Seitzman, "CH^* chemiluminescence modeling for combustion diagnostics" *Proceedings of the Combustion Institute* **32** (2009) 895-903.

[34] P.W. Fairchild, G.P. Smith, D.R. Crosley, "Collisional quenching of $A\,^2\Sigma^+$ OH at elevated temperatures" *The Journal of Chemical Physics* **79** (1983) 1795-1807.

[35] M. Tamura, P.A. Berg, J.E. Harrington, J. Luque, J.B. Jeffries, G.P. Smith, D.R. Crosley, "Collisional quenching of CH(*A*), OH(*A*), and NO(*A*) in low pressure hydrocarbon flames" *Combustion and Flame* **114** (1998) 502-514.

[36] P. Heinrich, F. Stuhl, "Electronic quenching of CH($A\,^2\Delta$) and NH($A\,^3\Pi$) between 300 and 950 K" *Chemical Physics* **199** (1995) 105-118.

[37] J.W. Thoman, J.A. Gray, J.L. Durant, P.H. Paul, "Collisional electronic quenching of NO $A\,^2\Sigma^+$ by N_2 from 300 to 4500 K" *The Journal of Chemical Physics* **97** (1992) 8156-8163.

[38] M. Bozkurt, M. Fikri, C. Schulz, "Investigation of the kinetics of OH^* and CH^* chemiluminescence in hydrocarbon oxidation behind reflected shock waves" *Applied Physics B* **107** (2012) 515-527.

[39] Y. Hidaka, S. Takahashi, H. Kawano, M. Suga, W.C. Gardiner, "Shock-tube measurement of the rate constant for excited OH($A\,^2\Sigma^+$) formation in the hydrogen-oxygen reaction" *The Journal of Physical Chemistry* **86** (1982) 1429-1433.

4. METHODOLOGY OF SHOCK-TUBE OPTICAL DIAGNOSTICS

The theoretical techniques summarized in the previous Sections can be applied to optical diagnostics in a shock tube. Described in this Section are the various experimental apparatus utilized in this study. First, the theoretical aspects of the shock tube, including the shock-wave analysis and the issue of vibrational relaxation, are discussed along with the physical setup of the shock tube and its associated hardware. The physical, electrical, and optical aspects of the H_2O laser diagnostic setup are then addressed, along with the selection and spectroscopic modeling of the selected H_2O transition; sample calculations related to the H_2O transition are provided. Experimental challenges involved in shock-tube laser absorption measurements are explored, and potentials solutions are suggested. The OH* chemiluminescence diagnostic and associated data analysis are then presented along with examples of experimental efforts to characterize interfering emission. Finally, the physical setup of the LED diagnostic for NO_2 and the related data analysis are described, and the calculation and experimental verification of the NO_2 absorption coefficient are outlined.

4.1 Shock tube

A pressure-driven, single-diaphragm shock tube was used for all measurements. The measurements of interest were obtained behind the reflected shock wave. Test times were typically limited to 3 ms. Pressures behind the reflected shock wave were typically 1 atm, while temperatures behind the reflected shock wave ranged from 900 to 1800 K. In the following pages, a brief overview of the analysis used to calculate the properties behind

a shock wave is given. Next, the topic of vibrational relaxation is introduced, with sample calculations of the vibrational relaxation time provided. Finally, the hardware of the shock-tube setup and the diagnostics and data processing used to obtain useful information are described.

4.1.1 Analysis of a normal shock wave

A control volume analysis of a shock wave is shown in Fig. 4.1. Two coordinate frames are illustrated: a lab-fixed frame, where the shock wave traverses the fixed control volume, and a shock-fixed frame, where the control volume is fixed to the moving shock wave. The shock-fixed frame in Fig. 4.1(b) is more convenient and is used here. Assuming there is 1-D flow, no heat loss from the control volume, and no friction of the shock wave against any surfaces, the conservation laws for mass, momentum, and energy for the control volume in Fig. 4.1(b) can be respectively written as

$$\rho_1 u_1 = \rho_2 u_2 \tag{4.1}$$

$$P_1 + \rho_1 u_1^2 = P_2 + \rho_2 u_2^2 \tag{4.2}$$

$$h_1 + \frac{1}{2}u_1^2 = h_2 + \frac{1}{2}u_2^2. \tag{4.3}$$

Here, ρ is the gas density [kg/m^3], u is velocity of the gas [m/s], and h is the mass-specific enthalpy [J/kg]. Additional equations needed to close the system are the ideal gas and thermally perfect gas equations of state:

$$P = \frac{\rho R_u T}{M} \tag{4.4}$$

$$h = h(T), \tag{4.5}$$

where $h(T)$ is some function of T. The ideal gas assumption is valid as real gas effects are not of concern at the near-atmospheric pressures used in this dissertation; see Davidson and Hanson [1] for more on real gas considerations.

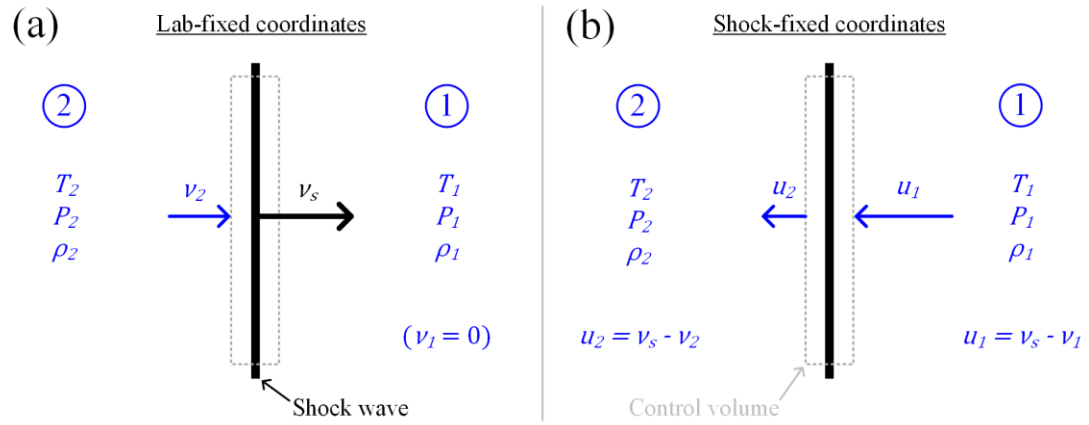

Figure 4.1 Control volume around a normal shock wave with velocity v_s using (a) lab-fixed coordinates and (b) shock-fixed coordinates. Although $v_1 = 0$ in this case, it is included in the definition of u_1 for generality.

With ten unknown variables (ρ, u, h, P, and T for each region) and seven equations (realizing Eqs. (4.4) and (4.5) apply to each region), there are three unknown variables remaining. In the context of shock-tube experiments, the temperature and pressure in region 1 are measured so T_1 and P_1 are known. The remaining unknown variable obtained by measurement is the velocity of the incident shock wave, v_s [m/s]. Typically, high-speed pressure transducers are utilized for this measurement; see Sect. 4.1.4 for further explanation. Ultimately, with knowledge of initial gas properties and the velocity of a shock wave propagating into that gas, the properties of the gas behind the shock wave can

be computed. The same analysis can be applied to the reflected shock wave to calculate T_5 and P_5.[1]

Analytical expressions for the ratios T_5/T_1 and P_5/P_1 can be readily obtained by making the assumption of constant specific heats; see Ch. II of Gaydon and Hurle [2]. This assumption is valid for monatomic species but becomes increasingly inaccurate for diatomic and polyatomic species with increasingly stronger shock waves. Iterative algorithms that solve Eqs. (4.1)-(4.5) using polynomial fits for $h(T)$ are readily available in the literature [1, 3-5]. In this work, the FROSH routine (see the Appendix of Campbell et al. [5]) was used to calculate the post-shock conditions assuming equilibrated vibrational states behind both the incident and reflected shock waves.

4.1.2 Vibrational relaxation

A shock wave passing through a gas introduces a rapid change in conditions to the gas molecules. Ideally, the molecules would instantaneously achieve an equilibrium (i.e., Boltzmann) distribution. In reality, the rotational and, in particular, vibrational energy distributions can require an appreciable amount of time to reach equilibrium. When discussing the distribution of molecules in translational, rotational, and vibrational energy modes, the term "temperature" is used interchangeably with "energy distribution" since these two can be directly related through the Boltzmann distribution, Eq. (3.29).

Behind a shock wave, the translational temperature increases immediately to a value far above the equilibrium temperature (see pgs. 189-193 of Gaydon and Hurle [2]).

[1] A notable difference in the analyses of the incident and reflected shock waves is that in the reflected-shock analysis, the velocity of the gas into which the shock wave is propagating is no longer 0 due to the flow induced by the incident shock wave.

On the other hand, the rotational and vibrational temperatures initially remain frozen at their pre-shock values and only gradually move, or relax, toward equilibrium. While the study of both rotational and vibrational relaxation rates has been the topic of a great deal of study, it is well known that rotational relaxation is much faster than vibrational relaxation (see Ch. 4 of Stupochenko et al. [6]), so vibrational relaxation is of greater importance. One reason vibrational relaxation is of concern in shock tubes is that non-equilibrated environments can affect rate coefficient determinations [7, 8]. While much work was done on vibrational relaxation in previous decades, recent investigations [5, 9-11] have demonstrated the continued importance of this issue.

In the SHO approximation, the rate of change in the vibrational energy E_{vib} can be shown (see pgs. 198-202 of Vincenti and Kruger [12]) to be

$$\frac{dE_{vib}}{dt} = \frac{E^*_{vib} - E_{vib}}{\tau_{vib}}, \tag{4.6}$$

where E^*_{vib} is the vibrational energy at equilibrium and τ_{vib} [μs] is the 1/e characteristic time associated with the vibrational energy levels achieving LTE. Equation (4.6) states the rate of change in E_{vib} at time t is linearly proportional (by the constant $1/\tau_{vib}$) to the departure from equilibrium at that instant, and that E_{vib} also moves toward E^*_{vib}, as expected. Assuming the conditions are fixed so τ_{vib} and E^*_{vib} are constant, Eq. (4.6) can be integrated in time to yield

$$\frac{E_{vib} - E^*_{vib}}{E_{vib,0} - E^*_{vib}} = \exp(-t/\tau_{vib}), \tag{4.7}$$

where $E_{vib,0}$ is the initial vibrational energy after the disturbance from equilibrium (i.e., after the shock wave). Figure 4.2 shows an illustration of the vibrational relaxation time, highlighting the fact that τ_{vib} is the 1/e characteristic time.

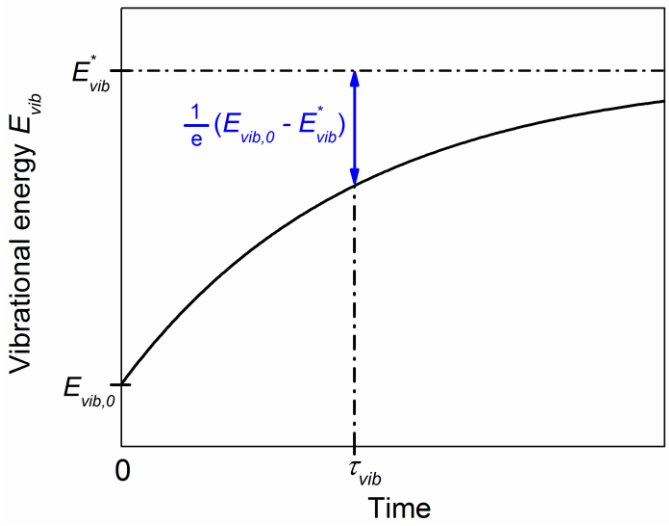

Figure 4.2 Illustration of the 1/e vibration relaxation time τ_{vib}. At τ_{vib}, the difference $E_{vib,0} - E^*_{vib}$ has fallen to ~36.8% of its original value.

τ_{vib} is highly dependent on the absorbing species, the collisional partner(s), the pressure, and the temperature. While modern numerical techniques for predicting τ_{vib} have been developed (e.g., Mott et al. [3]), various analytical expressions can provide reasonable estimates. For example, according to Vincenti and Kruger [12], the analytical relations developed by Landau and Teller [13] give τ_{vib} as

$$\tau_{vib} = \frac{K_1 T^{5/6} \exp[(K_2/T)^{1/3}]}{P(1-\exp[-\theta_{vib}/T])} \approx C\frac{\exp[A/(T^{1/3})]}{P}, \tag{4.8}$$

where K_1 [μs·K$^{-5/6}$·atm], K_2 [K], C [μs·atm], and A [K$^{1/3}$] are constants and θ_{vib} [K] is the

characteristic vibrational temperature of the relaxing species, hv/k. The approximation in Eq. (4.8) is a slight deviation from Vincenti and Kruger according to Millikan and White [14] and can also be written in the form

$$\ln(\tau_{vib}P) = AT^{1/3} + \ln(C) \tag{4.9}$$

Millikan and White compiled a large amount of data and found that the constants A and C could be described by

$$C = \exp(-0.015A\mu^{1/4} - 18.42) \times 10^6 \tag{4.10}$$

$$A = c_{vib}\mu^{1/2}\theta_{vib}^{4/3}, \tag{4.11}$$

c_{vib} is a molecule-specific constant; however, Millikan and White found that this constant varied quite little across several collider pairs and proposed an average value of 1.16×10^{-3} when θ_{vib} is in [K]. This average value of c_{vib} can be used in the absence of molecule-specific data. The reduced mass μ for a collider pair with molecular weights M_1 and M_2 is

$$\mu = \frac{M_1M_2}{M_1+M_2}. \tag{4.12}$$

The factor of 10^6 in Eq. (4.10) converts C from [s·atm], as given in Millikan and White, to [μs·atm]. In the interest of calculating τ_{vib} for multi-component mixtures, Millikan and White also provided a rule for the vibrational relaxation time, $\tau_{vib,mix}$ [μs], of a relaxing species A in a mixture. The mixture rule can be generalized to

$$\frac{1}{\tau_{vib,mix}} = \sum_i \frac{X_{B_i}}{\tau_{vib,A-B_i}}, \tag{4.13}$$

where X_{B_i} is the mole fraction of the collisional partner B_i, and $\tau_{vib,A-B_i}$ [μs] is the vibrational relaxation time of the relaxing species with B_i as a collisional partner. The summation in Eq. (4.13) extends over all collisional partners, including the relaxing species A.[2] Equation (4.13) assumes the linear mixing rule is valid, which has been verified at least in the case of H_2 vibrational relaxation [15].

In the present work, vibrational relaxation was determined not to be a concern due to the following reasons. First, the calculated τ_{vib} values for a mixture of 0.2% H_2 in balance Ar at 1 atm were only ~50 μs at the low-temperature end of this work and ~5 μs at the high-temperature end, as shown in Fig. 4.3. Both timescales are small in comparison to the timescales of the H_2-NO_2 oxidation in the present experiments (~0.2-3 ms). Second, vibrational relaxation times for NO_2 could not be found in the literature, but it is known that polyatomic molecules are typically highly efficient colliders (e.g., H_2O [16]), partially due to the transfer of energy between the different modes of the molecule (pg. 197 of Gaydon and Hurle [2]). Therefore, if NO_2 were included in the calculations of Fig. 4.3, τ_{vib} for the mixture would likely decrease noticeably. The notion of a short NO_2 vibrational relaxation time was supported by the interfering absorption experiments described in Sect. 5.3.6. Finally, the τ_{vib} modeling used herein primarily accounts for vibration-to-translation (V-T) energy transfer; vibration-to-vibration (V-V) energy transfer can be highly efficient

[2] For example, in a mixture of CO, H_2, and Ar, where CO is the relaxing species, Eq. (4.13) would be evaluated as $1/\tau_{vib,mix} = X_{CO}/\tau_{vib,CO-CO} + X_{H_2}/\tau_{vib,CO-H_2} + X_{Ar}/\tau_{vib,CO-Ar}$, where $\tau_{vib,CO-CO}$, $\tau_{vib,CO-H_2}$, and $\tau_{vib,CO-Ar}$ can each be obtained using Eq. (4.9).

[17] and could possibly shorten τ_{vib} considerably.

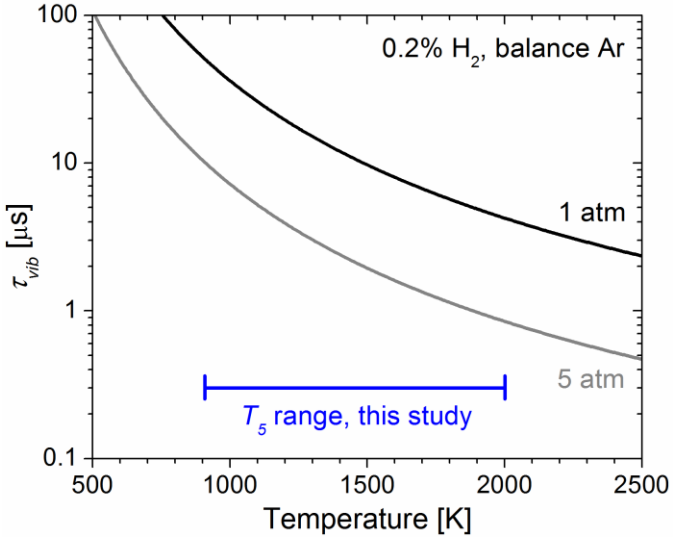

Figure 4.3 τ_{vib} versus temperature at 1 atm and 5 atm for a mixture of 0.2% H_2, balance Ar. Calculations used A = 80 $K^{1/3}$, C = 2.06×10^{-3} μs·atm for H_2-H_2 and A = 104 $K^{1/3}$, C = 1.11×10^{-3} μs·atm for H_2-Ar according to Dove and Teitelbaum [15].

Most of the historical work on vibrational relaxation in shock tubes has focused on the issue of gases that are initially present when the reflected shock wave arrives. Interestingly, recent studies [9, 10, 18] have suggested CO is formed at different rates depending on the vibrational level. This may not be surprising as CO is known to possess a large τ_{vib} due to its high vibrational frequency [14]. However, a similar issue with H_2O seems unlikely since H_2O is an efficient collider with expected τ_{vib} values of less than 1 μs at the experimental conditions tested herein [16].

4.1.3 Configuration of the shock tube

The setup of the shock tube is shown in Fig. 4.4. The driven section of the shock

tube had a diameter of 16.24 cm and a length of 7.88 m. The driver section of the shock tube had a diameter of 7.62 cm and a length of 3.25 m. The driven and driver sections were separated by a diaphragm section, which contained a removable cylindrical diaphragm package used to exchange diaphragms between experiments; a four-bladed cutter was used just after the diaphragm on the driven section side to reduce diaphragm fragmentation. The diaphragms were polycarbonate with a thickness of 0.254 mm. To burst the diaphragms, the driver side was filled with He from a bottle to typical pressures of ~70 psi, as measured by a pressure gauge with a range of 0-250 psi (model 225 from Setra). For some experiments, a small quantity (~5 psi) of air was left in the driver before the He fill to reduce the strength of the shock wave; varying this amount of air can be useful in maintaining a more-consistent P_5.

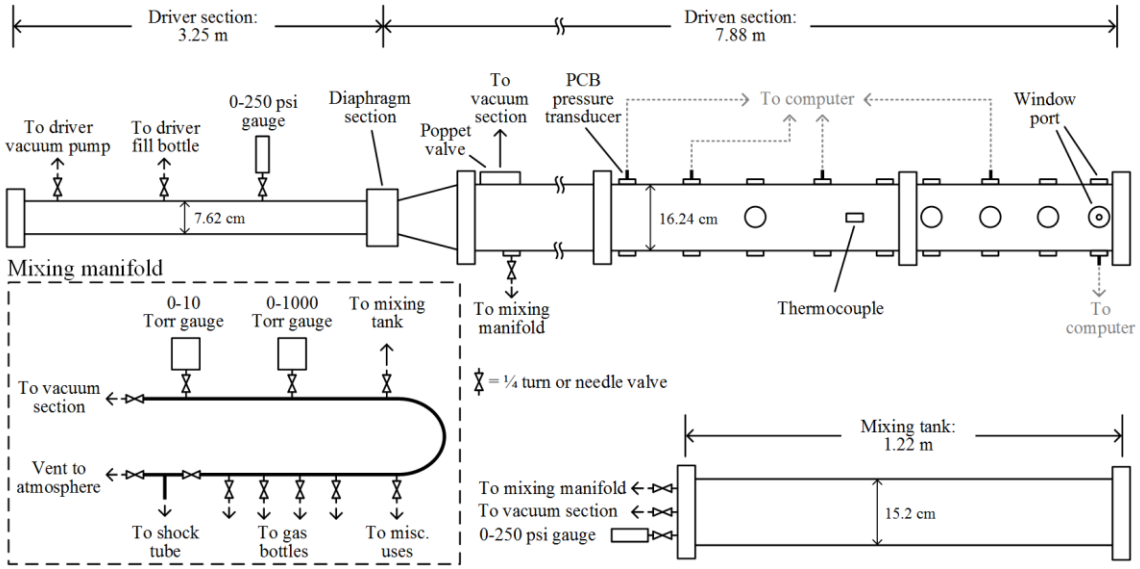

Figure 4.4 Schematic of the shock tube, mixing tank, and mixing manifold (not drawn to scale).

A series of pumps was employed to clear out potentially harmful gases following each experiment and to ensure high-purity conditions prior to each experiment. A rotary vane pump (model DS602 from Varian), attached to the vacuum section by a pneumatic valve, was used for general pumping purposes. A turbomolecular pump (model Turbo-V1001 from Agilent), attached to the vacuum section by a gate valve, was used to obtain ultimate pressures of 10^{-5}-10^{-6} Torr within the shock tube and mixing tank. The outlet of the turbomolecular pump was connected to a second rotary vane pump (model DS402 from Varian). The vacuum section was connected to the shock either indirectly through the mixing manifold via 6-mm diameter tubing or directly through a pneumatically controlled, 12.7-cm poppet valve to reduce pumping time. Finally, a third rotary vane pump (model DS102 from Varian), separate from the vacuum section, was used to pump out the driver section prior to filling with He.

Mixtures were prepared manometrically in a separate, stainless steel mixing tank. Partial pressures of the various constituents were measured using one of three pressure gauges: (1) a capacitance manometer with a range of 0-10 Torr (model Baratron 626 from MKS Instruments), (2) a capacitance manometer with a range of 0-1000 Torr (model Baratron 626 from MKS Instruments), or (3) a pressure transducer with a range of 0-250 psi (model 225 from Setra). As illustrated in Fig. 4.4, a mixing manifold was employed to facilitate control of gas flow throughout the various parts of the experimental setup. The manifold included needle valve connections to the gas bottles to provide fine control of the partial pressure of each constituent and a valve for atmospheric venting to permit the diaphragm section to be opened. The 0-1000 Torr gauge was used to fill the shock tube to the desired P_1, while a thermocouple attached to the shock tube measured T_1.

Test gases were supplied by Praxair. The Ar and H_2 were supplied at a stated purity level of 99.999%. The NO_2 was supplied at 99.5% purity but was prepared by Praxair as a mixture of either 1.02% (±2%) or 1.03% (±2%) NO_2 in balance Ar (99.999% purity). All gases were used without further purification.

When preparing mixtures, it is generally preferred to fill the final constituent (i.e., the diluent, which is typically Ar) at a high rate to promote turbulent mixing. Perforated tubing inserted into the mixing tank is sometimes used to further promote mixing. However, the compression of the gases in the mixture causes the temperature within the mixing tank to rise. Although the mixing tank used in this study was not equipped with an internal thermocouple, experience with other thermocouple-equipped mixing tanks has indicated that filling the final constituent from ~10 psi to a final mixture pressure of ~80 psi can induce a temperature rise of ~3 K, or a 1% change from an initial temperature of 300 K; larger final pressures can produce larger temperature increases. Such a temperature rise can lead to errors in the partial pressure method due to changes in density. To combat this problem, it is recommended to either (1) fill at a slower rate or (2) wait for ~10 minutes after reaching the desired pressure before returning to top off the mixture, which will have decreased in pressure in the interim. The first method will not strongly encourage turbulent mixing, so it may be prudent to allow more time for gradual mixing after completing the filling process. Mixtures prepared used one of these two methods to minimize the mixture uncertainty due to changes in temperature. Completed mixtures were allowed to mix for at least 1 hour prior to performing experiments.

4.1.4 Diagnostic access

A variety of sidewall and endwall ports provided diagnostic access to the shock tube. Five fast-response, piezoelectric pressure transducers (model 113A from PCB) were situated in sidewall ports along the last ~1.9 m of the driven section. The first four piezoelectric pressure transducers were placed along the top of the shock tube, while the last was placed on the bottom to permit access for the OH* diagnostic from the top window port (see below). Each pressure transducer recorded the sudden spike in pressure following the passage of the incident shock wave. The signal from each transducer was sent to a signal conditioner (model 482C05 from PCB) with adjustable gain settings of ×1, ×10, and ×100; a setting of ×100 was used for the low-pressure tests in this study. Each conditioned signal was then sent to the computer-based data acquisition system (DAQ). For some of the experiments, a set of four programmable timers/counters (model PM 6666 from Fluke) were utilized instead of the DAQ. By measuring the time intervals between successive shock arrivals at each of the pressure transducers and through knowledge of the distance between each transducer, the incident shock velocity was calculated at the four midpoints between the transducers. The incident shock wave velocity experienced a slight attenuation due to effects such as the viscous boundary layer, non-ideal diaphragm breakage, and test-to-test variations in diaphragm characteristics [19]. The attenuation behavior was well-approximated by a linear fit and had typical values of 0.5-1.0 %/m in the present work. The attenuation was extrapolated to the position at the endwall, and the 1-D normal shock relations described in Sect. 4.1.1 were utilized with this measured incident shock wave velocity to calculate T_5 and P_5. Figure 4.5 shows an example of the incident shock wave velocity measurement and extrapolation, demonstrating the method of defining the shock

arrival. The downward trend in Fig. 4.5(b) is due to shock-wave attenuation. The estimated uncertainties in T_5 and P_5 arising from uncertainty in v_s are estimated to be ±0.8% and ±1.0%, respectively [20].

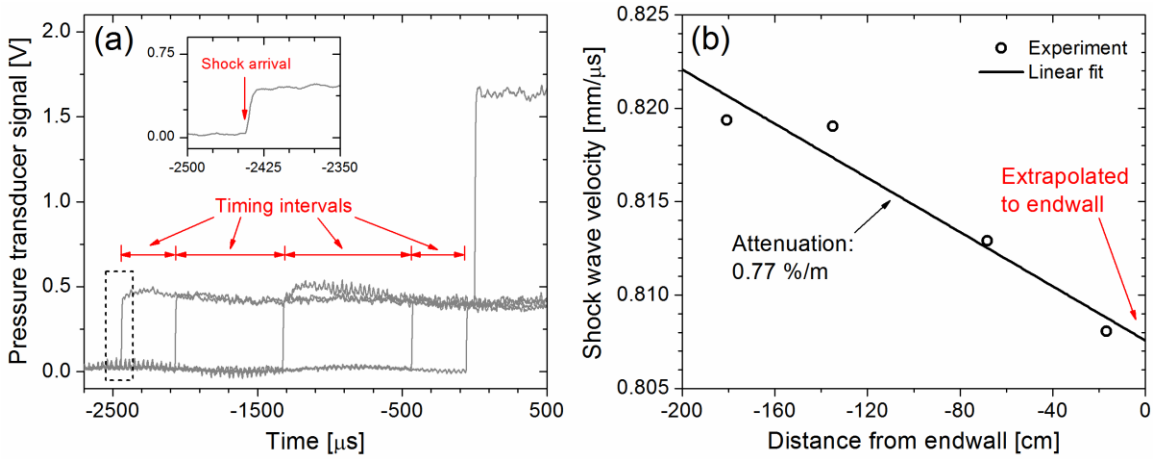

Figure 4.5 Sample (a) raw pressure transducer signals and (b) measured values of v_s at the different measurement locations (i.e., in between each pair of transducers). The linear fit in (b) was extrapolated to obtain the value of v_s at the endwall, 0.8076 mm/μs, and had R^2 = 0.94.

The remaining diagnostic ports were focused near the endwall of the shock tube. Three window ports were located 1.6 cm from the endwall of the shock tube; two on either side of the shock tube and one on top of the shock tube. The windows were sapphire, which transmits at both 300 nm and 1.39 μm. Five endwall ports provided the potential for endwall pressure and/or optical diagnostics but were not utilized in this study. Typically, a high-speed quartz pressure transducer (model 603B1 from Kistler) is used to monitor the sidewall pressure. However, since the window port was used for the OH* diagnostic, it was necessary to use the last PCB piezoelectric pressure transducer to measure not only v_s but also the sidewall pressure. The sidewall pressure transducer was shielded with room-

temperature vulcanizing silicone to mitigate heat transfer effects that can adversely alter the pressure traces [21] and was located in the same plane as the window ports (1.6 cm from the endwall). The output from the last PCB transducer was sent to the DAQ regardless of whether the DAQ or the Fluke timers/counters were used to record the intervals between the PCB transducers.

The DAQ was a CompuScope digital oscilloscope card (model CS8382 from Dynamic Signals) with 8 available channels. This digitizer had a resolution of 14 bits, an onboard memory of ~16 MB, and a maximum sampling rate of 25 MHz and was coupled to a desktop computer. All experiments in this study were conducted at a sampling rate of 1 MHz. The impedance of the digitizer was set to 1 MΩ.

4.2 H_2O laser absorption diagnostic

The primary optical diagnostic in this study was a laser absorption diagnostic for H_2O that used narrow-line-width light at 1388.140 nm to acquire quantitative time histories of H_2O concentrations behind reflected shock waves. First described in this subsection are the operation and setup of the laser, detectors, and accompanying optics. Next, the selection of the laser wavelength and the modeling of the chosen spectral feature are outlined, with sample calculations of the spectral database surveys and absorption coefficient modeling provided. Finally, the analysis of the laser data is briefly introduced, as are the potential experimental challenges of broadband emission and other absorbing species. Finer details of the laser diagnostic are addressed more fully in Appendices A, B, and C.

4.2.1 Tunable diode laser

The backbone of the H_2O diagnostic was an external-cavity, grating-stabilized tunable diode laser (TDL) (model DL 100 from Toptica Photonics). The TDL was configured in the Littrow configuration, wherein the lasing cavity is created by the interaction of the laser diode and the first-order diffraction from a reflective diffraction grating. The TDL had a manufacturer-characterized tunable range of 1310 to 1400 nm, a maximum power output of 14 mW, and a line width of about 1 MHz according to the manufacturer. The laser diode was situated atop a Peltier cooling element. The wavelength and power output of the laser were controlled in three ways: the angle of the diffraction grating, the diode temperature, and the diode current.

The angle of the diffraction grating allowed for coarse adjustments in the laser wavelength and was adjusted by turning a finely threaded set screw within the laser housing. This method was only utilized when making large (>0.01 nm) adjustments to the laser wavelength. The diode temperature and current were controlled by separate controller elements (models DTC 110 and DCC 110, respectively, both from Toptica Photonics) both contained within a modular control kit (model DC 110 from Toptica Photonics). These controllers allowed for fine tuning of the laser wavelength and permitted consistent, stable laser operation at a wavelength of 1388.140 nm. Typical TDL operating conditions were 90-100 mA and 20.0-21.0 °C. For more details on the tuning and stable operation of the TDL, see Appendix C.

4.2.2 Configuration of the laser diagnostic

The setup of the laser diagnostic is shown in Fig. 4.6. Upon exiting the TDL, 10%

of the beam was split off to a scanning Michelson interferometer (model WA-1000 from Burleigh); this wavemeter was used to monitor the wavelength of the laser with a resolution of 0.001 nm. The remaining 90% of the beam impinged upon a 50/50 beamsplitter. Half of the beam was directed into a rotatable linear polarizer grid before striking a plano-convex lens (focal length f = 10 cm) that focused the beam onto the I_0 detector, which was fitted with an optical bandpass filter (center wavelength λ_c = 1384 nm, FWHM = 10 nm). The other half of the beam was directed through the shock-tube window ports and then through an adjustable aperture before being focused onto the I_t detector (the I_t focusing lens and bandpass filter were identical to the I_0 side). The power of the I_t leg was typically ~3 mW, as measured downstream of the 50/50 beamsplitter using a power meter (model 918D-IR-OD3 from Newport).

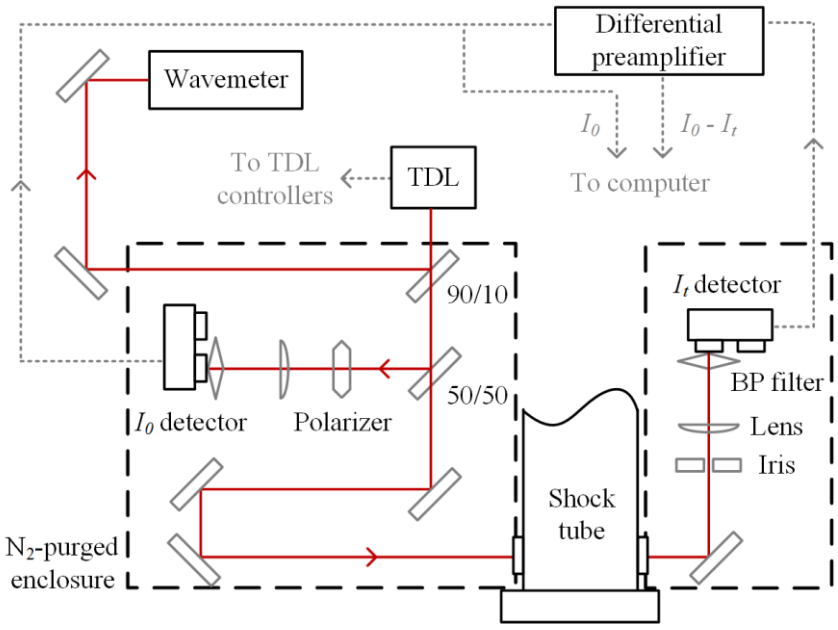

Figure 4.6 Schematic of the H_2O laser absorption diagnostic. Solid red lines: laser beam, dotted grey lines: information flow, dashed black lines: N_2-purged enclosures. 90/10 and 50/50 indicate beamsplitters. BP = bandpass.

The detectors were DC-coupled, photovoltaic, Ge photodiodes (model 2317NF from Newport). Each detector contained a pair of photodiodes and output the difference in signal between the two photodiodes; only one photodiode on each detector was utilized in the present work, while the other side was shielded. The detectors could operate in one of three bandwidth/gain modes: (1) high-bandwidth, low-gain, (2) medium-bandwidth, medium-gain, or (3) low-bandwidth, high-gain. In this work, the high-bandwidth (150 kHz), low-gain (2×10^3 V/A) mode was utilized. The detectors were powered by an external ±15 VDC power source to avoid complications with changing batteries while the enclosures were purged with N_2.

The two detector voltage outputs were sent via BNC cables to a differential preamplifier (model SR560 from Stanford Research Systems). The differential preamplifier was set to a gain of ×1 with no filtering options selected and was configured to output the difference $I_0 - I_t$ between the two detector signals. The rotatable linear polarizer in front of the I_0 detector was used to selectively attenuate the highly polarized laser light to balance the detector signals (i.e., to make $I_0 - I_t = 0$), although it was neither possible nor necessary to have the signals perfectly balanced prior to every experiment. The two voltage signals $I_0 - I_t$ and I_0 (the latter of which was teed off from the input to the differential preamplifier) were sent to the DAQ. To minimize bit noise, the input range of the channel used to monitor I_0 was set to ±2 V, while that of the channel for $I_0 - I_t$ was set to ±100 mV; see Appendix A for more on bit noise and the differential preamplifier.

At typical indoor conditions of 25 °C and 50% relative humidity, a standard psychrometric chart indicates that there is ~1% H_2O by mass (~1.5% H_2O by volume). Such a relatively large H_2O concentration can lead to noticeable attenuation of the laser

beam when it is tuned to resonance at the $5_{5,1} \leftarrow 5_{5,0}$ transition, which has an appreciable line strength (~0.07 $cm^{-2} \cdot atm^{-1}$) at room temperature. To mitigate this attenuation, a polycarbonate enclosure was fashioned around each detector and its accompanying optics, as shown in Fig. 4.6. Prior to performing shock-tube experiments, both enclosures were purged with N_2 at a high flow rate until the relative humidity fell below 0.1% as measured by a hygrometer (model RH85 from Omega) on the larger I_0 enclosure. The flow rate of the N_2, as measured by a rotameter, was then decreased to still maintain the relative humidity below 0.1% during experiments while eliminating fluctuations in laser wavelength (possibly due to vibrations of the enclosure walls) that were observed on the wavemeter readout at higher flow rates. The enclosures were sealed to the metal faces of the shock-tube window ports to minimize leaks. An earlier setup had the TDL included within the polycarbonate enclosure. However, since the TDL is an external-cavity laser and the refractive index n is a function of pressure and gas composition [22], the N_2 purge slightly altered the wavelength of the laser ($\Delta\lambda \approx 0.008$ nm) when the laser was within the enclosure. The TDL was placed immediately adjacent to but outside the I_0 enclosure to eliminate this wavelength shift.

The N_2-purged enclosures complicated the balancing of the detectors. Due to the differing path lengths of the I_0 and I_t legs of the laser beam, the two detectors experienced significantly different changes in incident laser intensity as the H_2O vapor was purged from the boxes such that balancing the beams before the N_2 purge would lead to egregiously unbalanced beams after the N_2 purge. To combat this, the laser was first detuned to near 1388.175 nm to sit in a region of very low H_2O absorption and the detectors were balanced using the polarizer. The laser was then tuned back to resonance (1388.140 nm) and the N_2

purge was initiated, with the result that the beams were typically balanced to within an acceptable margin of ±20 mV.[3] For more details on the laser diagnostic setup and methods by which to achieve high-SNR laser measurements, see Appendix A.

4.2.3 Selection and modeling of the H_2O transition

When designing a laser absorption diagnostic, it is desirable to select a molecular transition that is (1) strong to provide sensitive measurements, (2) well-characterized to provide accurate measurements, (3) distant from the spectra of other species to provide interference-free measurements, and (4) accessible using available laser sources.

Figure 4.7 shows a survey of H_2O line strengths from the HITRAN 2004 database [23] that have been scaled to a typical T_5 of 1600 K using Eq. (3.36) and the partition function from Laraia et al. [24]. The tuning range of the TDL corresponds to the fundamental $v_1 + v_3$ band (i.e., the 101←000 band). Within this band, the $5_{5,1}$←$5_{5,0}$ transition was found to be the strongest at typical shock-tube temperatures. As for characterization of the selected transition, measurements of the collisional broadening parameters $\gamma_{Ar}(T_0)$ and n_{Ar} have been performed by Nagali et al. [25] for three nearby H_2O transitions in the 101←000 band and one in the 200←000 band. Nagali et al. reported a $\gamma_{Ar}(T_0)$: $\gamma_{N_2}(T_0)$ ratio of 0.4 for all three 101←000 transitions. This ratio was used in conjunction with the value of $\gamma_{air}(T_0)$ from HITRAN 2004 to calculate $\gamma_{Ar}(T_0)$. Nagali et al. also reported n_{Ar}:n_{N_2} ratios; the same method as for γ_{Ar} was used to calculate n_{Ar}. The collisional shift parameters were taken from Li et al. [26], who investigated two nearby

[3] If small adjustments to the polarizer were required while the enclosures were purged, a small (~1 cm × 1 cm), resealable opening in the top of the I_0 enclosure allowed for temporary access to the polarizer. The polarizer adjustments were performed quickly and the opening was rapidly closed to prevent major infiltration of H_2O vapor into the enclosure.

lines. The full set of spectroscopic parameters is given in Table 4.1. As for interference from other species, HITRAN 2004 indicates that the major combustion products CO and CO_2 do not interfere near 1.39 µm; see Sect. 4.2.6 for more on interfering absorption.

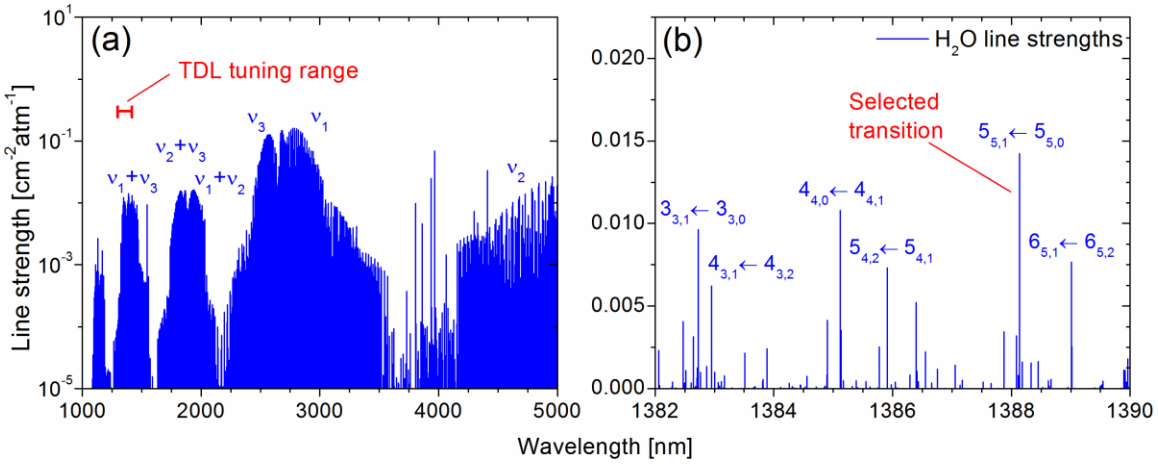

Figure 4.7 H_2O line strengths at 1600 K according to HITRAN 2004 [23], showing (a) vibrational structure across the near/mid-IR and (b) rotational structure near the selected transition. Calculations used $Q(T)$ from Laraia et al. [24].

Table 4.1 Spectroscopic parameters of the $5_{5,1}$←$5_{5,0}$, 101←000 transition of H_2O.

Symbol	Value	Units	Reference
$\bar{v}_{12}$	7203.890410 [a]	[cm^{-1}]	[23]
$S_{12}(T_0)$	2.977×10^{-21}	[cm^{-1}/(molecules·cm^{-2})]	[23]
$\bar{E}''$	742.0763	[cm^{-1}]	[23]
$\gamma_{Ar}(T_0)$	0.0214 [b]	[cm^{-1}·atm^{-1}]	[25]
n_{Ar}	0.69	--	[25]
$\gamma_{self}(T_0)$	0.3200	[cm^{-1}·atm^{-1}]	[23]
n_{self}	0.69 [b]	--	[23]
$\delta_{Ar}(T_0)$	-0.0241	[cm^{-1}·atm^{-1}]	[26]
m_{Ar}	1.11	--	[26]

[a] Equivalent to 1388.138829 nm.
[b] Assumed to be the same as n_{air}.

Utilizing the spectroscopic parameters from Table 4.1, the H_2O absorption coefficient k_ν was calculated using the methods described in Section 3. Figure 4.8(a) shows the results of this calculation versus temperature at 1, 3, and 5 atm. As expected from the strong T dependence of $S_{12}(T)$ (see Eq. (3.36) and Fig. 3.5), k_ν decreases with increasing temperature in the temperature range of Fig. 4.8. Additionally, the moderate effect of pressure in Fig. 4.8(a) is due to the broadening of the line shape ϕ, which moves the transition probability away from the line center. The decrease in k_ν with increasing P is offset by the increase in P_{abs} in the Beer-Lambert law (Eq. (3.15)) such that a higher amount of absorption might be achieved at higher pressures. However, this increase in pressure generally comes at the cost of increased noise in the laser signal.

When calculating k_ν for a fixed-wavelength application, it is necessary to consider the collisional line shift Δ_s. Figure 4.8(b) shows Δ_s at the same conditions as Fig. 4.8(a), calculated using Eq. (3.46) and the parameters in Table 4.1. Δ_s increases in absolute magnitude with increasing pressure but decreases with increasing temperature. For the case of P = 1 atm (a typical pressure for the experiments in this study), the average Δ_s in Fig. 4.8(b) is -4.14×10^{-3} cm^{-1}. This leads to an average shifted line center of 1388.1396 nm, which is the reason the laser was fixed at 1388.140 nm for all experiments herein. For higher pressures, it may be prudent to shift the laser wavelength slightly with T_5 so the laser remains tuned to the peak of the transition to obtain maximum absorption.

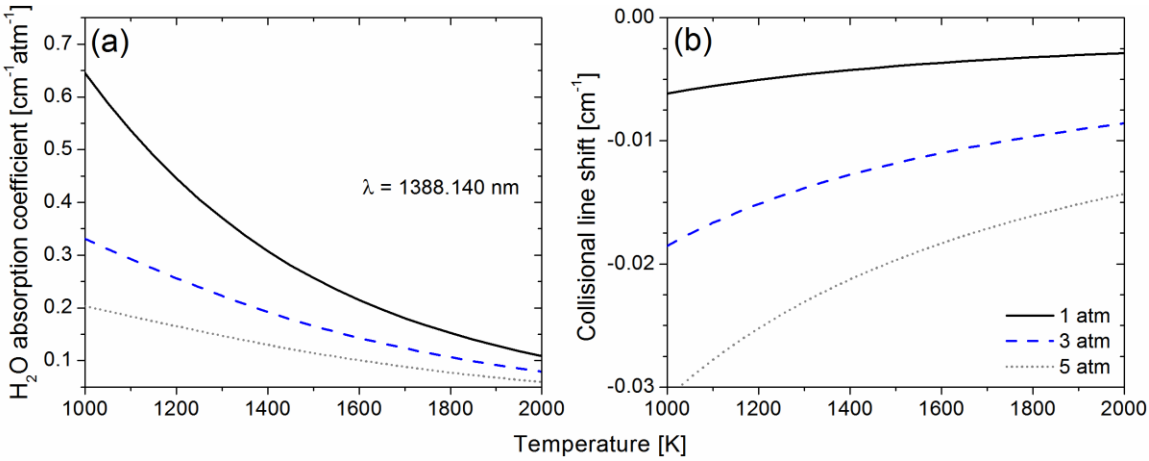

Figure 4.8 Temperature and pressure dependence of (a) k_v and (b) Δ_s for the $5_{5,1}\leftarrow5_{5,0}$, 101←000 transition of H_2O. Calculations used X_{Ar} = 99%, X_{H_2O} = 0.2%, the spectroscopic parameters of Table 4.1, and $Q(T)$ from Laraia et al. [24].

4.2.4 Analysis of laser data

In the experimental setup used herein, the raw laser data were acquired in the form of two separate voltage signals: I_0 and $I_0 - I_t$. The fractional transmission I_t/I_0 can be written in terms of these two signals as

$$I_t/I_0 = 1 - (I_0 - I_t)/(I_0). \tag{4.14}$$

I_t/I_0 can then be used in the Beer-Lambert law. A sample laser transmission trace is shown in Fig. 4.9(a), with the corresponding sidewall pressure trace shown in Fig. 4.9(b). Several features common to the experiments herein can be noted. First, the passages of the incident and reflected shock waves can be observed in both the laser transmission and sidewall pressure traces; the two so-called Schlieren spikes in the laser signal are due to the sharp density gradients associated with shock waves and do not signify any actual formation of H_2O. When laser data were available, the peak of the second Schlieren spike was used to

define time zero. Second, the laser transmission begins to decrease immediately after the reflected shock wave as H_2O is formed due to the reacting mixture. The rate of this H_2O formation is of course dependent on the fuel/oxidizer system and T_5; for example, H_2-O_2 mixtures exhibit an induction delay time before forming H_2O [27]. Third, a slight, non-ideal pressure rise (dP/dt) can be observed behind the reflected shock wave. This pressure rise alters the ideal post-reflected-shock P_5 (and, concomitantly, the value of T_5). Finally, the end of the experiment is marked by the decrease in pressure; this decrease may occur due to the arrival of the expansion fan or the interaction of the reflected shock wave with the contact surface. The end of the experiment can be somewhat observed in the laser transmission trace, although the sidewall pressure trace is usually more useful in defining the end of the test time.

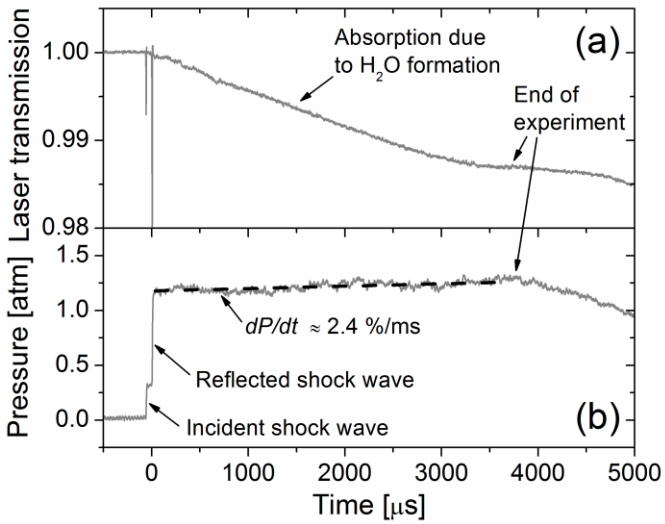

Figure 4.9 Sample experimental traces for (a) I_t/I_0 and (b) sidewall pressure. Conditions are 1213 K and 1.17 atm in a mixture of 0.178% NO_2, 0.444% H_2, balance Ar.

In practice, several issues complicate the laser signal analysis using the Beer-Lambert law. First, detector offsets and imbalances make Eq. (4.14) an oversimplification, and a more-complicated relation must be used. Second, dP/dt effects must be incorporated into the P term of the Beer-Lambert law. Finally, k_v is a function of time, primarily due to the exothermicity of the mixture but also due to dP/dt effects. For more details on data analysis issues, see Appendix B.

4.2.5 Interference from broadband emission

A matter of potential concern in shock-tube laser absorption experiments is broadband emission. Broadband emission can arise from the shock-heated gases in the initial mixture, from the gases formed during the ensuing combustion event, or even from the shock-tube walls (the latter is generally only important at higher pressures; see Petersen [19]). The emission from the hot gases/surfaces can exit the shock tube through the window ports and strike the I_t detector, creating an artificially lower level of apparent absorption. The optical configuration described in Fig. 4.6 made the I_0 detector immune to broadband emission,[4] so employing the methods outlined below for the I_0 detector is likely an exercise in compulsivity.

To minimize the effects of broadband emission on the I_t detector, several methods can be employed. The first method is to utilize optical bandpass filters to permit only certain frequencies of light to enter the detectors. In general, filters with smaller FWHM values are preferred. A second method is to employ irises to block the broadband emission

[4] A possible exception to this is if the I_0 detector is placed with a clear line of sight to the shock-tube window that is separate from the beam path (not the case in the present work). The bandpass filter may still eliminate the emission in such a case, but best practice is to somehow block the I_0 detector from the sight of the window.

from traveling to the detector. It is most useful to place one iris immediately before the focusing lens that focuses the laser into the detector; placing the iris before the detector element but after the lens can allow broadband emission to be focused and pass through the iris. Additional irises can also be placed throughout the I_t beam path. The ideal aperture diameter for the iris would be such that the laser beam does not contact the iris at any point; see Appendix A for more on this. The third method is to move the I_t detector farther from the shock tube, as the emitted light will diverge at a much greater angle than the laser beam and thus the emission intensity will vary as the inverse square of the distance from the shock-tube window. Of course, this method must be weighed against the side effect of the increasing laser beam size (see Appendix A) and may also conflict with space limitations. In the present work, the I_t detector was placed rather close to the shock tube due to space limitations.

Broadband emission can be characterized by performing a shock experiment with the laser blocked or turned off so that the amount of emission entering the I_t detector can be directly observed.[5] Emission would manifest itself after the reflected shock wave as a nearly instantaneous change in signal (in the case of a gas in the initial mixture emitting radiation) and/or a gradual change in signal (in the case of a combustion product and/or the shock-tube walls emitting radiation). This check should be performed at the high-temperature end of a set of experiments since emission generally increases with temperature;[6] if the emission at the high-temperature extreme is negligible, it can also be

[5] Of course, such experiments can also be used to confirm the lack of broadband emission in the I_0 detector (e.g., Fig. 4.10). However, for reasons discussed in the text, the concern over background emission is usually associated with the I_t detector.

[6] The emission intensity is proportional to the number density in the upper state (Sect. 3.4). The total number density will decrease with increasing temperature; however, this decrease is generally overshadowed by the increase in the upper state population due to thermal excitation and/or chemical reactions.

neglected at lower temperatures. A representative emission check in an H_2-NO_2 mixture is shown in Fig. 4.10. The completely flat signals in Fig. 4.10 signify a lack of broadband emission in both I_0 and $I_0 - I_t$. Such a lack of emission is to be expected in the near-IR, where thermal excitation is unlikely to populate the upper levels to a significant extent.

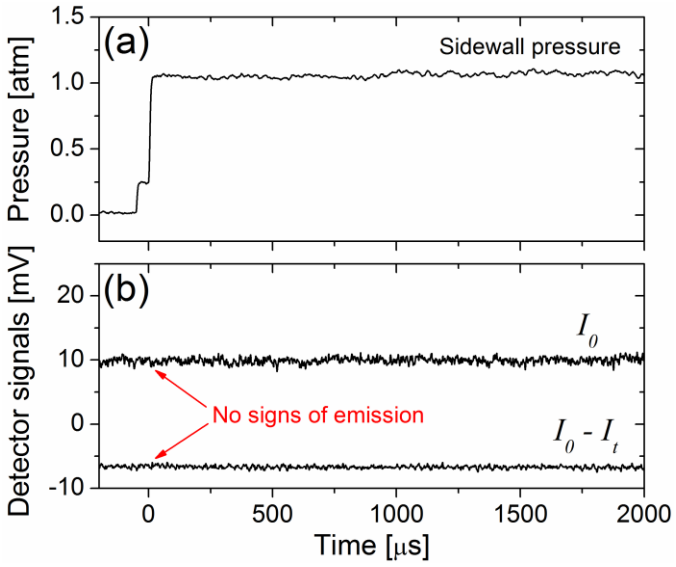

Figure 4.10 Experimental (a) sidewall pressure and (b) detector signals during a shock experiment with the laser turned off to check for broadband emission. Conditions were 1895 K, 1.05 atm in a mixture of 0.222% H_2, 0.392% NO_2, 99.386% Ar.

For diagnostics at higher wavelengths, the likelihood of background emission increases due to increasing population of the upper level (Fig. 3.8). In some cases, broadband emission in the I_t detector is still significant despite the best experimental efforts. In such cases, the emission can be characterized as a function of temperature (and pressure, if needed) and then appropriately removed from the recorded absorption signal. For an example of characterization and subsequent removal of broadband interference, see Mulvihill and Petersen [28].

4.2.6 Interference from other absorbing species

Another potential concern in laser absorption experiments is interference from other absorbing species. Ideally, the laser radiation would only be absorbed by the target species, but this may not always be the case. An initial method of checking for such interference is to search spectroscopic databases for interfering species at the target wavelength (see Appendix D for examples of such databases). However, such databases might not contain the molecules that are interfering. Furthermore, the databases may be designed for lower temperatures and therefore lack the hot bands[7] associated with high-temperature spectra. For example, HITRAN is not designed for temperatures much above 296 K. A better method of simulating high-temperature spectra might be the HITEMP database [29]: Mulvihill and Petersen recently found for high-temperature CO_2 absorption near 2190 cm^{-1}, the HITRAN 2004 database underpredicted the absorption by a factor of ~10 while HITEMP closely matched the experiment [28]. HITEMP is limited to the molecules H_2O, CO_2, CO, NO, and OH. In general, care should be taken when accessing spectroscopic databases to simulate high-temperature spectra.

A second method of identifying interfering species is to perform experimental checks with the laser offline (i.e., detuned from the target transition). By modeling the absorption spectra of the target absorbing species, nearby regions of low or no absorption can be identified. Figure 4.11 shows an example of such a calculation for the H_2O transition used in this study, demonstrating that ~1388.105 nm and ~1388.170 nm may be useful regions for such offline experiments. The laser can be tuned to one of these regions and a shock experiment performed; if a noticeable amount of absorption is observed, this could

[7] The term "hot bands" refers to bands that are insignificant at/near room temperatures but become significant at higher temperatures.

represent absorption from an interfering species.[8] Of course, if the interfering species happens to absorb only at precisely the same wavelength as the target species, the offline experiment will produce a false negative. If the interfering species can be identified or postulated, it may be possible to prepare a mixture with only that species included and perform a shock experiment with the laser tuned to the target wavelength (e.g., 1388.140 nm in this study) to characterize the interfering absorption; in the case of fixed-wavelength lasers such as gas lasers, this option is the only known recourse.

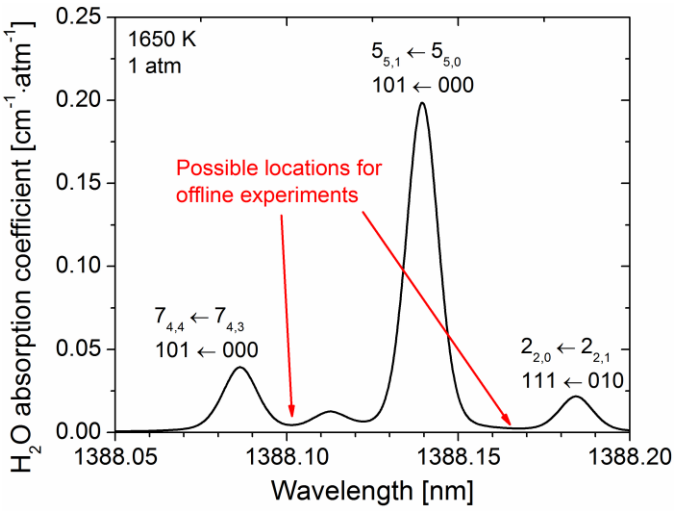

Figure 4.11 Neighboring absorption spectra of the $5_{5,1} \leftarrow 5_{5,0}$ transition of H_2O. Calculations performed with 0.2% H_2O, 99% Ar using HITRAN 2004 [23] and $Q(T)$ from Laraia et al. [24]. Broadening and shift coefficients for all lines were assumed to be those in Table 4.1.

If interfering absorption is discovered, one possible remedy is to correct the absorption time histories using predictions from chemical kinetics mechanisms; such a

[8] A hallmark signature of absorption from an interfering species in an offline test is a time-history shape that is markedly different from the time-history shape of the target species (although interference can still be present if the time-history shapes are similar); see Sect. 5.3.6 for an example of such interference.

method has been used in previous studies of CO absorption [9, 30, 31]. This method is inherently mechanism-dependent and thus somewhat circular. However, if the corrections are small, any errors in the mechanism predictions used for the corrections will have only a second-order effect on the final experimental mole fraction. In this study, such corrections were necessary due to interference from NO_2 that was discovered via offline shock experiments. These offline experiments and the subsequent corrections to the absorption time histories are discussed in more detail in Sect. 5.3.6.

4.3 OH* chemiluminescence diagnostic

In addition to the H_2O laser diagnostic, a second shock-tube optical diagnostic was employed in this study to measure OH* emission near 307 nm from the $A\,^2\Sigma^+ \rightarrow X\,^2\Pi$ band of OH. Described in what follows are the setup of the diagnostic, analysis of the emission data, and considerations of interfering emission.

4.3.1 Configuration of the emission diagnostic

The setup of the OH* diagnostic is shown in Fig. 4.12. Light emission exited the shock tube through the third window port mounted on top of the tube. An adjustable slit, set to a width of ~1.5 mm for this work, was used to constrain the amount of the shock tube imaged by the diagnostic since the axial dimension of the tube correlates to time [32]. The emitted light was focused by a mirror (f = 25 cm) and a plano-convex lens (f = 10 cm) before passing through a bandpass filter and terminating on the detector. All emission experiments in this study were performed with the same optical configuration: no optics were touched except to carefully exchange the bandpass filter on occasion.

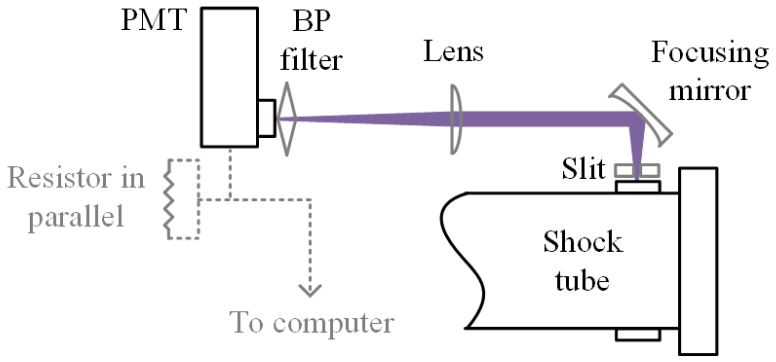

Figure 4.12 Schematic of the OH* chemiluminescence diagnostic. In the present study, the top window of the shock tube was utilized for this diagnostic.

The detector was a photomultiplier tube (PMT) (model 1P21 from Hamamatsu) contained within a custom housing. The PMT had a rise time of 2.2 ns and a spectral range of 300 to 650 nm. The PMT was powered by a high-voltage power supply (model PF1053 from Burle). The voltage output of the PMT was wired in parallel with an 8-kΩ resistor to reduce the amount of voltage that was sent to the DAQ via a BNC cable. PMTs generally exhibit good linearity but can become non-linear above a certain limit. This linearity limit is a function of the resistance of the resistor in parallel as well as the voltage of the power supply. In-house characterizations of the PMT linearity indicated that for an 8-kΩ resistor in parallel, a PMT output limit of 500 mV should be more than adequate to maintain linearity. PMT output levels in this study were kept below 400 mV.

4.3.2 Analysis of emission data

Sample pressure and OH* emission data traces are shown in Fig. 4.13. Following the passage of the reflected shock wave, there is an instantaneous increase in the absolute magnitude of the PMT signal corresponding to the formation of OH*, followed by a peak and then a gradual decline to a steady value near 0 mV. In the absence of laser Schlieren

features, the initial rise in pressure due to the arrival of the reflected shock wave at the measurement location (1.6 cm from the endwall) was used to define time zero. In processing the raw emission traces, the signals were shifted in cases of slight initial offsets from zero and also inverted to represent OH* formation (see Sect. 5.4.1 for examples of processed OH* traces). A timing parameter, $\tau_{50\%}$ [μs], was extracted from the OH* profiles by finding the delay between time zero and the point at which the OH* signal had decayed to 50% of its peak value; this definition is illustrated in Fig. 4.13.

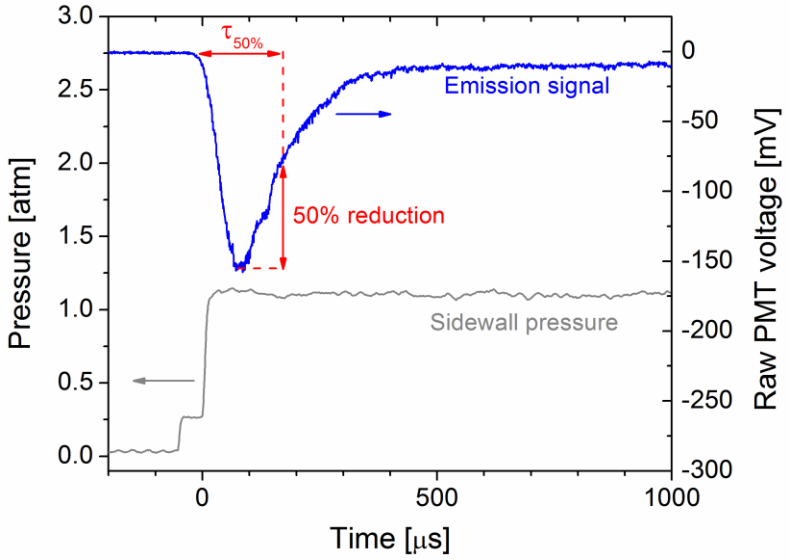

Figure 4.13 Sample OH* measurement and sidewall pressure trace, showing the definition of $\tau_{50\%}$. Conditions are 1807 K, 1.11 atm in a mixture of 0.222% H_2, 0.392% NO_2, balance Ar.

Over the course of a typical set of chemiluminescence tests (including those in this study), it is usually necessary to adjust the supply voltage of the PMT to either avoid damaging the DAQ with excessive signal at higher temperatures where more OH* is formed or to obtain adequate signal levels at lower temperatures where less OH* is formed.

Therefore, to make accurate relative measurements of [OH*], it was necessary to take into account the gain of the PMT as a function of the PMT supply voltage. According to the PMT datasheet, this relationship follows a power law dependence, which was confirmed via the measurements shown in Fig. 4.14. The relative gain measurements were performed by illuminating the PMT with a broadband light source and recording the ratio of the PMT outputs at different supply voltages. All measured peak OH* levels in [mV] from the H_2-NO_2-Ar experiments (Sect. 5.4.1) were scaled according to the gain versus supply voltage curve shown in Fig. 4.14 to obtain the relative peak OH* levels.

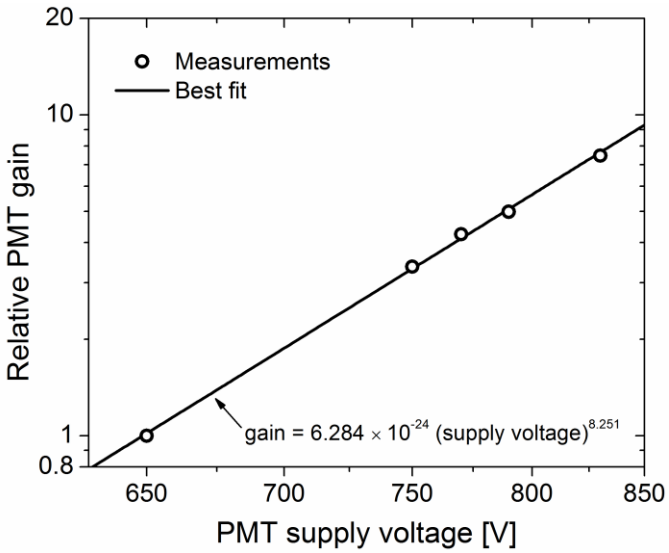

Figure 4.14 Log-log plot of the gain versus the supply voltage for the PMT. The *y* axis was normalized to the gain at 650 V. For the best fit shown, $R^2 = 0.999$.

4.3.3 Interference from other emitting species

Broadband emission is not only a concern in laser diagnostics (Sect. 4.2.5) but can also be an issue in emission diagnostics. The spatial filtering techniques (e.g., irises) useful in laser diagnostics are no longer helpful for emission diagnostics; instead, the elimination

of broadband emission within emission diagnostics must be accomplished by correctly choosing the bandpass filter. Figure 4.15 shows line strengths in the $A\,^2\Sigma^+ \rightarrow X\,^2\Pi$ band of OH at 1800 K along with the measured transmission curves of two bandpass filters: one with λ_c = 300 nm, FWHM = 40 nm and one with λ_c = 307 nm, FWHM = 10 nm. (For a detailed discussion of the OH $A\,^2\Sigma^+ \rightarrow X\,^2\Pi$ band, see pgs. 227-243 of Hanson et al. [33].) The transmission curves of the filters were measured using a spectrometer (model HR2000+ from OceanOptics) and a spectral lamp (model 66003 from Oriel). The spectrometer was calibrated using a Hg/Ar pen lamp (model 6035 from Oriel). The filter with FWHM = 40 nm is not only spectrally wider but also has a higher peak transmission; consequently, it allowed more light to enter the PMT.

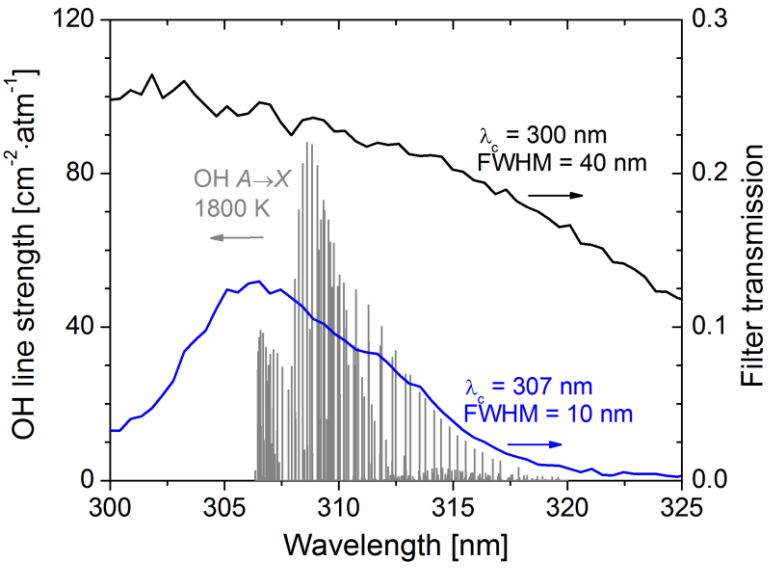

Figure 4.15 OH line strengths in the $A\,^2\Sigma^+ \rightarrow X\,^2\Pi$ band at 1800 K and measured transmission curves of two bandpass filters. OH calculations used HITRAN 2016 [34] and $Q(T)$ from Laraia et al. [24].

To determine the potential impact of the bandpass filter choice, comparative shock-tube experiments were performed in a mixture of H_2-NO_2-Ar. Two experiments were performed at nearly identical conditions; one with the λ_c = 300 nm, FWHM = 40 nm filter and one with the λ_c = 307 nm, FWHM = 10 nm filter. The resulting normalized OH* profiles from these two tests are shown in Fig. 4.16. Other than small differences in timing due to small differences in T_5 and P_5, there is little difference in the two profiles. If there were significant broadband emission present, one would expect more of this emission to be gathered by the broader filter and so to observe different shapes in the two OH* time histories. The similarities in shape between the two experiments suggest such broadband emission is not a large issue, or at least that it is not significantly hindered by using a narrower bandpass filter. Consequently, the broader filter (λ_c = 300 nm, FWHM = 40 nm) was used for all OH* experiments to achieve a better SNR.

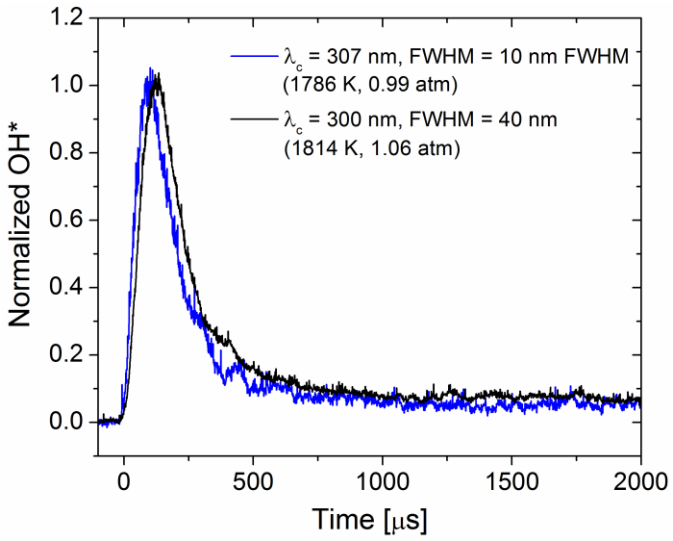

Figure 4.16 Comparison of normalized emission signals obtained using different bandpass filters. The mixture was 0.222% H_2, 0.392% NO_2, balance Ar.

Another experiment performed to check for NO_2 emission interference is shown in Fig. 4.17. Two experiments with identical optical setups were performed using mixtures with and without H_2. Interestingly, the NO_2-Ar mixture shows a noticeable amount of emission (4 mV, or ~9% of the peak value obtained in the case with H_2 included). An additional test at ~2050 K (not shown) indicated that the percentage of the NO_2 interference relative to the signal in the H_2-NO_2-Ar mixture increased to ~14% at this higher temperature, suggesting the significance of the NO_2 interference decreased at lower temperatures. Since the conditions in Fig. 4.17 represent the high-temperature end of this study, the NO_2 interference is expected to be less than 9% of the OH* signal for all experiments and is likely negligible at the low-temperature end of this study.

In the present study, the NO_2 concentration was ~10 orders of magnitude greater than the OH* concentration according to chemical kinetics modeling estimates (see Sect. 5.2 for more on modeling). Although prior work on NO_2 thermal emission has indicated NO_2 emission decreases rapidly below 330-390 nm [35, 36], the high sensitivity of the PMT and the large concentration of NO_2 relative to OH* may be responsible for the slight NO_2 interference observed in Fig. 4.17.

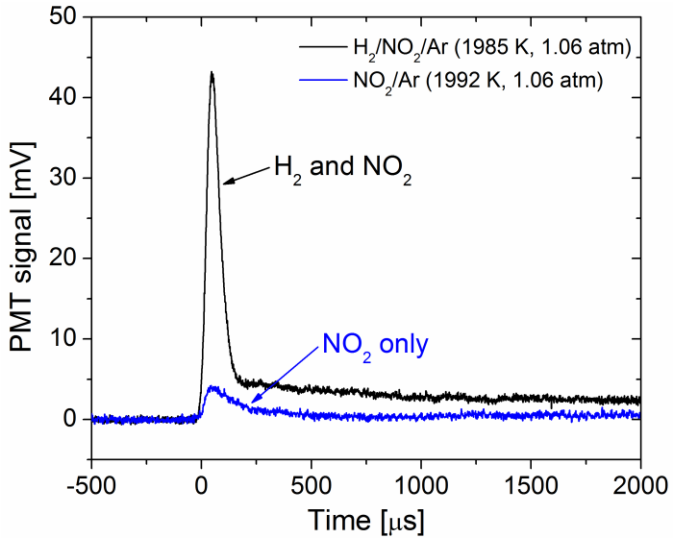

Figure 4.17 Comparison of PMT signals obtained at similar conditions in mixtures with H_2 (0.222% H_2, 0.392% NO_2, balance Ar) and without H_2 (0.392% NO_2, balance Ar). Both experiments used the λ_c = 300 nm, FWHM = 40 nm filter. Due to low signal levels, the lower curve was digitally filtered using lowpass first-order Butterworth filter with a 300-kHz cutoff.

It was suspected that excited-state NH (NH*) might have been partly responsible for the observed interference in Fig. 4.17 given the relatively large FWHM (40 nm) of the bandpass filter used for the OH* measurements. The $A\ ^3\Pi \rightarrow X\ ^3\Sigma^-$ band of NH manifests itself between 328 and 344 nm [37, 38]. To search for potential NH* interference, a final emission check was conducted. Two shock-tube experiments at similar conditions were performed in a H_2-NO_2-Ar mixture using different bandpass filters: one with λ_c = 307 nm, FWHM = 10 nm and one with λ_c = 335 nm, FWHM = 10 nm. The λ_c = 335 nm filter was characterized using the same spectrometer and spectral lamp described earlier. The results from the two shock-tube experiments are shown in Fig. 4.18(a). No discernible emission was observed when using the λ_c = 335 nm filter, confirming that NH* emission was not being captured during the OH* experiments with the λ_c = 300 nm filter. Shown in Fig. 4.18(b) are the filter transmission curves for the λ_c = 307 nm and λ_c = 335 nm filters,

demonstrating the nearly identical peak transmissions of the two filters and confirming a lack of ambiguity in the interpretation of Fig. 4.18(a) due to different filter transmission levels. As a final note, the spectral responsivity of the PMT is ~1.3 times greater at 335 nm than at 307 nm, according to the manufacturer's datasheet. When comparing emission results from different wavelength regions with the goal of making accurate comparisons on a relative basis, the spectral responsivity of the detector should be considered. For the example case in Fig. 4.18(a), the results shown were not corrected for the detector responsivity. However, reducing the results at 335 nm by a factor of 1.3 would only further confirm the lack of emission at 335 nm.

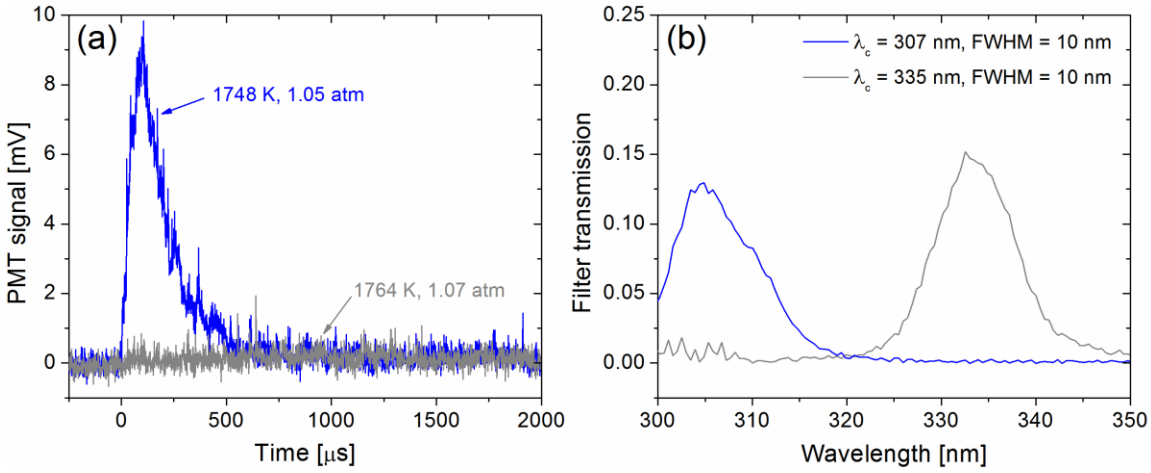

Figure 4.18 Comparison of (a) PMT signals obtained using different bandpass filters at similar conditions and (b) measured transmission curves for the two filters. Both profiles in (a) were measured in a mixture of 0.222% H_2, 0.392% NO_2, balance Ar. The transmission curve for the filter with λ_c = 307 nm is the same as shown in Fig. 4.15.

4.4 NO_2 LED absorption diagnostic

The final optical diagnostic employed was an absorption diagnostic based on a light-emitting diode (LED) to measure NO_2 concentrations in the prepared mixtures.

Presented in this subsection are the setup of the NO_2 diagnostic, the data reduction methods employed, and the calculation/verification of the absorption coefficient.

4.4.1 Configuration of the LED diagnostic

The setup of the NO_2 diagnostic is shown in Fig. 4.19. A blue LED was powered by an adjustable benchtop DC power supply at 3.5 V and ~70 mA. The LED light passed through two sapphire windows of an aluminum absorption cell with a path length of 11.74 cm before terminating on a Si photodiode (model 2032 from Newport). The detector was set to the low-bandwidth (150 kHz), high-gain (2×10^6 V/A) option due to low signal levels. A series of focusing lenses with varying focal lengths were placed along the beam path to maintain a roughly collimated beam. A bandpass filter (λ_c = 459 nm, FWHM = 5 nm) was situated in the beam path to increase the average NO_2 absorption coefficient since the unfiltered LED spectrum (not shown) ranged from 425 to 525 nm. An iris blocked stray light from entering the detector. The output of the detector was sent to the computer-based DAQ. To avoid possible leak effects, the detector output was recorded just after filling the cell to the desired pressure and the cell was vacuumed out after each measurement.

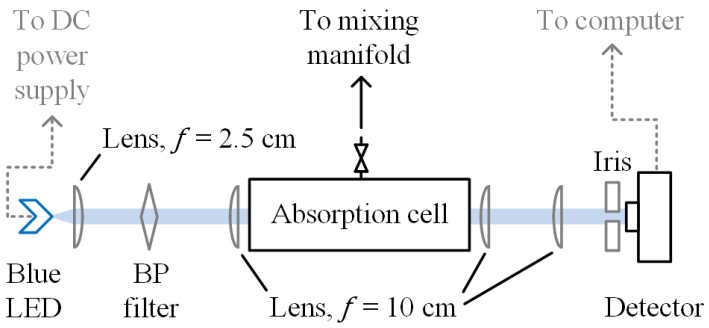

Figure 4.19 Schematic of the LED-based NO_2 diagnostic. The setup was employed on an optical table and attached to the mixing manifold.

Low transmission of light to the detector resulted in a low SNR in the detector signal. However, since the NO_2 measurements were performed at steady state and not during shock-tube experiments, the signals were averaged over the ~19-ms acquisition time. Figure 4.20 shows representative raw and averaged detector signals before and after adding the mixture to the cell. Also shown in Fig. 4.20 is the detector offset due to the photodiode dark current; this offset was measured by blocking the LED and was subtracted from all measured detector signals (see Appendix B for more on detector offsets).

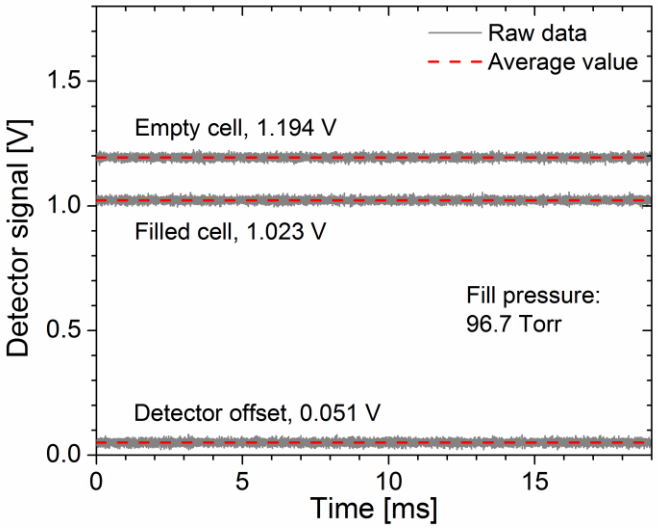

Figure 4.20 Raw and averaged detector signals from a LED absorption measurement in a mixture of 1.03% NO_2, balance Ar before and after filling the absorption cell. Also shown is the detector offset. After subtracting out the detector offset from both signals, the measured absorbance was 0.162.

4.4.2 Modeling and validation of the NO_2 absorption coefficient

To make quantitative NO_2 absorption measurements, it was necessary to obtain a value for the NO_2 absorption coefficient. The absorption of NO_2 in the UV/visible range is due to a complex overlay of electronic states [39] and has been well-characterized near

room temperature [40-43]. Shown in Fig. 4.21 are the absorption coefficients of NO_2 as measured at 298 K by Schneider et al. [41]. These values were obtained in a bath gas of air rather than Ar, but prior work by Liu et al. [44] has demonstrated that NO_2 absorption coefficients in this region are pressure-independent in the pressure range of interest (0 to ~250 Torr), suggesting the collisional partner has a negligible effect on k_v. The spectrally averaged k_v used herein further decreased the dependence of k_v on pressure. Figure 4.21 also plots the absorption coefficient of the NO_2 dimer N_2O_4, as measured by Hall and Blacet [40]. N_2O_4 has negligible absorption in the region of the blue LED spectrum, meaning that N_2O_4 did not interfere with the NO_2 measurements.

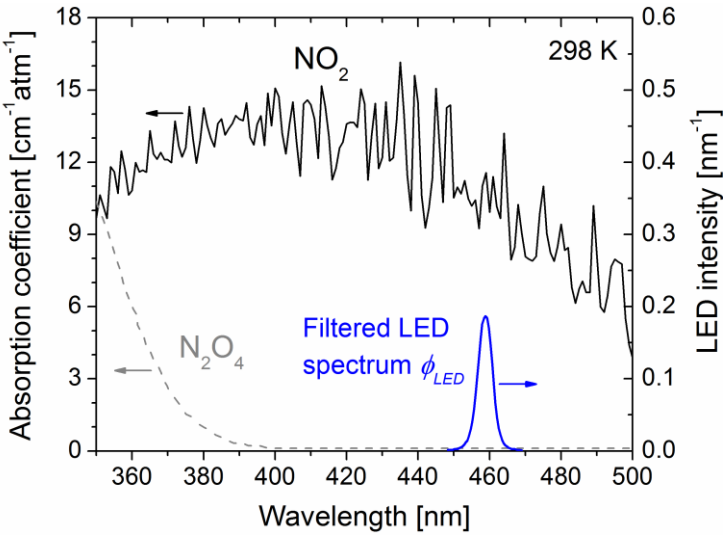

Figure 4.21 Literature values for absorption coefficients of NO_2 [41] and N_2O_4 [40] at 298 K in air. Also shown is the measured spectrum of the blue LED, normalized to an area of 1.

The spectrum of the LED was characterized using the same spectrometer and spectral lamp described in Sect. 4.3.4. The LED spectrum, ϕ_{LED} [nm^{-1}], can be thought of as a line shape and was accordingly normalized to have an area of 1. To calculate the

effective NO_2 absorption coefficient as seen by the LED, $k_{v,LED}$ [$cm^{-1} \cdot atm^{-1}$], the following expression was used:

$$k_{v,LED} = \int \phi_{LED}\, k_{v,NO_2}\, d\lambda. \tag{4.15}$$

In Eq. (4.15), k_{v,NO_2} [$cm^{-1} \cdot atm^{-1}$] is the NO_2 absorption coefficient plotted in Fig. 4.21, and the integral extends over the entire LED spectrum. Evaluating Eq. (4.15) with the values plotted in Fig. 4.21, a value of 10.59 $cm^{-1} \cdot atm^{-1}$ was obtained[9] for $k_{v,LED}$.

To validate the calculated $k_{v,LED}$, a series of measurements were performed with a known amount of NO_2. A bottle of 1.03% NO_2 in balance Ar was used as the calibration mixture. This mixture was prepared by Praxair using the gravimetric method, making the concentration of NO_2 insensitive to dimerization effects (see Sect. 5.1 for more on NO_2 dimerization). Six absorption measurements were made between 20 and 120 Torr and are plotted in Fig. 4.22. Also plotted are the predictions using the known concentration of NO_2 along with the calculated value of $k_{v,LED}$. The excellent agreement between the predictions and the measurements in Fig. 4.22 verified the calculated value of $k_{v,LED}$ and demonstrated the usefulness of the LED diagnostic for determining unknown NO_2 concentrations.

At the low fill pressures employed in the absorption cell, chemical equilibrium calculations indicated that the 1.03% NO_2, balance Ar mixture would experience only a slight tendency toward dimerization of NO_2 (see Sect. 5.1): the calculated equilibrium N_2O_4 mole fraction was only 2.2% of the NO_2 mole fraction at 250 Torr and only 0.9% of

[9] The resolution of the spectrometer was ~0.5 nm, while the resolution of the Schneider et al. NO_2 absorption coefficients were reported at a resolution of 1.0 nm in their Table 2. The two datasets were interpolated to identical resolutions of 0.5 nm for numerical evaluation of Eq. (4.15).

the NO_2 mole fraction at 100 Torr.

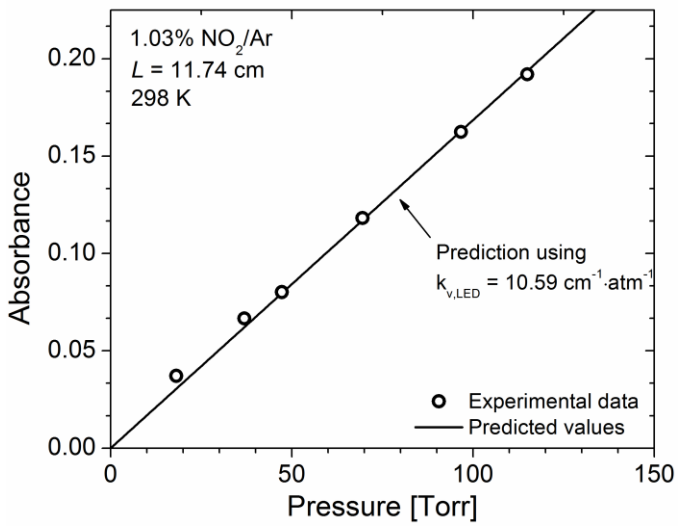

Figure 4.22 Experimental and predicted absorbance values in a mixture of 1.03% NO_2, balance Ar. The solid line was calculated using $k_{v,LED}$ = 10.59 $cm^{-1}{\cdot}atm^{-1}$.

4.5 Summary

The theory and practical realization of the shock tube used in this study was first addressed. The conservation laws around a 1-D normal shock wave were provided and can be solved with iterative numerical solvers that are available in the literature. Vibrational relaxation is an issue that has received much study but can still cause problems in shock-tube experiments; analytical relations were provided to estimate the vibrational relaxation time. The addition of efficient colliders such as H_2 and He is one method for reducing vibrational relaxation issues. Vibrational relaxation effects were determined to not be of concern for the mixtures in this dissertation.

The H_2O diagnostic was described in detail, including the physical setup and the operational procedures. The selection and spectroscopic parameters of the H_2O transition

were developed. The challenges of broadband emission and interfering absorption were discussed, and methods of assessing and/or eliminating these issues were provided. Broadband emission was found to not be an issue for the H_2-NO_2 mixtures studied herein (interfering absorption is addressed in Sect. 5.3.6). The various techniques described should be useful for any laser diagnostic paired with a shock tube.

The OH* chemiluminescence diagnostic was described. The PMT gain versus the supply voltage was characterized for use in measuring accurate absolute or relative OH* values. Methods of assessing broadband interference from other species, selecting the proper bandpass filter, and accounting for the spectral responsivity of the detector were discussed. Interference in the measured OH* signals from NO_2 was discovered and quantified at less than 10% of the total emission signal for all temperatures studied herein. Possible interference from NH* was investigated and found to be negligible. These methods presented for this diagnostic are useful for any shock-tube chemiluminescence or emission diagnostic.

Finally, the LED-based absorption diagnostic for NO_2 was described. Example raw data were provided, and the low SNR in these data was overcome by averaging the data for these static LED measurements. The spectrum of the filtered LED was measured and used to calculate an effective NO_2 absorption coefficient by integrating over absorption coefficient data from the literature. Using a mixture with a known NO_2 calibration, excellent agreement between the calculated and experimental data was obtained, verifying both the calculated absorption coefficient and the NO_2 diagnostic.

4.6 References

[1] D.F. Davidson, R.K. Hanson, "Real gas corrections in shock tube studies at high pressures" *Israel Journal of Chemistry* **36** (1996) 321-326.

[2] A.G.H. Gaydon, I.R., "The Shock Tube in High-Temperature Chemical Physics" Reinhold Pub. Corp., New York (1963).

[3] D.R. Mott, T.A. Gally, L.A. Carlson, "Viscous normal shock solutions including chemical, thermal, and radiative nonequilibrium" *Journal of Thermophysics and Heat Transfer* **9** (1995) 577-585.

[4] M.F. Campbell, D.R. Haylett, D.F. Davidson, R.K. Hanson, "AEROFROSH: A shock condition calculator for multi-component fuel aerosol-laden flows" *Shock Waves* **26** (2016) 429-447.

[5] M.F. Campbell, K.G. Owen, D.F. Davidson, R.K. Hanson, "Dependence of calculated postshock thermodynamic variables on vibrational equilibrium and input uncertainty" *Journal of Thermophysics and Heat Transfer* **31** (2017) 586-608.

[6] Y.V. Stupochenko, S.A. Losev, A.I. Osipov, "Relaxation in Shock Waves" Springer-Verlag, New York, NY (1967).

[7] M.S. Wooldridge, R.K. Hanson, C.T. Bowman, "A shock tube study of the CO+OH→CO_2+H reaction" *Symposium (International) on Combustion* **25** (1994) 741-748.

[8] C.-L. Yu, M. Frenklach, D.A. Masten, R.K. Hanson, C.T. Bowman, "Reexamination of shock-tube measurements of the rate coefficient of H + O_2 → OH + O" *The Journal of Physical Chemistry* **98** (1994) 4770-4771.

[9] O. Mathieu, C.R. Mulvihill, E.L. Petersen, "Assessment of modern detailed kinetics mechanisms to predict CO formation from methane combustion using shock-tube laser-absorption measurements" *Fuel* **236** (2019) 1164-1180.

[10] F. Sen, B. Shu, T. Kasper, J. Herzler, O. Welz, M. Fikri, B. Atakan, et al., "Shock-tube and plug-flow reactor study of the oxidation of fuel-rich CH_4/O_2 mixtures enhanced with additives" *Combustion and Flame* **169** (2016) 307-320.

[11] K.G. Owen, D.F. Davidson, R.K. Hanson, "Oxygen vibrational relaxation times: Shock tube/laser absorption measurements" *Journal of Thermophysics and Heat Transfer* **30** (2016) 791-798.

[12] W.G. Vincenti, C.H. Kruger, "Introduction to Physical Gas Dynamics" John Wiley and Sons, New York, NY (1965).

[13] L. Landau, E. Teller, "Zur theorie der schalldispersion" *Physik Z. Sowjetunion* **10** (1936) 34-43.

[14] R.C. Millikan, D.R. White, "Systematics of vibrational relaxation" *Journal of Chemical Physics* **39** (1963) 3209-3213.

[15] J.E. Dove, H. Teitelbaum, "The vibrational relaxation of H_2. I. Experimental measurements of the rate of relaxation by H_2, He, Ne, Ar, and Kr" *Chemical Physics* **6** (1974) 431-444.

[16] R.T.V. Kung, R.E. Center, "High temperature vibrational relaxation of H_2O by H_2O, He, Ar, and N_2" *Journal of Chemical Physics* **62** (1975) 2187-2194.

[17] D.R. White, R.C. Millikan, "Vibrational relaxation in air" *AIAA Journal* **2** (1964) 1844-1846.

[18] S. Wang, D.F. Davidson, R.K. Hanson, "Shock tube and laser absorption study of CH_2O oxidation via simultaneous measurements of OH and CO" *Journal of Physical Chemistry A* **121** (2017) 8561-8568.

[19] E.L. Petersen, "A shock tube and diagnostics for chemistry measurements at elevated pressures with application to methane ignition" Ph.D. dissertation, Stanford University, (1998).

[20] E.L. Petersen, M.J. Rickard, M.W. Crofton, E.D. Abbey, M.J. Traum, D.M. Kalitan, "A facility for gas- and condensed-phase measurements behind shock waves" *Measurement Science and Technology* **16** (2005) 1716-1729.

[21] E.L. Petersen, R.K. Hanson, "Nonideal effects behind reflected shock waves in a high-pressure shock tube" *Shock Waves* **10** (2001) 405-420.

[22] B.H. Sang, T.-I. Jeon, "Pressure-dependent refractive indices of gases by THz time-domain spectroscopy" *Optics Express* **24** (2016) 29040-29047.

[23] L.S. Rothman, D. Jacquemart, A. Barbe, D.C. Benner, M. Birk, L.R. Brown, M.R. Carleer, et al., "The HITRAN 2004 molecular spectroscopic database" *Journal of Quantitative Spectroscopy and Radiative Transfer* **96** (2005) 139-204.

[24] A.L. Laraia, R.R. Gamache, J. Lamouroux, I.E. Gordon, L.S. Rothman, "Total internal partition sums to support planetary remote sensing" *Icarus* **215** (2011) 391-400.

[25] V. Nagali, D.F. Davidson, R.K. Hanson, "Measurements of temperature-dependent argon-broadened half-widths of H_2O transitions in the 7117 cm^{-1} region" *Journal of Quantitative Spectroscopy and Radiative Transfer* **64** (2000) 651-655.

[26] H. Li, A. Farooq, J.B. Jeffries, R.K. Hanson, "Diode laser measurements of temperature-dependent collisional-narrowing and broadening parameters of Ar-perturbed H_2O transitions at 1391.7 and 1397.8 nm" *Journal of Quantitative Spectroscopy and Radiative Transfer* **109** (2008) 132-143.

[27] C.R. Mulvihill, E.L. Petersen, "Concerning shock-tube ignition delay times: An

experimental investigation of impurities in the H_2/O_2 system and beyond" *Proceedings of the Combustion Institute* **37** (2019) 259-266.

[28] C.R. Mulvihill, E.L. Petersen, "High-temperature argon broadening of CO_2 near 2190 cm^{-1} in a shock tube" *Applied Physics B* **123** (2017) 255.

[29] L.S. Rothman, I.E. Gordon, R.J. Barber, H. Dothe, R.R. Gamache, A. Goldman, V.I. Perevalov, et al., "HITEMP, the high-temperature molecular spectroscopic database" *Journal of Quantitative Spectroscopy and Radiative Transfer* **111** (2010) 2139-2150.

[30] C.R. Mulvihill, C.L. Keesee, T. Sikes, R.S. Teixeira, O. Mathieu, E.L. Petersen, "Ignition delay times, laminar flame speeds, and species time-histories in the H_2S/CH_4 system at atmospheric pressure" *Proceedings of the Combustion Institute* **37** (2019) 735-742.

[31] O. Mathieu, C.R. Mulvihill, Y. Zhang, H.J. Curran, E.L. Petersen, "CO and H_2O time-histories in shock-heated blends of methane and ethane for assessment of a chemical kinetics model" *Journal of Engineering for Gas Turbines and Power* **139** (2017) 12150701-12150708.

[32] E.L. Petersen, "Interpreting endwall and sidewall measurements in shock-tube ignition studies" *Combustion Science and Technology* **181** (2009) 1123-1144.

[33] R.K. Hanson, R.M. Spearrin, C.S. Goldenstein, "Spectroscopy and Optical Diagnostics for Gases" Springer, Cham, Switzerland (2016).

[34] I.E. Gordon, L.S. Rothman, C. Hill, R.V. Kochanov, Y. Tan, P.F. Bernath, M. Birk, et al., "The HITRAN2016 molecular spectroscopic database" *Journal of Quantitative Spectroscopy and Radiative Transfer* **203** (2017) 3-69.

[35] B.P. Levitt, "Thermal emission from nitrogen dioxide" *Transactions of the Faraday Society* **58** (1962) 1789-1800.

[36] D.E. Paulsen, W.F. Sheridan, R.E. Huffman, "Thermal and recombination emission of NO_2" *The Journal of Chemical Physics* **53** (1970) 647-658.

[37] A.Y. Chang, R.K. Hanson, "Measurements of absorption lineshapes in the $A\ ^3\Pi_i \leftarrow X\ ^3\Sigma^-(0,0)$ band of NH in the presence of Ar broadening" *Journal of Quantitative Spectroscopy and Radiative Transfer* **42** (1989) 207-217.

[38] C.R. Brazier, R.S. Ram, P.F. Bernath, "Fourier transform spectroscopy of the $A\ ^3\Pi$-$X\ ^3\Sigma^-$ transition of NH" *Journal of Molecular Spectroscopy* **120** (1986) 381-402.

[39] C.F. Jackels, E.R. Davidson, "An ab initio potential-energy surface study of several electronic states of NO_2" *The Journal of Chemical Physics* **65** (1976) 2941-2957.

[40] T.C. Hall, F.E. Blacet, "Separation of the absorption spectra of NO_2 and N_2O_4 in the

range of 2400–5000A" *The Journal of Chemical Physics* **20** (1952) 1745-1749.

[41] W. Schneider, G.K. Moortgat, G.S. Tyndall, J.P. Burrows, "Absorption cross-sections of NO_2 in the UV and visible region (200-700 nm) at 298 K" *Journal of Photochemistry and Photobiology A* **40** (1987) 195-217.

[42] M.F. Mérienne, A. Jenouvrier, B. Coquart, "The NO_2 absorption spectrum. I: Absorption cross-sections at ambient temperature in the 300–500 nm region" *Journal of Atmospheric Chemistry* **20** (1995) 281-297.

[43] A.C. Vandaele, C. Hermans, P.C. Simon, M. Carleer, R. Colin, S. Fally, M.F. Mérienne, et al., "Measurements of the NO_2 absorption cross-section from 42 000 cm^{-1} to 10 000 cm^{-1} (238–1000 nm) at 220 K and 294 K" *Journal of Quantitative Spectroscopy and Radiative Transfer* **59** (1998) 171-184.

[44] J.T.C. Liu, R.K. Hanson, J.B. Jeffries, "High-sensitivity absorption diagnostic for NO_2 using a blue diode laser" *Journal of Quantitative Spectroscopy and Radiative Transfer* **72** (2002) 655-664.

5. MEASUREMENTS AND MODELING OF H_2-NO_2 OXIDATION*

In this Section, the theoretical and experimental techniques described in the previous three Sections are applied to shock-tube measurements of H_2-NO_2 oxidation. The mixture verification results are presented first. Next, a brief introduction to chemical kinetics modeling is provided, with details on the methods employed in this dissertation. The H_2O time histories are then provided alongside modeling analyses to highlight the important reactions. Experimental challenges related to interfering absorption are addressed. Finally, the OH* time histories are presented. The identification and fitting of the new chemiluminescent reaction is provided, with several insights drawn concerning the interpretation of chemiluminescence experiments.

5.1 Verification of shock-tube test mixtures

An experimental difficulty encountered in this work was the dimerization of NO_2, which presented challenges in preparing accurate mixtures. Described herein are the ways in which this problem manifested itself and a brief chemical equilibrium analysis of the problem. The application of the NO_2 and H_2O diagnostics to overcome the issue is then presented along with the final compositions of the four mixtures used in the study.

5.1.1 NO_2 dimerization issues

While measuring H_2O profiles in H_2-NO_2 mixtures, a fuel-lean mixture (where H_2 is the limiting reactant involved in H_2O formation) yielded precisely the amount of H_2O

* Part of this section is reprinted with permission from C.R. Mulvihill, O. Mathieu, E.L. Petersen, "H_2O time histories in the H_2-NO_2 system for validation of NOx hydrocarbon kinetics mechanisms" *International Journal of Chemical Kinetics*, doi:10.1002/kin.21286 (2019), copyright 2019 by Wiley Periodicals, Inc. [1].

expected from the mixture composition upon achievement of a plateau value of H_2O. For example, a fuel-lean mixture of 0.222% H_2, 0.375% NO_2, balance Ar would be expected to yield 0.1% H_2O by fully consuming the H_2; the experimental confirmation of this is demonstrated in Fig. 5.1(a). However, a fuel-rich mixture (where NO_2 is the limiting reactant) yielded significantly lower-than-expected H_2O concentrations. For example, a mixture of 0.222% NO_2, 1.778% H_2, balance Ar (the expected mixture composition in Fig. 5.1(b) based on the partial pressure method of mixture preparation) would be expected to yield 0.222% H_2O by fully consuming the NO_2 since only one of the O atoms will break off from NO_2 during the experimental timescales at the temperatures of the current study.[1] Experimentally, however, a ~25%-lower-than-expected value of H_2O was obtained at the plateau in the fuel-rich experiments, as shown in Fig. 5.1(b).

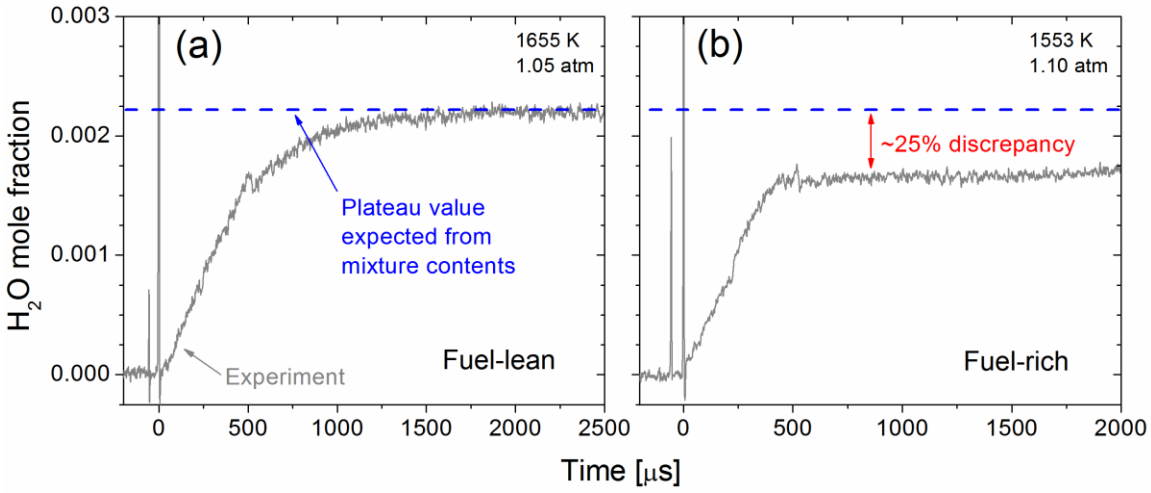

Figure 5.1 Experimental plateau H_2O values for (a) fuel-lean and (b) fuel-rich mixtures of H_2-NO_2-Ar. The data in (a) have been slightly corrected for NO_2 interference (see Sect. 5.3.6). Adapted with permission from [1].

[1] Chemical kinetic modeling with several mechanisms confirmed the second O atom would require several minutes to fully react with the hydrogen even at the high-temperature end of the H_2O experiments.

The results of Fig. 5.1 suggested less NO_2 was being added to the mixtures than expected according to partial-pressure calculations due to the dimerization of NO_2 to N_2O_4 ($2NO_2 \rightleftarrows N_2O_4$). To briefly investigate the behavior of NO_2 dimerization in the mixing tank, chemical equilibrium calculations were performed. The equilibrium constant K_{eq} relates the equilibrium mole fractions of NO_2 and N_2O_4 at constant pressure and temperature to the maximization of entropy (see pgs. 38-46 of Turns [2]):

$$K_{eq} = \exp\left(-\frac{\Delta\bar{G}}{R_u T}\right) = \frac{X_{N_2O_4}}{\left(X_{NO_2}\right)^2}\left(\frac{P}{P_0}\right)^{-1}. \tag{5.1}$$

Here, P_0 is a reference pressure of 1 atm and $\Delta\bar{G}$ [cal/mol] is the molar-specific change in Gibbs free energy. $\Delta\bar{G}$ is given in the case of $2NO_2 \rightleftarrows N_2O_4$ by

$$\Delta\bar{G} = \left(\bar{h}_{N_2O_4} - 2\bar{h}_{NO_2}\right) - T\left(\bar{s}_{N_2O_4} - 2\bar{s}_{NO_2}\right). \tag{5.2}$$

$\bar{h}$ [cal/mol] and $\bar{s}$ [cal/(mol·K)] denote the molar-specific enthalpy and entropy, respectively, as functions of temperature and were evaluated at different temperatures using the NIST-JANAF thermochemical tables [3]. Figure 5.2 shows the calculated equilibrium N_2O_4 mole fraction as a function of pressure at several temperatures in (initially) pure NO_2. Increasing pressure shifts equilibrium toward N_2O_4, while increasing temperature shifts equilibrium toward NO_2.

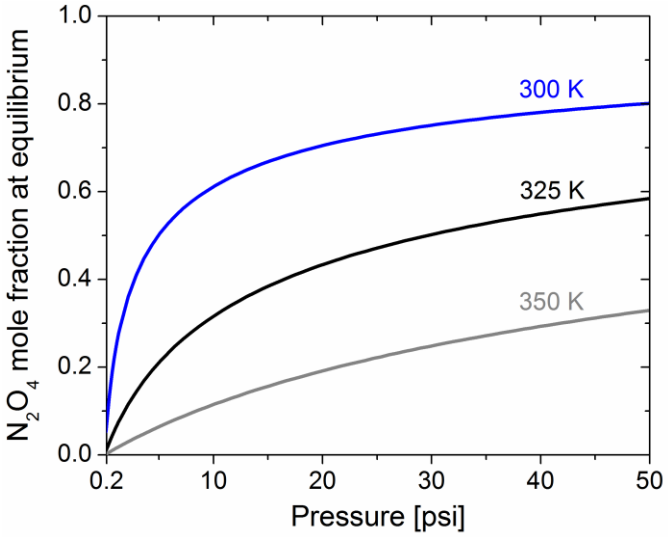

Figure 5.2 Equilibrium mole fractions of N_2O_4 in initially pure NO_2 assuming constant pressure and constant temperature.

Similar calculations[2] were performed for an initial mixture of 1% NO_2 in balance Ar, to better simulate the conditions of the gaseous mixtures used in this study (Sect. 4.1). These calculations indicated that at typical mixing-tank conditions of 1000 Torr and 296 K, the mixture will equilibrate to 0.45% NO_2, 0.28% N_2O_4, 99.27% Ar. Although the low fill pressures (< 50 Torr) of the driven section caused equilibrium to shift back toward NO_2, creating negligibly small N_2O_4 concentrations prior to the arrival of the incident shock wave, the dimerization distorted the number of moles being added to the mixture and led to actual NO_2 concentrations in the mixture that were lower than predicted using partial pressure calculations.

[2] The calculations in Fig. 5.2 employed the constant-pressure, constant-temperature assumption. For non-dilute mixtures such as pure NO_2, this assumption has a large effect on the outcome and varies significantly from, say, a constant-pressure, constant-enthalpy constraint. However, for highly dilute mixtures such as the 99% Ar mixture, this assumption has a negligible effect on the results.

5.1.2 Measurements of mixture NO_2 concentrations

To ascertain the amount of NO_2 being added to the mixtures, two methods were utilized. The first method was the LED absorption diagnostic (Sect. 4.4). Using the calculated and experimentally verified value of 10.59 $cm^{-1}\cdot atm^{-1}$ for $k_{v,LED}$, quantitative measurements of NO_2 concentrations were conducted for the two fuel-lean mixtures used in this study. Figure 5.3 shows the results of one such mixture characterization. The y axis in Fig. 5.3 is the measured absorbance of the filtered LED light by the mixture within the cell, while the x axis is the fill pressure of the cell. The slope of the best fit to the data was 0.4875 atm^{-1}. Using the definition of the absorbance, Eq. (3.16), and the known values of $k_{v,LED}$ and L yielded a NO_2 concentration of 0.392% for the mixture shown here. The uncertainty bars of ±2% on each data point (assuming an uncertainty of ±1 mV in the detector signals) are slightly smaller than the symbols in Fig. 5.3. The total uncertainty in the measured NO_2 concentration using the LED diagnostic is estimated to be ±4%.

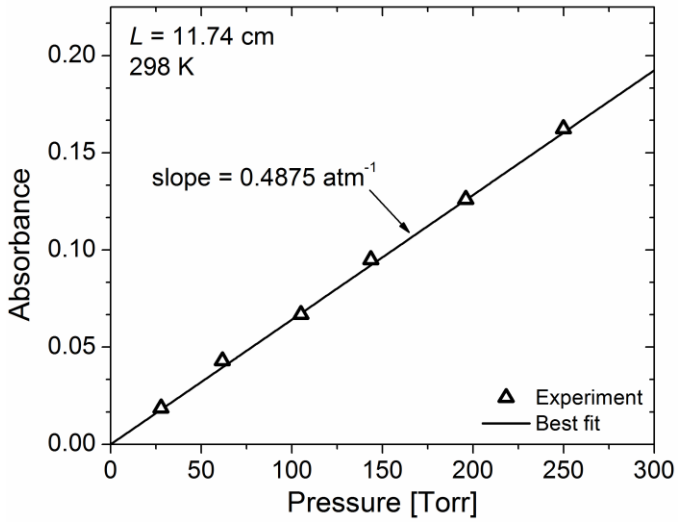

Figure 5.3 Experimental absorbance data and their best-fit line for a set of tests using the LED absorption diagnostic. Using these data, the measured NO_2 concentration in this mixture was 0.392%.

The second method of measuring the NO_2 mixture concentration was inference from the H_2O time histories. Since NO_2 was the limiting reactant in the fuel-rich and near-stoichiometric mixtures,[3] it was possible to infer the amount of NO_2 in these two mixtures by observing the plateau value of H_2O achieved at higher temperatures, recalling the fact that only one of the atoms in the NO_2 was free to react. For example, the H_2O profile in Fig. 5.1(b) plateaus at about 0.167% H_2O, implying a NO_2 concentration of 0.167% for the mixture. Using the H_2O inference method for the fuel-rich and near-stoichiometric mixtures, averages across several experiments were used to determine the NO_2 concentrations in the two mixtures. The compositions of all four mixtures used in this study are shown in Table 5.1. The NO_2 concentrations were 12-25% lower than expected from the partial pressure preparation method. Additionally, a comparison of the LED and H_2O methods was performed and is shown in Fig. 5.4. The flat line corresponding to the LED measurement is the plateau H_2O level expected according to the LED-measured NO_2 concentration. The expected H_2O value agrees well with the measured H_2O time history, further verifying the use of both methods for determining NO_2 mixture concentrations.

Table 5.1 H_2-NO_2 mixture compositions. Adapted with permission from [1].

	% H_2	% NO_2	% Ar	ϕ [c]	T_5 [K]	Diagnostic
Mix 1	0.222	0.375 [a]	99.403	0.30	1313-1782	H_2O
Mix 2	0.444	0.178 [b]	99.378	1.25	1087-1662	H_2O
Mix 3	1.778	0.168 [b]	98.054	5.29	917-1520	H_2O
Mix 4	0.222	0.392 [a]	99.386	0.28	1535-2003	OH*

[a] Measured using LED diagnostic.
[b] Inferred using plateau H_2O method.
[c] Calculated according to $H_2 + ½\ NO_2 \rightleftarrows H_2O + ¼\ N_2$.

[3] Due to the lower-than expected amounts of NO_2 in the mixtures, the mixture intended to be stoichiometric according to the partial pressure method was actually slightly fuel-rich (see Table 5.1), meaning that the H_2O inference method could be used for this mixture.

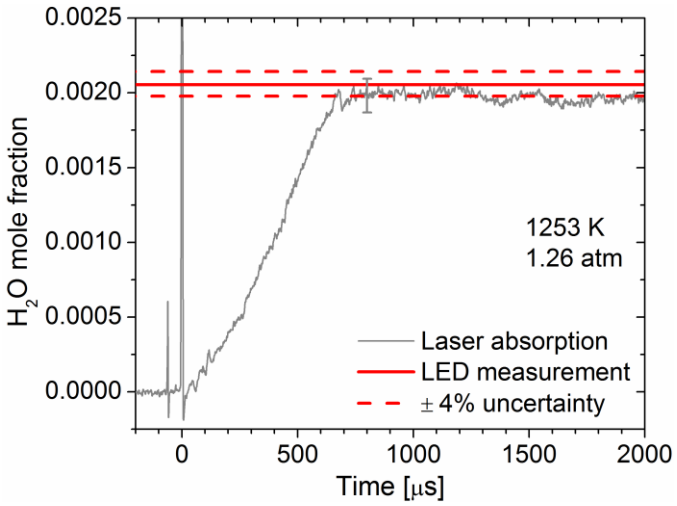

Figure 5.4 Comparison of the LED and H_2O measurement methods of determining the NO_2 concentration in the mixtures. Uncertainty in the H_2O mole fraction is ±5.7% [4]. Adapted with permission from [1].

5.2 Chemical kinetics modeling

In this study, numerous comparisons between experimental data and predictions from chemical kinetics mechanisms[4] are drawn. This subsection introduces the modeling methods employed herein and also describes the updates to the OH*-quenching reactions. A basic understanding of chemical kinetics is assumed such that only a very brief introduction to the topic is provided; numerous texts are available on this subject [2, 5-7].

5.2.1 Introductory comments on chemical kinetics

A general bimolecular reaction can be written as AB + C ⇄ A + BC. The rate of change in the concentration of A, [A], is given in the forward direction by

$$\frac{d[\mathrm{A}]}{dt} = k[\mathrm{AB}][\mathrm{C}], \tag{5.3}$$

[4] Chemical kinetics mechanisms are interchangeably referred to as "models" or simply "mechanisms".

where k is the forward rate constant. Accounting for the reverse direction of the reaction, the rate of change in [A] is properly

$$\frac{d[\mathrm{A}]}{dt} = k[\mathrm{AB}][\mathrm{C}] - k_{-}[\mathrm{A}][\mathrm{BC}], \tag{5.4}$$

where k_{-} is the reverse rate constant and is related to k by

$$\frac{k}{k_{-}} = K_{eq}. \tag{5.5}$$

Some reactions are termolecular and are typically written in the general form A + B + M ⇄ AB + M, where M is a third-body collider that does not participate chemically in the reaction. Unimolecular reactions (e.g., AB ⇄ A + B) also exist.

Of great interest in chemical kinetics modeling is the value of the rate constant. A large number of rate constants can be described as a function of temperature using the modified Arrhenius form

$$k = A\,T^{n} \exp(-E_a/R_u T), \tag{5.6}$$

where A is the pre-exponential factor, n is the temperature coefficient, and E_a is the activation energy. The dimensionality of k and A depends on the molecularity of the reaction. The unit system must be specified for clarity; in gas-phase chemical kinetics, a common system is [cal], [mol], [cm^3], [s] and is adopted by Chemkin. For example, Chemkin receives E_a in [cal/mol] and calculates k for bimolecular reactions in

[cm^3/(mol·s)]. For reactions whose rate constants do not follow the form of Eq. (5.6), a sum of multiple Arrhenius equations can be used to describe k (e.g., CO + OH ⇄ CO_2 + H [8]). Pressure dependence of the rate constant can also be considered (see pgs. 67-74 of Law [6]).

Sensitivity analysis is a useful tool for identifying the most-important reactions for a specific species (see pgs. 116-120 of Steinfeld et al. [5]). The normalized sensitivity coefficient S_{ij} can be defined as

$$S_{ij} = \frac{A_i}{X_j}\frac{\partial X_j}{\partial A_i}, \tag{5.7}$$

where A_i is the pre-exponential factor of reaction i and X_j is the mole fraction of species j. A positive value of S_{ij} implies that increasing A_i will increase the mole fraction X_j of the species of interest, while a negative value of S_{ij} implies that decreasing A_i will decrease X_j. The partial derivative in Eq. (5.7) holds all other variables constant and is therefore calculated at a specific time, but S_{ij} will change with time as the system evolves. The Chemkin definition of S_{ij} is slightly different (see Ch. 16 of [9]), but the trends and implications are unchanged from those described here.

5.2.2 Numerical solution techniques

By writing equations in the form of Eq. (5.4) and accounting for every species and reaction in a chemical system, the time dependence of a chemical kinetic system can be expressed as a system of differential equations that are first-order in time. Additionally, the conservation of mass and energy are considered. In principle, this is simple to solve. In

practice, there are complications involved, and several numerical algorithms have been developed to address these complications. In this dissertation, the Chemkin software package was used for all kinetics computations. All mechanism predictions were calculated in Chemkin via the Closed Homogenous Batch Reactor using the constant-energy, constant-volume assumption. For highly dilute mixtures such as Mixes 1-4, the constant-pressure assumption yields nearly identical predictions to the constant-volume assumption.

When modeling the H_2O profiles, predictions were performed using the volume time-history method, as described by Chaos and Dryer [10]. This method accounts for slight, non-ideal dP/dt effects by super-imposing a time-varying volume profile upon the model conditions. The volume time history is specified by the experimental $P(t)$ trace and by assuming isentropic compression, such that the time-varying volume $V(t)$ is

$$\frac{V(t)}{V_0} = \left(\frac{P(t)}{P_0}\right)^{-\frac{1}{\gamma}}, \tag{5.8}$$

where V_0 and P_0 are the initial volume and pressure, respectively. When calculating $V(t)$ for input to Chemkin, the ratio of specific heats γ was assumed to be that for Ar, 1.667. The value of V_0 is inconsequential to the Chemkin input; it is only the relative change in $V(t)$ that is important. All model predictions for the H_2O experiments were simulated with the average dP/dt across all H_2O experiments herein of 2.4%/ms.

The mechanisms used were those of Zhang et al. [11], Mathieu et al. [12], GRI 3.0 [13], and Glarborg et al. [14]. The Zhang et al. mechanism was modified slightly to incorporate the two minor changes proposed recently by Mulvihill et al. [4, 15]. The Glarborg et al. mechanism includes two low-pressure limit expressions for NO + O + M

⇆ NO_2 + M: one from the review by Tsang and Herron [16] for M = N_2 and one from the measurements by Yarwood et al. [17] for M = Ar. The expression for M = Ar is 1.2 and 1.6 times greater than that for M = N_2 at the low- and high-temperature ends of this study, respectively. By default, the Glarborg et al. mechanism uses the M = N_2 expression. The present work instead utilized the M = Ar expression. The Mathieu et al. and GRI 3.0 mechanisms were used without any modifications.

5.2.3 Updates to OH-quenching reactions*

A key aspect of any OH* sub-mechanism is the set of quenching reactions and corresponding rate constants involved in the mechanism. As discussed in Sect. 3.4, much work has been performed on measuring the quenching of various electronic states by various collisional partners across a range of temperatures. In the present work, several updates were made to the OH*-quenching reactions and rate constants, including three new species which, to the best of the author's knowledge, have not been previously considered in any OH* mechanisms.

The first update was to the OH*-quenching rate constant for Ar. The OH* sub-mechanism by Kathrotia et al. [18] developed an Ar-quenching rate constant by fitting the high-temperature data of Paul et al. [19], as shown in Fig. 5.5(a). However, the fit by Kathrotia et al. is not consistent with the room-temperature data of Becker et al. [20] (Fig. 5.5(a)). A new fit, shown as the solid line in Fig. 5.5(a), was adopted to take into account both of these datasets by selecting the appropriate Arrhenius parameters to fit the data. Using a similar methodology, literature data on OH* quenching by NO, NH_3, and N_2O across a range of temperatures were assembled and are plotted in Figs. 5.5(b-d). Best-fit

Arrhenius parameters were determined for each quenching partner, and the values of the rate constants are plotted as solid lines in Fig. 5.5. The general trends of the best-fit Arrhenius parameters (n = 0.5, E_a<0) followed the harpooned collisional complex model of Paul [21]. The rate constants for quenching by other collisional partners (H, H_2, H_2O, N_2, OH, O_2) were taken from Tamura et al. [22]. The rate constant for OH* spontaneous emission was taken from Dimpfl and Kinsey [23]. The Arrhenius parameters for all quenching reactions are provided in Sect. 5.4.2 along with the full OH* sub-mechanism.

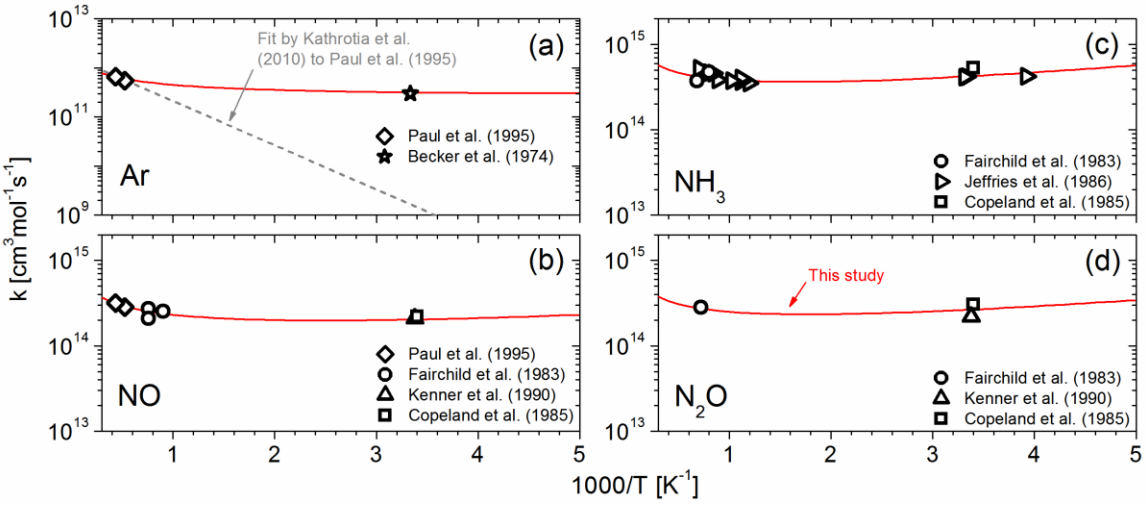

Figure 5.5 Rate constants for quenching of the OH $A\,^2\Sigma^+$ state by (a) Ar, (b) NO, (c) NH_3, and (d) N_2O. Symbols: literature data, solid lines: fits used in this study, dashed line: fit used by Kathrotia et al. [18]. Data are from Paul et al. [19], Becker et al. [20], Fairchild et al. [24], Kenner et al. [25], Copeland et al. [26] (rotational quantum number N = 0), and Jeffries et al. [27].

5.3 H_2O time histories and modeling

H_2O absorption measurements were carried out in Mixes 1-3 over a T_5 range of 917 to 1782 K near 1 atm. In this subsection, several representative H_2O time histories are first presented along with plots of a timing-related parameter extracted from the time histories.

Model predictions from four mechanisms are also shown alongside the data. Reaction pathway analyses at fuel-lean and fuel-rich conditions are then discussed, followed by a sensitivity analysis at similar conditions. The discrepancies observed between the experiments and model predictions in Mixes 2 and 3 at colder temperatures are briefly discussed. Finally, the process used to identify and correct the interfering NO_2 absorption in Mix 1 is outlined.

5.3.1 H_2O time histories

A total of 21 H_2O absorption experiments were performed across Mixes 1-3. A set of 12 H_2O time histories are displayed in Fig. 5.6 and all display similar trends: immediately following the passage of the reflected shock wave, H_2O begins to form at a temperature- and mixture-dependent rate before eventually achieving a plateau level for the hotter experiments.

Also shown in each panel of Fig. 5.6 are the modeled H_2O profiles predicted by four chemical kinetic mechanisms: those of Zhang et al. [11], Mathieu et al. [12], GRI 3.0 [13], and Glarborg et al. [14]. In general, the GRI 3.0 mechanism is under-reactive, predicting H_2O formation that is slower than the experimental data. The H_2O formation predicted by the Mathieu et al. mechanism is generally a bit faster than that of GRI 3.0 but is still quite a bit slower than the data. The Zhang et al. and Glarborg et al. mechanisms do a fair job of predicting the experimental data except at the coldest temperatures for Mix 2 and Mix 3, where the predicted H_2O formation at the end of the experiment is ~30% and ~80% of the experimental value, respectively.

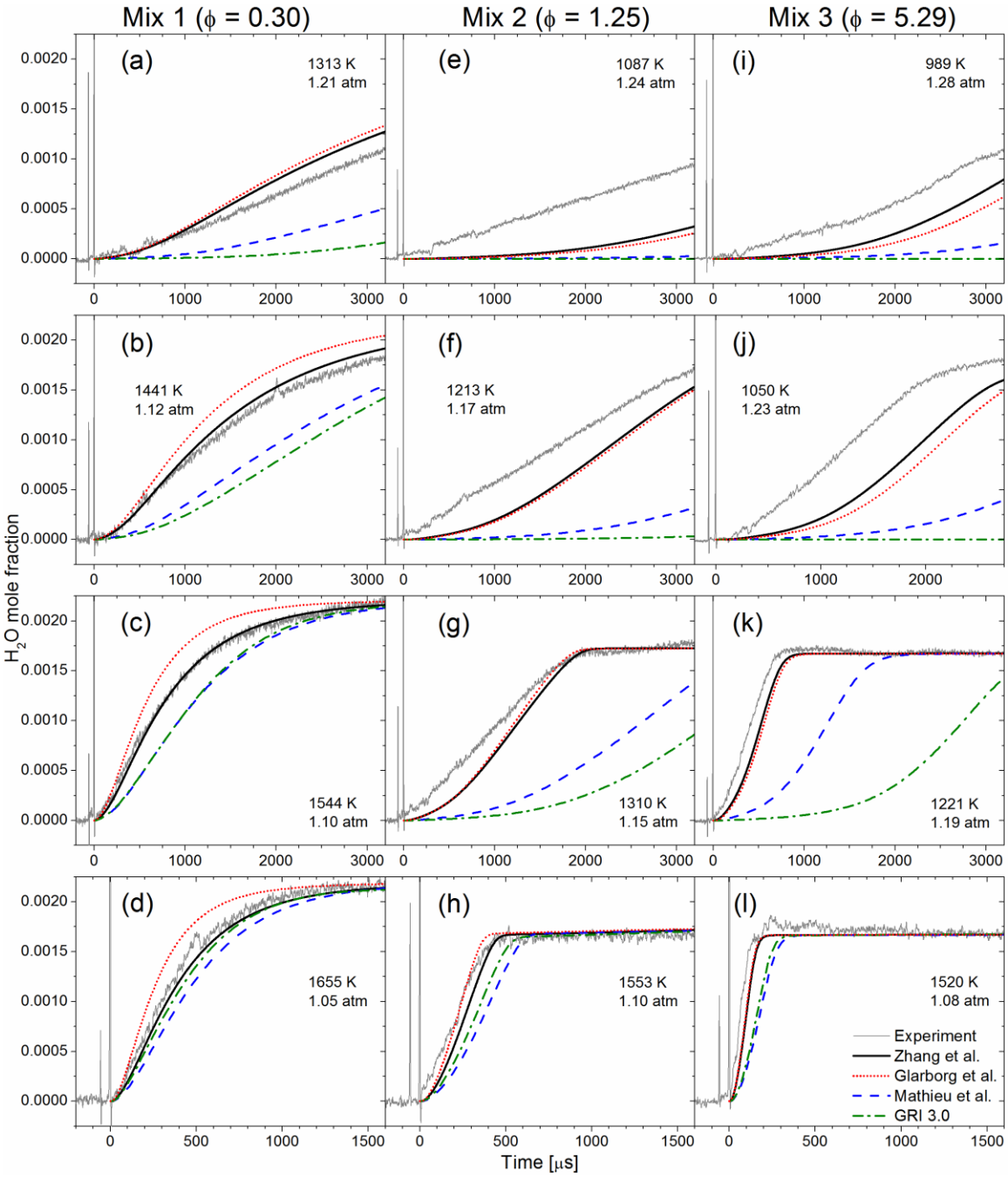

Figure 5.6 Representative H_2O time histories measured in (a-d) Mix 1, (e-h) Mix 2, and (i-l) Mix 3 compared to the results of several chemical kinetics mechanisms. Thick solid lines: Zhang et al. [11], dashed lines: Mathieu et al. [12], dash-dot lines: GRI 3.0 [13], dotted lines: Glarborg et al. [14] The Mix 1 data have been slightly corrected for NO_2 interference (see Sect. 5.3.6). Adapted with permission from [1].

The general trends noted for Fig. 5.6 are further illustrated in Fig. 5.7, which shows the time required to reach half of the maximum H_2O value possible for the mixture in question (assuming as before that only one of the O atoms from NO_2 is free to form H_2O) versus the inverse temperature. As was also evident in Fig. 5.6, the Zhang et al. and Glarborg et al. mechanisms perform the best overall in Fig. 5.7, performing particularly well in the fuel-lean case and at higher temperatures.

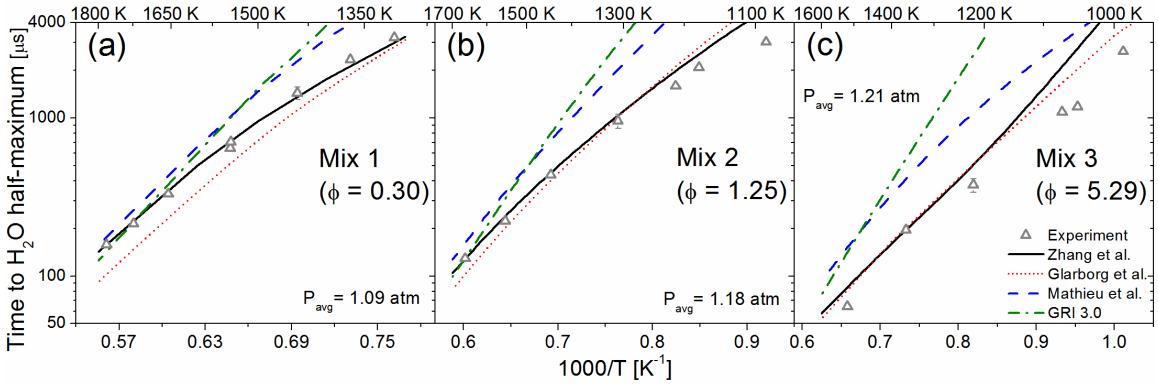

Figure 5.7 Arrhenius plot of the time to half the maximum possible H_2O for (a) Mix 1, (b) Mix 2, and (c) Mix 3. The estimated *y* axis uncertainty is ±10%. Thick solid lines: Zhang et al. [11], dashed lines: Mathieu et al. [12], dash-dot lines: GRI 3.0 [13], dotted lines: Glarborg et al. [14]. The Mix 1 data points correspond to the NO_2-corrected data. Adapted with permission from [1].

5.3.2 Reaction pathway analysis at fuel-lean conditions

To explore the important routes of H_2O formation and the promoting effect of NO_2, a reaction pathway analysis was performed using the Zhang et al. mechanism in Mix 1 (ϕ = 0.30) at 1441 K, 1.12 atm (i.e., the conditions of Fig. 5.6(b)). This analysis revealed that during the first ~50 μs, NO_2 decomposition takes place primarily through the reaction

$$2NO_2 \leftrightarrows NO_3 + NO. \qquad \text{(R1)}$$

Although the NO produced by R1 can be viewed as a stable product at the timescales of the current experiments, the NO_3 is immediately recycled to NO_2 via

$$NO_3 + M \leftrightarrows NO_2 + O + M. \quad \text{(R-2)}$$

Thus, the sequence of R1 and R-2 ultimately produces one O atom and one NO molecule from one NO_2 molecule. NO_2 decomposition also takes place during the initial ~5 μs due to

$$NO_2 + M \leftrightarrows NO + O + M, \quad \text{(R-3)}$$

but this reaction rapidly becomes less important in favor of NO_2 consumption by the O atoms produced by R-2 and, to a smaller extent, R-3 through the reaction

$$NO_2 + O \leftrightarrows NO + O_2. \quad \text{(R4)}$$

R-2 and R-3 are written here in the backward direction relative to their notation in three mechanisms considered herein, save that GRI 3.0 does not contain R-2.

NO_2 is also attacked by H_2 via

$$NO_2 + H_2 \leftrightarrows HONO + H. \quad \text{(R5)}$$

This channel is relatively minor in the fuel-lean mixture but is discussed in more detail for

fuel-rich conditions (Sect. 5.3.3).

The O atoms formed by R-2 and R-3 are primarily consumed by R4. However, a small portion of the O atoms (~10% during the initial ~20 μs) react with H_2 in the chain-branching reaction

$$H_2 + O \leftrightarrows H + OH. \quad \text{(R6)}$$

The role of R6 is critical in two regards. First, it supplies OH radicals, which can react with H_2 via

$$H_2 + OH \leftrightarrows H + H_2O, \quad \text{(R7)}$$

which is the dominant pathway of H_2O formation in all 3 mixtures. The second role of R6 is the formation of an H atom, which is then free to react with NO_2:

$$NO_2 + H \leftrightarrows NO + OH. \quad \text{(R8)}$$

R8 produces OH, which can then react via R7 to form further H_2O and H, thereby establishing a catalytic cycle between R7 and R8.

The HO_2 radical also plays a noticeable role in H_2-NO_2 chemistry. Throughout the entirety of the experimental timescales considered, HO_2 is produced almost exclusively via

$$NO_2 + OH \leftrightarrows HO_2 + NO \quad \text{(R-9)}$$

and proceeds to react with OH atoms via

$$HO_2 + OH \leftrightarrows H_2O + O_2. \quad \text{(R10)}$$

Although the sequence R-9 and R10 does ultimately produce H_2O, it does so by consuming two OH radicals, thus inhibiting the overall reactivity of the mixture by competing with R7 for OH. R-9 is written here in the backward direction from its notation in the mechanisms.

5.3.3 Reaction pathway analysis at fuel-rich conditions

An additional reaction pathway analysis was conducted using the Zhang et al.[11] mechanism in Mix 3 (ϕ = 5.29) at 1050 K, 1.23 atm (i.e., the conditions of Fig. 5.6(j)). Many of the key reactions for fuel-lean conditions were still found to play a role. However, R5 becomes a much more significant pathway at fuel-rich conditions partly due to increased H_2 concentration, accounting for ~20% of the NO_2 consumption of R1 and providing a direct route for H-atom formation. These H atoms can then react with NO_2 via R8 to strengthen the catalytic cycle between R7 and R8.

Another reaction between NO_2 and H_2,

$$NO_2 + H_2 \leftrightarrows HNO_2 + H, \quad \text{(R11)}$$

becomes more important at fuel-rich conditions, producing H atoms at ~10% of the rate of R5. Furthermore, the HNO_2 formed by R11 immediately isomerizes to HONO, and a portion of the HONO produced by R5 and ultimately by R11 can decompose via

$$HONO + M \leftrightarrows OH + NO + M \quad \text{(R-12)}$$

to further supply R7 with OH radicals. R-12 is written here in the backward direction from its notation in the mechanisms, save that GRI 3.0 does not contain R-12.

Finally, the fuel-rich mixture (Mix 3) was tested at lower temperatures as it was more reactive than the fuel-lean mixture (Mix 1) due to the influence of R5 and R11. These lower temperatures generally caused the NO_2 consumption via R1 and R2 to take place at a much slower rate, meaning that O atoms were generally less available and less critical to the overall reaction for fuel-rich conditions.

5.3.4 Sensitivity analysis

To better understand the differences between the mechanism predictions, comparative H_2O sensitivity analyses were conducted with all four mechanisms in all three mixtures, and the results for two of the mixtures are shown in Fig. 5.8. The analyses were performed at a fixed time of 500 μs after the reflected shock wave. Not shown in Fig. 5.8 are the results of Mix 2 as they were intermediates of the results for Mix 1 and Mix 3. The results of the Glarborg et al. mechanism [14] were nearly identical to those of the Zhang et al. mechanism [11] and are not shown in Fig. 5.8.

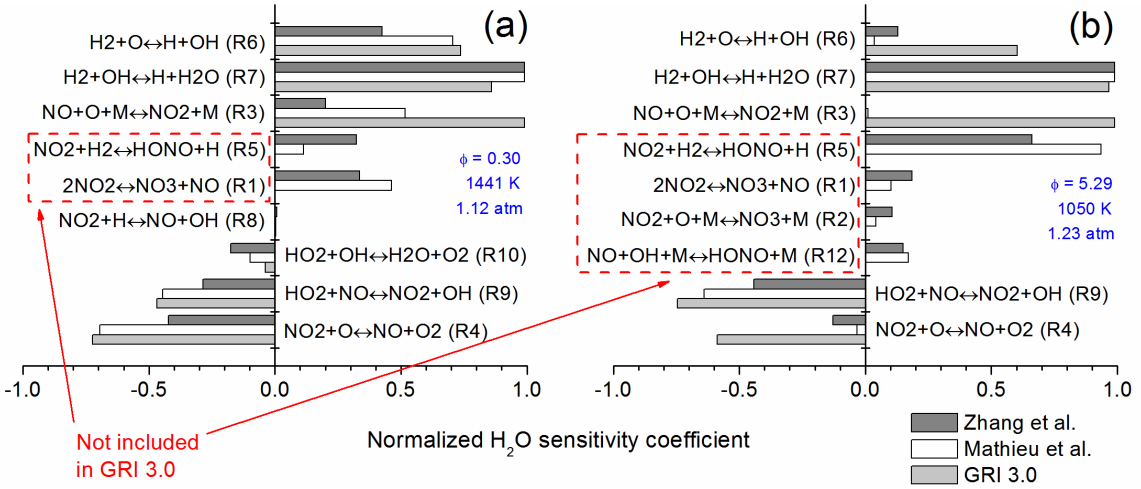

Figure 5.8 Normalized H_2O sensitivity coefficients at conditions corresponding to (a) Fig. 5.6(b) and (b) Fig. 5.6(j). Analysis was performed at 500 µs after the reflected shock wave using Zhang et al. [11], Mathieu et al. [12], and GRI 3.0 [13]. Adapted with permission from [1].

Figure 5.8 illuminates several differences between the fuel-lean and fuel-rich cases discussed during the reaction pathway analysis for the results using the Zhang et al. mechanism. For example, the NO_2 decomposition reaction R-3 was negligible for both Zhang et al. and Mathieu et al. for fuel-rich conditions. Additionally, the reduced O-atom concentration at fuel-rich conditions caused a reduced sensitivity to R6 relative to the fuel-lean case.

Highlighted in Fig. 5.8 are several reactions that are absent from GRI 3.0. These missing reactions explain a large part of the general inability of GRI 3.0 to accurately reproduce the experimental data. First, GRI 3.0 does not contain the species NO_3, meaning it is missing the key NO_2 decomposition pathway of R1 and the subsequent O-producing reaction R-2. This absence is particularly marked at fuel-lean conditions but also plays a role at fuel-rich conditions. Second, GRI 3.0 does not contain HONO, which plays a key role through the R5 and R11 pathways of H-atom production. The absence of these

reactions and key species in GRI 3.0 leads to an overdependence on the NO_2 decomposition pathway R-3, which is far too slow to reproduce the experimental data, particularly at lower temperatures. Of course, the inability of GRI 3.0 to reproduce these data is not particularly surprising since GRI 3.0 was developed for more common systems (e.g., natural gas in air).

In general, the Mathieu et al. mechanism outperforms GRI 3.0 (except for slight differences at the high-temperature end of the experiments) but is still noticeably less reactive than both the Zhang et al. mechanism and the experimental data. Since the Mathieu et al. and Zhang et al. mechanisms contain the same key species NO_3 and HONO, the differences between the two mechanisms arise from the reaction rates employed in each. For example, Zhang et al. used k_1 from Tsang and Herron [16], while Mathieu et al. used k_1 from Konnov [28]. The Tsang and Herron value of k_1 is ~60% faster than the Konnov value at the high-temperature end of this study (~1660 K) and over 7 times faster at the low-temperature end (~915 K). The smaller value of k_1 from Konnov partially explains the less-reactive nature of the Mathieu et al. mechanism. Additionally, k_5 used by Zhang et al. is ~12 times faster than that used by Mathieu et al. at the high-temperature end of this study and ~2.4 times faster at the low-temperature end, which further explains the differences between the two mechanisms (see Sect. 5.3.5 for more on R5).

5.3.5 Initial H_2O formation

A consistent discrepancy between the models and the data is apparent in Fig. 5.6 for the near stoichiometric and fuel-rich conditions (Mixes 2 and 3), where the experimental data reveal a much faster rate of H_2O formation immediately after the reflected shock wave than do the model predictions. A sensitivity analysis was performed

using the mechanism of Zhang et al. at the conditions of Fig. 5.6(f). This analysis revealed that the two dominant reactions at early times (< 100 μs) are R5 and R7. Zhang et al. (as well as Glarborg et al.) used k_5 from the theoretical work of Chai and Goldsmith [29], who only provided an uncertainty estimate for their activation energy (±1.5 kcal/mol). An uncertainty factor of 1.5 was assumed for k_5. An uncertainty factor of 1.5 for k_7 was taken from the review by Baulch et al. [30]. Figure 5.9 shows the effects of independently increasing k_5 and k_7 by these uncertainty factors. Even with these changes, the initial predicted H_2O formation is still much slower than the experimental data; nearly identical results were obtained when performing the same analysis with the Glarborg et al. mechanism. At this point, it remains unclear as to what could be causing the discrepancy between the experiments and models in the fuel-lean and fuel-rich mixtures at lower temperatures. Further work, such as the possible addition of a new reaction pathway, is needed to address this issue.

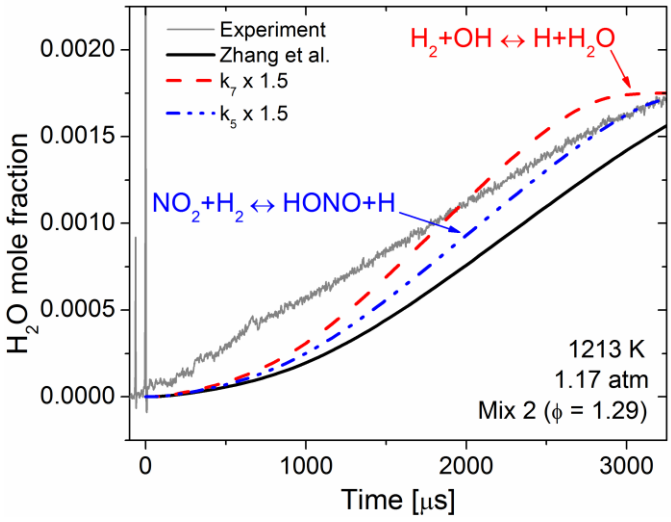

Figure 5.9 H_2O time history at the conditions of Fig. 5.6(f) alongside model predictions from Zhang et al. [11] with variations in k_7 and k_5. Thick solid line: unmodified mechanism, dashed line: $k_7 \times 1.5$, dash-dot-dot line: $k_5 \times 1.5$.

Adapted with permission from [1].

5.3.6 Interfering absorption from NO_2

In the fuel-lean mixture (Mix 1), a small amount of absorption was observed immediately behind the reflected shock wave, and this absorption increased with increasing T_5. The cause of this immediate baseline shift was not broadband emission entering the I_t detector, as such emission was found to be negligible even at the highest temperatures by performing tests with the laser turned off; see Fig. 4.10. Furthermore, broadband emission would create an apparent decrease in absorption rather than an increase (see Sect. 4.2.5). Instead, it was determined that the small amount of initial absorption was due to interfering absorption by another species. This interference was discovered by performing an offline laser test, in which the laser was tuned to 1388.104 nm to sit in a region of low H_2O absorption, as determined by the spectral modeling in Fig. 4.11. The results of the offline laser test are shown in Fig. 5.10 alongside an online test at similar conditions. The markedly different shapes of the absorption time histories from the online and offline tests strongly suggest the initial absorption at time zero was due to some species other than H_2O. To demonstrate the result of correcting for such interference, the offline absorption was subtracted from the online absorption to yield a corrected absorption time history, which is also shown in Fig. 5.10. The interference has a small effect at early times and becomes negligible at later times.

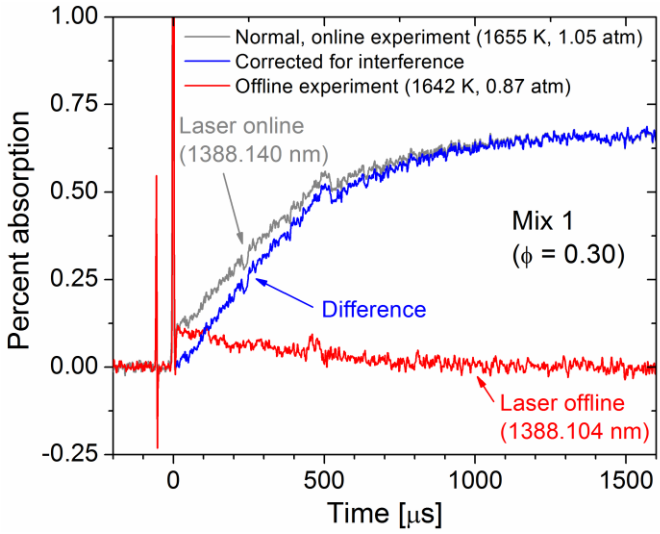

Figure 5.10 Offline and online laser tests in Mix 1 at similar conditions. The online test corresponds to the conditions of Fig. 5.6(d). Also shown is the difference between the online and offline tests. Adapted with permission from [1].

The obvious candidate for the interfering species is NO_2 since it is present in the initial mixture and is also infrared-active due to its permanent dipole moment, unlike H_2 and Ar. An additional offline shock experiment with a mixture of NO_2/Ar was performed, which is shown in Fig. 5.11. This H_2-free experiment yielded a nearly identical shape to the offline test in Fig. 5.10. Furthermore, the time-history shapes from both Fig. 5.10 and Fig. 5.11 closely matched the predicted shapes for NO_2 decay predicted by the Zhang et al. mechanism, which is shown as the solid black line in Fig. 5.11. These observations together confirmed that NO_2 was the interfering species.

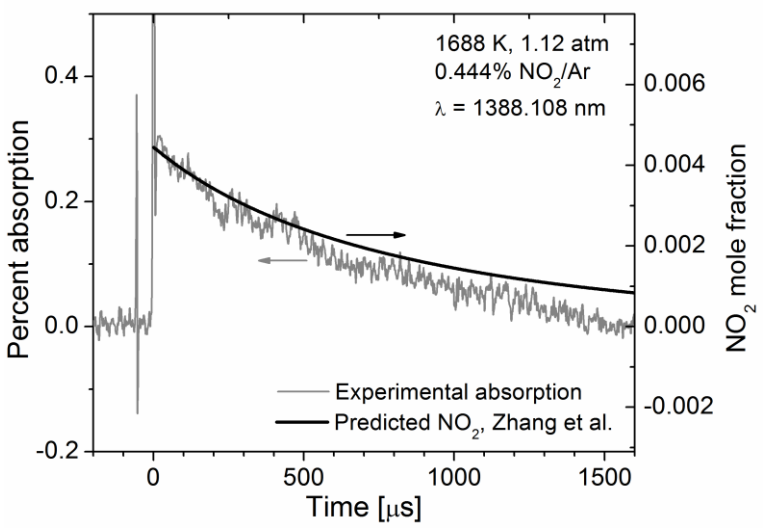

Figure 5.11 Absorption time history in a mixture of 0.444% NO_2/Ar with the laser tuned offline to 1388.108 nm. The solid black line is the NO_2 time history predicted by the Zhang et al. mechanism [11]. Adapted with permission from [1].

The initial absorption immediately after the reflected shock wave was recorded for all experiments performed using Mix 1. Using the known value of the NO_2 mole fraction in Mix 1, 0.375%, the NO_2 absorption coefficient was determined for each experiment. The variation of the absorption coefficient with temperature is shown in Fig. 5.12. Interestingly, HITRAN 2004 [31] does not predict any NO_2 absorption in this region. The nearly linear increase of the NO_2 absorption coefficient with temperature in Fig. 5.12 suggests the NO_2 absorption may stem from a hot band. HITRAN 2004 is designed for lower temperatures and was found by Mulvihill and Petersen [32] to be highly inaccurate in predicting the hot bands of CO_2 near 2190 cm^{-1}. Absorption coefficients in the hot bands of CO_2 displayed a similar temperature trend to that displayed in Fig. 5.12. The NO_2 absorption appears to be somewhat broad in this spectral region, as measurements at 1388.104, 1388.108, and 1388.140 nm all indicated similar values of the NO_2 absorption coefficient.

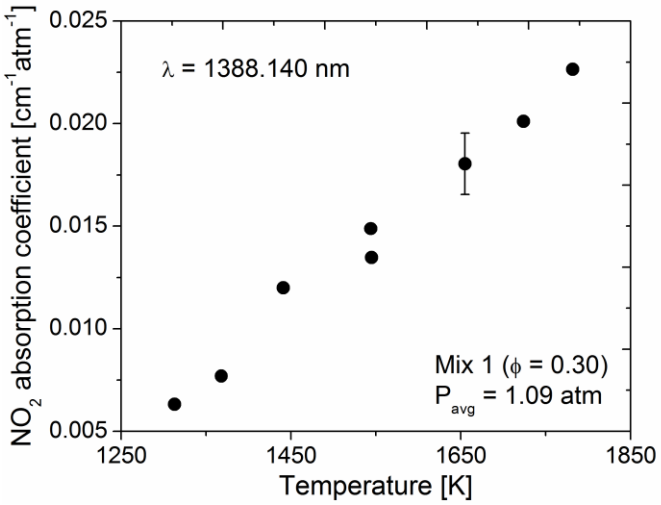

Figure 5.12 NO_2 absorption coefficients versus temperature at 1388.140 nm, derived from the initial level of absorption immediately after the reflected shock wave in the Mix 1 experiments using the known value of 0.375% NO_2. Adapted with permission from [1].

In keeping with the conclusion that the interference was from NO_2, the following method was used to make slight corrections to the data for Mix 1. The initial absorption at time zero was used to calculate an effective NO_2 absorption coefficient (Fig. 5.12). The NO_2 time history predicted by the Zhang et al. mechanism was then used in conjunction with this effective absorption coefficient to subtract out the portion of the absorption time history corresponding to NO_2 interference, with the balance being attributed to H_2O. This correction decreased with temperature; the experiment shown in Figs. 5.6(d) and 5.10 is the worst-case scenario for which the NO_2 correction is a maximum. The Mix 1 data shown in Figs. 5.6 and 5.7 have all been NO_2 corrected. The NO_2 correction was not applied to Mix 2 or Mix 3 because no definitive signs of NO_2 interference at time zero were observed for these mixtures. The lack of NO_2 interference in Mix 2 and Mix 3 was due to the lower NO_2 content in these mixtures and the lower temperatures at which these mixtures were tested.

5.4 OH* time histories and modeling

In addition to the H_2O absorption measurements carried out in Mixes 1-3, a series of OH* measurements were performed in Mix 4 (ϕ = 0.28) between 1535 and 2003 K near 1 atm. These measurements were then modeled using two chemical kinetic measurements. A new chemiluminescent reaction,

$$NH + NO_2 \leftrightarrows N_2O + OH^* \quad \text{(R13)}$$

was necessary to model the experimental OH* data. Two other well-known chemiluminescent reactions,

$$N_2O + H \leftrightarrows N_2 + OH^* \quad \text{(R14)}$$

$$O + H + M \leftrightarrows OH^* + M \quad \text{(R15)}$$

were also included in the OH* sub-mechanism, although they had a relatively minor role in producing OH* in this H_2-NO_2 mixture. The importance of both R14 [33-37] and R15 [18, 38-40] to the modeling of OH* have been experimentally confirmed on multiple occasions, primarily in H_2-O_2 and H_2-NO_2 mixtures.

In this subsection, experimental OH* time histories are first presented along with peak- and timing-related parameters extracted from the profiles. Modeling predictions are also shown alongside the data. Next, the process of identifying R13 and fitting k_{13} is described, as is the adjustment of k_{14} to fit literature data. The mechanism-dependent nature of such deriving chemiluminescent reaction rates is then discussed. Finally, a brief

discussion is given on the screening process for identifying potential chemiluminescent reactions based on energetic considerations.

5.4.1 OH time histories*

Figure 5.13 shows several normalized OH* profiles obtained in Mix 4. The OH* profiles exhibit an immediate rise followed by a peak and then a gradual decay. The timing of the peak varies relatively little with T_5 but the value of $\tau_{50\%}$ (defined in Sect. 4.3.2) is a marked function of temperature. The dashed lines in Fig. 5.13 indicate predictions of the Glarborg et al. mechanism [14] supplemented with the current OH* sub-mechanism but without R13 included. These predictions exhibit large deficiencies, particularly at higher temperatures. However, when R13 is included in the model (solid lines), the predictions are strikingly improved. The presence/absence of R14 in the mechanism had no effect on the predictions since there is a negligible amount of N_2O produced in this mixture.

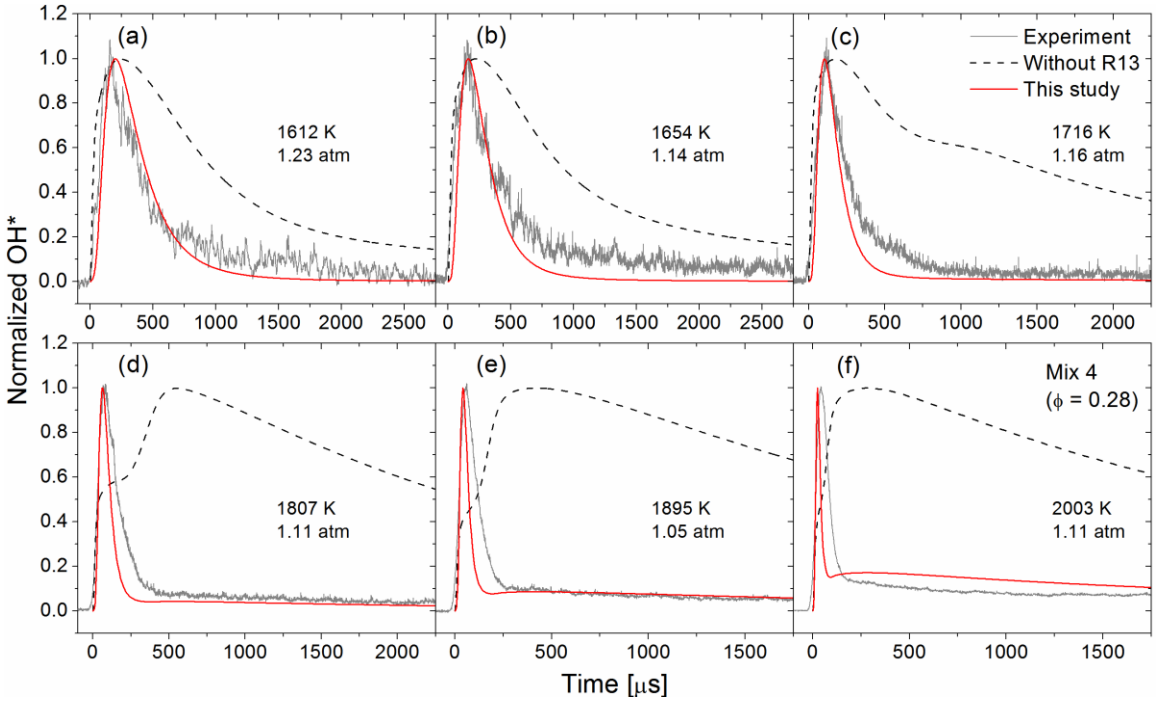

Figure 5.13 Normalized OH* profiles in Mix 4 at various temperatures. Thick solid lines: [14] plus the OH* sub-mechanism of this study, dashed lines: [14] plus this study with R13 removed.

Figure 5.14(a) shows the peak OH* values obtained in Mix 4 as a function of temperature. Since an absolute OH* calibration was not performed in this study, the peak OH* values were normalized to the hottest run (2003 K). To ensure accurate relative OH* values, the peak PMT voltages were scaled according to the PMT gain versus supply voltage behavior (Fig. 4.14), and care was taken to ensure that the optical setup remained undisturbed during these tests. Figure 5.14(b) shows $\tau_{50\%}$ as a function of temperature for the same tests in Mix 4, as well as the same model predictions shown in Fig. 5.13. The peak OH* values are moderately improved by the addition of R13, while the $\tau_{50\%}$ values are significantly improved, particularly at higher temperatures. Since quantitative observations are masked by normalization in Fig. 5.14(a), it is worth noting that the

predicted absolute peak OH* values of the solid line are ~20 times higher than those of the dashed line at the high-temperature extreme.

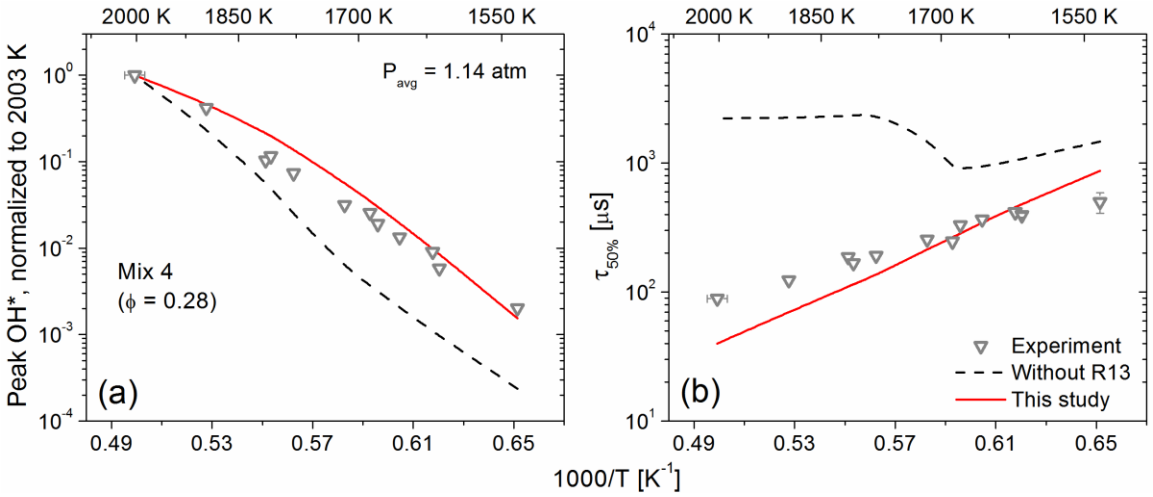

Figure 5.14 Arrhenius plots of (a) normalized peak OH* and (b) $\tau_{50\%}$ in Mix 4. Solid lines: [14] plus the OH* sub-mechanism of this study, dashed lines: [14] plus this study with R13 removed. The y-axis uncertainty bars are (a) ±15% and (b) experiment-specific and are smaller than the symbols if not visible.

5.4.2 Identifying a new chemiluminescent reaction

The OH* profiles from Mix 4 (Fig. 5.13) could not be explained by the OH* formation from R14 and R15 alone and suggested a new OH*-forming reaction was needed. To search for such a reaction, a set of 3 criteria was utilized. These criteria stipulated an OH*-forming reaction of the form A + B ⇆ C + OH* should:

(i) Possess a corresponding OH-forming reaction that is exothermic, with a higher preference granted to more-exothermic reactions,
(ii) Yield a multiplicative product of the reactants (i.e., [A][B]) that displays similar shapes to the experimentally observed OH* profiles, and
(iii) Retain a rate coefficient approximately equal to or less than that of the corresponding OH-forming reaction.

Criterion (i) is discussed in more detail in Sect. 5.4.5. Criterion (ii) simply dictates the predictions should match the experimental data in terms of time-history profile shapes. Criterion (iii) is supported by the rates of R14 and R15, which are ~4 and ~3 orders of magnitude slower than their ground-state counterparts, respectively. Criterion (iii) is strongly tied to the shapes of the experimental OH* profiles since R15 produces a small amount of OH*, such that any new OH*-forming reaction must produce a sufficiently large quantity of OH* to surpass the OH* production from R15 and produce the sharper OH* profiles observed experimentally.

To satisfy criterion (i), the heat of reaction $\Delta\bar{H}_R^0$ [kcal/mol] was calculated for every reaction in the H_2-NOx system. The standard-state heat of reaction is defined as

$$\Delta\bar{H}_R^0 = \sum_i \left(N_i\, \bar{h}_{f,i}^0\right)_{prod} - \sum_j \left(N_j \bar{h}_{f,j}^0\right)_{reac}, \tag{5.9}$$

where N represents the stoichiometric coefficients and $\bar{h}_f^0$ [kcal/mol] represents the standard-state heat of formation for the reactant i or product j. Table 5.2 shows $\Delta\bar{H}_R^0$ for the 10 most-exothermic OH-forming reactions that involve N in the H_2-NOx system. The values in Table 5.2 were calculated using the thermochemistry sets of Glarborg et al. [14] and Zhang et al. [11]; the results from the two mechanisms generally agree to within < 1 kcal/mol.

Table 5.2 $\Delta\bar{H}_R^0$ for N-containing reactions that produce OH with $\Delta\bar{H}_R^0$ < -50 kcal/mol.

Reaction	Glarborg et al. [14]	Zhang et al. [11]	Difference
NNH + O ⇆ N_2 + OH	-110.3	-110.9	0.6
NH + NO ⇆ N_2 + OH	-98.6	-97.8	-0.8
HON + O ⇆ NO + OH	-- [a]	-80.1	--
NH + NO_2 ⇆ N_2O + OH	-65.2	-63.6	-1.6
N_2O + H ⇆ N_2 + OH	-62.9	-62.9	0.0
H_2NN + O ⇆ NNH + OH	-62.8	-62.8	0.0
N_2H_3 + O ⇆ N_2H_2 + OH	-56.5	-55.9	-0.6
NH + O_2 ⇆ NO + OH	-55.0	-54.5	-0.5
HNO + O ⇆ NO + OH	-54.4	-54.8	0.4
NO_3 + H ⇆ NO_2 + OH	-52.7	-55.2	2.5

[a] This reaction is not included in the Glarborg et al. mechanism.

To satisfy criterion (ii), the product [A][B] for each of the exothermic OH-forming reactions was assessed using the Glarborg et al. mechanism [14]. Out of the 10 reactions in Table 5.2, only the reaction

$$NH + NO_2 \leftrightarrows N_2O + OH^* \quad \text{(R13)}$$

produced [A][B] profile shapes that closely resembled the experimental OH* profiles. The rate of R13 was then adjusted to match the modeled OH* profiles with the experimental data. The magnitude of the pre-exponential factor A was primarily determined by agreement with the shapes of the OH* profiles. The effect of varying k_{13} on the agreement between the model and the data can be seen in Fig. 5.15. It can also be seen in Fig. 5.15 that R14 has a negligible effect on the predictions for the H_2-NO_2 mixture. The activation energy E_a was primarily determined by agreement with the slope of the normalized peak

OH* data (Fig. 5.14(a)). The best-fit expression for k_{13} was k_{13} = 5.0×10^{16}·exp(-40,000/RT), with k_{13} in [cm^3/(mol·s)]and T in [K]. This expression for k_{13} remains a factor of 2-50 below the ground-state rate for this reaction, thus satisfying criterion (iii), at least in the temperature range of this study. The accepted rate constant for the ground-state reaction NH + NO_2 ⇆ N_2O + OH is a constant value of 4.1×10^{12} cm^3/(mol·s), based on NH fluorescence decay rates in the presence of NO following photolysis of N_2H_4 as performed by Harrison et al. [41] between 270 and 380 K.

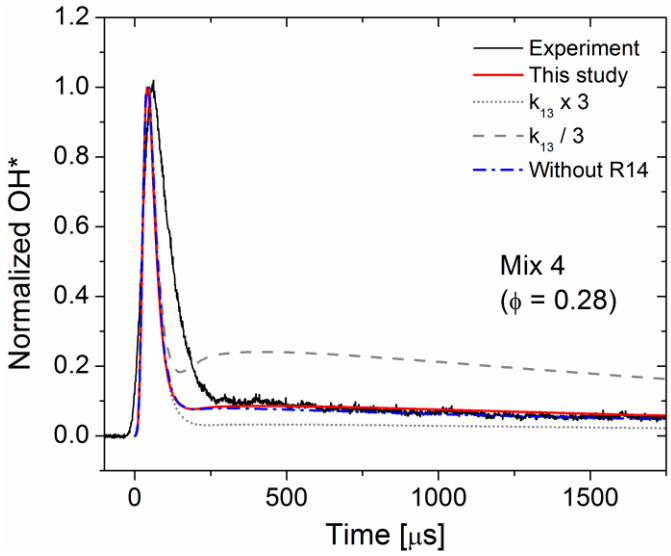

Figure 5.15 Effects of varying k_{13} and removing R14. Conditions are 1895 K, 1.05 atm. Model predictions calculated using Glarborg et al. [14] plus the OH* sub-mechanism of this study, with the changes indicated in the legend.

Several other reactions displayed potential for satisfying all three criteria. The reaction H_2NN + O ⇆ NNH + OH is nearly as exothermic as R13 and produced predicted [A][B] profiles that somewhat resembled the experimental OH* profiles. However, the predicted quantities of H_2NN produced were so small that the required H_2NN + O ⇆ NNH

+ OH* rate would have to be ~9 orders of magnitude larger than the ground-state rate to produce OH* profiles in agreement with the experimental profiles. The reaction NO_3 + H ⇆ NO_2 + OH is quite exothermic and required rates of NO_3 + H ⇆ NO_2 + OH* well beneath the ground-state rate. However, the predicted normalized peak [OH*] values using this reaction were in poor agreement with the experiment, as were the predicted OH* profile shapes; future changes to NO_3 chemistry might reveal this reaction is a possible source of OH*. Less-exothermic reactions not shown in Table 5.2 suffered from similar issues and/or were viewed less favorably as they were far less-exothermic than R13. The full OH* sub-mechanism proposed in this study is provided in Table 5.3.

Table 5.3 The OH* sub-mechanism of this work. Units are [cal], [mol], [cm^3], [s].

No.	Reaction	A	n	E_a	Reference
13	NH + NO_2 ⇆ N_2O + OH*	5.00×10^{16}	0	40,000	This study
14	N_2O + H ⇆ N_2 + OH*	1.60×10^{15}	0	50,300	This study
15	O + H + M ⇆ OH* + M	1.50×10^{13}	0	5,975	[18]
16	H + OH* ⇆ H + OH	1.31×10^{13}	0.5	-167	[22]
17	H_2 + OH* ⇆ H_2 + OH	2.95×10^{12}	0.5	-445	[22]
18	H_2O + OH* ⇆ H_2O + OH	5.93×10^{12}	0.5	-862	[22]
19	N_2 + OH* ⇆ N_2 + OH	1.08×10^{11}	0.5	-1,240	[22]
20	OH + OH* ⇆ OH + OH	6.01×10^{12}	0.5	-763	[22]
21	O_2 + OH* ⇆ O_2 + OH	2.10×10^{12}	0.5	-483	[22]
22	Ar + OH* ⇆ Ar + OH	1.30×10^{10}	0.5	-199	This study
23	NH_3 + OH* ⇆ NH_3 + OH	9.00×10^{12}	0.5	-596	This study
24	N_2O + OH* ⇆ N_2O + OH	6.00×10^{12}	0.5	-556	This study
25	NO + OH* ⇆ NO + OH	6.00×10^{12}	0.5	-397	This study
26	OH* ⇆ OH	1.45×10^{6}	0	0	[23]

5.4.3 Modifications to k_{14}

The addition of R13 to the OH* sub-mechanism was found to have a significant effect on modeling OH* time histories in the H_2-N_2O system. The explanation for this observation is that in the presence of sufficient quantities of N_2O, the reverse reaction R-1 becomes dominant such that R1 actually serves as a sink of OH*, thereby altering the shapes of the predicted OH* profiles in H_2-N_2O mixtures. A demonstration of the effect of R13 on modeling the H_2-N_2O system is shown in Fig. 5.16, which displays the quantitative peak OH* shock-tube data from Hidaka et al. [34] obtained in three H_2-N_2O mixtures. The predictions of the current mechanism when the Hidaka et al. value of k_{14} was used are roughly an order of magnitude too low, as shown in Fig. 5.16. To resolve the discrepancy in Fig. 5.16, the current study tentatively proposes a value of k_{14} that is 10 times that of Hidaka et al., which brings the model predictions to within less than a factor of 3 of the OH* data of Hidaka et al.

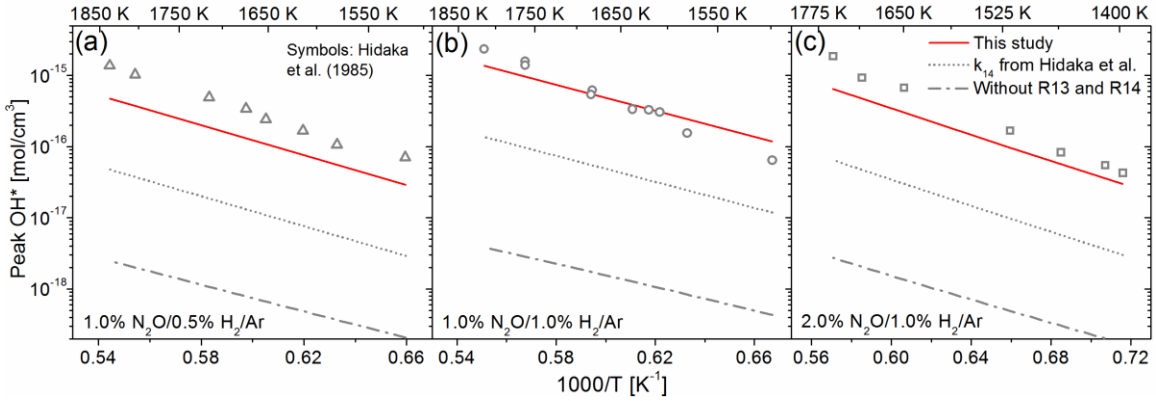

Figure 5.16 Quantitative OH* levels from Hidaka et al. [34] in (a) 1.0% N_2O, 0.5% H_2, (b) 1.0% N_2O, 1.0% H_2, and (c) 2.0% N_2O, 1.0% H_2, all in balance Ar. Symbols: experiments, solid lines: [14] plus the OH* sub-mechanism of this study, dotted lines: [14] plus this study but with k_2 from Hidaka et al., dash-dot lines: [14] plus this study with R13 and R14 removed. The average pressure was not explicitly given by Hidaka et al.; 2 atm was assumed.

5.4.4 Mechanism-dependent nature of fitting

The k_{13} fitting used Glarborg et al. [14] as the base mechanism. An unavoidable aspect of this fitting is its mechanism-dependent nature. A repeat fitting of k_{13} was performed using Zhang et al. [11] (including the minor modifications of Mulvihill et al. [4, 15]) as the base mechanism. The best-fit value of k_{13} using the Zhang et al. mechanism was an order of magnitude higher than the value obtained with the Glarborg et al. mechanism. This large difference is because the best-fit k_{13} is highly sensitive to the mechanism predictions of absolute NH quantities, which vary by large degrees in both shape and magnitude between the two mechanisms. Of course, slight differences in predictions of NO_2 destruction also contribute to differences between mechanism predictions, but to an inconsequential degree compared to the NH chemistry.

Rate-of-production, sensitivity, and reaction pathway analyses using the mechanism of Glarborg et al. [14] indicated that in Mix 4, NH is primarily produced by NH + O_2 ⇆ HNO + O and NH + OH ⇆ HNO + H (both in reverse) and is primarily consumed by NH + NO ⇆ N_2O + H. The HNO is predominantly produced by HNO + O_2 ⇆ HO_2 + NO (in reverse), where the HO_2 is exclusively produced by the reaction NO + HO_2 ⇆ NO_2 + OH (in reverse). The NH profiles have strong positive sensitivity to NO + O + M ⇆ NO_2 + M and NO + HO_2 ⇆ NO_2 + OH, with strong negative sensitivity to OH + H_2 ⇆ H + H_2O and to O + H_2 ⇆ OH + H. As another example of the sensitivity of the best-fit value of k_{13}, the change to the M = Ar expression for NO + O + M ⇆ NO_2 + M (see Sect. 5.2.2) produced a best-fit k_{13} which was twice the value obtained using M = N_2.

The value of k_{15} proposed by Hall and Petersen [40] was tested during the fitting of k_{13}. This value of k_{15} is 5.4 and 7.5 times greater than the Kathrotia et al. [18] rate at

the low- and high-temperature ends of this study, respectively. Due to the higher amounts of OH* produced in the tails of the predicted profiles, employing the Hall and Petersen value for k_{15} produced a best-fit k_{13} nearly an order of magnitude higher than the best-fit k_{13} obtained using the Kathrotia et al. value for k_{15}. However, this higher value of k_{13} would cause R13 to become an even stronger sink for OH*, requiring an increase in k_{14} even larger than the ×10 increase already proposed to model the OH* data of Hidaka et al. [34]. To keep the proposed change in k_{14} to a minimum, the Kathrotia et al. value of k_{15} was employed.

The purpose of the present work is not to suggest changes to the ground-state reactions surrounding NH chemistry but rather to point out the mechanism-dependent nature of fitting experimental OH* data. This dependence on the ground-state rates used in mechanisms is often disregarded during such fitting efforts but can have quite a large effect on the final outcomes.

5.4.5 Energetic considerations for chemiluminescent reactions

Since at least 1951 [42], a common practice in searching for possible chemiluminescent reactions has been to only consider reactions for which $\Delta\bar{H}_R^0$ of the ground-state form of the reaction exceeds the ΔE associated with the wavelength of the observed chemiluminescence. For emission at wavelength λ, the associated ΔE is given by

$$\Delta E = N_A hc/\lambda. \tag{5.10}$$

Assuming λ = 307 ± 7 nm for the OH $A \rightarrow X$ band, ΔE is 93.2 ± 2.1 kcal/mol. Interestingly,

$\Delta\bar{H}_R^0$ for the ground-state forms of both R13 and R14 are well below this limit, as illustrated in Fig. 5.17 (also see Table 5.2). The presence of R14 has been repeatedly confirmed by previous studies, while R13 is being proposed herein for the first time.

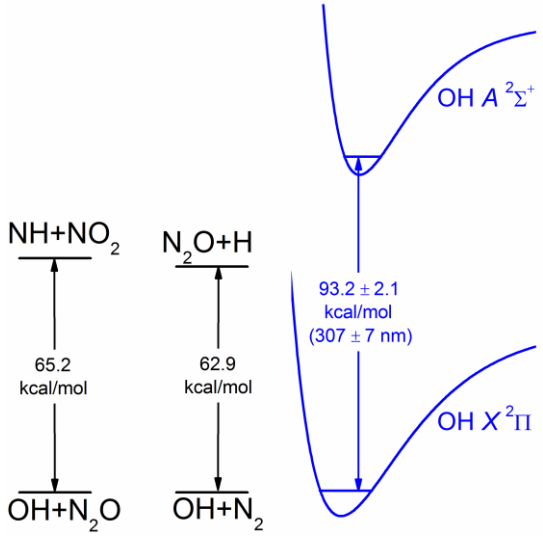

Figure 5.17 Illustrations of $\Delta\bar{H}_R^0$ for the ground-state forms of R13 and R14 alongside an illustration of ΔE for the OH $A\ ^2\Sigma^+ \rightarrow X\ ^2\Pi$ transition (potential energy curves for OH not drawn to scale).

The notion that $\Delta\bar{H}_R^0$ should exceed ΔE follows from simple intuition. However, such a stipulation does not account for the existence of energetic transition states which may permit the creation of excited-state species from less-exothermic reactions. Of course, it is difficult to imagine a reaction which is endothermic in the ground state creating electronically excited species, so it still seems reasonable to only permit reactions which are exothermic in the ground state to create excited-state species, with a stronger likelihood granted to more-exothermic reactions. Based on the results herein, the requirement that $\Delta\bar{H}_R^0$ for the ground-state reaction exceed ΔE could be relaxed to permit less-exothermic reactions to form excited-state species. This observation applies to OH* and may also apply

to other chemiluminescent species such as CH*.

5.5 Summary

Shock-tube experiments were conducted in four Ar-diluted H_2-NO_2 mixtures ranging from $\phi = 0.28$ to $\phi = 5.29$. The test conditions ranged from 917 to 2003 K, all near 1 atm. H_2O and OH* time histories were separately measured using respective laser absorption and emission diagnostics.

To validate the NO_2 concentrations in the mixtures and overcome NO_2 dimerization effects, LED-based absorption measurements were employed for the fuel-lean mixtures. An inference method based on the H_2O time histories was used for the near-stoichiometric and fuel-rich mixtures. The two methods showed good agreement in a comparative test.

Chemical kinetics modeling was performed using several mechanisms from the literature. OH*-quenching reactions were updated for Ar and added for the first time for NO, NH_3, and N_2O.

The H_2O time histories in the fuel-lean mixture were prone to slight interfering absorption effects from NO_2. The NO_2 absorption was likely due to a hot band, as it was not predicted in spectral databases. The NO_2 interference was characterized and subtracted from the measured H_2O time histories. The H_2O time histories were relatively well-predicted by two recent mechanisms, but discrepancies between the models and data persisted at lower temperature for $\phi > 1$ despite exploratory alterations to the most-sensitive reaction rates. The species NO_3 and HONO and their associated reactions were found to be important for predicting the H_2O profiles; the absence of these species in GRI 3.0 explains its inability to predict the experimental data.

The measured OH* time histories were significantly different from mechanism predictions using established OH*-forming reactions. A search for a new chemiluminescent reaction, employing such factors as agreement with the OH* profiles and $\Delta\bar{H}_R^0$ considerations, led to the reaction NH + NO_2 ⇆ N_2O + OH* (R13) being proposed, with a best-fit rate of k_{13} = $5.0\times10^{16}\cdot\exp(-40{,}000/R_uT)$ [$cm^3/(mol\cdot s)$]. The best-fit rate was quite dependent on the NH chemistry of the base H_2-NO_2 mechanism employed and likely represents an upper limit on k_{13} since the rate constant of another OH*-forming reaction, R14, had to be increased by a factor of 10 in light of the addition of k_{13}. Finally, the oft-used screening technique for identifying potential chemiluminescent reactions based on $\Delta\bar{H}_R^0$ may need to be relaxed in future studies as both R13 and R14 violate the condition that $\Delta\bar{H}_R^0 < \Delta E$.

5.6 References

[1] C.R. Mulvihill, O. Mathieu, E.L. Petersen, "H_2O time histories in the H_2-NO_2 system for validation of NOx hydrocarbon kinetics mechanisms" *International Journal of Chemical Kinetics*, doi:10.1002/kin.21286 (2019).

[2] S.R. Turns, "An Introduction to Combustion: Concepts and Applications" 3rd ed., McGraw-Hill, New York, NY (2012).

[3] M.W. Chase, "NIST-JANAF thermochemical tables, Parts I and II" 4th ed., American Institute of Physics, College Park, MD (1998).

[4] C.R. Mulvihill, O. Mathieu, E.L. Petersen, "The unimportance of the reaction $H_2 + N_2O$ ⇆ $H_2O + N_2$: A shock-tube study using H_2O time histories and ignition delay times" *Combustion and Flame* **196** (2018) 478-486.

[5] J.I. Steinfeld, J.S. Francisco, W.L. Hase, "Chemical Kinetics and Dynamics" 2nd ed., Prentice-Hall, Upper Saddle River, NJ (1999).

[6] C.K. Law, "Combustion Physics" Cambridge Univ. Press, New York, NY (2006).

[7] F.A. Williams, "Combustion Theory" 2nd ed., Perseus Books, Reading, MA (1985).

[8] A.V. Joshi, H. Wang, "Master equation modeling of wide range temperature and pressure dependence of CO + OH → products" *International Journal of Chemical Kinetics* **38** (2006) 57-73.

[9] "ANSYS Chemkin theory manual 17.0" Reaction Design, San Diego (2015), accessed May 1 2019, www.ems.psu.edu/~radovic/ChemKin_Theory_PaSR.pdf

[10] M. Chaos, F.L. Dryer, "Chemical-kinetic modeling of ignition delay: Considerations in interpreting shock tube data" *International Journal of Chemical Kinetics* **42** (2010) 143-150.

[11] Y. Zhang, O. Mathieu, E.L. Petersen, G. Bourque, H.J. Curran, "Assessing the predictions of a NO_x kinetic mechanism on recent hydrogen and syngas experimental data" *Combustion and Flame* **182** (2017) 122-141.

[12] O. Mathieu, A. Levacque, E.L. Petersen, "Effects of N_2O addition on the ignition of H_2–O_2 mixtures: Experimental and detailed kinetic modeling study" *International Journal of Hydrogen Energy* **37** (2012) 15393-15405.

[13] G.P. Smith, D.M. Golden, M. Frenklach, N.W. Moriarty, B. Eiteneer, M. Goldenberg, C.T. Bowman, et al., "GRI-Mech 3.0" (1999), accessed May 1 2019, www.me.berkeley.edu/gri_mech/

[14] P. Glarborg, J.A. Miller, B. Ruscic, S.J. Klippenstein, "Modeling nitrogen chemistry in combustion" *Progress in Energy and Combustion Science* **67** (2018) 31-68.

[15] C.R. Mulvihill, O. Mathieu, E.L. Petersen, "Corrigendum to ``The unimportance of the reaction $H_2 + N_2O \leftrightarrows H_2O + N_2$: A shock-tube study using H_2O time histories and ignition delay times" [Combustion and Flame 196 (2018) 478-486]" *Combustion and Flame* **204** (2019) 430.

[16] W. Tsang, J.T. Herron, "Chemical kinetic data base for propellant combustion I. Reactions involving NO, NO_2, HNO, HNO_2, HCN and N_2O" *Journal of Physical and Chemical Reference Data* **20** (1991) 609-663.

[17] G. Yarwood, J.W. Sutherland, M.A. Wickramaaratchi, R.B. Klemm, "Direct rate constant measurements for the reaction O + NO + Ar → NO_2 + Ar at 300-1341 K" *The Journal of Physical Chemistry* **95** (1991) 8771-8775.

[18] T. Kathrotia, M. Fikri, M. Bozkurt, M. Hartmann, U. Riedel, C. Schulz, "Study of the H+O+M reaction forming OH*: Kinetics of OH* chemiluminescence in hydrogen combustion systems" *Combustion and Flame* **157** (2010) 1261-1273.

[19] P.H. Paul, J.L. Durant, J.A. Gray, M.R. Furlanetto, "Collisional electronic quenching of OH $A\,^2\Sigma$ (v'=0) measured at high temperature in a shock tube" *The Journal of Chemical Physics* **102** (1995) 8378-8384.

[20] K.H. Becker, D. Haaks, T. Tatarczyk, "The natural lifetime of OH ($^2\Sigma^+$, v = 0, N = 2,

J = 32) and its quenching by atomic hydrogen" *Chemical Physics Letters* **25** (1974) 564-567.

[21] P.H. Paul, "A model for temperature-dependent collisional quenching of OH $A\ ^2\Sigma^+$" *Journal of Quantitative Spectroscopy and Radiative Transfer* **51** (1994) 511-524.

[22] M. Tamura, P.A. Berg, J.E. Harrington, J. Luque, J.B. Jeffries, G.P. Smith, D.R. Crosley, "Collisional quenching of CH(*A*), OH(*A*), and NO(*A*) in low pressure hydrocarbon flames" *Combustion and Flame* **114** (1998) 502-514.

[23] W.L. Dimpfl, J.L. Kinsey, "Radiative lifetimes of OH($A\ ^2\Sigma$) and Einstein coefficients for the *A-X* system of OH and OD" *Journal of Quantitative Spectroscopy and Radiative Transfer* **21** (1979) 233-241.

[24] P.W. Fairchild, G.P. Smith, D.R. Crosley, "Collisional quenching of $A\ ^2\Sigma^+$ OH at elevated temperatures" *The Journal of Chemical Physics* **79** (1983) 1795-1807.

[25] R.D. Kenner, F.P. Capetanakis, F. Stuhl, "Kinetic isotope effects in the electronic quenching of OD/OH($A\ ^2\Sigma^+$,v = 0) at 296 ± 4 K" *The Journal of Physical Chemistry* **94** (1990) 2441-2446.

[26] R.A. Copeland, M.J. Dyer, D.R. Crosley, "Rotational-level-dependent quenching of $A\ ^2\Sigma^+$ OH and OD" *The Journal of Chemical Physics* **82** (1985) 4022-4032.

[27] J.B. Jeffries, R.A. Copeland, D.R. Crosley, "Quenching of OH($A\ ^2\Sigma^+$, v' = 0) by NH_3 from 250 to 1400 K" *The Journal of Chemical Physics* **85** (1986) 1898-1903.

[28] A.A. Konnov, "Implementation of the NCN pathway of prompt-NO formation in the detailed reaction mechanism" *Combustion and Flame* **156** (2009) 2093-2105.

[29] J. Chai, C.F. Goldsmith, "Rate coefficients for fuel+NO_2: Predictive kinetics for HONO and HNO_2 formation" *Proceedings of the Combustion Institute* **36** (2017) 617-626.

[30] D.L. Baulch, C.T. Bowman, C.J. Cobos, R.A. Cox, T. Just, J.A. Kerr, M.J. Pilling, et al., "Evaluated kinetic data for combustion modeling: Supplement II" *Journal of Physical and Chemical Reference Data* **34** (2005) 757-1397.

[31] L.S. Rothman, D. Jacquemart, A. Barbe, D.C. Benner, M. Birk, L.R. Brown, M.R. Carleer, et al., "The HITRAN 2004 molecular spectroscopic database" *Journal of Quantitative Spectroscopy and Radiative Transfer* **96** (2005) 139-204.

[32] C.R. Mulvihill, E.L. Petersen, "High-temperature argon broadening of CO_2 near 2190 cm^{-1} in a shock tube" *Applied Physics B* **123** (2017) 255.

[33] R.I. Soloukhin, "High-temperature oxidation of hydrogen by nitrous oxide in shock waves" *Symposium (International) on Combustion* **14** (1973) 77-82.

[34] Y. Hidaka, H. Takuma, M. Suga, "Shock-tube study of the rate constant for excited OH* ($^2\Sigma^+$) formation in the N_2O-H_2 reaction" *The Journal of Physical Chemistry* **89** (1985) 4903-4905.

[35] R. Mével, F. Lafosse, L. Catoire, N. Chaumeix, G. Dupré, C.-E. Paillard, "Induction delay times and detonation cell size prediction of hydrogen-nitrous oxide-diluent mixtures" *Combustion Science and Technology* **180** (2008) 1858-1875.

[36] R. Mével, S. Javoy, F. Lafosse, N. Chaumeix, G. Dupré, C.-E. Paillard, "Hydrogen–nitrous oxide delay times: Shock tube experimental study and kinetic modelling" *Proceedings of the Combustion Institute* **32** (2009) 359-366.

[37] R. Mével, S. Pichon, L. Catoire, N. Chaumeix, C.-E. Paillard, J.E. Shepherd, "Dynamics of excited hydroxyl radicals in hydrogen-based mixtures behind reflected shock waves" *Proceedings of the Combustion Institute* **34** (2013) 677-684.

[38] Y. Hidaka, S. Takahashi, H. Kawano, M. Suga, W.C. Gardiner, "Shock-tube measurement of the rate constant for excited OH($A\ ^2\Sigma^+$) formation in the hydrogen-oxygen reaction" *The Journal of Physical Chemistry* **86** (1982) 1429-1433.

[39] G.P. Smith, C. Park, J. Luque, "A note on chemiluminescence in low-pressure hydrogen and methane–nitrous oxide flames" *Combustion and Flame* **140** (2005) 385-389.

[40] J.M. Hall, E.L. Petersen, "An optimized kinetics model for OH chemiluminescence at high temperatures and atmospheric pressures" *International Journal of Chemical Kinetics* **38** (2006) 714-724.

[41] J.A. Harrison, A.R. Whyte, L.F. Phillips, "Kinetics of reactions of NH with NO and NO_2" *Chemical Physics Letters* **129** (1986) 346-352.

[42] K.J. Laidler, K.E. Shuler, "Elementary reactions in the gas phase involving excited electronic states" *Chemical Reviews* **48** (1951) 153-224.

6. CONCLUSIONS

Given below are point-by-point summaries of the four main Sections of this dissertation: molecular spectroscopy, quantitative optical diagnostics, experimental methodology, and H_2-NO_2 experiments and modeling. Finally, a brief future outlook is provided.

6.1 Molecular spectroscopy

1. Only molecules with a permanent dipole moment will possess pure rotational absorption/emission spectra. For example, homonuclear diatomic molecules such as N_2 and H_2 will not possess rotational spectra. Likewise, only vibrations associated with movement of a dipole moment will manifest themselves as absorption/emission spectra. For example, the symmetric stretching of CO_2 will not be IR-active.

2. The simple formulae used to describe rovibrational spectra of diatomic molecules were developed, as were the selection rules. Due to the rovibrational selection rules, $\Delta J = 0, \pm 1$, three possible branches can manifest themselves: the P ($\Delta J = -1$), Q ($\Delta J = 0$), and R ($\Delta J = 1$) branches, each of which possesses unique features. Examples of the P and R branch were demonstrated with a sample spectrum of the fundamental band of CO.

3. The terminology used to describe electronic spectra was explored. The electronic

term symbols were developed by introducing the symbols and meanings of the relevant quantum numbers. An example spectrum of the $A\ ^2\Delta \leftarrow X\ ^2\Pi$ band of CH was provided, illustrating the P, Q, and R branches as well as Λ-type doubling.

4. The Hund's coupling cases between the different types of angular momenta in electronic spectroscopy are merely models and are rarely exact. Some electronic states, such as the $X\ ^2\Pi$ state of OH, will experience a gradual shift from one coupling case to another as J increases.

5. Polyatomic rotational spectra of asymmetric tops cannot be represented by the simple formulae used for diatomic molecules and symmetric tops. Instead, analytical approximations or numerical solutions using computers must be employed.

6. The vibrational modes of polyatomic molecules follow general naming conventions and notation; the vibrational modes of H_2O were provided as an illustration.

6.2 Quantitative optical diagnostics

1. The Beer-Lambert law was derived by beginning with a radiative energy balance. The two-level spectroscopic model was employed. The various assumptions made in the derivation were discussed and found to be valid for shock-tube experiments.

2. In the two-level model, radiative processes include spontaneous emission,

stimulated emission, and stimulated absorption. Non-radiative processes include chemical reactions and collisional excitation/quenching. Only radiative processes are associated with the emission or absorption of photons, but both radiative and non-radiative processes can transfer molecules between the upper and lower states.

3. A new relation for determining the limits of spectroscopic saturation was developed for application to narrow-line-width spectral sources such as typical continuous wave lasers in the IR. The spectroscopic saturation limit for the conditions of the present study was found to be ~4 orders of magnitude higher than the laser intensity utilized, making saturation not of concern in this study.

4. The Boltzmann distribution and the partition function were introduced as a means of calculating population levels. Based on these population levels, an expression for the temperature dependence of the line strength was derived. Tabulated values of the line strength at a reference temperature and the partition function should be employed in calculating the line strength of a transition at combustion-relevant temperatures.

5. Relations for describing molecular line shape functions were developed in terms of the Gaussian, Lorentzian, and Voigt functions. Doppler (Gaussian) broadening is independent of pressure, while collisional (Lorentzian) broadening depends on both pressure and temperature. Doppler broadening can dominate the Voigt line shape at sufficiently high temperatures and/or frequencies. The validity of the power law

for modeling the broadening coefficient of collisional broadening was discussed.

6. The collisional line shift was introduced. Typically, the shift coefficients are modeled with a power-law dependence on temperature (analogous to that of collisional broadening), although the power-law dependence has been called into question in recent years. For fixed-wavelength measurements at higher pressures where the collisional shift becomes more significant, it may be wise to shift the laser wavelength slightly to stay tuned to the peak of the transition for maximum absorption.

7. The principles of emission diagnostics were briefly explored. A simple equation for the emitted intensity was obtained from the equation of radiative transfer by making different assumptions. The emitted intensity depends on the population of the upper (excited) state. Therefore, emission diagnostics can provide information only on the upper state. The mechanisms controlling the upper-state population were described, including collisional quenching and excitation reactions.

8. A challenge associated with quantitative or even relative emission measurements is the dependence on the optical setup. This challenge can be overcome through calibration of the diagnostic using a known amount of the emitter. In the case of measuring an excited radical species (which cannot be directly introduced into a mixture), a high-temperature calibration method can be used that only requires accurate knowledge of the collisional quenching rates.

6.3 Experimental methodology

1. The basic theory of shock-tube experimentation was described. The conservation laws for mass, momentum, and energy were written in shock-fixed coordinates around a 1-D normal shock wave These relations can be iteratively solved by a number of solvers available in the literature.

2. Vibrational relaxation is the time required for the shock-heated molecules to achieve an equilibrium distribution throughout the vibrational energy mode. The vibrational relaxation time was defined as the 1/e characteristic time required to achieve vibrational equilibrium. To estimate τ_{vib}, analytical formulae were taken from the literature. Using these formulae, which likely overestimated τ_{vib} due to the lack of data for NO_2, it was determined that vibrational relaxation was nonetheless not a concern for the mixtures in the present study. If vibrational relaxation is an issue, efficient colliding species such as H_2 and He can be added to the mixtures to accelerate the relaxation.

3. The hardware and instrumentation of the shock tube was described. Sample shock-velocity measurements were provided. Details on mixture preparation were provided, with particular attention paid to methods for minimizing mixture uncertainty due to increases in temperature during the compression of the gases in the mixing tank.

4. The operating conditions of the tunable diode laser and the physical setup of the

H_2O diagnostic were described. The challenge of achieving balanced detectors after the N_2 purge was overcome by using a detuning technique. It was determined the laser should not be placed within the N_2-purged enclosure due to wavelength shifting issues.

5. The selection and modeling of the H_2O transition were described, and the parameters used to model the line strength, line shape, and collisional shift were provided. Sample calculations of the absorption coefficient at 1388.140 nm were provided, as were calculations of the collisional line shift. At the pressures tested in this study (~1 atm), the collisional line shift varied only slightly with temperature, so the laser was fixed at 1388.140 nm. For higher pressures, tuning the laser slightly to stay at the peak absorption of the transition may be prudent.

6. Experimental challenges regarding broadband emission and interfering absorption were addressed. The preferred technique for identifying broadband emission is to turn off the laser and perform a shock experiment; such a test revealed a lack of broadband emission effects in the present study. If broadband emission is an issue, techniques for its reduction include the use of irises, the use of bandpass filters, and the placement of the detectors. The technique for identifying interfering absorption is to perform an offline laser experiment. If interfering absorption is detected, it may be possible to identify the interfering species by performing experiments in mixtures containing only the suspected interfering species.

6.4 H_2-NO_2 experiments and modeling

1. Experiments were performed in four mixtures of H_2-NO_2-Ar at ~99% Ar dilution with ϕ = 0.28 to 5.29. Test conditions were from 917 to 2003 K at around 1 atm. The H_2O laser diagnostic was employed for three of the mixtures, and the OH* diagnostic was employed for the fourth.

2. A lower-than-expected amount of NO_2 was discovered in the mixtures by way of the H_2O diagnostic. This low NO_2 concentration was due to the dimerization of NO_2 to N_2O_4. To overcome this issue, the NO_2 and H_2O diagnostics were employed to either measure or infer the amount of NO_2 present in the mixture. The two methods agreed well within their uncertainties.

3. Chemical kinetics modeling was performed using a total of four NOx mechanisms from the literature. For the OH* modeling, updates to the OH*-quenching reactions were made using quenching data available in the literature across a range of quenching partners and temperatures. Using these data, best-fit Arrhenius parameters were fit to rate constants for quenching by Ar, NO, NH_3, and N_2O. The Arrhenius fit to the Ar-quenching rate represents a correction to an earlier, incorrect fit found in the literature, while the fits to NO, NH_3, and N_2O represent the first of their kind. Rate constants for other quenching partners were taken from the literature.

4. A total of 21 H_2O time histories were acquired in three H_2-NO_2 mixtures. The H_2O

profiles were reasonably well-predicted by two recent mechanisms. However, discrepancies between the models and data persisted at lower temperatures for the near-stoichiometric and fuel-rich mixtures.

5. Reaction pathway analyses were conducted for the fuel-lean and fuel-rich mixtures, and sensitivity analyses were performed for all three mixtures tested with the H_2O diagnostic. These are the first high-temperature reaction pathway analyses to be performed in the H_2-NO_2 system, and they revealed the species NO_3 and HONO were quite important in the reaction sequence. The GRI 3.0 mechanism does not include these species, explaining the general inability of GRI 3.0 to predict the experimental data.

6. The discrepancy between the models and data at lower temperatures for the near-stoichiometric and fuel-rich mixtures was investigated via a sensitivity analysis. This analysis revealed that the reactions $NO_2 + H_2 \rightleftarrows HONO + H$ (R5) and $H_2 + OH \rightleftarrows H + H_2O$ (R7) were the most-sensitive reactions at early times. However, varying each reaction by its estimated uncertainty (a factor of 1.5) did not yield good agreement with the experimental data. At this point, it remains unclear as to what is causing the discrepancy. Further modeling work is needed to address the issue.

7. A small amount of absorption was observed immediately behind the reflected shock wave for the fuel-lean mixture. Offline laser absorption experiments revealed that

NO_2 was providing interfering absorption despite the lack of NO_2 transitions in this spectral region according to the HITRAN database. The observed absorption is, therefore, likely due to a hot band of NO_2. The fuel-lean H_2O time histories were corrected slightly for the interfering NO_2 absorption.

8. The OH* time histories were found to be poorly predicted when only the OH*-forming reactions $N_2O + H \rightleftarrows OH^* + N_2$ (R14) and $H + O + M \rightleftarrows OH^* + M$ (R15) were included in the mechanism. An extensive search for a new OH*-forming reaction was conducted by attempting to match the shapes of the OH* time histories as well as considering the exothermicity of the OH-forming reactions. The reaction $NH + NO_2 \rightleftarrows OH^* + N_2O$ (R13) was eventually identified, with a rate of $k_{13} = 5.0\times10^{16}\cdot\exp(-40{,}000/R_uT)$, with k_{13} in $[cm^3/(mol\cdot s)]$. The best-fit k_{13} constant is a factor of 2-50 below the accepted rate constant for the ground-state reaction.

9. The addition of R13 serves as a sink for OH* in the presence of sufficient amounts of N_2O. To maintain agreement with predictions of peak OH* data obtained in H_2-N_2O mixtures in the literature, a factor-of-10 increase was proposed for k_{14}.

10. The best-fit value of k_{13} was found to be highly dependent on the base (i.e., ground-state) NOx mechanism. Using a different NOx mechanism yielded a best-fit k_{13} that was nearly an order of magnitude higher due to significant differences in NH chemistry between the two mechanisms. The base mechanism used was chosen as it required the smallest increase to k_{14}.

11. A screening process commonly used to identify potential new chemiluminescent reactions is that the heat of reaction, $\Delta\bar{H}_R^0$, of the ground-state reaction should be greater than the energy associated with the wavelength of the chemiluminescence. However, both R13 and R14 fall well shy of this requirement at roughly 70% of the required energy. The results herein, as well as the numerous studies of R14 in the past, suggest this screening requirement could be relaxed to permit less-exothermic reaction to be considered as potential chemiluminescent reactions.

6.5 Future outlook

1. Measurements of the line shape and line shift parameters of the selected H_2O transition at shock-tube relevant temperatures would be helpful in reducing the uncertainty in the calculated absorption coefficient. The line shape and line shift parameters employed in this study were measured at relatively low temperatures and for neighboring transitions.

2. A better method of controlling the TDL temperature is desirable. Better temperature control would reduce the sensitivity of the TDL to laboratory temperature fluctuations and would reduce the likelihood of mode hops. One realization of better temperature control could take the form of an external thermoelectric cooler attached to the base of the TDL along with an insulated enclosure for the TDL and its components.

3. Measurements of vibrational relaxation times of NO_2 in various bath gases should

be measured to confirm the lack of vibrational relaxation effects. In light of the newly discovered hot band of NO_2, these measurements may be possible using the tunable diode laser of the present study, although the relatively low bandwidth of the detectors used (150 kHz) may necessitate a different detector scheme for such experiments.

4. An improved understanding of H_2-NO_2 chemistry leading to H_2O formation is still needed at lower temperatures. Measurements of the key intermediates NO_3 and HONO would help to facilitate this understanding. Absorption diagnostics for NO_3 and/or HONO at their strong absorption features near 662 nm [1] and 7.9 μm [2], respectively, could be explored in future work.

5. The addition of R13 into the OH* sub-mechanism increased the amount of predicted OH* by a factor of ~20. Performing a quantitative calibration of the chemiluminescence diagnostic to obtain quantitative OH* data would greatly constrain the fitting of the model and would provide more insight on the OH* kinetics in this system.

6. Predictions of the chemistry of the NH radical had a strong effect on the fitting of the new chemiluminescent reaction in this study. However, predictions of NH concentrations varied by around an order of magnitude between the different mechanisms. Measurements of NH concentrations in similar mixtures, perhaps using the strong $A\ ^3\Pi \leftarrow X\ ^3\Sigma^-$ band near 335 nm [3], might elucidate shortcomings

in NH chemistry in current mechanisms. Although the predicted amounts of NH were quite small (~10^{-10} mole fraction) for the conditions and dilute mixtures studied herein, other conditions and/or mixtures might produce detectable levels of NH.

6.6 References

[1] J. Orphal, C.E. Fellows, P.-M. Flaud, "The visible absorption spectrum of NO_3 measured by high-resolution Fourier transform spectroscopy" *Journal of Geophysical Research: Atmospheres* **108** (2003) 4077.

[2] D. Luckhaus, "The vibrational spectrum of HONO: Fully coupled 6D direct dynamics" *Journal of Chemical Physics* **118** (2003) 8797-8806.

[3] A.Y. Chang, R.K. Hanson, "Measurements of absorption lineshapes in the $A\,^3\Pi_i \leftarrow X\,^3\Sigma^-$ (0,0) band of NH in the presence of Ar broadening" *Journal of Quantitative Spectroscopy and Radiative Transfer* **42** (1989) 207-217.

APPENDIX A

NOISE REDUCTION TECHNIQUES FOR LASER ABSORPTION EXPERIMENTS

Noise in laser signals increases uncertainty in the results. The purpose of this Appendix is to outline useful methods for cleaning up noisy signals in shock-tube laser absorption experiments. The noise is categorized herein as either vibrational, electrical, or optical, and methods for remedying each category of noise are given. These techniques were developed through experience with the TAMU shock tubes and laser diagnostics but should be generally applicable to any similar diagnostics. A table summarizing various sources of noise and their possible solutions is provided at the conclusion of this Appendix.

It is worth pointing out that some levels of noise elimination may be unnecessary if sufficient levels of absorption are achieved. For example, meticulous noise elimination will be much more important for a laser diagnostic that provides only ~1% absorption than for a diagnostic that routinely provides ~30% or more absorption. Incorporating the below methods has been found to be effective at achieving a SNR of 25:1 or better for laser diagnostics with 1% absorption or less.

A.1 Vibrational noise: Physical suppression of vibrations

The arrival of the shock wave at the endwall test section[1] induces vibrations in the shock tube and its supporting structures. Accordingly, much of the noise observed in a shock-tube laser experiment may be due to vibration. The vibration may cause noise by

[1] Vibrations from the diaphragm breakage reach the endwall section ~10 ms before the incident shock wave due to the high sound speed of stainless steel (the timing depends on the test conditions and shock-tube dimensions). These vibrations are generally small but not always negligible and can confound the the determination of the baseline laser signal before the beginning of the reflected-shock experiment.

shaking optical components such as lenses, mirrors, detectors, or even lasers. Or, the vibration of the shock tube may introduce noise via the movement of the windows.

There are essentially two methods of removing vibrational noise. One method is to physically suppress the vibrations, while the other is to reduce the sensitivity of the optical setup to the vibrations. The effectiveness of some methods can be qualitatively assessed by tapping some part of the optical or shock-tube setup to introduce vibrations and observing the noise introduced in the detector signal. However, the only way to be certain of the effectiveness of a method is to perform a shock experiment and observe the level of noise present.

In this subsection, the noise-removal technique of physical suppressing vibrations is discussed. Out of the five methods tested, three have yielded promising results while the other two methods are ineffective or not worth the trouble.

A.1.1 Clamping of TEC fans

Thermoelectric coolers (TECs) are often employed to maintain a desired temperature. These active heat sinks require heat rejection to the surrounding environment, which is usually realized through forced convection using fans. While the power consumption of these fans is typically rather small (on the order of 10 W), they can still be a continuous source of vibrations. This source of noise can be identified by temporarily shutting off the fans. To combat fan-induced noise, one should ensure all fan-containing devices are rigidly fastened.[2] This method is recommended in all optical setups.

[2] Another solution is to separate the fan and the optic so each is supported by a different structure. The separation distance must be small so the forced convection remains effective. This method quickly becomes complicated and should only be a last resort.

A.1.2 Isolation of shock tube and optics

Since the shock tube is subjected to significant levels of vibration, the shock tube and its supporting structures should not contact the optical table. This method should be employed in all optical setups.

A.1.3 Placement of shock-tube supports

If the last section of the shock tube is allowed to freely hang off the end of a support, the resulting cantilever will be more susceptible to vibrations. It is better to support the shock tube at the endwall or as close as possible to the endwall. This method is recommended for all optical setups.

A.1.4 Actively damped optical table

Even with proper isolation of the optical table from the shock tube and its supports, vibrations are still free to travel through the floor of the lab and up through the legs of the optical table. To combat this, some commercially available optical tables possess active damping capabilities employing self-leveling pneumatic actuators (similar systems with passive damping only are also available). This method has been met with moderate success: while the vibration damping is quite effective, the self-leveling feature is imperfect and requires the optical table leg heights to be adjusted prior to each experiment so as to not disturb the alignment of the laser through the shock-tube windows. This slight drift in table position also makes the simultaneous alignment of multiple optical diagnostics quite difficult. Furthermore, such optical tables are quite expensive. For these reasons, this method is not recommended.

A.1.5 Straps

Tie-down straps were utilized to secure the shock tube to the support just below the endwall in an attempt to reduce vibrations in the vertical direction. These straps were found to have no noticeable effect on the vibrations. This method is not recommended.

A.2 Vibrational noise: Reduction of sensitivity to vibrations

It is difficult or impossible to completely isolate shock-tube optical diagnostics from all vibrations. Accordingly, this subsection describes a number of techniques to reduce the sensitivity of an optical setup to vibrations.[3] Some of these methods, particularly the alignment through the shock-tube windows, seem to only be helpful when small amounts of absorption (~1%) are expected and small amounts of noise (1 mV or less) are consequently of concern.

A number of the techniques outlined here are of great importance for the I_t detector but of relatively little importance for the I_0 detector. The signal in the I_t detector is influenced by the vibrations of the shock tube and the change in conditions behind the reflected shock wave, whereas the I_0 should not be influenced by any of these issues.

A.2.1 Tightening of optics

Clearly, all optics should be well tightened to reduce vibrations. This does not always happen, however, due primarily to human error and possibly to the gradual loosening of optics with successive vibrations from shock experiments occurring over weeks or months. Individual optics that need tightening can often be located by

[3] Some methods are actually related to the change in conditions behind the reflected shock wave and not strictly vibrations but are included here nonetheless

successively applying a light tap to each optic in the beam path and observing the response the in the detector signal; excessive noise appearing in the detector signal may indicate a need to tighten the corresponding optic.

A.2.2 Lens orientation

Plano-convex lenses are easier to manufacture than bi-convex lenses, making them significantly cheaper. However, plano-convex lenses are more susceptible to spherical aberrations than are bi-convex lenses (pg. 255 of [1]). As shown in Fig. A.1, this aberration is more pronounced with a particular orientation of the lens, thus plano-convex lenses should always be oriented with the flat side facing the focal point (i.e., the detector).

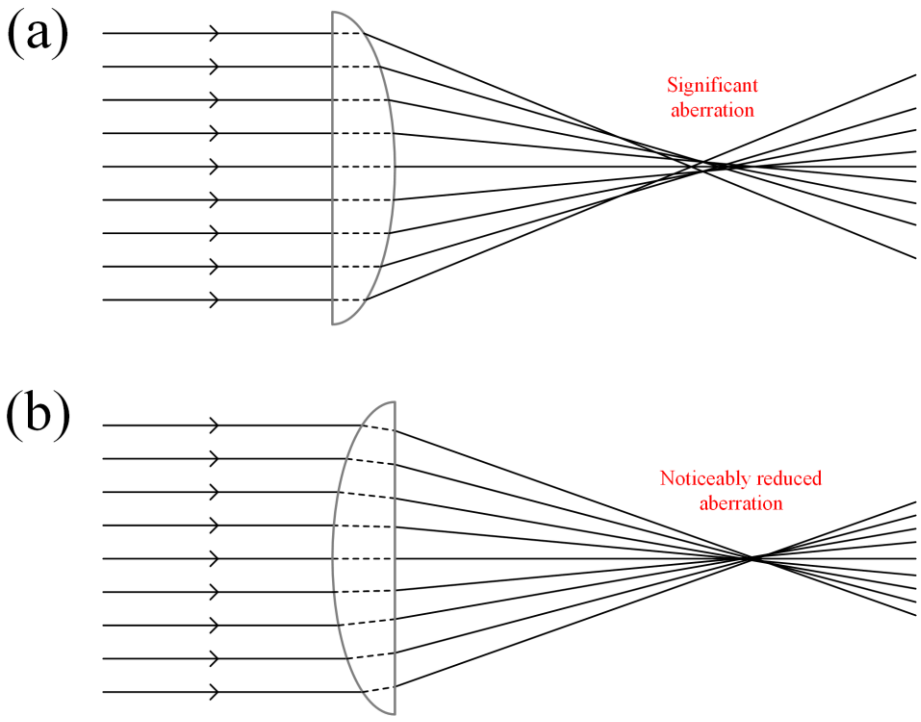

Figure A.1 Representative ray-tracing diagram for a plano-convex lens with the planar side (a) away from and (b) toward the focal point. The spherical aberrations, while not eliminated, are significantly reduced in (b).

A.2.3 Centering through lenses

If the laser beam was completely motionless over the course of a shock experiment, the aberrations shown in Fig. A.1 would be of little concern. However, the laser beam may be slightly steered across the face of the lens due to changes in shock-tube conditions, and the optics (e.g., the lens) may also move due to vibrations. Since the rays passing through the lens in Fig. A.1 are refracted to slightly different focal points depending on their position on the lens, movements of the laser across the lens can create movement of the laser beam on the detector face. This can introduce noise in the detector signal either through (1) removing part of the beam from striking the detector surface or (2) by influencing the detector signal through the position-sensitive nature of the detector element.[4] Consequently, it is ideal to have the laser beam centered through the lens and perpendicular to the planar surface of the lens. These alignment procedures will produce the least sensitivity to movement of the lens and/or laser beam.

A.2.4 Cleaning of windows

Over time, small diaphragm fragments or residue from chemical kinetics experiments can accumulate on the inside of the shock-tube windows. These create a non-uniform optical surface that introduces noise when the shock-tube windows move slightly due to vibrations or the laser beam is steered across the face of the second window. Figure A.2 shows an example of the effects of dirty windows and also the benefits of cleaning them. In light of this potential problem, the shock-tube windows should be frequently

[4] The first issue is typically more of a concern for smaller detector elements, which are typically employed in the mid-IR range (~2 μm and above). For larger detector elements, such as those sometimes employed in the near-IR range (<2 μm), the second issue will likely be more of a concern. The solution is the same in either case.

inspected and cleaned if necessary. If the windows are made of a softer material such as CaF_2, care should be taken not to scratch the window surfaces since scratched windows essentially represent a case of a permanently dirty window.

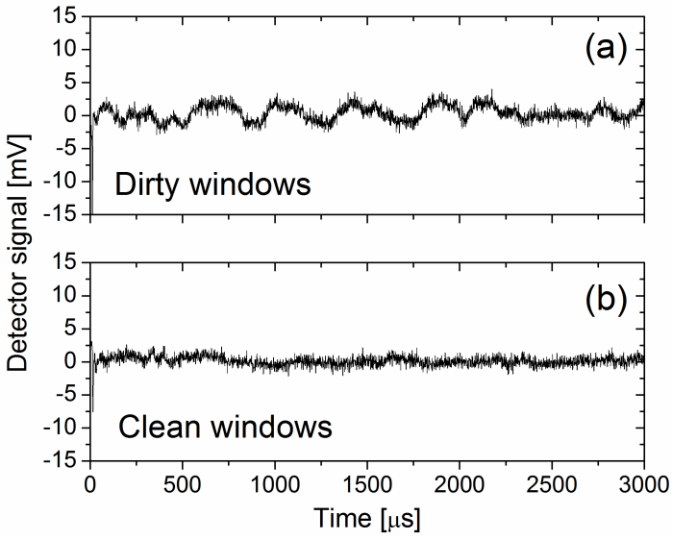

Figure A.2 Shock-tube laser experiments in Ar near 1 atm (a) before and (b) after cleaning the windows. The detector signal is $I_0 - I_t$.

A.2.5 Iris opening size

The use of irises (or apertures) throughout the transmitted side of the laser diagnostic is desirable because these optics can reduce the amount of broadband emission that can enter the transmitted detector. To minimize this broadband emission, it is desirable to close the irises as tight as possible without cutting off the laser beam. However, the laser beam is often slightly deflected following the passage of the reflected shock wave due to (1) beam-steering effects from the shock-heated gases and/or (2) vibration effects from refraction of the light passing through the shock-tube windows if the laser beam is not perfectly perpendicular to both windows. Deflection of the laser beam can cause clipping

on the iris edges which will manifest itself as noise in the detector signal. Thus, it is recommended to open the irises slightly wider than the laser beam width.

In cases of excessive broadband emission, it may appear that a tightly closed iris is unavoidable. However, it is generally preferable to have a cleaner laser signal rather than a smaller amount of broadband emission. The other methods of reducing broadband emission, bandpass filters and detector placement, should be implemented rather than excessively tightened irises. As discussed in Sect. 4.2.5, broadband emission can be characterized and subtracted out from the absorption signal if necessary.

A.2.6 Detector face orientation

Detector windows are typically fashioned from materials (e.g., ZnSe) that provide 80-90% transmission across a wide range of wavelengths, but even such materials still reflect a portion of the incident light. Occasionally, the transmitted detector can be aligned so perpendicularly to the laser beam that reflections from the detector window (or the bandpass filter in front of the window) can travel back through the optical setup and strike the incident detector. This source of noise can be initially identified by tapping the transmitted detector and observing noise in the incident detector and can be further confirmed by blocking the beam immediately in front of the transmitted detector and then tapping the transmitted detector once more; if the noise is no longer present, it was due to reflections from the transmitted detector window. A small, nearly imperceptible tweak to the angle of the transmitted detector should fix this issue without disturbing the alignment of the laser beam on the transmitted detector.

A.2.7 Alignment through shock-tube windows

The passages of the incident and reflected shock waves create a sudden change in test gas density and a concomitant increase in the test gas refractive index n. An application of Snell's law (Fig. A.3) shows the ideal alignment through the shock-tube windows is perfectly orthogonality to both surfaces, as this case will produce no change in angle upon the sudden change in n. A stationary beam (Fig. A.3(a)) is desirable for noise reduction due to reasons discussed earlier. While such alignment is impossible to achieve in practice since the two shock-tube windows are not perfectly parallel, it can be closely approximated.

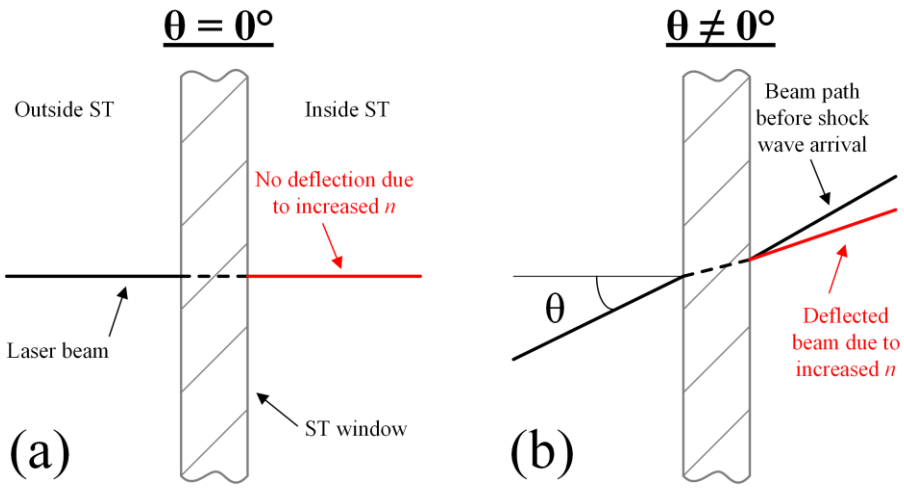

Figure A.3 Exaggerated demonstration of the behavior of a laser beam passing through a shock-tube window for an incident angle θ of (a) 0° and (b) greater than 0°. Beam behavior after the arrival of the shock wave is shown in red.

However, there is a confounding factor at work here: internal reflections from the window surfaces within the shock tube can introduce noise in the transmitted detector, as shown in Fig. A.4(a). These internal reflections introduce noise because they are subject to the same beam deflection and vibrational issues as the primary laser beam. This noise may

be significant if low absorption levels are available. For measurements with low absorption levels (~1%), it may be necessary to purposefully align the beam in the manner shown in Fig. A.4(b) such that the stray reflections do not make it into the transmitted detector. This type of alignment will likely prevent shock experiments much above $P_5 \approx 2$ atm due to the increased beam deflection noise from changes in n (Fig. A.3) but is very effective for reducing noise in experiments with $P_5 \approx 1$ atm.

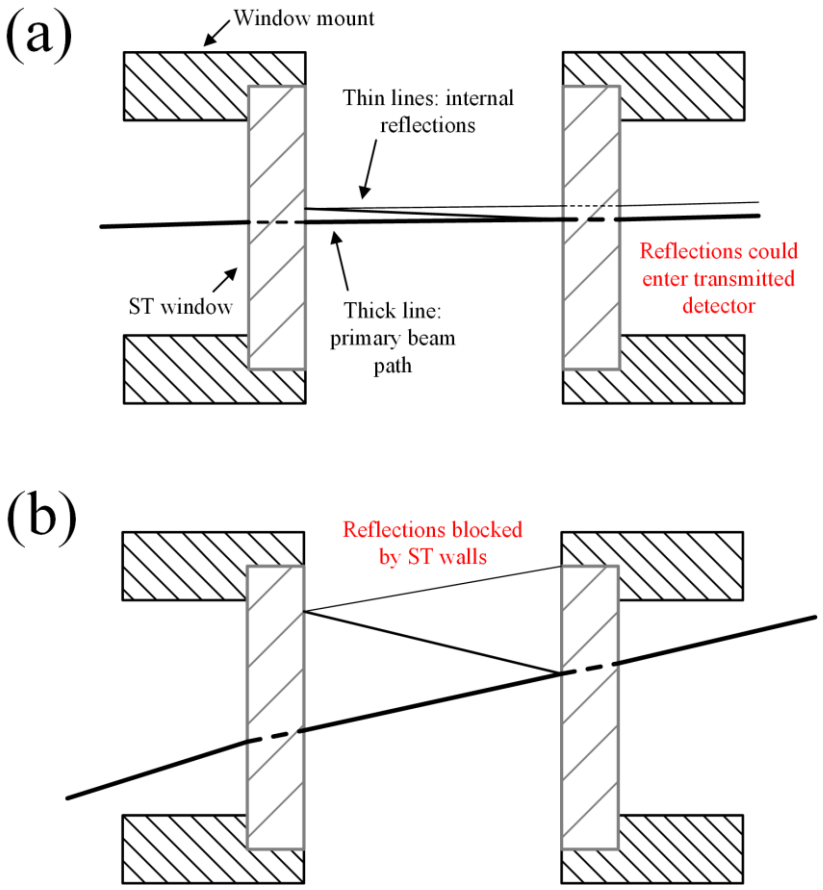

Figure A.4 Exaggerated demonstration of the behavior of stray internal reflections for a case of (a) nearly dead-center alignment through both windows and (b) intentional misalignment. Not drawn to scale.

A.2.8 Relocation of polarizers

Adjustable polarizers seated in rotating mounts are often used in differential absorption setups to balance the incident and transmitted beams. As the transmission of these optics is inherently position-sensitive, they can be particularly sensitive to vibrations. To mitigate this issue in the transmitted detector (of greater concern than the incident detector when dealing with noise), the polarizer for the transmitted detector can be placed on the incident side of the shock tube, although it must be placed downstream of the beamsplitter to be able to balance the beams.

A.2.9 Overhanging optical tables

It is often necessary to extend the physical footprint of an optical setup. One method of accomplishing this goal is to place a small optical table hanging off the edge of a larger optical table. This is undesirable because the cantilevered optical table will be more susceptible to vibrations but is sometimes unavoidable. To reduce vibration effects, the minimum number of optics should be placed on the overhanging table. Optics that are particularly vibration-sensitive (e.g., lenses, detectors, and polarizers) should be placed elsewhere.

A.2.10 Shortening optical path length

The assumptions of a Gaussian beam are often used in modeling laser beam behavior (see pgs. 358-364 of Demtröder [2]). One ramification of Gaussian beam behavior is that every laser beam, no matter how perfectly it is initially collimated, will inevitably diverge. The half-divergence angle θ_d (in radians) of a Gaussian beam is given by

$$\theta_d = \frac{\lambda}{\pi w_0}, \tag{A.1}$$

where λ is the wavelength of the laser and w_0 is the waist of the beam. The divergence angle reported in laser datasheets may either be θ_d or $2\theta_d$. The waist w_0 is defined as the radius of the beam at its smallest possible (i.e., diffraction-limited) spot size. An important implication of Eq. (A.1) is that beam divergence increases with increasing wavelength. Thus, UV and visible lasers show relatively little beam divergence, but $2\theta_d$ can be quite large (> 2 mrad) for IR lasers of increasing wavelength.

IR lasers can therefore grow to significant beam sizes with increasing path length. This introduces several problems, including (1) cutting off part of the laser beam on mirrors or irises, thus making the optical setup more sensitive to beam deflection and/or vibrations, and (2) reducing the effectiveness of the focusing lens in concentrating the laser beam onto the small IR detector element. A series of properly selected lenses could somewhat correct for the increased beam size. However, this would increase the complexity of the optical setup, and a simpler alternative is to simply shorten the path length of the optical setup to the minimum possible length while still maintaining adequate space between optics for necessary adjustments to be made by hand.

A.3 Electrical noise

Several issues associated with electronics can introduce noise into laser measurements. These issues can each be addressed through prior preparation or through post-processing methods.

A.3.1 Bit noise

The most significant yet most easily avoided source of electronic noise is bit noise. Bit noise is an artifact of using digital oscilloscopes with limited resolution. For example, the digitizer used in this study had a resolution of 14 bits. Measured voltage signals were thus discretized into one of 2^{14} digital "bins". The bin size could be indirectly selected by the user by changing the voltage input range of the digital oscilloscope. The software associated with the CompuScope cards used in this study allowed the user to select ranges in multiples of 1,2, or 5 (±100 mV, ±200 mV, ±500 mV, ±1 V, etc.). The bin size varied according to the setting selected. For example, if the selected voltage range was ±2 V, the full-scale range was 4 V and thus each bin spanned a range of $4/2^{14}$ V or 0.244 mV. For smaller voltage range settings, the bins were accordingly smaller.

As the oscilloscope samples the incoming voltage signals and sorts them into the appropriate bins, the limited resolution of the bins becomes visible and is referred to as bit noise. This is demonstrated in Fig. A.5, which shows measured voltages from the digitizer when no transducer was attached using input ranges of ±2 V and ±100 mV. Inspection of the light grey signal (±2 V) reveals a definitive pattern of striations. The gap between each striation is precisely equal to the calculated value of $4/2^{14}$ V = 0.244 mV for the ±2 V input range. However, the dark grey signal, although reading the same signal as the light grey, shows a much lower level of noise due to the factor-of-20 reduction in the bin size.

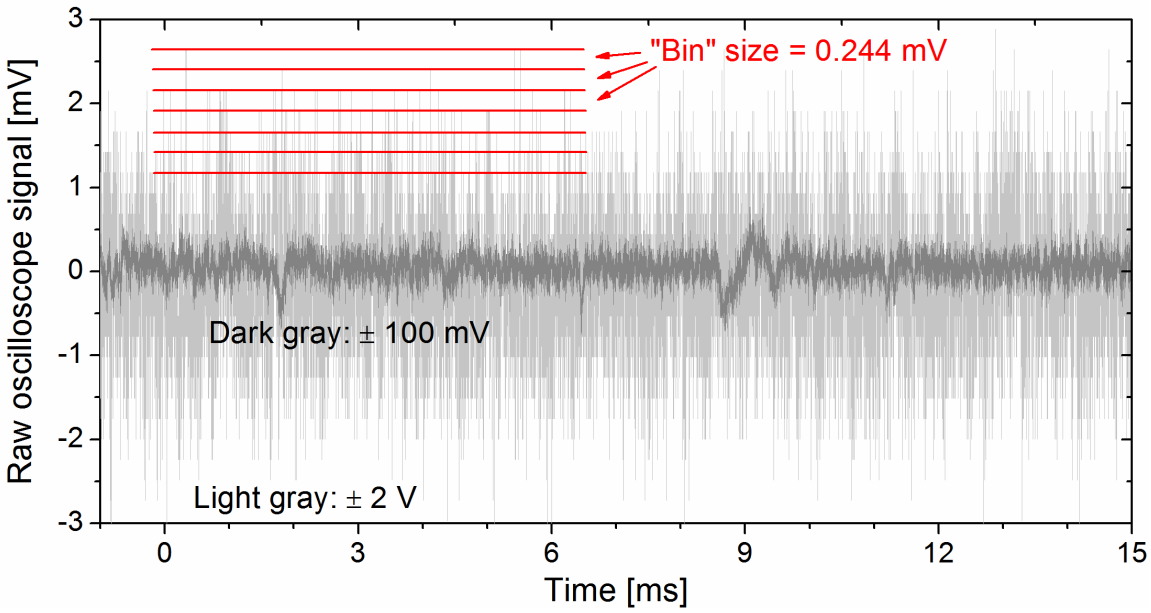

Figure A.5 Demonstration of the effect of oscilloscope voltage input setting on the level of bit noise. The red lines show the uniform spacing between discretized levels for the ±2 V setting.

Bit noise can be easily reduced by setting the oscilloscope input range to a lower value. Of course, if the oscilloscope input range is set at a range smaller than the experimental signal being received, the recorded data will be clipped at this limit. Thus, the proper methodology is to always set the input range of the digital oscilloscope to the minimum voltage input range needed to capture the desired signal. For example, if one expects a signal of ranging from 0 to -150 mV, the oscilloscope input range should be set to ±200 mV.

A.3.2 Differential preamplifier

It is desirable to make the incident detector signal I_0 as large as possible to increase the SNR of the absorption signal well above the inherent noise levels of the detectors and the oscilloscope. It is also desirable to make the initial value of the transmitted detector

signal I_t equal to I_0 so that common noise in the two detectors can be cancelled out (more on this in the following paragraph). However, if the oscilloscope input range is set to ±2 V to capture the I_0 signal and only ~1% absorption is expected, then bit noise (see App. A.3.1) will dominate the 20-mV absorption signal observed in I_t.

A useful tool for cutting down on bit noise in such a low-absorption case is the differential preamplifier. This device receives two voltage inputs and then outputs the difference between them. Therefore, if the I_t and I_0 signals are balanced prior to an experiment, the initial output of the differential preamplifier, $I_0 - I_t$, will be 0 mV. Continuing with the sample case given in the preceding paragraph, the 20-mV signal to be measured will now start at 0 mV, meaning the oscilloscope input range can be set to ±100 mV, resulting in significantly reduced bit noise. The differential preamplifier has the added benefit of cancelling out common noise in both detectors due to laser fluctuations; hence, this scheme is often referred to as common-mode rejection.

The benefits of the differential preamplifier typically diminish with increasing levels of absorption for two reasons. First, if the percent absorption levels are much larger than 1% ($\gtrsim$25%) then reducing bit noise becomes less critical as the absorption signal becomes larger compared to the I_0 signal level. Second, the common-mode rejection scheme becomes less effective at removing common laser fluctuations as the I_0 and I_t signals become increasingly disparate.

Careful attention should be given to the calibration of the differential preamplifier as these devices can incorrectly subtract the input signals after extended periods of usage. This problem can be remedied by recalibrating the preamplifier.

A.3.3 Cable impedance

Coaxial cables provide significantly lower noise than twisted pair cables and are thus preferred in scenarios requiring sensitive measurements. The BNC cable is a standard type of coaxial cable. BNC cables have an identifying code that is printed along the side of the cable that identifies the impedance of the cable; typical codes are RG-59/U (corresponding to an impedance of 75 Ω) or RG-58/U (corresponding to an impedance of 50 Ω). Stringing together BNC cables of different impedances can introduce electrical noise via impedance mismatching, so it is necessary to ensure all cables have the same impedance. Generally, better success has been found with the RG-58/U (50 Ω) cables.

A.3.4 Signal filtering

All transducers have a finite bandwidth above which they cannot detect incoming signals. However, the acquisition system (in this case, the digital oscilloscope) can often pick up extraneous noise well above this frequency. For example, all data in the present study were acquired at a sampling frequency of 1 MHz, but the IR detector bandwidths were 150 kHz. In accordance with these bandwidths, digital filters were applied to the detector signals. Figure A.6 shows a raw $I_0 - I_t$ data from a sample H_2O measurement along with the filtered signal. Since the H_2O detectors have a bandwidth of 150 kHz, a first-order Butterworth filter with a cutoff of 150 kHz was applied. It is observed that the filtering does not obscure any features of the H_2O profile, not even the high-frequency Schlieren spikes, but rather only removes spurious electronic noise.

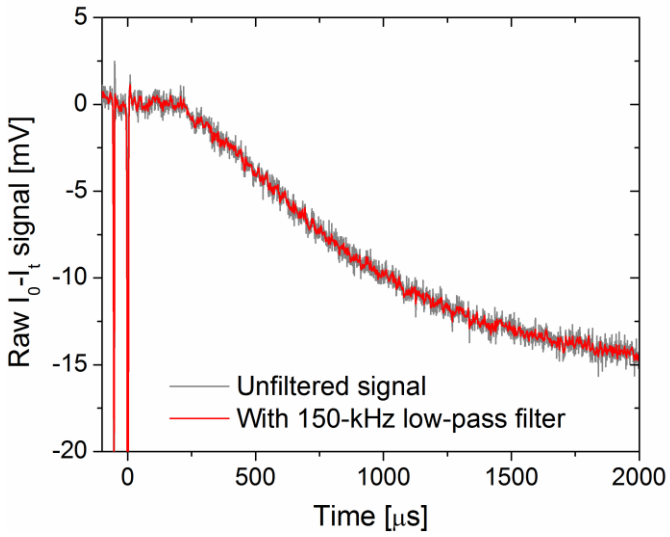

Figure A.6 Effect of filtering raw $I_0 - I_t$ data with a first-order, low-pass Butterworth filter with a 150-kHz cutoff.

A.3.5 Wall-socket noise

Cyclical noise present in signals may be due to noise from electronics running on wall-socket AC power (60 Hz in the USA). For example, 120-Hz noise was observed in a quantum cascade laser whose injection current came from a wall-socket-powered current controller. A possible remedy for this source of noise might be to use batteries to power the offending electronics, although this has not been tested. At the very least, being able to identify this source of noise means it can be filtered out during post-processing if needed.

A.3.6 Grounding of electronics

A small amount of noise can be generated from electronics connected to different electrical grounds. Grounding noise can be remedied by grounding all electronics to a common ground such as an optical table.

A.4 Optical noise

Occasionally, the alignment of certain optics will be in such a perpendicular manner that unwanted reflections between two optical surfaces will create an effective Fabry-Perot etalon, generating high-frequency noise in the detector signal. This high-frequency noise is characteristic of etalons with long path lengths, and such long path lengths often exist between optics (typically ~10-50 cm). Shown in Figure A.7(a) is an example of such noise.

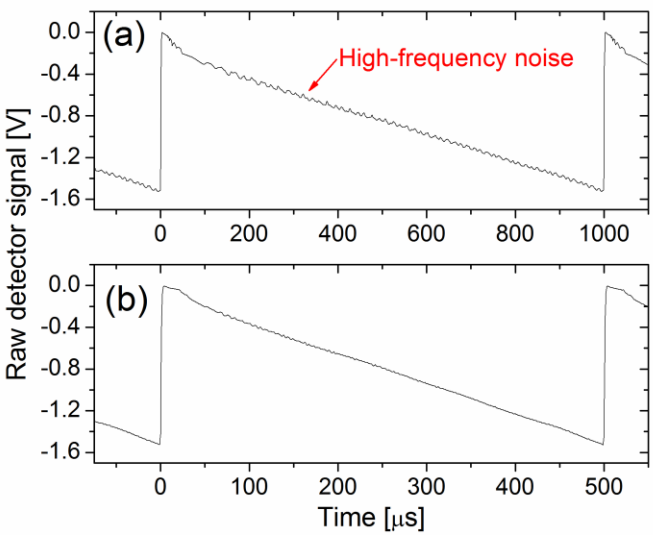

Figure A.7 Demonstration of (a) high-frequency optical noise and (b) its removal through an extremely small change in angle of the optic creating the noise. The sawtooth shape is due to the scanning of the laser over a range of frequencies via injection current modulation at (a) 1 kHz and (b) 2 kHz.

The solution to this problem is similar to that used to fix the detector face orientation problem (App. A.2.6). A slight tweak to the angle of one of the optical surfaces should be sufficient to disrupt the effective etalon cavity. For longer path lengths between optics, this tweak can be especially small; for shorter path lengths, a slightly larger tweak might be required. Figure A.7(b) illustrates the effectiveness of such a minute change in

the angle of the optic in removing the high-frequency optical noise.

A.5 Summary

Noise in laser absorption experiments is a persistent but surmountable issue. In this Appendix, various sources of noise in shock-tube experiments were explored, and possible solutions were proposed for each noise source. Finally, each type of noise has a general frequency range wherein it typically manifests itself. These frequency ranges and associated noise sources are summarized in Table A.1 along with possible solution methods. Table A.1 is not a set of rules but rather a set of guidelines to help identify and troubleshoot noise.

Table A.1 Typical frequencies of various noise sources and their possible solutions.

Frequency (kHz)	Possible causes	Possible solutions
< 1	- Fans	- Tighten fans, isolate from optics
	- Wall-socket AC power	- Utilize battery sources, apply filters in post-processing
1-10	- Vibrations of optical posts	- Tighten optics, center laser on lenses, widen irises, orient lenses correctly
	- Vibrations of the cantilevered shock tube or optical table extensions	- Provide better support for the shock tube, remove most optics from extensions
	- Beam steering	- Clean windows, realign laser through window ports at a different angle, center laser on lenses, orient lenses correctly
10-100	- Etaloning between optics	- Slightly tweak the angle of an optic
	- Cable impedance mismatching	- Match all cable impedances
>100	- Bit noise	- Set digitizer full-scale range to smallest value possible, apply filters in post-processing according to detector bandwidth
	- Grounding noise	- Connect all electronics to common ground

A.6 References

[1] E. Hecht, "Optics" 4th ed., Addison Wesley, Reading, MA (2002).

[2] W. Demtröder, "Laser Spectroscopy: Basic Concepts and Instrumentation" 2nd enlarged ed., Springer, Berlin, Germany (1996).

APPENDIX B

DATA ANALYSIS PROCEDURES FOR LASER ABSORPTION EXPERIMENTS

The cornerstone equation of absorption spectroscopy is the Beer-Lambert law,

$$I_t/I_0 = \exp(-k_\nu X_{abs} PL), \tag{B.1}$$

which was derived in Sect. 3.1. In the measurement or calculation of nearly every variable in Eq. (B.1), there are potential confounding factors to take into account. The goal of this Appendix is to address a number of these confounding factors and to propose remedies for each. Finally, a discussion on the analysis of scanned-wavelength experiments is provided along with sample experimental data.

B.1 Detector offsets and imbalances

The incident and transmitted detectors (I_0 and I_t) each output an amount of current linearly proportional[1] to the number of incident photons. However, inherent in photovoltaic detectors is a phenomenon known as dark current. This current is caused by background radiation from the surrounding environment and thermal excitation of electrons within the detector itself (pgs. 220-221 of Hanson et al. [1]). The manifestation of this current is an offset voltage that is present even when no light source is incident on the detector. Careful attention must be given to these offsets to obtain the true values of I_0 and $I_0 - I_t$ (other pairs of detectors signals could also be measured, such as I_t and $I_t - I_0$).

[1] This is assuming that the linearity limit of the detectors is not exceeded. This limit is typically specified by the manufacturer.

Experimentally, detector offsets can be determined by shutting off the light source or shielding the detector. In the case of IR detectors, particularly those at longer wavelengths, it is recommended to shut off the light source or to block the light source at a distance far from the detector, as even a room-temperature shield placed near the detector could emit radiation that might be detected and provide a false reading of the detector offset. Figure B.1 shows synthesized sample signals for the case of measuring the detector offsets prior to an experiment (Fig. B.1(a)) and the actual signal traces for the shock-tube speciation experiment (Fig. B.1(b)), where the formation of some absorbing species caused a decrease in the transmission of the laser.[2]

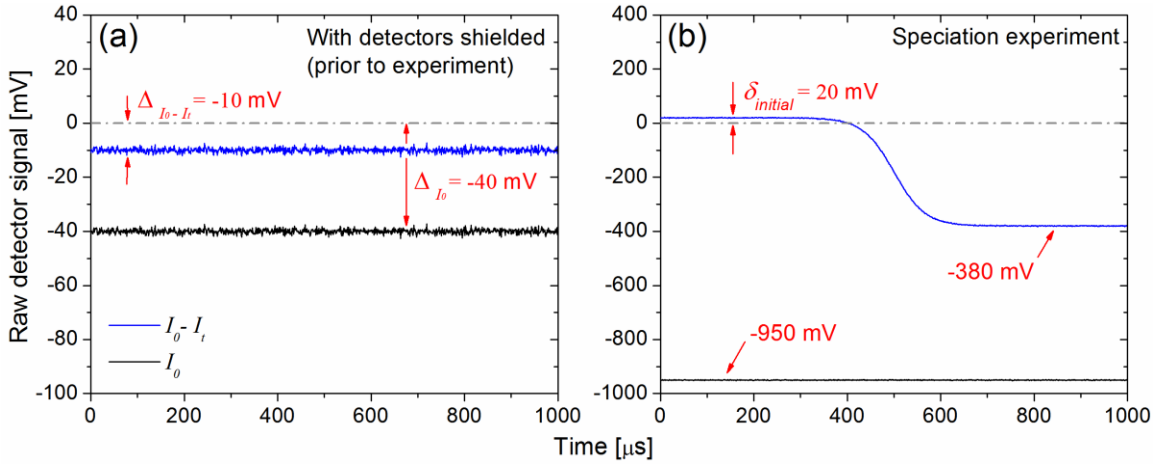

Figure B.1 Synthesized examples of (a) detector offsets Δ_{I_0} and $\Delta_{I_0-I_t}$ measured prior to an experiment by shielding the detectors and (b) a speciation experiment, showing the initial imbalance $\delta_{initial}$ in $I_0 - I_t$. The grey dash-dot lines mark the baseline of 0.

The measured detector offsets are called Δ_{I_0} [V] and $\Delta_{I_0-I_t}$ [V]. To obtain the true

[2] The example case here is for pair of detectors with negative polarity. For detectors with positive polarity, the shapes of the curves would be inverted but the analysis procedure would remain unchanged.

values of the I_0 and $I_0 - I_t$ signals, $(I_0)_{true}$ and $(I_0 - I_t)_{true}$, the respective offsets should be subtracted out from the measured signals, $(I_0)_{meas}$ and $(I_0 - I_t)_{meas}$. However, there is also an initial imbalance in the detector signals, $\delta_{initial}$ [V]: this imbalance must be subtracted from both $(I_0)_{meas}$ and $(I_0 - I_t)_{meas}$. The final caveat is that the offset $\Delta_{I_0 - I_t}$ is still a part of the measured imbalance $\delta_{initial}$ so that $\Delta_{I_0 - I_t}$ must be subtracted from $\delta_{initial}$. Ultimately, the following expression can be written for the true fractional transmission, $(I_t/I_0)_{true}$:

$$(I_t/I_0)_{true} = 1 - \frac{(I_0 - I_t)_{true}}{(I_0)_{true}} = 1 - \frac{\{(I_0 - I_t)_{meas} - \Delta_{I_0 - I_t}\} - \{\delta_{initial} - \Delta_{I_0 - I_t}\}}{\{(I_0)_{meas} - \Delta_{I_0}\} - \{\delta_{initial} - \Delta_{I_0 - I_t}\}}. \qquad \text{(B.2)}$$

The two $\Delta_{I_0 - I_t}$ terms in the numerator of Eq. (B.2) cancel each other but are included for clarity. The notation used herein is admittedly quite confusing, so values from the example case in Fig. B.1 are provided in Table B.1 in attempt to elucidate the use of Eq. (B.2). The values taken for the purpose of demonstration were taken from the final values in Fig. B.1(b), but in analyzing an experimental time history, the time-varying values of $(I_0 - I_t)_{meas}$ and $(I_0)_{meas}$ should be used in Eq. (B.2) to obtain the true fractional transmission versus time. An example of a fractional time history calculated using the example case in Fig. B.1 is shown in Fig. B.2. Also shown in Fig. B.2 is an incorrectly calculated fractional transmission curve that excluded the detector offsets $\Delta_{I_0 - I_t}$ and Δ_{I_0} from the calculation of Eq. (B.2). This mistake would lead to a 4.2% error in the calculated mole fraction X_{abs} according to Eq. (B.1). Of course, the importance of the detector offsets depends on their magnitude relative to the magnitude of $(I_0 - I_t)_{meas}$ and $(I_0)_{meas}$: for

smaller values of $\Delta_{I_0-I_t}$ and Δ_{I_0} such as those observed in this study (5-10 mV), the offsets could be neglected with only a ~0.3% error in X_{abs}.

Table B.1 Values of terms in Eq. (B.2) according to the example in Fig. B.1.

Symbol	Meaning	Value [mV]
$\Delta_{I_0-I_t}$	Measured offset in $I_0 - I_t$	-10
Δ_{I_0}	Measured offset in I_0	-40
$\delta_{initial}$	Initial imbalance between I_0 and $I_0 - I_t$	20
$(I_0 - I_t)_{meas}$	Raw recorded signal from the $I_0 - I_t$ channel	-380 [a]
$(I_0)_{meas}$	Raw recorded signal from the I_0 channel	-950 [a]
$(I_0 - I_t)_{true}$	True value of $I_0 - I_t$ after offset and imbalance corrections	-400 [a]
$(I_0)_{true}$	True value of I_0 after corrections	-940 [a]
$(I_t/I_0)_{true}$	True fractional transmission	0.5744 [a]

[a] Value taken from or calculated for the end of the experiment in Fig. B.1(b).

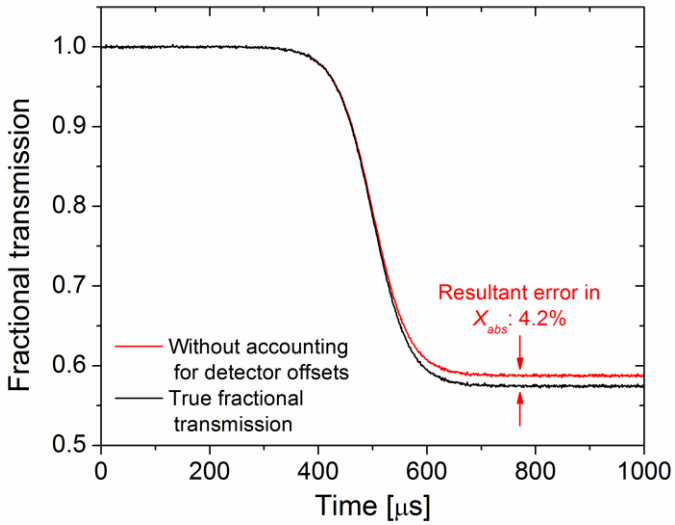

Figure B.2 $(I_t/I_0)_{true}$ time history for the example in Fig. B.1(b) according to Eq. (B.2). Also shown is an incorrectly calculated fractional transmission curve that excluded $\Delta_{I_0-I_t}$ and Δ_{I_0} from Eq. (B.2).

B.2 Correcting for the non-ideal pressure rise

Various non-ideal effects can cause a rise in P_5 called dP/dt, meaning the P term in the Beer-Lambert law is no longer a constant but instead varies with time, i.e.,

$$I_t/I_0 = \exp(-k_v X_{abs} P(t) L). \tag{B.3}$$

A typical method of quantifying dP/dt is by fitting a straight line through the pressure profile starting just after the reflected shock wave and reporting the rate of the rise in pressure as a percentage increase of the ideal P_5 in units of %/ms (for an example of experimentally observed dP/dt, see Fig. 4.9). Sidewall pressure traces are not always linear, meaning the linear value of dP/dt is sometimes merely an approximation. The value of dP/dt can depend on the gas, shock-tube inner diameter, Mach number, and other facility effects such as surface roughness or diaphragm breakage characteristics [2]. Typical dP/dt values in the TAMU shock tubes are 2-3 %/ms.

As an example of the effect of correcting for dP/dt in the Beer-Lambert law, consider Fig. B.3. For a dP/dt value of 2.0 %/ms, assuming a constant pressure leads to a 2.2% error in the calculated mole fraction X_{abs} after ~1 ms. This discrepancy will grow larger at longer times.

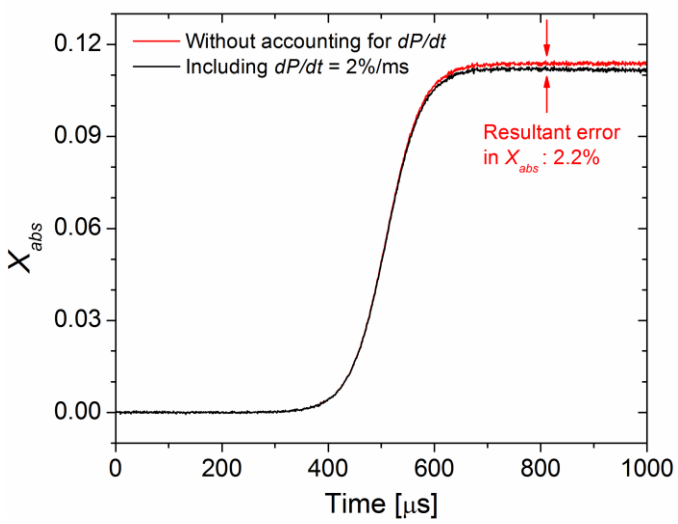

Figure B.3 Effects of the non-ideal pressure rise dP/dt on the evaluation of X_{abs} using the Beer-Lambert law. Values of k_ν = 0.3 cm^{-1}·atm^{-1}, P_5 = 1 atm, and L = 16.24 cm were used along with the sample transmission time history in Fig. B.2.

Another consideration is the temperature rise accompanying dP/dt. It has been experimentally demonstrated in Ar-diluted mixtures that the temperature rise due to dP/dt can be modeled by assuming isentropic compression [3]. Employing this assumption, the time-dependent temperature $T(t)$ can be written as

$$T(t) = T_5 \left(\frac{P(t)}{P_5}\right)^{\frac{\gamma-1}{\gamma}}. \tag{B.4}$$

Since $\gamma > 1$, Eq. (B.4) states the percentage temperature rise due to dP/dt will always be smaller than the pressure rise. For example, in Ar (γ = 1.667), a dP/dt value of 2 %/ms over a 2 -ms test time leads to a 4% rise in $P(2\text{ ms})$ relative to P_5, resulting in a 1.6% increase in $T(2\text{ ms})$ relative to T_5.

The temperature rise resulting from dP/dt influences the evaluation of the Beer-

Lambert law through the calculation of k_v by slightly altering both the line strength S_{12} and the line shape ϕ. Of course, the pressure rise from dP/dt will also have an effect on k_v by affecting ϕ. The relative effects on k_v of the temperature and pressure rise resulting from dP/dt depends on the molecule and the transition in question. For example, a visible or UV transition could have a Doppler FWHM that is over 10 times greater than the collisional FWHM (e.g., [4]). In such a case, the pressure rise will have almost no effect. The same will likely not be true in the IR, and these effects should be evaluated on a case-by-case basis.

In conclusion, to accurately model the effect of dP/dt on the evaluation of the Beer-Lambert law, both the effect of the pressure rise on the P term and the effects of the pressure and resultant temperature rise on k_v should be considered. For a description of the ways in which the influence of dP/dt can also be included in the chemical kinetic modeling, see Sect. 5.2.

B.3 Correcting for temperature changes due to reactivity

Yet another source of uncertainty in the laser absorption measurements is the change in conditions due to reactivity. During the combustion event behind a reflected shock wave, the reacting mixture will typically undergo exothermic reactions and experience a concomitant rise in temperature.[3] The magnitude of the temperature rise depends greatly on the dilution level and also on the fuel. For 98% dilution mixtures, the change in temperature ΔT could be 200-300 K [5] or even higher, while for a mixture of

[3] An exception to this is the case of pyrolysis, wherein the mixture temperature will actually decrease as the fuel decomposes.

0.1% O_2, 0.9% H_2, 99% Ar ΔT is only ~15 K [6, 7]. In the latter case, it was acceptable to ignore the effect of ΔT on k_v; in the former, ignoring such an effect could lead to a ~50% error in k_v.

In the absence of an experimental temperature measurement, the method for correcting k_v is to use the simulated temperature rise from a chemical kinetics mechanism. An example of such a temperature correction is shown in Fig. B.4 for sample CO measurements using the R(12) line of the fundamental band. Neglecting the temperature correction to k_v results in an 8% error in X_{abs}.

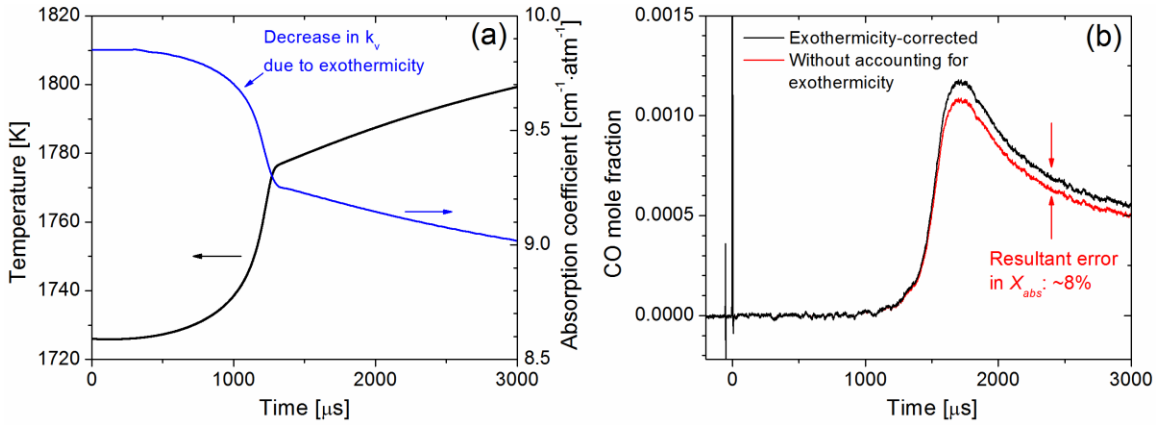

Figure B.4 Representative (a) temperature rise due to exothermicity with the corresponding change in k_v and (b) effect on the calculated X_{abs} profile. Experimental data and mechanism adapted from [8]. Conditions are 1726 K, 1.00 atm in a mixture of 0.0638% H_2S, 0.1492% CH_4, 0.787% O_2, balance Ar.

The method of correcting the data with the modeled temperature rise is admittedly somewhat circular, and minimizing this correction is desirable. Accordingly, in designing shock-tube laser absorption experiments on chemical kinetics, a trade-off must be made between minimizing the exothermic temperature rise while still maintaining an adequate

amount of fuel to produce measurable levels of the target species.

B.4 Scanned-wavelength measurements

Although not utilized in this dissertation, scanned-wavelength diagnostics are powerful tools for investigating spectral line shapes [9-11] or for performing high-speed, two-color temperature measurements [12]. In this context, "scanned-wavelength" refers to direct absorption measurements wherein the laser is scanned over one or more spectral features; this is not to be confused with frequency-modulation spectroscopy or wavelength-modulation spectroscopy (see pgs. 202-203 of Hanson et al. [1]).

The details of the experimental setup of a shock-tube scanned-wavelength diagnostic are not provided here since the focus of this section is the data analysis procedures. For details on the particular experimental setup employed in this example, see [10] and [11].

Figure B.5 shows sample experimental data from a scanned-wavelength experiment. A quantum cascade laser (QCL) was scanned over the R(12) line in the fundamental band of CO at a scan rate of 2 kHz. The data in Fig. B.5 were obtained during a shock-tube experiment, save the baseline scan, which was recorded prior to filling the shock tube with the test mixture.[4] The baseline scan data I_{base} was used in conjunction with the transmitted detector data I_{trans} to calculate the experimental transmission

$$I_t/I_0 = \frac{I_{trans} - \Delta_{trans}}{I_{base} - \Delta_{trans}}, \tag{B.5}$$

[4] The average of several baseline scans can be used to account for scan-to-scan fluctuations in the laser behavior, although such fluctuations are typically negligibly small (<0.3%).

where the slight detector offset Δ_{trans} has been subtracted from both signals in accord with the methodology of App. B.1. Δ_{trans} can be measured in the same way as for Δ_{I_0} and $\Delta_{I_0-I_t}$: either by blocking the laser or shielding the transmitted detector. Detector offset is not a concern in the etalon detector signal because it is only the timing of the fringe peaks that is of interest for the etalon detector,

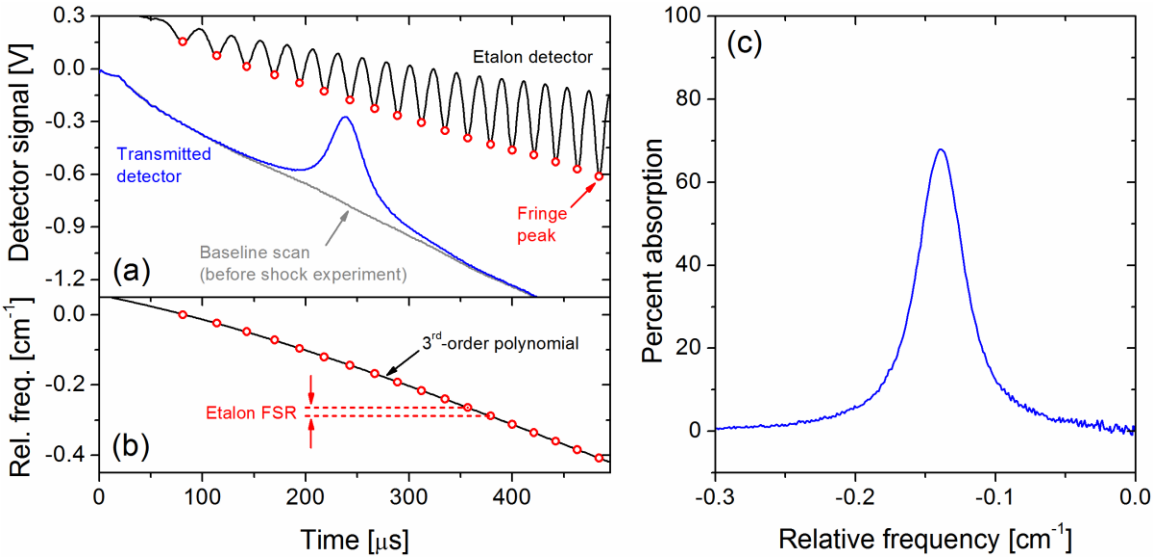

Figure B.5 Example data analysis procedure for a scanned-wavelength experiment showing (a) signals obtained during the shock experiment, (b) the third-order polynomial fit to the etalon fringe peaks, and (c) the processed absorption versus frequency. Data adapted from [10]. The etalon detector data have been shifted upward for clarity. The FSR was 0.024 cm^{-1}. A detector offset Δ_{trans} of -40 mV was subtracted out to yield the two baseline and experimental transmitted detector signals in (a).

Perhaps the main challenge in scanned-wavelength measurements is the conversion of the scan time to the relative frequency. This can be accomplished with a Fabry-Perot etalon. Briefly, light traversing a Fabry-Perot etalon will experience interference effects and will therefore exhibit maxima and minima as the frequency of the laser is changed (see

pgs. 140-147 of Demtröder [13]). The frequency spacing between the cavity modes of an etalon can be related to the refractive index n of the material and the length of the cavity d [cm] by (pg. 135 of [13])

$$FSR = \frac{1}{2dn}, \tag{B.6}$$

where FSR [cm^{-1}] is the free spectral range of the etalon. Therefore, by passing a laser beam through an etalon and into a detector, each fringe peak observed in the detector signal as the frequency of the laser is scanned represents a change in laser frequency of one FSR. The observed fringe peaks can be used to describe the relationship between scan time and relative frequency, typically by fitting a polynomial (Fig. B.5(b)). The polynomial can then be used to convert the experimental transmitted detector data from the time domain (Fig. B.5(a)) to the frequency domain (Fig. B.5(c)).

B.5 Summary

Various factors can confound accurate evaluation of the Beer-Lambert law. Factors addressed here were detector offsets and imbalances, dP/dt, and exothermicity of reacting mixtures. A method of measuring and taking into account the effect of the detector offsets and/or imbalances was outlined. Calculation procedures for using the measured dP/dt to account for the changes in P and k_v were demonstrated or discussed. The use of the predicted temperature rise from a chemical kinetics mechanism to correct k_v as a function of time was demonstrated.

The corrections to X_{abs} associated with the above effects ranged from 2 to 8%. The

magnitude of these corrections depends on factors such as the detector offsets and the dilution level of the mixture. These techniques should be useful tools in analyzing fixed-wavelength laser absorption data.

Additionally, sample detector data from a scanned-wavelength experiment were provided and analyzed. The method of calculating the fractional transmission, including the correction for the measured detector offset, was introduced. The procedure of using the extrema in the etalon detector in conjunction with the known etalon FSR to convert the time domain to the frequency domain was explained and demonstrated.

B.6 References

[1] R.K. Hanson, R.M. Spearrin, C.S. Goldenstein, "Spectroscopy and Optical Diagnostics for Gases", Springer, Cham, Switzerland (2016).

[2] J.W. Hargis, E.L. Petersen, "Shock-tube boundary-layer effects on reflected-shock conditions with and without CO_2" *AIAA Journal* **55** (2017) 902-912.

[3] A. Farooq, J.B. Jeffries, R.K. Hanson, "CO_2 concentration and temperature sensor for combustion gases using diode-laser absorption near 2.7 μm" *Applied Physics B* **90** (2008) 619-628.

[4] C.R. Mulvihill, M.W. Crofton, D.G. Arnold, E.L. Petersen, K.Y. Lam, "A laser diagnostic at 427 nm for quantitative measurements of CH in a shock tube" *Applied Physics B* **125** (2019) 78.

[5] O. Mathieu, C. Mulvihill, E.L. Petersen, "Shock-tube water time-histories and ignition delay time measurements for H_2S near atmospheric pressure" *Proceedings of the Combustion Institute* **36** (2017) 4019-4027.

[6] Z. Hong, D.F. Davidson, E.A. Barbour, R.K. Hanson, "A new shock tube study of the $H + O_2 \rightarrow OH + O$ reaction rate using tunable diode laser absorption of H_2O near 2.5 μm" *Proceedings of the Combustion Institute* **33** (2011) 309-316.

[7] C.R. Mulvihill, E.L. Petersen, "Concerning shock-tube ignition delay times: An experimental investigation of impurities in the H_2/O_2 system and beyond" *Proceedings of the Combustion Institute* **37** (2019) 259-266.

[8] C.R. Mulvihill, C.L. Keesee, T. Sikes, R.S. Teixeira, O. Mathieu, E.L. Petersen,

"Ignition delay times, laminar flame speeds, and species time-histories in the H_2S/CH_4 system at atmospheric pressure" *Proceedings of the Combustion Institute* **37** (2019) 735-742.

[9] A.Y. Chang, R.K. Hanson, "Measurements of absorption lineshapes in the $A\,^3\Pi_i \leftarrow X\,^3\Sigma^-$ (0,0) band of NH in the presence of Ar broadening" *Journal of Quantitative Spectroscopy and Radiative Transfer* **42** (1989) 207-217.

[10] C.R. Mulvihill, S.A. Alturaifi, E.L. Petersen, "High-temperature He- and O_2-broadening of the R(12) line in the 1←0 band of carbon monoxide" *Journal of Quantitative Spectroscopy and Radiative Transfer* **217** (2018) 432-439.

[11] C.R. Mulvihill, E.L. Petersen, "High-temperature argon broadening of CO_2 near 2190 cm^{-1} in a shock tube" *Applied Physics B* **123** (2017) 255.

[12] W. Ren, A. Farooq, D.F. Davidson, R.K. Hanson, "CO concentration and temperature sensor for combustion gases using quantum-cascade laser absorption near 4.7 μm" *Applied Physics B* **107** (2012) 849-860.

[13] W. Demtröder, "Laser Spectroscopy: Basic Concepts and Instrumentation" 2nd enlarged ed., Springer, Berlin, Germany (1996).

APPENDIX C

THEORY AND TECHNIQUES FOR STABLE OPERATION OF THE TUNABLE DIODE LASER

Various noise sources can be a hindrance to high-quality laser experimentation, as discussed in Appendix A. In addition to the vibrational, electrical, and optical sources of noise addressed therein, the laser itself can introduce noise to the system via intensity fluctuations. Furthermore, for the fixed-wavelength measurements employed in this study, a steady value of the wavelength is desirable so constant value of the absorption coefficient can be utilized. For these reasons, stable behavior of the laser is critical. Addressed in this Appendix are basic laser theory, tunable diode laser principles, and practical techniques for obtaining stable laser operation with the TDL used in this study.

C.1 Basic laser theory

Presented in this subsection are the fundamental components and principles associated with laser operation including stimulated emission, population inversion, and the lasing threshold. The primary reference for this material is Ch. 5 of Demtröder [1].

C.1.1 Components of a laser

Lasers vary widely in their operating principles and characteristics (see Ch. 9 of Hollas [2] for a broad introduction to the various classes of lasers). However, general similarities can be drawn between all lasers. At its core, every laser consists of three basic components:

(i) A gain medium, providing amplification via stimulated emission;
(ii) A pump, energizing the gain medium to sustain population inversion; and
(iii) A resonator, oscillating the stimulated emission for further amplification.

The gain medium is the portion of the laser wherein the oscillating light is amplified via stimulated emission[1] (more on stimulated emission below). The gain medium may be a gas (e.g., Ar, Ne, CO_2), a liquid (e.g., organic dyes), or a solid (e.g., ruby, sapphire, semiconductors). When a laser is referred to as a CO_2 laser or a dye laser or a solid-state laser, it is the gain medium that is being specified. The pump is the source of energy necessary to sustain the population inversion (see below). The pump may take many forms; flash lamps, injection current through a diode, and outside laser sources are a few examples. Finally, the resonator (also referred to as the cavity) is the optical enclosure wherein oscillation of the stimulated emission takes place. The resonator may consist entirely of the gain medium (e.g., internal cavity diode lasers) or it may contain external-cavity elements; such external elements are almost always necessary to obtain single-mode operation.

These three elements compose the basis of every laser system. There are many more complications to consider, a few of which will be addressed below, but it is helpful to keep in mind the three base components described above.

C.1.2 Population inversion

The term "population inversion" is ubiquitous in laser technology, and the following serves as a brief explanation of its importance. Consider light that is passing through some medium (in the case of a laser, the gain medium). The attenuation of the light

[1] The paramount role of stimulated emission in lasers is the source of their name, which is never capitalized in modern literature but is an acronym for Light Amplification by the Stimulated Emission of Radiation.

will be subject to the Beer-Lambert law, which, rearranging Eq. (3.12), can be written

$$I_t/I_0 = -\kappa_\nu L. \tag{C.1}$$

Recalling the definition of κ_ν from Eq. (3.9) and rearranging using Eq. (3.32), one can obtain

$$\kappa_\nu = \frac{h\nu_{12}}{c^2} B_{21} \left(\frac{g_2}{g_1} N_1 - N_2\right) \phi, \tag{C.2}$$

From Eq. (C.2), if the condition

$$N_2 > \frac{g_2}{g_1} N_1 \tag{C.3}$$

is satisfied, κ_ν will be negative so the incident light is amplified rather than attenuated according to Eq. (C.1). The condition of Eq. (C.3) is generally referred to as a population inversion because this condition deviates strongly from the equilibrium distribution described by the Boltzmann distribution. Creating this condition is at the core of every laser and is also one of the challenges in designing and operating lasers. However, the threshold population inversion for creating laser action is actually a higher standard than Eq. (C.3) implies due to losses in the system, as discussed next.

C.1.3 Lasing threshold

In the absence of any losses, incident light making a round trip through a gain

medium with length L_{gain} will experience a round-trip gain $G(v)$ of

$$G(v) = I_t/I_0 = \exp(-2\kappa_v L_{gain}), \tag{C.4}$$

where $G(v)$ is a function of v due to the frequency dependence of κ_v. In an actual laser cavity, various losses such as reflection, absorption by the optics, scattering, and diffraction serve to attenuate the beam. Lumping the losses into a loss coefficient Ψ associated with a round trip through the cavity, the losses per round trip can be written

$$I_t/I_0 = \exp(-\Psi). \tag{C.5}$$

The length of the cavity may be equal to the length of the gain medium, or it may be longer. Combining the losses and gain together, the net change in the radiation intensity is

$$I_t/I_0 = \exp\big(-2\kappa_v L_{gain} - \Psi\big). \tag{C.6}$$

The radiation will therefore be amplified if the gain surpasses the losses, i.e., if

$$-2\kappa_v L_{gain} > \Psi. \tag{C.7}$$

Combining Eq. (C.7) with Eq. (C.2), the threshold condition for the population difference ΔN to create laser action can be stated as

$$\Delta N = N_2 - \frac{g_2}{g_1} N_1 > N_{thr} = \frac{\Psi}{2\phi L_{gain} \frac{h\nu_{12}}{c^2} B_{21}}. \quad \text{(C.8)}$$

If ΔN surpasses ΔN_{thr}, then a light wave traversing the cavity will amplified.

The wave is initially created by spontaneous emission. Those spontaneously emitted photons traveling along the longitudinal axis of the cavity will create new photons as they traverse the gain medium by the process of stimulated emission due to the large, non-equilibrium population N_2. Initially, ΔN will be much greater than ΔN_{thr}, but at steady state, the depletion by the stimulated emission will balance the input by the pump and the population difference ΔN will equilibrate to ΔN_{thr}.

C.2 External-cavity diode lasers

The laser used in this study was a tunable diode laser (TDL). A subset of TDLs is that of external-cavity diode lasers (ECDLs). The ECDL used in this study was in the Littrow configuration. Discussed here are the basic concepts of diode lasers, the Littrow configuration, and the suppression of unwanted modes. The primary reference for this subsection is Zorabedian [3].

C.2.1 Diodes

A diode is generally a *p-n* junction of semiconductor material; light-emitting diodes are a subset of this class of materials. Laser diodes are typically 250-500 μm long and about ~60 μm thick. When a forward bias is applied, the electrons and hole recombine in the active region of the *p-n* junction (~0.1 μm thick) and emit light. Numerous materials can be used to fashion laser diodes. For diodes emitting at wavelengths near 1.4 μm, common

materials are InGaAsP and InP (see Fig. 7 of [3] for more materials).

In the absence of any wavelength-selective elements, most solitary laser diodes will emit multi-mode output. Such output is acceptable in applications such as handheld laser pointers but is undesirable for high-resolution spectroscopy. Accordingly, external cavities can be appended to the simple laser diode with the benefits of (1) selection of a single laser mode and (2) an increased tunability range. The Littrow configuration is one possible external-cavity configuration and is discussed next.

Many other factors of diode design can be considered. The type of active region, cleaving of the facets, and astigmatism of the output are examples of such considerations. For more on these aspects of diodes, the interested reader is referred to [3].

C.2.2 The Littrow configuration

Before introducing the Littrow configuration, it is helpful to briefly introduce diffraction gratings. A diffraction grating is essentially a surface with a set of periodic peaks separated by a period on the order of the wavelength of the incident light. The periodic peaks act as small radiation sources, producing regions of constructive and destructive interference according to the Huygens-Fresnel principle (pgs. 104-105 of [4]). Ultimately, the light is diffracted from the grating according to the relation

$$g(sin\alpha \pm sin\beta) = m\lambda, \tag{C.9}$$

where g is the groove spacing of the grating, α is angle of the incident light relative to the normal of the grating, β is angle of the diffracted light relative to the normal of the grating,

and m is an integer corresponding to the order of the diffraction grating. The $\pm$ is a plus if α and β are on the same side of the grating normal and a minus otherwise. The grating order m is typically selected to be 1 as the higher orders are generally weaker.[2] 0^{th}-order diffraction ($m = 0$) corresponds to simple reflection.

A Littrow grating mount is one wherein a diffraction grating is placed at an angle such that the diffracted light is diffracted directly along the path of the incident light. In other words, $\alpha = \beta$ and Eq. (C.9) becomes

$$2g \sin(\alpha) = m\lambda. \tag{C.10}$$

In essence, a Littrow-mounted diffraction grating acts as a wavelength-selective reflector. For the grating used in the present laser, the line density was 1000 mm^{-1} such that g was 1 μm. For the target wavelength of 1388.140 nm, α was therefore ~43.9°. For more on diffraction gratings, see Ch. 4.1 of [1].

External-cavity diode lasers take advantage of the Littrow setup by introducing the grating as part of the laser cavity. The grating is angled so the desired wavelength output of the laser is diffracted back into the diode. Therefore, the wavelength selected by the grating angle is amplified while other wavelengths are diffracted outside the cavity axis.

A schematic of the setup used in the laser of the present study is shown in Fig. C.1. The diode output was highly divergent and was consequently collimated by a lens. The rear face of the laser diode acted as one end of the cavity, while the grating acted as the other end. The front face of the laser diode was coated with an anti-reflection (AR) coating,

[2] An exception to this is the blazed diffraction grating, wherein the peak diffraction is in $m = 2$ or higher.

which is typical in external-cavity setups to improve stability of the laser performance (see pg. 365 of [3]). Upon each round trip of the cavity, a portion of the light was reflected out of the laser cavity via the 0^{th}-order diffraction of the grating; this was the output of the laser.

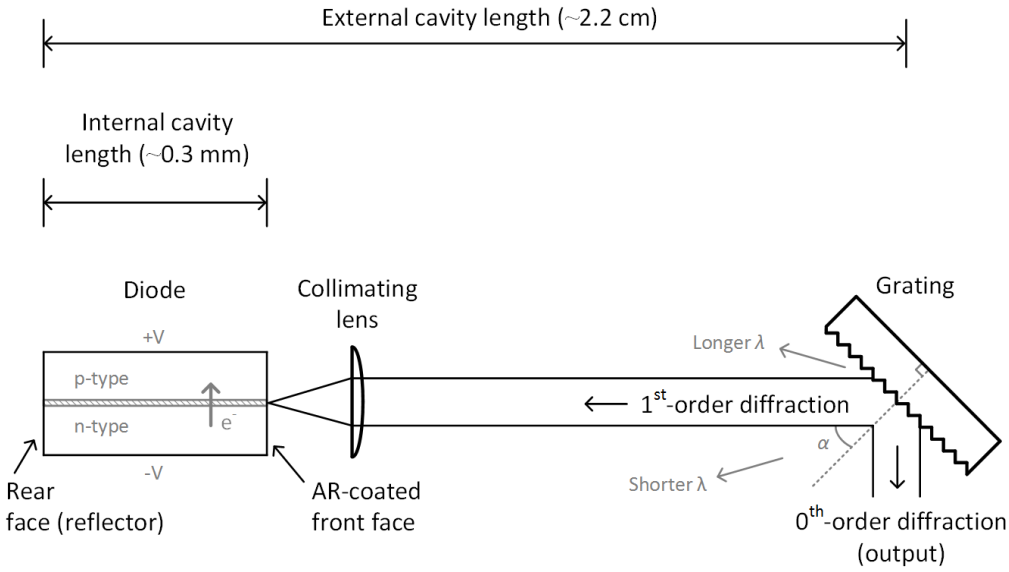

Figure C.1 Schematic of the Littrow-configured TDL used in the H_2O experiments. The diode has been greatly enlarged.

Two additional components of the laser are not shown in Fig. C.1: a beam-steering mirror and an optical isolator, both placed downstream of the grating. The beam-steering mirror permitted control of the laser output direction to compensate for changes in α, while the optical isolator prevented unwanted optical feedback into the laser (see pg. 397 of [3]).

Another configuration of grating-stabilized ECDLs is the grazing-incidence (or Littman-Metcalf) mounting. Furthermore, some ECDLs in the Littrow configuration will use the rear face of the diode as the laser output rather than the 0^{th}-order of the grating.

C.2.3 Suppression of longitudinal modes

A laser will oscillate at all possible modes, i.e. for all frequencies which meet the threshold condition of Eq. (C.8) (see Ch. 5.3 of [1]). However, for the purposes of the present study, single-mode operation was necessary to obtain a singular value of k_v. Furthermore, multi-mode operation is associated with strong frequency fluctuations (pgs. 255-259 of [1]). These reasons necessitate the use of the Littrow configuration or some other wavelength-selective technique. The selective aspects of the internal cavity modes, the external cavity modes, and the grating are discussed below.

The internal cavity is the cavity created by the faces[3] of the diode. The spacing of the internal cavity modes Δv_{int} [Hz] is given by (pg. 355 of Zorabedian [3]):

$$\Delta v_{int} = \frac{c}{2 n_{eff} L_{gain}}, \tag{C.11}$$

where n_{eff} is the effective refractive index of the diode and L_{gain} is the length of the diode.[4] With typical values of 3.5 and 300 μm for n_{eff} and L_{gain}, respectively, Δv_{int} is ~140 GHz.

The external cavity refers to the total cavity including the gain medium (i.e., the diode) and the air gap between the diode front face and the grating. The spacing of the external cavity modes Δv_{ext} [Hz] is given by (pg. 370 of [3]):

[3] The diode faces are frequently called facets in the literature.
[4] This equation is the well-known Fabry-Perot interference relation. It was also used in Appendix B, Eq. (B.6), and is written here with slightly different variables and units.

$$\Delta v_{ext} = \frac{c}{2(L_{ext}+n_{eff}L_{gain})} \tag{C.12}$$

where L_{ext} is the length of the external portion of the cavity (i.e., excluding the gain medium). Assuming L_{ext} is 2.2 cm, Δv_{ext} is ~6.5 GHz. As is the nature of all Fabry-Perot interferometers, the modes are more tightly spaced with increasing length of the cavity. Consequently, with the addition of the grating, there are more possible modes in which the laser can oscillate. Therefore, it is necessary to have an element of the setup that will select the desired wavelength by suppressing other longitudinal modes;[5] this role is fulfilled by the grating. The width of the grating profile was estimated at 50 GHz according to the manufacturer's manual.

The laser will oscillate at all allowable modes where the gain surpasses the losses. Ideally, oscillation will only occur at one frequency so the laser can operate in single-mode operation. The mode behavior of the laser is controlled by the overlap of the various types of loss in the system. An illustration of these modes is provided in Fig. C.2. The gain medium is seen to be broadband compared to the sources of loss in the system (i.e., the grating, the internal modes, and the external modes), so it appears as nearly a flat line. An important observation is that the gain medium is the only part of the laser that actually amplifies the oscillating radiation; the other components are only destructive in nature such that their respective peaks in Fig. C.2 are essentially those locations where they allow laser oscillation. Therefore, due to the broadband nature of the gain medium, it is the overlap (or lack thereof) of the various modes controlling the emitted wavelength(s) of the laser.

[5] Transverse modes also exist; see pgs. 264-266 of [1] on suppression of these modes.

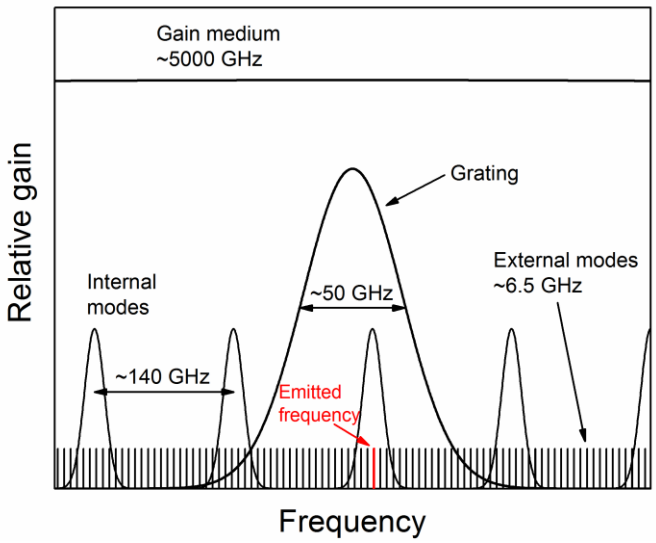

Figure C.2 Behavior of the various gain or loss modes within the TDL. The ideal case of a single mode of laser action at the intersection of the different modes is highlighted in red. The y-axis scale is arbitrary.

In Fig. C.2, it can be seen that the laser would theoretically operate among many modes simultaneously were the wavelength-selective grating not present. Even with the grating in place, it is still possible to achieve multi-mode laser operation, but single-mode operation becomes attainable.[6]

C.3 Techniques for stable operation

In this subsection, practical techniques for operating the TDL used in this study are provided. With the basic understanding of the theoretical principles and the physical construction of the TDL, stable laser operation can be obtained.

[6] Multi-mode operation may appear inevitable in Fig. C.2, but only those modes which achieve the threshold condition will oscillate. So, some of the modes that appear attainable will instead be sufficiently attenuated.

C.3.1 Tuning the laser

The tuning of the laser followed two steps. First, the laser was coarsely tuned using the diffraction grating adjustment screw as illustrated in Fig. C.3. The finely threaded screw was turned carefully as the wavelength was very sensitive. If the grating block has been shifted or a new laser diode or grating has been installed, the screws fastening the grating block (not shown in Fig. C.3) will need to be loosened so the block can be roughly adjusted to the proper angle for the desired wavelength according to Eq. (C.10). Once the laser had been coarsely tuned, the temperature and current of the Peltier element and diode injection, respectively, were finely adjusted to obtain the exact desired wavelength. The adjustments to the grating, temperature, and current each shifted one or more of the profiles in Fig. C.2 to some degree, often affecting different profiles in asynchronous manners. In this manner, a host of different possible wavelengths were achieved with the proper settings.

Not shown in the Fig. C.3 is the piezoelectric actuator that can be used to slightly modulate the position of the grating. This can be useful for scanned-wavelength measurements by simultaneously modulating the diode injection current along with the piezo movement, although such experiments were not conducted in this study.

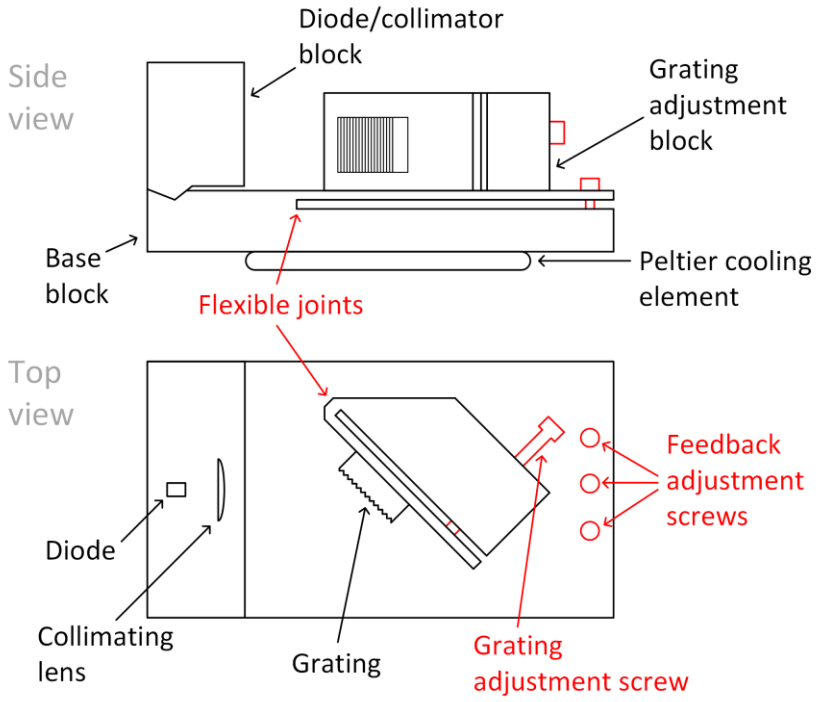

Figure C.3 Schematic of the physical layout of the TDL, with features pertinent to laser tuning highlighted in red. Not shown are the piezoelectric actuator, the beam-steering mirror, the optical isolator, or any of the cables associated with the electronics.

C.3.2 Single-mode operation

In practice in the laboratory, multi-mode operation of the laser was rather easily detected by the large intensity fluctuations produced in the detector signals. With stable, single-mode operation, the voltage signal in the detectors for the particular laser/detectors used herein were less than three times the combined detector and bit noise observed when the laser was blocked or turned off. This is only a rule of thumb but was helpful in ascertaining the operation of the laser. Additionally, the wavemeter employed in this study also made clear when the laser was operating in multi-mode output as the wavelength reading would fluctuate rapidly.

In the case of multi-mode operation, small tweaks to the temperature (typically

±0.5°C) and current (typically ±5 mA) often allowed the laser to achieve single-mode output once more. However, in the case of complete coherence breakdown, the grating occasionally needed to be adjusted (see App. C.3.4). A further problem, typically experienced when adjusting the laser current, was mode hopping, as discussed next.

C.3.3 Mode-hopping issues

Mode hopping is perhaps the single largest difficulty in working with TDLs. Mode hopping occurs when the laser "hops" from operating in single-mode at one mode to the next mode. At least for the TDL of the current study, these mode hops were found to occur between the external modes shown in Fig. C.2, as the mode hops observed on the wavemeter were roughly 6.5 GHz (equivalent to ~0.030 nm near 1388 nm).

Mode hopping was typically associated with changes in the laser current. A typical current adjustment range of ±7 mA was possible before the laser would mode hop to another wavelength. It was undesirable to operate the laser near the bounds of the mode-hop-free current range as these regions tended to produce noisier laser operation. To avoid this, the upper current at which the mode hop occurred was assessed by increasing the current until a mode hop was observed. Then, decreasing the current to return to the original external cavity mode, the current was further decreased until another mode hope was observed. The value of injection current at which the mode hops occurred were recorded,[7] and an effort was made to maintain the laser current roughly in between these current values.

Mode hops also occurred on a month-to-month or even day-to-day basis due to

[7] These values were approximated since the laser displayed a fair bit of hysteresis.

changing laboratory temperature, which was prone to fluctuate by ±3 °C over the course of a year. Although the Peltier element was designed to maintain the laser elements at a constant temperature, they could not fully control the temperature of the entire diode/grating configuration. Such long-term mode hops required adjustments to the temperature and current and often to the grating to return to the desired wavelength.

C.3.4 Adjusting the feedback

In the case of relatively large-scale adjustments to the grating and/or grating block, it was quite likely a coherence breakdown would occur, wherein the lasing action ceased completely due to misalignment of the grating and the diode. In such a case, the feedback of the grating into the diode required adjustment. Such adjustment was accomplished through use of the three screws illustrated in Fig. C.3, which controlled the angle of the top portion of the mounting block on which the grating block was fastened. The middle screw pushed the two portions of the block apart, while the outer two screws pulled the two portions together. The three feedback adjustment screws primarily controlled the vertical adjustment of the feedback, while the grating adjustment screw controlled the horizontal alignment.

In the case of complete coherence breakdown (i.e., no laser action, as indicated by very small and noisy detector signals as well as no consistent reading on the wavemeter), the feedback adjustment screws could be used to align the output of the diode and the diffraction of the grating. Placing a viewing card[8] after the output of the grating, the feedback adjustment screws were tweaked until the spots on the card corresponding to the

[8] The viewing card was quite difficult to utilize, and better success was achieved with an IR camera.

0^{th} and 1^{st} orders were aligned. This alignment was indicated by a significant increase in the brightness of the overlapping spots corresponding to successful laser action.

Following the course alignment of the feedback described in the preceding paragraph, an optimization of the feedback was also performed. Removing the viewing card, a power meter was used to monitor the power output of the laser beam. Slight tweaking of the feedback adjustment screws allowed for the power output of the laser beam to be maximized. This procedure was also occasionally used after making significant adjustments to the grating angle, even though no coherence breakdown was observed.

C.4 Summary

Understanding the operating principles of the TDL will aid the experimenter in troubleshooting inevitable problems. The basic theory of lasers was covered, as well as the principles and mechanics specific to ECDLs. Techniques for recognizing and solving various problems such as mode hopping and coherence breakdown were presented. The principles introduced in this Appendix should generally apply to the application of this laser to scanned-wavelength experiments.

C.5 References

[1] W. Demtröder, "Laser Spectroscopy: Basic Concepts and Instrumentation" 2nd enlarged ed., Springer, Berlin, Germany (1996).

[2] J.M. Hollas, "Modern Spectroscopy" 4th ed., John Wiley & Sons, Chichester, UK (2004).

[3] P. Zorabedian, "Tunable external-cavity semiconductor lasers" in: "Tunable Lasers Handbook" F.J. Duarte (Ed.), Academic Press, San Diego, CA (1995) 349-442.

[4] E. Hecht, "Optics" 4th ed., Addison Wesley, Reading, MA (2002).

APPENDIX D

UTILIZATION OF THE HITRAN DATABASE

The modeling of spectral lines can be a daunting task to the aspiring spectroscopist due both to the complexity of the matter and to the large number of available tools. These tools, which take the form of computer programs, can be broken down into two categories: spectral databases and spectral fitting/predicting programs. A list of several example tools in each category are given in Table D.1. Some programs listed are periodically updated.

Table D.1 Example spectral databases and fitting/prediction programs.

Database (year) [a]	Reference	Fitting/prediction program (year)	Reference
GEISA (2016)	[1]	JB95 (2016)	[2]
HITEMP (2010)	[3]	PGOPHER (2017)	[4]
HITRAN (2017)	[5]	SPFIT/SPCAT (1998)	[6]

[a] The year given is the most recently updated version of the database.

The differences between the two types of programs should be highlighted so the proper tool can be selected. Spectral databases contain large amounts of information on certain molecules (anywhere from one to several hundred molecules). This information is typically provided in the form of transition frequencies, transition probabilities/line strengths, broadening coefficients, and absorption cross-sections. The information in the database cannot be modified by the user but is instead available to be sorted through depending on the user's needs. Spectral fitting/prediction programs, on the other hand, are tools that allow for the user to either fit their own measured spectra or to predict a set of spectra for a molecule. Both the fitting and prediction of spectral lines are accomplished

through the use of a set of molecular parameters. Predicting the spectra of a molecule may be necessary if the molecule is less common and thus not included in a spectral database.

In this Appendix, basic aspects concerning the use of HITRAN are outlined. It should be noted that HITRAN is not a spectral absorption modeling code. Rather, HITRAN is a database that provides spectroscopic parameters such as transition frequencies and line strengths which can then be used to perform spectral absorption calculations. To perform spectral absorption modeling, the methods described in Section 3 can be used in conjunction with the spectroscopic parameters afforded by the HITRAN database.

D.1 Overview of the database

The HITRAN (**HI**gh-resolution **TRAN**smission) molecular absorption database was first released under this name in the 1986 edition with the goal of providing "a large database representing the discrete molecular transitions that affect radiative propagation throughout the electromagnetic spectrum" [7]. In accordance with this goal, the main information contained in the database are line-by-line lists of specific transitions between molecular energy levels. The other portion of the database includes absorption cross sections for molecules that are not amenable to line-by-line lists (e.g., heavy hydrocarbons). The focus of this Appendix is on the line-by-line portion of HITRAN.

HITRAN has experienced periodic updates since 1986 (e.g., [5, 8-10]). Additionally, a sister version of HITRAN called HITEMP was released in 2010 [3]. HITEMP contains many transitions that are negligibly weak at room temperature but become important at high temperatures, making it suitable for high-temperature predictions. However, HITEMP is limited to the molecules H_2O, CO_2, CO, NO, and OH.

D.2 The line-by-line format

The line-by-line portion of HITRAN contains information on individual molecular transitions. One possible output format is the 160-character format described in Table D.2. The 160-character format was implemented at the release of HITRAN 2004 [8] and utilizes a fixed-width text format. Using this format, a query of the HITRAN database on, say, 1000 transitions would result in a text file of 1000 rows, each row comprising 160 characters. A computer routine can be used to parse through such output text files and quickly return the desired parameters. The sorting programs described in App. D.1.3 can also provide convenient ways of accessing the desired data in HITRAN.

Table D.2 Description of the line-by-line, 160-character output format of HITRAN.

Symbol [a]	Units	Field length	Description
M	--	2	Molecule identifier
I	--	1	Isotopologue identifier
$\bar{v}_{12}$	[cm^{-1}]	12	Transition frequency
$S_{12,H}(T_0)$	[cm^{-1}/(molecule·cm^{-2})]	10	Line strength at T_0 [b]
A_{21}	[Hz]	10	Spontaneous emission coefficient
$\gamma_{air}(T_0)$	[cm^{-1}·atm^{-1}]	5	Air-broadening Lorentzian HWHM at T_0
$\gamma_{self}(T_0)$	[cm^{-1}·atm^{-1}]	5	Self-broadening Lorentzian HWHM at T_0
$\bar{E}''$	[cm^{-1}]	10	Lower state energy
n_{air}	--	4	Temperature exponent for γ_{air}
$\delta_{air}(T_0)$	[cm^{-1}·atm^{-1}]	8	Pressure shift coefficient in air at T_0
G'	--	15	Global upper quanta
G''	--	15	Global lower quanta
L'	--	15	Local upper quanta
L''	--	15	Local lower quanta
I_{err}	--	6	Uncertainty indices
I_{ref}	--	12	Error indices
*	--	1	Flag for line mixing
g'	--	7	Upper state statistical weight
g''	--	7	Lower state statistical weight

[a] The symbols used here were chosen to align with those in Section 3; HITRAN employs some symbols that are slightly different.
[b] T_0 = 296 K in HITRAN.

To acquaint the new user with the meaning of each parameter, a brief discussion of each is given below. For a more detailed discussion, see the Appendix of the HITRAN 1996 paper [11]. Some of the symbols used here for the various parameters were chosen for the sake of agreement with the symbolism used in Section 3; HITRAN employs slightly different terminology.

M and *I*

The molecule and isotopologue identifiers *M* and *I* are HITRAN-specific and can help the user ensure that the correct isotope of the correct molecule is being considered. The term "isotopologue" refers to a form of a molecule that varies only in its isotopic composition. Typically, the most common isotopologue is the most abundant by far. For example, according to HITRAN, the terrestrial abundance of $^{12}C^{16}O$ is 98.65%, while the second most-abundant isotopologue, $^{13}C^{16}O$, has an abundance of only 1.11%.

$\bar{v}_{12}$

The transition frequency is the center frequency at which a transition will take place. In the idealized (and unattainable) case of no broadening phenomena, absorption and emission would take place at only this precise frequency.

$S_{12,H}(T_0)$

The units of $S_{12,H}(T_0)$ are [cm^{-1}/(molecule·cm^{-2})]; the H in the subscript is present to highlight the different units. These units could be simplified to [cm/molecule]. However, this simplification would obscure the physical significance of this unit choice, which is wavenumbers (i.e., energy) per column number density. The HITRAN value of $S_{12,H}(T_0)$ has been weighted by the natural, terrestrial abundance of each isotopologue for a given molecule, meaning that no adjustment should be needed assuming a naturally occurring, terrestrial sample of the given molecule. This is a valid assumption for shock-tube experiments unless a study of a specific isotope is being conducted and a sample with concentrated amounts of that isotope are in use.

A_{21}

The Einstein spontaneous absorption coefficient has several utilities (for example, it is independent of both T and I_a), but the line strength is preferred for use herein. In HITRAN, $S_{12,H}(T)$ is related to A_{21} by

$$S_{12,H}(T) = I_a \frac{A_{21}}{8\pi c\, \bar{\nu}_{12}^2} \frac{g' \exp(-c_2 E''/T)(1-\exp(-c_2\, \bar{\nu}_{12}/T)}{Q(T)}. \tag{D.1}$$

This simply a statement of Eq. (3.35) in a different unit system: the units of S_{12} in Eq. (3.35) are [cm^{-2}·atm^{-1}] while the units of $S_{12,H}(T)$ in Eq. (D.1) are [cm^{-1}/(molecule·cm^{-2})]. Also, Eq. (D.1) contains a scaling factor for the abundance of the isotopologue corresponding to the transition, as stated earlier. c_2 [cm·K] is the second radiation constant:

$$c_2 = \frac{hc}{k}, \tag{D.2}$$

with a value of 1.438777 cm·K. The partition function $Q(T)$ is discussed in more detail in App. D.3.

$\gamma_{air}(T_0)$

This parameter is the Lorentzian broadening coefficient for air at 296 K (see Sect. 3.3.2).

$\gamma_{self}(T_0)$

This parameter is the Lorentzian broadening coefficient for the absorbing species

at 296 K (see Sect. 3.3.2). In dilute shock-tube laser experiments, the concentration of the absorber is typically quite low (< 3000 ppm), so this term will likely make a rather small contribution to the collisional FWHM but should still be included in calculations for completeness.

$\bar{E}''$

The energy level of the lower state of the transition plays an important role in the calculation of the line strength at temperatures other than T_0 (see Sect. 3.2.2).

n_{air}

This is the temperature exponent describing the power law dependence of $\gamma_{air}(T)$ on T. This parameter can be used as an estimate for the value of n_{self} since HITRAN does not contain a value for n_{self}.

$\delta_{air}(T_0)$

This is the collisional shift coefficient for air at 296 K. This value may be employed as an estimate for the collisional shifting due to other bath gases (e.g., Ar) in the absence of data for those gases. HITRAN does not contain any data on the temperature exponent m (see Sect. 3.3.4).

G', G'', L', and L''

These parameters identify the upper and lower quantum numbers of the transition. The parameters G' and G'' are "global" parameters and define in which band (electronic

and/or vibrational) of the molecule the transition of interest is located. The format and meaning of G' and G'' vary widely from molecule to molecule; a summary of the different options can be found in Table 3 of [8]. Similarly, the parameters L' and L'' are "local" parameters that define the precise location of the transition within the band specified by G' and G''. As with G' and G'', the format and meaning of L' and L'' vary widely from molecule to molecule and are summarized in Table 4 of [8]. Several example cases are shown in Table D.3.

Table D.3 Sample global and local quantum numbers using the HITRAN format.

Molecule	G'	G''	"Global" interpretation	L'	L''	"Local" interpretation
H_2O	0 1 0	0 0 0	v_2 fundamental band	6 1 6	7 4 3	$6_{1,6} \leftarrow 7_{4,3}$
H_2O	1 0 1	00 0	$v_1 + v_3$ combination band	5 5 1	5 5 0	$5_{5,1} \leftarrow 5_{5,0}$
CO	2	1	2←1 band		R 21 [a]	22 ← 21
CO	3	0	3←0 band		P 48 [a]	47← 48

[a] In some cases, certain quantum numbers might not be specified. For example, here L' is empty and only R(J'') or P(J'') are given since this specifies both J'' and J' (see Sect. 2.2.3).

I_{err}, I_{ref}

I_{err} and I_{ref} are the error and reference indices, respectively. I_{err} is a six-digit code that indicates the estimated uncertainty of each of six parameters: $\bar{\nu}_{12}$, $S_{12,H}(T_0)$, $\gamma_{air}(T_0)$, $\gamma_{self}(T_0)$, n_{air}, and $\delta_{air}(T_0)$. Each digit is a value from 0-8; the uncertainty associated with each value of 0-8 is described in Table 5 of the HITRAN 2004 publication [8]. Similarly, I_{ref} is a 12-digit code that indicates the source of the same six parameters according to the HITRAN reference list. This list of references can be found for each version of HITRAN at the official HITRAN website, https://hitran.org.

*

This parameter is a flag that indicates if line-mixing data are available for the selected transition. Line mixing is a complicated phenomenon that involves the transfer of energy from weakly absorbing regions to strongly absorbing regions. In the 2004 version of HITRAN, only CO_2 had line-mixing data available, but subsequent versions of HITRAN have continually added more line-mixing data. Line-mixing data is not available in the standard HITRAN database; rather, the line-mixing flag is meant to alert the user to the availability of line-mixing data, which can often be found in the references associated with that transition. See Chapter IV of Hartmann et al. [12] for an introduction to line mixing.

g', g''

The parameters g' and g'' are the upper- and lower-level statistical weights (i.e., degeneracies), respectively.

D.3 Using HITRAN at high temperatures

As indicated in Table D.3, the parameters stored in the HITRAN database are given at the reference temperature T_0 (296 K), making them inappropriate for the high temperatures of shock-tube experiments. Thus, a method of scaling these parameters from T_0 to the desired experimental temperature T is needed. The HITRAN parameters related to collisional broadening (i.e., $\gamma_{air}(T_0)$, $\gamma_{self}(T_0)$, n_{air}, and $\delta_{air}(T_0)$) can be scaled from T_0 to T using the power-law formulations discussed in Sect. 3.3. The transition center $\bar{\nu}_{12}$ is independent of temperature. In the HITRAN units of [cm^{-1}/(molecule·cm^{-2})], $S_{12,H}(T)$ can be written as

$$S_{12,H}(T) = S_{12,H}(T_0)\frac{Q(T_0)}{Q(T)}\left[\frac{\exp(-c_2\bar{E}''/T)}{\exp(-c_2\bar{E}''/T_0)}\right]\left[\frac{1-\exp(-c_2\,\bar{\nu}_{12}/T)}{1-\exp(-c_2\,\bar{\nu}_{12}/T_0)}\right]. \quad \text{(D.3)}$$

Equation (D.3) differs from Eq. (3.36) in the absence of the term $\frac{T_0}{T}$ due to the choice of units. Both Eq. (3.36) and Eq. (D.3) require knowledge of $Q(T)$.

The partition function $Q(T)$ is defined in Eq. (3.30) and increases with temperature as the higher energy levels of the molecule become more populated. Before the advent of modern computing, simplifying assumptions were often made to approximate $Q(T)$ [13]. In modern applications, detailed calculations of the various energy levels of a molecule yield tabulated values of the partition function as a function of temperature for that molecule; these tabulated values are often referred to as total internal partition sum (TIPS). A HITRAN user who wishes to scale the line strength of a molecule to a temperature other than T_0 will need to access tabulated values of TIPS. An example of such values are those provided by Laraia et al. [14], who calculated values of $Q(T)$ over the temperature range 70-3000 K for a variety of molecules. HITRAN 2016 [5] contains its own set of partition sums that can be accessed at https://hitran.org.

As stated, $S_{12,H}(T_0)$ is given by HITRAN in units of [cm^{-1}/(molecule·cm^{-2})]. To convert from [cm^{-1}/(molecule·cm^{-2})] to [cm^{-2}·atm^{-1}], the use of the Loschmidt number is required. The Loschmidt number $N_{L,0}$ [molecule/(cm^3)] gives the number density of molecules at a standard pressure and temperature.[1] The recommended value of $N_{L,0}$ at 273.15 K and 1 atm is 2.6867811 × 10^{19} molecule/(cm^3) [15]. Assuming ideal-gas

[1] Actually, the recommended value is given in units of number density, [1/m^3], as most authors choose to exclude the units of [molecule] from their definitions and leave them implied. However, because HITRAN explicitly includes [molecule] in its definition of $S_{12,H}(T_0)$, [molecule] is included here in $N_{L,0}$.

behavior, the Loschmidt number N_L at a temperature T can be obtained by

$$N_L(T) = N_{L,0}\left(\frac{273.15}{T}\right). \tag{D.4}$$

Evaluating Eq. (D.4) at 296 K, $N_L(T_0) = 2.4794 \times 10^{19}$ molecule/(cm^3). Recalling that $N_{L,0}$ and $N_L(T_0)$ are both defined at 1 atm, the line strength $S_{12}(T_0)$ in [cm^{-2}·atm^{-1}] can be obtained by multiplying the HITRAN value (in units of [cm^{-1}/(molecule·cm^{-2})]) by 2.4794 × 10^{19} molecules/(cm^3·atm), or

$$S_{12}(T_0) = 2.4794 \times 10^{19}\, S_{12,H}(T_0). \tag{D.5}$$

$S_{12}(T_0)$ can then be scaled to other temperatures using Eq. (3.36) with tabulated values of $Q(T)$.

D.4 Sorting through HITRAN

The HITRAN 2016 database contains line-by-line information on 49 molecules with a total of over 9 million lines. The importance of sorting through the database becomes clear in light of this enormous size. Sorting programs make accessing HITRAN tenable, allowing for results to be filtered by molecule, isotopologue, wavenumber range, line strength, and even by spectral band. Most modern databases provide their own methods of sorting through the database, and user-developed programs are also often available. For HITRAN, two modern tools for sorting through the database are the HITRAN Application Programming Interface (HAPI) [16] and the online interface available at https://hitran.org.

Note that hitran.org allows for the user to select the desired output format, thus freeing the user from the 160-character output of HITRAN 2004. An older sorting program called JavaHAWKS (**Java H**ITRAN **A**tmospheric **W**or**KS**tation) is also useful but is no longer supported and thus may experience hang-ups when sorting through versions of HITRAN released since the 2004 version.

D.5 Summary

The HITRAN database is a powerful tool that is undergoing constant updates and improvements. With such a wealth of information, however, comes complexity. This Appendix has briefly covered the identity and significance of the various HITRAN outputs in the 160-character format. The use of HITRAN at high temperatures was also covered, with particular attention granted to the oft-confusing units of the line strength. A few sorting tools were also mentioned, which are invaluable in sifting through the huge amount of data afforded by HITRAN.

D.6 References

[1] N. Jacquinet-Husson, R. Armante, N.A. Scott, A. Chédin, L. Crépeau, C. Boutammine, A. Bouhdaoui, et al., "The 2015 edition of the GEISA spectroscopic database" *Journal of Molecular Spectroscopy* **327** (2016) 31-72.

[2] D. Plusquellic, "JB95 spectral fitting program", v6.02.00 (2016), accessed May 1 2019, www.nist.gov/services-resources/software/jb95-spectral-fitting-program

[3] L.S. Rothman, I.E. Gordon, R.J. Barber, H. Dothe, R.R. Gamache, A. Goldman, V.I. Perevalov, et al., "HITEMP, the high-temperature molecular spectroscopic database" *Journal of Quantitative Spectroscopy and Radiative Transfer* **111** (2010) 2139-2150.

[4] C.M. Western, "PGOPHER: A program for simulating rotational, vibrational and electronic spectra" *Journal of Quantitative Spectroscopy and Radiative Transfer* **186** (2017) 221-242.

[5] I.E. Gordon, L.S. Rothman, C. Hill, R.V. Kochanov, Y. Tan, P.F. Bernath, M. Birk, et al., "The HITRAN2016 molecular spectroscopic database" *Journal of Quantitative Spectroscopy and Radiative Transfer* **203** (2017) 3-69.

[6] H.M. Pickett, R.L. Poynter, E.A. Cohen, M.L. Delitsky, J.C. Pearson, H.S.P. Müller, "Submillimeter, millimeter, and microwave spectral line catalog" *Journal of Quantitative Spectroscopy and Radiative Transfer* **60** (1998) 883-890.

[7] L.S. Rothman, R.R. Gamache, A. Goldman, L.R. Brown, R.A. Toth, H.M. Pickett, R.L. Poynter, et al., "The HITRAN database: 1986 edition" *Applied Optics* **26** (1987) 4058-4097.

[8] L.S. Rothman, D. Jacquemart, A. Barbe, D.C. Benner, M. Birk, L.R. Brown, M.R. Carleer, et al., "The HITRAN 2004 molecular spectroscopic database" *Journal of Quantitative Spectroscopy and Radiative Transfer* **96** (2005) 139-204.

[9] L.S. Rothman, I.E. Gordon, A. Barbe, D.C. Benner, P.F. Bernath, M. Birk, V. Boudon, et al., "The HITRAN 2008 molecular spectroscopic database" *Journal of Quantitative Spectroscopy and Radiative Transfer* **110** (2009) 533-572.

[10] L.S. Rothman, I.E. Gordon, Y. Babikov, A. Barbe, D.C. Benner, P.F. Bernath, M. Birk, et al., "The HITRAN2012 molecular spectroscopic database" *Journal of Quantitative Spectroscopy and Radiative Transfer* **130** (2013) 4-50.

[11] L.S. Rothman, C.P. Rinsland, A. Goldman, S.T. Massie, D.P. Edwards, J.-M. Flaud, A. Perrin, et al., "The HITRAN molecular spectroscopic database and HAWKS (HITRAN Atmospheric WorKStation): 1996 edition" *Journal of Quantitative Spectroscopy and Radiative Transfer* **60** (1998) 665-710.

[12] J.-M. Hartmann, C. Boulet, D. Robert, "Collisional Effects on Molecular Spectra", Elsevier Science, Amsterdam, Netherlands (2008).

[13] R.W. Zwanzig, "Transition from quantum to "classical" partition function" *Physical Review* **106** (1957) 13-15.

[14] A.L. Laraia, R.R. Gamache, J. Lamouroux, I.E. Gordon, L.S. Rothman, "Total internal partition sums to support planetary remote sensing" *Icarus* **215** (2011) 391-400.

[15] P.J. Mohr, D.B. Newell, B.N. Taylor, "CODATA recommended values of the fundamental physical constants: 2014" *Journal of Physical and Chemical Reference Data* **45** (2016) 043102.

[16] R.V. Kochanov, I.E. Gordon, L.S. Rothman, P. Wcisło, C. Hill, J.S. Wilzewski, "HITRAN Application Programming Interface (HAPI): A comprehensive approach to working with spectroscopic data" *Journal of Quantitative Spectroscopy and Radiative Transfer* **177** (2016) 15-30.